MONTE CARLO LAGRANGIAN MODELING OF ICE MICROPHYSICAL PROCESSES IN WINTERTIME CLOUDS

DISSERTATION

ZUR ERLANGUNG DES GRADES

"DOKTOR DER NATURWISSENSCHAFTEN"

AM FACHBEREICH PHYSIK, MATHEMATIK UND INFORMATIK

DER JOHANNES GUTENBERG-UNIVERSITÄT
IN MAINZ

VORGELEGT VON

JAN-NIKLAS WELSS

GEB. AM 27.12.1992 IN NEUSTADT AM RBG.

HANNOVER, DEN 28.08.2025

This dissertation was recommended for acceptance by

SUPERVISORS:
1. Examiner: Prof. Dr. Peter Spichtinger
2. Examiner: Dr. habil. Miklós Szakáll

The **oral examination** took place on **November 18, 2025**.

Jan-Niklas Welß: *Monte Carlo Lagrangian Modeling of Ice Microphysical Processes in Wintertime Clouds*

ABSTRACT

This study explores the intricate processes governing ice microphysics, particularly the evolution of ice habits and their consequential impact on cloud microphysics and precipitation patterns. Leveraging the Lagrangian Monte-Carlo ice microphysics model *McSnow*, several methodological advancements are introduced to refine the representation of ice habits.

McSnow is extended by an explicit habit prediction scheme, combined with the hydrodynamic theory of Böhm. Böhm's original cylindrical shape assumption for prolates is compared against recent lab results, showing that interpolation between cylinder and prolate yields the best agreement. For constant temperature and supersaturation, the predicted mass, size, and density agree well with the laboratory results, and a comparison with real clouds using the polarizability ratio shows regimes capable of improvement.

An updated form of the inherent growth function to describe the primary habit growth tendencies is proposed and combined with a habit-dependent ventilation coefficient. The modifications contrast the results from general mass size relations and significantly impact the main ice microphysical processes. Depending on the thermodynamic regime, ice habits significantly alter depositional growth and affect aggregation and riming.

The findings underscore the critical importance of explicit ice habit prediction in accurately capturing the variability inherent in ice microphysics. Through comprehensive simulations, the research demonstrates that these detailed representations are essential for modeling the complex feedback mechanisms that occur between microphysical processes and large-scale cloud dynamics. This is especially pertinent in mixed-phase clouds, where the interaction of liquid and ice phases exerts a substantial influence on cloud longevity, precipitation efficiency, and radiative properties. A key aspect of the research involves synthesizing model simulations with observational data to enhance the realism of the simulations. By incorporating polarimetric radar observations, the study evaluates microphysical processes within more realistic atmospheric scenarios. Although constrained to one-dimensional simulations, these efforts yield significant insights into the feedback loops between cloud microphysics and cloud dynamics, with a particular focus on mixed-phase cloud conditions. The study thereby highlights the necessity of observational data in both validating and refining model outputs.

In addition to the advancements in microphysical modeling, the research addresses the phenomenon of secondary ice production (SIP), with particular emphasis on ice-ice collisions and fragmentation processes. A revised fragmentation model is proposed, which incorporates an approach for the fragmentation potential based on fragility of particles. This development is essential for elucidating the rapid increases in ice particle concentrations observed in certain cloud regimes, which hold profound implications for cloud evolution and precipitation development.

The implications of these findings are far-reaching, particularly in the context of atmospheric modeling, where they contribute to enhancing the accuracy of weather forecasting and climate models. The study concludes by identifying several avenues

for future research, including the need for further laboratory experiments aimed at refining our understanding of ice habits and their role in cloud microphysical processes. Higher-dimensional simulations, coupled with the integration of advanced observational techniques, can serve as a crucial step forward in advancing the field of cloud microphysics.

Ultimately, this research contributes to the ongoing efforts to improve the fidelity of atmospheric models, thereby supporting the broader objectives of advancing weather prediction, cloud process understanding, and climate modeling.

Contents

List of Figures

List of Tables

1

INTRODUCTION

1.1 THE MOTIVATION FOR ADVANCING CLOUD MICROPHYSICAL MODELS

In the atmospheric realm, microphysics investigates the physical and chemical effects that arise at the level of individual cloud and precipitation particles, known as hydrometeors. Inside clouds, atmospheric conditions are highly variable, often containing gaseous, liquid, and frozen water simultaneously in spatial and temporal heterogeneity (e. g. Morrison et al., 2012). Clouds are fundamental modulators of Earth's climate and hydrological cycle, yet their accurate representation remains a formidable challenge in atmospheric modeling due to the intricate microphysical processes governing their formation, evolution, and radiative properties. The complex transitions involving all three phases are challenging when trying to describe and understand the microphysical processes within mixed-phase clouds (Morrison et al., 2020). The hydrometeors undergo complex processes, such as nucleation, growth via water vapor diffusion, sublimation, collision and coalescence mechanisms, freezing and melting, evaporation and secondary ice production (SIP) mechanisms. The existence of aerosol of varying type can modify processes and interact with hydrometeors (Fan et al., 2016; Flossmann and Wobrock, 2010). Within these complex mixed-phase cloud environments, where supercooled liquid water and ice crystals coexist, SIP mechanisms may play a critical role. Unlike primary nucleation, SIP can rapidly amplify ice crystal concentrations, fundamentally altering cloud glaciation, radiative properties, and precipitation development. Therefore, a comprehensive understanding of mixed-phase cloud microphysics necessitates detailed investigation into these critical ice multiplication processes.

When attempting to comprehend the intricate interplay of the aforementioned processes that frequently result in feedbacks within cloud dynamics, it is necessary to understand the processes on a molecular scale to examine the impact that individual particles can have on singular clouds, mesoscale systems, or even cyclones. Given the vast number and variability of hydrometeors in the atmosphere compared to limited observation capabilities, the scientific community faces the daunting task of filling knowledge gaps. Despite significant advancements in atmospheric science, a critical knowledge gap persists in accurately representing complex ice microphysical processes within mixed-phase clouds, particularly concerning the intricate interplay of hydrometeors. This uncertainty propagates directly into the predictive capabilities of Numerical Weather Prediction (NWP) and climate models, impacting forecasts of precipitation, cloud lifetime, and radiative forcing. Interactions involving ice crystals are challenging because of the variety of possible shapes, often referred to as *ice crystal habits*. These ice habits and their characteristics are critical for the cold phase microphysical processes as they influence sedimentation, deposition/sublimation, riming, aggregation, and especially radiative properties. In particular, cloud-radiative interactions have been identified as a major source of uncertainty in NWP and climate models (Bodas-Salcedo et al., 2019; Climate Change (IPCC), 2023).

Specialized observational methods to gather information on the rates of ice-microphysical processes are constantly being developed and improved, ranging from ground and in-situ (e. g. Field et al., 2004; Locatelli and Hobbs, 1974) to remote sensing observations (e. g. Dias Neto et al., 2019; Tridon et al., 2019). Classification and categorization of observed ice particles is an ongoing task (Bailey and Hallett, 2009; Kikuchi et al., 2013). This helps to link the occurrence of ice crystal types to specific atmospheric conditions. Although these efforts yield datasets covering a range of variables, they only partially permit the attribution of effects to specific processes. This is due to the fact that different processes frequently overlap and are rarely observed in isolation.

The temperature dependence of snow crystal growth by deposition was first studied experimentally by Nakaya's group and published in Nakaya (1954). In a convection cloud chamber, it was observed that typical ice habits evolve within specific temperature regimes. Plate-like crystals form between temperatures of $0\,°C$ and about $-3\,°C$, as well as between $-9\,°C$ to about $-22\,°C$. Meanwhile, columnar or needle-shaped crystals form between temperatures of $-3°$ to $-9°$ and below $-22\,°C$. J and Mason (1958) use a diffusion cloud chamber to confirm the transition temperatures while showing that supersaturation has only a small effect, laying the groundwork for theories based on ice crystal formation mechanisms that are largely independent of supersaturation. Kobayashi (1961) constructed the first habit diagram based on the above results, often referred to as the "Nakaya diagram". The free-fall experiments conducted by Gonda (1980), Takahashi and Fukuta (1988), and Takahashi et al. (1991) support the observed growth regimes.

A recent version of the Nakaya diagram shown in Figure 1.1 (Libbrecht, 2023), includes not only a temperature dependence but also a supersaturation dependence, which was found to be essential for the formation of strong habits such as needles and dendrites. Note that this visualization is a simplified habit diagram for temperatures ranging from $T \in [0, -30]\,°C$ because the focus of this thesis will be on mixed-phase clouds and the primary and secondary habits present within them. Nakaya's original diagram, while groundbreaking, did not fully account for the formation of certain complex ice habits, such as polycrystalline ice, which consists of multiple individual ice crystal grains. This 'polycrystalline regime,' observed at specific temperature and supersaturation conditions, poses a particular challenge for habit prediction due to its intricate internal structure and its potential influence on particle properties and interactions. A comprehensive habit diagram that includes polycrystalline and other intricate geometries is available in Bailey and Hallett (2009, Fig. 5) for temperatures as low as $T = -70\,°C$.

One typical characteristic of ice crystals is their hexagonal prismatic shape, which is the original shape of both plates and columns. Several theories have been developed to explain why the hexagonal prismatic shape, adopted by small crystals, gives rise to different habits. According to Kuroda and Lacmann (1982) and Nelson (1998), layer nucleation can explain the primary features (and some of the secondary features) of the habits of snow crystals. Libbrecht (2017) find that layer nucleation plays a particularly important role and that the step energies are strongly temperature dependent. Attachment kinetics is the primary growth factor for small crystals, causing faceting. However, as the crystals get larger, their development becomes limited by diffusion, resulting in branching corners. This thesis does not cover the complete theory of crystal growth. The reader can refer to the aforementioned works

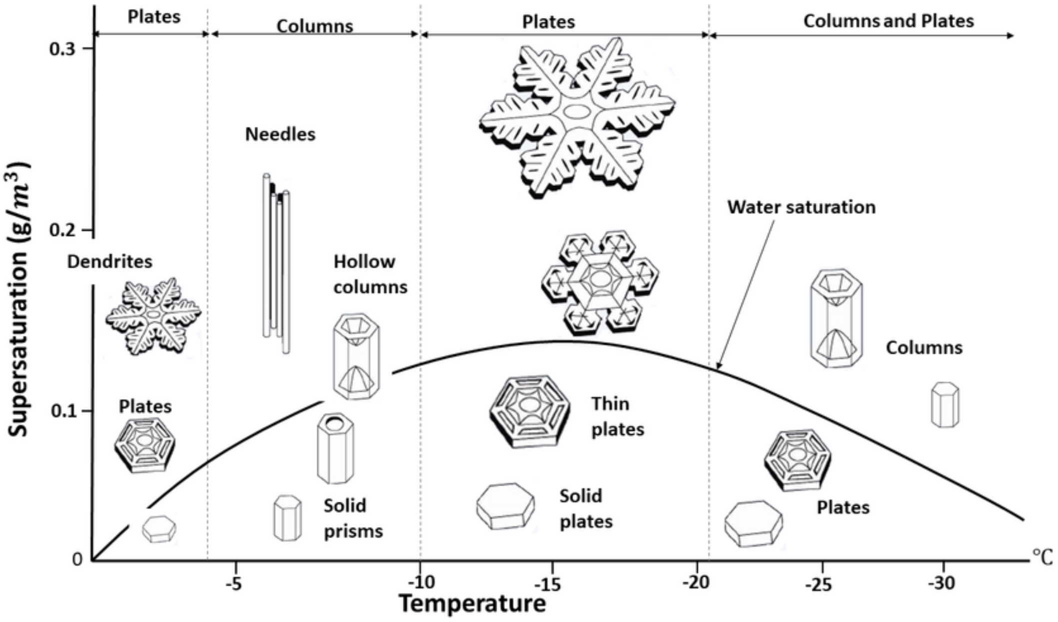

Figure 1.1: The Nakaya Diagram was originally published by Nakaya (1954). This particular version can be found at Libbrecht (2023). It is noteworthy that the formation of polycrystals can be observed at temperatures below $T < -20,^\circ C$.

and publications contained within them, as well as Pruppacher and Klett (1997). Laboratory measurements such as Takahashi et al. (1991) or Connolly et al. (2012) allow process isolation, but lack representation of the full range of atmospheric conditions and especially the transition from isolation to a fully interactive system. As a result, the resulting physical descriptions can become highly specialized and are often only generalizable by assuming certain atmospheric conditions or categorizing ice habit, introducing artificial thresholds. The challenge posed by individual growth histories under changing conditions is to describe the variety of simple (columns, plates) and more complex (branched and polycrystalline) ice habits coexisting with aggregates composed of crystals of different shapes and numbers.

The ever-changing atmospheric conditions affect the dynamic evolution of ice particles, leading to uncertain cloud microphysical descriptions in Large Eddy Simulation (LES), Numerical Weather Prediction (NWP), and climate models. In order to comprehend the implications of the models' representation of ice habits, this section seeks to elaborate on the general characteristics of the microphysical schemes that are utilized in these models.

One- or two-moment *bulk* schemes, such as those proposed by Kessler (1969), Koenig and Murray (1976), Lin et al. (1983), and Seifert and Beheng (2006), respectively, provide predictions for total mass or number concentration and summarize bulk cloud properties. Alternatively, three-moment schemes, such as those introduced by Milbrandt and Yau (2005) and Naumann and Seifert (2016), incorporate additional information like radar reflectivity. The bulk properties like density and fall speed are usually assumed to be hydrometeor-specific so that they follow a fixed form. The physical characteristics, including density and fall speed, are typically considered to pertain specifically to hydrometeors, which adhere to a standard format.

Although this simplifies the description of microphysics, it presents some challenges.

While the distributions of cloud water and rain water can be distinguished in the liquid phase, there are additional types of hydrometeors during the ice phase, such as cloud ice, snow, graupel, and hail. The categorization of ice necessitates multiple conversion processes to describe the transition from cloud ice to snow. This can be problematic because cloud ice may grow through various mechanisms such as vapor deposition, aggregation, and riming. In addition, the phase conversion leads to significant modifications in the bulk particle properties presumed for the revised classification, resulting in disjointed development of the particle range.

A more advanced method of microphysical modeling involves utilizing *bin* schemes. *Bin* schemes (e. g. Egan and Mahoney, 1972; Khain et al., 2008; Mason and Ramanadham, 1954, among others) can explicitly evolve the microphysical properties by predicting several variables within a "bin" or spectral range to represent the particle distributions by discrete distribution functions. This allows for independent evolution of microphysical variables within categories, without the assumption of bulk properties. The expansion of degrees of freedom to individually predict variables in each category results in a significant increase in computational requirements that scale with the number of properties whose distributions are evolved. This level of complexity is conceptually fitting for high model resolutions, where it can be argued that understanding cloud processes impacts the prediction beyond the bulk properties. Even at high resolutions in LES models, vanZanten et al. (2011) find that the differences in liquid water path (LWP) and the resulting precipitation flux are large, and the distributions between bulk and bin models are comparable. Eulerian models imply a continuous medium to predict particle-size distributions (PSDs). On the other hand, particle-based models offer a distinct approach.

The *Lagrangian particle-based* approach, also referred to as *Lagrangian particle modeling*, uses stochastic sampling to approximate the population of hydrometeors within clouds and explicitly predict PSD evolution (e. g. Andrejczuk et al., 2008; Brdar and Seifert, 2018; Ervens et al., 2011; Riechelmann et al., 2012; Shima et al., 2020; Sölch and Kärcher, 2010). A particle-based approach enables representing particle-level process knowledge and including additional predicted attributes without a significant increase in computational costs. One approach to reduce the computational cost is to represent a multitude of real particles with a single particle commonly referred to as "super-particles" (Shima et al., 2009). When ensuring numerical convergence for the collision process (Unterstrasser et al., 2017), this technique allows for particle-level simulations in box models up to complex three-dimensional experiments with limited numerical resources.

While bin and particle-based models offer unparalleled process detail, their computational expense remains a barrier for operational use. machine learning (ML) models trained on these detailed simulations can bridge this gap by emulating complex processes at a fraction of the cost (Lagerquist et al., 2021; Ukkonen, 2022). Recently, ML methods have emerged as a powerful complement to physics-based modeling, offering pathways to develop semi-automatic workflows from high-resolution simulations to computationally efficient parameterizations (Bauer et al., 2021; Seifert and Rasp, 2020; Seifert and Siewert, 2024). Supervised learning approaches, such as neural networks, can mimic physical process rates and retain interpretability and mass conservation, resembling traditional parameterizations.

All of the above models usually require specific geometric models of ice particles unless they explicitly forecast the hydrometeor shape. Mass-size and mass-area relations may be able to describe the average geometry of certain ice habits (Auer and Veal, 1970; Mitchell, 1996; Um et al., 2015), but cannot represent the natural variety and transitions due to the use of thresholds. Overcoming the threshold between ice categories to allow a natural transition is a goal of modern microphysical schemes (Liu et al., 2023; Milbrandt et al., 2021; Morrison and Grabowski, 2008). A notable approach to solving these challenges is the P3 (Predicted Particle Properties) scheme proposed by Morrison and Milbrandt (2015), which abandons fixed hydrometeor categories in favor of prognostic variables like rime mass and volume (alternate versions by Milbrandt and Morrison, 2016; Milbrandt et al., 2021). The P3 scheme allows for continuous transitions between hydrometeor types, such as snow to graupel, reflecting the physical nature of riming processes (Milbrandt et al., 2021; Seifert et al., 2012).

Previous studies show that it is generally beneficial to explicitly resolve habit development to improve the microphysical representation of ice in models: Jensen et al. (2017) show an effect of ice habit on the spatial precipitation pattern, Hashino and Tripoli (2007) find that dendrites extend dendritic growth regions further than atmospheric conditions suggest, and Sulia and Harrington (2011) conclude that the absence of ice habit underestimates ice growth and cloud glaciation time. Also, only models that resolve the evolving crystal shapes can make use of the wealth of data provided by radar polarimetry (Trömel et al., 2021) and combine the approaches to identify gaps in the interpretation of observations as well as in the microphysical descriptions when modeling clouds and precipitation (von Terzi et al., 2022).

1.1.1 *The Treatment of Ice Habits in Numerical Models*

To fully evaluate the effects of dynamically developing habits, detailed descriptions of processes at the particle level are needed. The approach of Chen and Lamb (1994b) simplifies the ice habits of individual crystals as porous spheroids. The scheme predicts the shape and density of ice particles, helping to depict the natural evolution of ice habits and minimizing artificial type classification. While no natural crystal resembles a spheroid, Jayaweera and Cottis (1969) show that spheroids are suitable for representing columnar or plate-like ice crystals. However, even a simplified geometry requires changes in the process description: Vapor growth depends crucially on the particle shape, which affects the water vapor field around the particle. The theoretical framework of Böhm allows the consideration of ice habits for fall speed and collision effects based on spheroids (Böhm, 1989, 1992a,b,c, 1994, 1999). In light of the constraints identified in the discussion of Böhm's theory in reference Böhm (2004), we conclude that it should be regarded as a parameterization rather than as a comprehensive, rigorous theory.

Based on investigations for oblates (Pitter et al., 1974), Hall and Pruppacher (1976) deduce that the ventilation is independent or only slightly dependent on the particle shape, but recent results suggest that this assumption underestimates the ventilation for prolate particles of larger sizes (Wang and Ji (2000), Ke et al. (2018) and others). For the collision of ice crystals with droplets, the results of Wang and Ji (2000) suggest the existence of preferred riming regions depending on the Reynolds number, which are difficult to represent in the spheroidal approach. Nevertheless, having a consistent and physically-based description of terminal fall velocity and collision efficiency is

very valuable in the framework of a particle-based habit prediction.
While it might not capture the details of the actual process, Jensen and Harrington (2015) propose a way to distribute rime on the particle surface perpendicular to the flow in an effort to evaluate the effect of ice habits on the onset of riming. The likelihood of ice crystal aggregation is enhanced by non-spherical geometry models because an increased cross-sectional area is a direct factor. However, it is difficult to describe the geometry of the resulting aggregates because of the many degrees of freedom involved in the collision event. Several descriptions attempt to characterize the geometry of aggregates after collisions (Chen and Lamb, 1994a; Gavze and Khain, 2022; Shima et al., 2020) but a general and accurate parameterization is not yet available.
Hoffmann (2020) (based on Ervens et al., 2011) and Shima et al. (2020) present first Lagrangian particle-based cloud models to predict ice morphologies based on the work of Chen and Lamb (1994b). Hoffmann (2020) uses empirical relations of Mitchell (1996) for the terminal velocity of ice crystals, and does not consider collisions of hydrometeors. Shima et al. (2020) use the theory of Böhm for the terminal velocity of ice crystals, but use a framework combining Beard and Grover (1974) and Erfani and Mitchell (2017) to describe the influence of habit on collision effects.

A more accurate representation of ice crystal habits is not merely a theoretical refinement; it is crucial for improving the interpretation of polarimetric radar observations, enhancing the simulation of latent heat release profiles, and refining estimates of cloud radiative forcing.

1.1.2 *Advances in Radar Observations and Ice Microphysical Process Fingerprints*

Recent satellite-based studies of Mülmenstädt et al. (2015), Field and Heymsfield (2015), or Heymsfield et al. (2020) emphasize the critical need to comprehend ice growth processes within clouds, as it has been determined that more than 60 % of global precipitation originates from the ice phase. Remote sensing tools, including meteorological radars, allow the study of clouds and precipitation over large areas and extended time periods, providing valuable insights into the spatiotemporal dynamics of microphysical processes (Brauer et al., 2024, e. g.). Numerous studies have demonstrated the application of millimeter-wave radar in retrieving profiles of ice water content (IWC) within clouds (e. g. Hogan et al., 2006). Nevertheless, the use of single-frequency radar is constrained by its inability to simultaneously determine microphysical characteristics such as ice particle size and shape without the reliance on empirical relations. To overcome this limitation, additional measurements are required to constrain multiple parameters, including IWC, size, and shape.
Promising techniques for obtaining microphysics information include the use of polarimetry and multi-frequency radar observations, as these leverage the scattering characteristics of ice particles. A typical example of a multi-frequency technique is the selection of a frequency in the Rayleigh regime, in which the particle size is significantly smaller than the radar wavelength, and the choice of a second frequency to be in the Mie regime, where the particle size is either comparable to or larger than the radar wavelength. Polarimetric radars offer the ability to detect signatures of processes like dendritic growth and SIP by transmitting and receiving polarized

electromagnetic waves. For illustrative examples of this approach, see the work of Matrosov (1998) and Gosset and Sauvageot (1992) on dual frequency, and Gaussiat et al. (2003) and Yoshida et al. (2006) on triple frequency techniques.

Various factors, including the presence of supercooled liquid water, particle sizes, temperature ranges, and interactions between liquid and ice particles, suggest different plausible SIP processes, each leaving unique fingerprints in the radar Doppler spectra (Kalesse et al., 2016; Schrom and Kumjian, 2016; Schrom et al., 2015; Shupe et al., 2004).

Vertically-pointing radars that measure multimodal Doppler spectra can detect hydrometeor populations with different characteristics within a single radar resolution volume, providing critical insights into precipitation microphysics. This method allows visualization of spatiotemporal features in radar time series, highlighting different mechanisms at different stages of a precipitation event. For example, Ryzhkov et al. (2016) and Griffin et al. (2018) employ the quasi-vertical profiles method to examine polarimetric radar data with the objective of studying the temporal evolution of microphysical processes that control precipitation production. Oue et al. (2018) combine quasi-vertical profiles with Doppler spectra from zenith-pointing radar to gain insight into mixed-phase clouds in Arctic deep precipitation systems. Barrett et al. (2019) use triple-wavelength Doppler spectrum radar analysis to identify regions of rapid aggregation and estimate the ice particle size distribution.

Such analysis, in conjunction with numerical models, can be employed to identify explanations for the discrepancy between ice nucleating particles (INP) and ice particle number concentration (IPNC) that has been reported by numerous studies like Hobbs et al. (1980), Kanji et al. (2017), Wex et al. (2019), or Petters and Wright (2015). A promising hypothesis is based on the occurrence of SIP processes which are assumed to play a critical role in the microphysics of clouds and precipitation. Although definitive proof of the occurrence of specific SIP mechanisms is challenging, radar data can provide several independent lines of evidence to support the proposed interpretations of ice microphysical process (IMP) fingerprints.

1.1.3 *Secondary Ice Production*

In contrast to primary ice production, which occurs at temperatures above −38 °C and necessitates the presence of active INPs for heterogeneous nucleation, SIP can amplify IPNC by several orders of magnitude (e. g. Sotiropoulou et al., 2024; Zhao et al., 2023). This increase affects the phase partitioning in mixed-phase clouds and influences precipitation patterns (Dedekind et al., 2023). An impact on the radiation budget has been found by both Sun and Shine (1994) and Young et al. (2019). Various mechanisms for ice multiplication have been identified and are critically discussed (Field et al., 2017; Korolev and Leisner, 2020). The three primary processes that are frequently highlighted in the literature will be introduced here.

The Hallett-Mossop (H-M) process, also referred to as rime splintering, occurs when supercooled water droplets rime onto ice particles, resulting in the production of ice splinters. This process is most efficient between temperatures of −8 °C and −3 °C, with peak effectiveness observed at −5 °C. However, the efficacy of this process remains a topic of debate due to conflicting experimental results, as evidenced by

Hartmann et al. (2023) and studies cited in Korolev and Leisner (2020).

Another SIP mechanism involves the shattering of supercooled droplets upon freezing upon contact with an ice particle or INP, a process documented by Takahashi and Yamashita (1977) and Phillips et al. (2018). In contrast to HM, droplet shattering is not limited to a specific temperature range. It occurs in both colder and warmer conditions, as evidenced by studies on raindrops recirculating above the melting layer (Korolev et al., 2020; Lauber et al., 2021).

Furthermore, secondary ice fragments can be generated through ice-ice collisions, particularly in turbulent areas or when ice particles exhibit different settling velocities. This phenomenon has been observed in various studies, including those by Vardiman (1974), Takahashi et al. (1995), and Schwarzenboeck et al. (2009). Collisional break-up is considered a significant source of secondary ice particles in specific settings, such as wintertime alpine clouds (Dedekind et al., 2021), particularly within the frequent seeder-feeder cloud configurations observed in Switzerland (Georgakaki et al., 2022; Grazioli et al., 2015; Proske et al., 2021). However, the precise physical mechanisms behind this process remain a topic of debate (Korolev and Leisner, 2020). The presence of rimed particles is believed to play a crucial role (Phillips et al., 2017a,b), as these particles, with their greater mass and fall speed, are more likely to cause effective break-up during high-energy collisions with other ice particles. Recent studies of SIP have demonstrated that it can cause extensive changes in IPNC in models, which helps to explain the mismatch under certain conditions. Still, there are significant gaps in the understanding of the underlying physics. Coupled with the lack of systematic laboratory studies, the development of physical descriptions that capture the quantitative and qualitative effects is often complicated, if not impossible.

In order to gain a comprehensive understanding of the intricacies of all in-cloud ice microphysical processes, including the multitude of unknowns, it seems a natural choice to combine available observational information with models that have the capacity to serve as a numerical laboratory, enabling the testing of process descriptions at the most detailed level currently available.

Significant advances in the understanding of SIP have been achieved through the integration of experimental, modeling, and observational methods. For instance, Billault-Roux et al. (2023) examine 30-minute intervals of a case study by employing detailed Doppler spectral data, dual-frequency radar measurements, and simulated atmospheric profiles in order to identify potential processes responsible for the observed signatures. The authors hypothesize that several SIPs may be responsible for the signatures found. In their study, Billault-Roux et al. (2023) present a straightforward modeling approach that suggests ice crystal concentrations are likely to exceed typical IPNCs by a substantial margin, potentially by one to four orders of magnitude.

Observations of von Terzi et al. (2022) show a persistently occurring slow secondary mode in the dendritic growth layer (DGL) for the temperature range between -13° C and -17° C (256 - 260 K) in their Doppler spectra. The combination of fragile structures of dendritic crystals and possible upwind generated by the latent heat released by depositional growth creates a regime of increased likelihood for ice-ice collisions. When ice particles collide, they may become mechanically fragmented and produce secondary ice. This hypothesis has been suggested by ground-based studies (Hobbs and Farber, 1972; Jiusto and Weickmann, 1973) and airborne observations of ice particle fragments collected (e. g. Hobbs and Farber, 1972; Takahashi, 1993). Several studies show that fragmentation can be a dominant process in heterogeneous ice initiation (Georgakaki et al., 2022; Phillips et al., 2017b; Sotiropoulou et al., 2020, 2021; Sullivan et al., 2018, and others). For example, Georgakaki et al. (2022) find that fragmentation can increase IPNC by three orders of magnitude in their simulations of seeder-feeder events and suggest that snowflake aggregation is an important driver of SIP.

To comprehend the intricate dynamics of ice-ice collisions, Vardiman (1978), Griggs and Choularton (1986), and Takahashi et al. (1995) have attempted to study the production of fragments due to ice-ice collisions by collecting crystals or generating them in laboratory studies. However, these efforts have yielded conflicting results, particularly regarding the significance of the rime fraction.

The first documented experiment on ice-ice collisions was conducted by Vardiman (1978) and involved natural ice particles colliding with a metal plate, with the collisions captured using a high-speed camera (see also Vardiman, 1974). Vardiman (1978) employed five types of ice particles and developed a theoretical model to estimate the number of fragments based on the momentum change of the incoming ice particles.

Griggs and Choularton (1986) conducted laboratory experiments on the fragmentation of rimed ice and crystals. Their setup involved freely falling glass beads of various sizes colliding with rimed ice or ice crystals growing on a target rod. The findings indicated that rimed structures did not efficiently produce secondary ice. In contrast, collisions between ice crystals and graupel likely generated secondary ice through the fragmentation of the crystals' fragile structure, consistent with Vardiman's conclusions. Additionally, spontaneous fragmentation of ice crystals due to aerodynamic drag forces was observed.

The most comprehensive study in this field was conducted by Takahashi et al. (1995), which built upon the in situ observations of ice crystals in cumulus clouds conducted by Takahashi (1993). Takahashi (1993) hypothesise that collisions between graupel particles could produce fragments from the breakup of these fragile branches and tested this hypothesis by conducting laboratory experiments using two centimetre-sized ice spheres as proxies for graupel. One sphere grew by vapor deposition while stationary, and the other grew by riming. The collision experiments revealed that fragment production increased with collision force and deposition growth time. This supports the idea that graupel collisions with ice crystals could generate significant secondary ice.

However, subsequent critiques have highlighted potential limitations of the experiments. For example, Vardiman's methodology could have been influenced by sublimation weakening, as pointed out by Phillips et al. (2017a). Additionally, Korolev and Leisner (2020) argue that rotational energy should be considered in collisions. Vardiman (1978) use of a fixed target may have resulted in an overestimation of fragment production. Nevertheless, Phillips et al. (2021) contend that the final rotational energy constitutes only a small fraction of the initial collision kinetic energy (CKE). The results of Griggs and Choularton (1986) indicate that to break rime, enormous velocities and therefore CKEs are necessary to break it, which is contrary to the findings of Vardiman (1978). The high CKE observed in the experiments conducted by Takahashi et al. (1995) has been the subject of criticism, as CKE is a crucial factor determining the effectiveness of fragmentation (Korolev and Leisner, 2020).

In a more recent study of Grzegorczyk et al. (2023), two experimental setups were developed to study ice particle collisions at around $-15\,^{\circ}\mathrm{C}$. In the first setup, collisions between graupel particles demonstrated that collisions with dendrites produced a substantial number of fragments, with the quantity increasing with collision kinetic energy CKE. The fragment sizes were mostly small, consistent with previous observations, and their number depended on CKE. In the second setup, collisions between a graupel particle and a dendritic ice crystal aggregate (simulating a snowflake) produced a significant range of fragments. The fragment size distribution showed two distinct modes. These setups addressed limitations of previous studies by using realistic particle sizes and incorporating updrafts during growth processes. The results highlight the significance of surface characteristics in fragment production and suggest further research under varying environmental conditions.

1.2 NAVIGATING THE CLOUDS: DEFINING SCIENTIFIC OBJECTIVES

The central objective of the priority program ("Schwerpunktprogramm", SPP 2115) of the Deutsche Forschungsgemeinschaft (DFG) called "**P**olarimetric **R**adar **O**bservations meet Atmospheric **M**odelling (PROM)" is an improvement of the current understanding of cloud and precipitation processes by combining radar polarimetry and atmospheric modeling. Within the scope of the Understanding **I**ce **M**icrophysical **P**rocesses by combining multi-frequency and spectral **R**adar polar**I**metry a**N**d superpar**T**icle modeling (IMPRINT) project, this dissertation was conducted with the primary aim of enhancing comprehension of IMPs by improving the microphysical representation of ice crystal habits in the Lagrangian Monte-Carlo particle model *McSnow* (Brdar and Seifert, 2018; Bringi et al., 2020).

In order to structure the thesis in a scientifically reasonable manner, the following three objectives have been identified:

The first objective is to reinforce the existing numerical laboratory in the form of the Lagrangian particle model (LPM) *McSnow* with the aim of enhancing the representation of developing ice habits. Accordingly, Chapter 2 will provide an overview of the theoretical framework underlying the model and its associated parameterizations. Subsequently, Chapter 3 discusses the theory of Böhm regarding its application for the explicit habit prediction. This is followed by a revision of the current theory of ventilation and the inherent growth function (IGF) in Chapter 4. Chapter 5 examines the sensitivity of *McSnow* with regard to the explicit habit prediction in relation to deposition, aggregation, and riming.

The second objective is to utilize the models' capabilities to examine the IMP fingerprints that are frequently observed in radar data in relation to the utilized physical parameterizations. Chapter 6 examines the IMP fingerprints of observations of a dendrite-dominant case and compares them with synthetic signals of numerical experiments.

The third objective is to investigate the potential impact of ice-ice collisions on the IMP fingerprints, based on a new particle-level description. In Chapter 7, the reader will find an updated fragmentation scheme, which is then applied to individual particle collisions as well as to the idealized and real case studies from the preceding chapters. The results of the three objectives are presented in Chapter 8 and a perspective on future research is provided, with an emphasis on building upon the findings of this thesis.

Prior to addressing the aforementioned objectives, the following subsections will provide a detailed overview of the proposed methods for achieving a comprehensive understanding of the subject matter.

1.2.1 *Part I: Improving the Representation of Ice Microphysical Processes with Respect to Ice Habits*

McSnow is based on the super-droplet method of Shima et al. (2009) and can be used to simulate the evolution of particles through microphysical processes in the liquid and ice phases. These processes include condensation/evaporation, deposition/sublimation, riming, aggregation, freezing/melting, sedimentation, and SIP. Brdar and Seifert (2018) evaluate the ability of the model to tackle the high-dimensional problem of particle properties in a box model and in one-dimensional simulations. Seifert et al. (2019) use *McSnow* with an updated geometry model of rimed snowflakes to find significant effects of the riming parameterization on the precipitation rate. Furthermore, Bringi et al. (2020) find that collisional breakup is essential for the shape of the drop size distribution by simulating the outer rain band of Hurricane Dorian with *McSnow*. Seifert and Rasp (2020) explore the application of neural network-based ML to cloud microphysical parameterizations, specifically focusing on the warm-rain formation process through collision-coalescence.
The extension of *McSnow* by an explicit habit prediction (HP) scheme using porous spheroids following Chen and Lamb (1994b, p. CL94) and Jensen and Harrington (2015, JH15) to replace the classical mass-size (m-D) relations, explained in paragraph 2.1.1, is a critical first objective. This enables the incorporation of the anticipated effects of ice crystal habits on the process rates. Furthermore, only an explicit habit prediction allows for a natural comparison with polarimetric observations.
Several implications introduced by asymmetric particles alter the models process sensitivities and in turn have to be examined. Incorporating the comprehensive theoretical framework of Böhm enables the examination of ice habits, conceptualized as porous spheroids, in relation to fall velocity and collision effects (Sec. 2.3). We show that the original shape assumption for prolates based on the cylinder can underestimate the fall velocity derived from recent laboratory studies, and provide an interpolation to overcome the observed mismatch (Sec. 3.1).
In an effort to resolve conflicting findings about the dependence of terminal velocity and collision efficiency on atmospheric conditions, we compare our version of the Böhm framework with the findings of Pinsky et al. (2001, Sec. 3.2), followed by an evaluation of the effect of habit on riming and aggregation (Sec. 3.3 & 3.4).
The original formulation of the ventilation effect (Hall and Pruppacher, 1976) is extended to include a habit-specific ventilation effect suggested by several studies as the first part of Chapter 4.
Following, we evaluate the performance of the habit prediction scheme against laboratory results and polarimetric observations (Sec. 4.2.1 and 4.2.2), and propose several changes to overcome identified deficiencies in Section 4.2.3. In particular, the core concept of the inherent growth function (IGF) and its deficiencies have been previously discussed in the literature (e. g. Connolly et al., 2012; Hashino and

Tripoli, 2007; Sheridan et al., 2009). The results of these recent studies should be integrated into the concept, including changes to the IGF itself and the criteria for the development of secondary habits.

The research will also highlight the advantages of using an explicit habit treatment over generalized mass-size relations in modeling. Such generalized relations often fail to capture the variance in particle properties necessary to accurately represent the complexity of in-cloud interactions. By emphasizing the role of detailed habit treatment, this study aims to enhance the accuracy of microphysical parameterizations in atmospheric models, thereby improving our ability to interpret and predict ice microphysical processes and, in Part II, their associated radar signatures. Experiments are conducted with an isolated one-dimensional snow shaft setup, gradually increasing in complexity. Two cases are considered: oblate-dominated and prolate-dominated. Initially, only deposition and sublimation are permitted. Subsequently, the aggregation process is activated, and finally, a liquid water zone (LWZ) is introduced, enabling riming. Two configurations of distinct parameterizations will be evaluated to illustrate the impact of the revisions on the evolving cloud pattern.

1.2.2 *Part II: Investigation of Ice Microphysical Features by Combining Numerical Modeling and Polarimetric Fingerprint Analysis*

The second objective of this thesis is to deepen our understanding of ice microphysical processes by combining detailed modeling with the analysis of polarimetric radar fingerprints. Part I showed that *McSnow*, with its consideration of prognostic geometries, offers a sophisticated approach to simulate particle characteristics such as shape and apparent density. These features are crucial for converting model simulations into synthetic observed variables through the use of forward models, enabling a more accurate representation of real-world observations. In order to achieve this, we will utilize the comprehensive particle descriptions provided by *McSnow* to evaluate the model's capacity to reproduce polarimetric radar signatures that have been observed in particular atmospheric conditions. The forward modeling approach of *McRadar*, based on the PyTMatrix package of Leinonen (2014) and further extended by von Terzi (2023), which is tailored for the rich information produced by *McSnow*, provides a robust framework for testing the model's ability to replicate observed signatures.

During the second observational campaign of the IMPRINT project, called **TRI**ple-frequency and **P**olarimetric radar **Ex**periment for improving process observation of winter precipitation (TRIPEx-pol)-scan, strong polarimetric signals were detected due to the presence of highly asymmetric ice particles. By integrating these findings with supplementary observations, particularly those obtained from radio sondes launched at noteworthy times, along with disdrometer data, we construct a dendrite-dominated simulation setup that is representative over a reasonable time span. The construction of a second case, which was dominated by columnar particles or needles, was unsuccessful based on the available observations. Consequently, it will not be included in this chapter.

Based on the dendrite-dominated setup, numerical experiments will be conducted to identify the most critical microphysical processes responsible for the observed polarimetric fingerprints. The experiments will focus particularly on monomer-dominated cases, in light of the findings of Part I, which indicated that the prediction of aggregate habit geometries is considered insufficient. Furthermore, we will demonstrate the capacity of *McSnow* to serve as a numerical laboratory for the comprehension of IMP fingerprints. To this end, we will analyze the consistency between several synthetic profiles and the observed ones, thereby demonstrating the influence a single parameterization can have.

The combined approach, integrating advanced modeling with polarimetric observations, will provide a more nuanced understanding of ice microphysics. A detailed examination of the aforementioned experiments has led to the formulation of a hypothesis regarding the potential absence of a SIP mechanism, which could explain the observed offset in one of the polarimetric variables. This hypothesis will provide the foundation for the development of an updated fragmentation scheme, which will be presented in Part III.

1.2.3 *Part III: Ice-Ice Collisions as a Potential Secondary Ice Production Process*

The final objective of this thesis is to enhance the understanding of secondary ice production (SIP) mechanisms, particularly through ice-ice collisions, as a potential explanation for the observed discrepancy between ice nucleating particles (INP) concentrations and ice particle number concentration (IPNC). This study builds on the hypothesis that collisional fragmentation could be a significant source of secondary ice particles, a topic that has garnered extensive attention within the scientific community due to its critical role in cloud microphysics.

The analysis of the literature presented in Korolev and Leisner (2020) indicates that the efficiency of ice-ice collisions to produce a significant number of fragments is dependent upon the properties of the colliding particles (mass, size, density, shape, degree of riming and potentially other factors), the relative terminal velocity (which is dependent upon hydrodynamic properties) of the particle pair, as well as the air temperature, which defines the physical properties of ice. The picture painted by the observational and laboratory studies presented in Section 1.1.3 (Griggs and Choularton, 1986; Takahashi et al., 1995; Vardiman, 1978) is not entirely clear regarding the underlying drivers of fragmentation. Nevertheless, various studies have endeavored to characterize the ice-ice collision process through an integration of physical principles and observational evidence pertaining to the aforementioned factors.

The theoretical approaches of Yano and Phillips (2011) and Yano et al. (2016), based on collision kinetic energy, explored the potential of explosive multiplication, resulting in a physical parameterization that employs the studies, despite the lack of consensus regarding the quantity involved. The parameterization scheme of Phillips et al. (2017a) considers some of the above, but relates the collision type to the ambient temperature. As originally designed for bulk microphysical models, this parameterization does not fully exploit the information available for individual particles.

To achieve a dependency on individual particles, the fragmentation model by Phillips et al. (2017a) will be adapted and refined within the *McSnow* framework to incorporate particle-based approaches. This involved replacing the original temperature-based categorization of particles with a more sophisticated system based on particle shape, apparent density, and monomer number. Drawing on insights from material science, the concept of fracture toughness will be integrated into the model, allowing for a more realistic treatment of fragile ice structures and their susceptibility to fragmentation during collisions. We define the CKE and the fragility of the involved particles as key quantities for the collision process rather than maximum dimension and ambient temperature. This approach allows us to consider the fragmentation as dependent on the ice particles' growth history, rather than being constrained by the actual ambient conditions.

The findings of studies from the field of material science can provide a basis for re-evaluating the critical parameters of the fragmentation parameterization in a manner that is both physically meaningful and controllable, thereby opening the scheme to new observations. A simplified geometry of breakable asperities will be introduced in order to facilitate the correlation between the fragility of the particle and the energy necessary to break these asperities. Furthermore, we examine how ice-ice collisions alter the fragmented particle in terms of shape, density, and monomer number.

A series of numerical experiments will be conducted to assess the influence of these new parameterizations on SIP in comparison to the original scheme of Phillips et al. (2017a), with a particular focus on idealized collisions between hailstones and various ice particle types.

Finally, the revised fragmentation schemes will be tested based on the case studies (Chapter 5) and real-case simulations (Chapter 6) to assess their potential to produce secondary ice under observed atmospheric conditions. The insights gained from these experiments offer a baseline for improving the representation of fragmentation as a SIP mechanisms in cloud microphysics models. Ultimately, the ensuing research questions could contribute to the refinement of weather prediction models and the advancement of cloud microphysical research.

2

THEORY

The main tool to investigate the research questions is the Monte-Carlo microphysical model *McSnow*. The focus of the development is to understand the evolution of individual ice crystals due to the ice microphysical processes of deposition/sublimation, riming, aggregation, melting, and, if present, SIP. We begin with an introduction to the basic principles of the model including descriptions of the methods and assumptions applied for the different microphysical properties. Special attention is given to the implications introduced by the assumption of non-spherical ice habits.

2.1 NOTION OF SUPER-PARTICLES

To represent hydrometeors in the atmosphere, we assume that we can fully characterize the behavior by a set of individual particle properties using Monte Carlo sampling. These properties result in a multidimensional microphysical space that allows spectral resolution of the particle distribution. The particle properties ($\mathcal{P}$) include an ice mass added by deposition m_i, a rime mass m_r, a rime volume (V_r), a frozen mass m_f, a water mass m_l, the number of monomers (N_m) collected by aggregation.

Since our definition of particles is based on the super-particle approach of Shima et al. (2009), the multiplicity (ξ) is used to represent the number of real particles represented by a super-particle. The ξ can be interpreted as the smallest representation of an ensemble of particles that exist within a volume rather than at the same position.

2.1.1 *Geometry*

MASS-SIZE RELATIONS To predict the terminal velocity and collision behavior of ice crystals we need to establish a relation between the particles' attributes and its' geometry. Classical power law relations have been derived from observations (e. g. Locatelli and Hobbs, 1974; Mitchell et al., 1990) and define functions between particle mass (m), maximum dimension (D), and projected area (A)

$$m = \alpha_i \, D_i^{\beta_i} \, , \tag{2.1}$$

$$A = \sigma_i \, D_i^{\gamma_i} \, , \tag{2.2}$$

with coefficients α_i, β_i, γ_i, and σ_i. In *McSnow* we chose a one-fit-all approach by assuming that particles follow the empirical relations of Mitchell (1996) for "aggregates of side planes, columns, and bullets (S3)" with coefficients (converted for SI units)

$$\begin{aligned}
\alpha_i &= 2.8 \times 10^{2\,\beta_i - 6}\ , \\
\beta_i &= 2.1\ , \\
\sigma_i &= 2.285 \times 10^{2\,\gamma_i - 5}\ , \\
\gamma_i &= 1.88\ .
\end{aligned}$$

The relations are only valid for the size range they have been derived from. To avoid nonphysical geometries, we assume sphericity and ice density for particles smaller than a critical size threshold D_{th}

$$D_{th} = \left(\frac{\pi\, \rho_i}{6\, \alpha_i} \right)^{\frac{1}{\beta_i - 3}}\ , \tag{2.3}$$

similar to Morrison and Milbrandt (2015) with the ice density $\rho_i = 917\,\mathrm{kg\,m^{-3}}$. The equivalent mass threshold is

$$m_{th} = \frac{\pi}{6}\, \rho_i\, D_{th}^3\ . \tag{2.4}$$

These mass-size relations can only serve as an average description of the particle population, but they prevent the development of the natural variety of particle types found in mixed-phase clouds. In the following, we introduce a geometry model that utilizes spheroids, enabling an explicit prediction of shape and density.

SPHEROIDAL MODEL In nature, the geometry and internal structure of ice particles can reach a high degree of complexity that defies any explicit description. A common approach is the use of z axis symmetric spheroids (Fig. 2.1) based on the two defining semi-axes: the equatorial radius (a) and the polar radius (c). We can assume that the approximation of oblate and prolate spheroids for the two dominant primary habits of plates and columns is superior to fixed mass-size (m-D), mass-area (m-A), and size-density (D-ρ) relations because this removes the need for categorization of crystal and allows the transition between ice shapes to be considered. The aspect

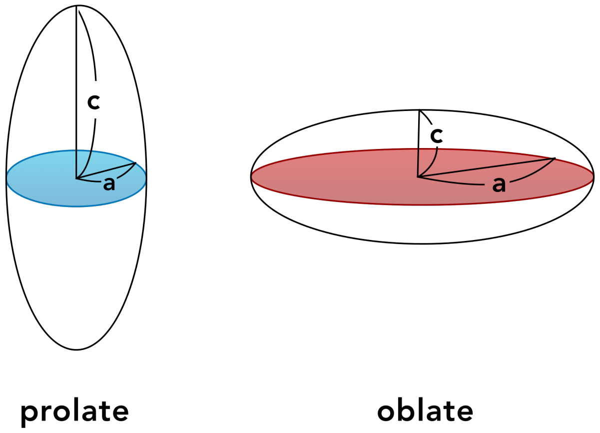

Figure 2.1: Geometry of prolate and oblate spheroids.

ratio (ϕ) (ratio of polar to equatorial radius) describes the shape of the spheroid

$$\phi = \frac{c}{a} \, . \tag{2.5}$$

With the introduction of an explicit particle geometry, the processes that might modify the shape, including vapor deposition, riming, and aggregation, must be adjusted accordingly. The details regarding the impact of individual processes are presented in Section 2.2. The maximum dimension of the spheroid is defined as $D = 2\max(a, c)$. We distinguish between the geometric area A, which is relevant for riming and collision processes, and the cross-sectional area $\widetilde{A}$. The geometric area A of a spheroid is defined as the circumscribing ellipse

$$\begin{aligned} A_{\text{prolate}} &= \pi\, a\, c \qquad \text{for prolates,} \\ A_{\text{oblate}} &= \pi\, a^2 \qquad \text{for oblates,} \end{aligned} \tag{2.6}$$

while the cross-sectional area $\widetilde{A}$ is the effective area presented to the flow (cf. Böhm, 1989).

The geometries based on mass-size relations and the spheroidal model are typical of ice crystals grown by vapor deposition, but the addition of rime alters the expected shape. To describe the transition between rimed snowflakes and graupel of particles whose geometry is based on mass-size relations, *McSnow* includes two parameterizations that will be presented in the following: the "fill-in" model of Heymsfield (1982) or the similarity model of Seifert et al. (2019). The shape changes in the spheroidal framework induced by riming are described in Section 2.2.4.

FILL-IN MODEL The fill-in model assumes that for a partially rimed snowflake the maximum dimension stays constant until a critical volume $V_{r,crit}$ is reached. This volume is that of a sphere with equal diameter and can be defined as

$$V_{r,crit} = \frac{\pi}{6} D^3 - V_i = \frac{\pi}{6} \left(\frac{m_i}{\alpha_i} \right)^{3/\beta_i} - \frac{m_i}{\rho_i} \, , \tag{2.7}$$

$$m_{r,crit} = \rho_r \, V_{r,crit} \, . \tag{2.8}$$

Here, $\rho_r = m_r \, V_r^{-1}$ is assumed to be the apparent rime density of the particle. For more details on the composition of the rime density, see Sec. 2.2.4. Brdar and Seifert (2018) point out two main caveats of the "fill-in" approach: First, in reality, the maximum dimension of the particles may increase even before the arbitrary threshold. Second, the approach provides only a m-D relation, but no assumption for the cross-sectional area. This problem can be solved by (linearly) interpolating the area between that of an unrimed aggregate and spherical graupel using the critical mass fraction $F_r = m_r / m_{r,crit}$.

SIMILARITY MODEL The similarity model uses self-similarity arguments to derive a parameterization from simulations of many individual rimed aggregates. It provides a continuous, functional relationship between mass, maximum dimension, and area, which is an improvement over the "fill-in" model's discontinuous, threshold-based approach. Utilizing the aggregation and riming algorithm described by Leinonen (2013), Leinonen and Moisseev (2015), and Leinonen and Szyrmer

(2015), three-dimensional shape models of snowflakes are created to model the transition from the two asymptotic regimes of unrimed aggregates to graupel. The mass of a size-equivalent spherical graupel particle m_g

$$m_g = \frac{\pi}{6}\,\rho_{\mathrm{rime}}\,D^3\ , \tag{2.9}$$

is used to normalize the rime mass and derive a nondimensional rime fraction

$$\mathcal{M} = \frac{m_{\mathrm{rime}}}{m_g}\ , \tag{2.10}$$

as well as a non-dimensional size

$$\mathcal{D} = \frac{D}{D_{\mathrm{agg}}}\ . \tag{2.11}$$

From the data of modeled aggregates Seifert et al. (2019) find a functional relation between $\mathcal{M}$ and D

$$\mathcal{M} = f_m(D) = \tanh\left[\widetilde{a}(\mathcal{D}-1)^{\widetilde{p}}\right]\ , \tag{2.12}$$

with $\widetilde{a} = 0.72$ and $\widetilde{p} = 0.52$ considering all data.
Rescaling the cross-sectional area $\mathcal{A}$

$$\mathcal{A} = \frac{A_{\mathrm{rimed}} - A_{\mathrm{agg}}}{A_{\mathrm{sphere}} - A_{\mathrm{agg}}} = f_a(\mathcal{M}) \tag{2.13}$$

yields a similar functional relation

$$\mathcal{A} = \hat{a}\tanh\left[\hat{b}\,\mathcal{M}\right] + \hat{c}\,\mathcal{M}\ , \tag{2.14}$$

with $\hat{a} = 0.32$, $\hat{b} = 7.36$, and $\hat{c} = 0.52$ to form a complete m-D-A-relation. The similarity model increases the riming rate due to a proper consideration of the rapid increase in maximum dimension in the early stages of riming that is missing when using the fill-in model.

2.1.2 *Terminal Velocity*

Hydrodynamic theory can be used to calculate the terminal fall velocity (v_t) of ice particles based on their geometry. The work of Abraham (1970) provides the basic model behind the terminal velocity schemes in *McSnow*. He shows a functional relation between the drag coefficient (C_d) and the Reynolds number (Re).

$$C = C_0\left[1 + \delta_0\,\mathrm{Re}^{-1/2}\right]^2\ . \tag{2.15}$$

Due to the complexity of the framework coupled with the shape dependency and links to the collision process, we dedicate a separate segment to the work of Böhm in Section 2.3. For now, it should be mentioned that *McSnow* includes full implementations of the terminal velocity parameterizations of Khvorostyanov and Curry (2005) and Heymsfield and Westbrook (2010), but these schemes will not be used as they lack a geometric consideration necessary for predicting explicit ice morphology.

2.2 ICE MICROPHYSICAL ASPECTS

2.2.1 *Nucleation*

Simply put, the formation of new hydrometeors can occur in two ways: The first process is called *homogeneous nucleation* and occurs when only water is present and is largely restricted to high altitudes in the troposphere with temperatures as low as $T \leqslant 233\,\mathrm{K}$.

In the majority of cloud formations, the initiation of droplet or crystal formation occurs in the presence of foreign matter and is therefore referred to as *heterogeneous nucleation*. The nucleation process involves a high degree of complexity and is a separate area of research that will not be covered in detail in this work. We simplify nucleation by specifying one or more nucleation zones where the number of particles initiated per time step is relative to the expected liquid water content (LWC) or ice water content (IWC) and the corresponding hydrometeor number concentration.

The initial particle size and mass can be found by sampling a PSD, typically assumed to be similar to a gamma distribution. Alternatively, the scheme of Meyers et al. (1992) provides nucleation rates per volume relative to supersaturation over ice

$$N_{\mathrm{nucl}} = 1000\ \exp(-0.639 + 12.96\,(p_{\mathrm{vap}} - p_{\mathrm{sat,i}}))\ , \tag{2.16}$$

with the vapor pressure (p_{vap}) and the saturation pressure with respect to ice $p_{\mathrm{sat,i}}$. To account for the natural variability of nucleation within clouds, the initial position is randomly chosen within a grid box (numerical discretization of the atmosphere).

2.2.2 *Sedimentation*

In addition to the set of properties, each particle carries information about its actual position, namely the height above ground (z) for one-dimensional or the positional vector ($\vec{v}$) in two- or three-dimensional simulations. In the scope of this thesis, we consider only the sedimentation process, which moves the particles along the vertical coordinate within one time step

$$S(z_{t_1}, \mathcal{P}) = S(z_{t_0} - v_t\,\Delta t, \mathcal{P})\ . \tag{2.17}$$

For simplicity, we assume that all particles accelerate immediately to their terminal velocity. Naumann and Seifert (2015) propose an alternative approach that attempts to account for deviations from the terminal fall velocity by solving the momentum equation of individual super-particles, but requires small time steps if the whole droplet spectrum is considered. It should be noted, however, that the effect of the simplification of instantaneous acceleration is non-negligible for larger drops, as shown by Wang and Pruppacher (1977, Fig. 3).

For the fall velocity of a droplet v_d of radius r_d we use the formulation of Beard (1976, Tab. 1).

2.2.3 *Deposition/Sublimation*

The equation for mass change through vapor deposition and sublimation is used to predict the change in ice mass due to vapor deposition and sublimation

$$\left(\frac{dm_i}{dt}\right)_v = 4\,\pi\,C(a,c)\,D_v\,f_v\,\frac{p_{vap} - p_{sat,i}}{R_v\,T}\,\left(1 + \frac{L_s^2\,D_v\,p_{sat,i}}{K_d\,R_v^2\,T^3}\right)^{-1} \quad . \tag{2.18}$$

The variables are the vapor diffusivity (D_v), the ventilation coefficient (f_v), the vapor pressure p_{vap}, the saturation pressure with respect to ice $p_{sat,i}$, as well as the temperature (T), the gas constant of water vapor (R_v), the latent heat of sublimation (L_s), and the thermal conductivity of dry air (K_d). The shape information is mainly considered via the capacitance of the ice particle (C), proposed by Chen and Lamb (1994b) and based on electrostatic analogy.

CAPACITANCE The idea to express the capacitance by using an electrostatic analog to describe the water vapor field around any given geometry was proposed by Jeffreys (1918) and is still used as a state-of-the-art description of the deposition process (cf. Mason, 1971; Pruppacher and Klett, 1997).

The capacitance C is linked to the geometry and for simple shapes, analytic solutions can be found (e. g. McDonald, 1963). More recent approaches try to calculate the capacitance of complex pristine ice crystals and aggregates (Westbrook et al., 2008). Analytical solutions for spheroids can be derived by solving the Laplace equation (Chen and Lamb, 1994b). For oblates spheroids ($\phi < 1$) this results in

$$C_{obl} = \frac{a\,\epsilon_{obl}}{\sin^{-1}\epsilon_{obl}} = \frac{d_{foci,obl}}{\sin^{-1}\epsilon_{obl}}\,, \tag{2.19a}$$

$$\epsilon_{obl} = \sqrt{1 - \frac{c^2}{a^2}} = \sqrt{1 - \phi^2}\,, \tag{2.19b}$$

$$d_{foci,obl} = \sqrt{a^2 - c^2}\,, \tag{2.19c}$$

and for prolate spheroids ($\phi > 1$) in

$$C_{pro} = \frac{c\,\epsilon_{pro}}{\ln[(1 + \epsilon_{pro})\,\phi]} = \frac{d_{foci,pro}}{\ln[(1 + \epsilon_{pro})\,\phi]}\,, \tag{2.20a}$$

$$\epsilon_{pro} = \sqrt{1 - \frac{a^2}{c^2}} = \sqrt{1 - \phi^{-2}}\,, \tag{2.20b}$$

$$d_{foci,pro} = \sqrt{c^2 - a^2}\,. \tag{2.20c}$$

This formulation uses the semi length of foci (d_{foci}).

Figure 2.2 shows the spheroid capacitance as an universal function of aspect ratio relative to the volume equivalent radius r_0. The dependency underlines the impact of the particle geometry on the depositional growth which can exceed a factor of 2 for strongly developed habits. McDonald (1963) and Podzimek (1966) found fair agreement between the capacitance for spheroids and the complex geometries formed by natural crystals. While Nelson and Baker (1996) show that the capacitance model of spheroids (e. g. CL94) cannot evolve faceted crystals because of inconsistent surface boundary conditions, it still produces relatively accurate estimates for mass and shape evolution.

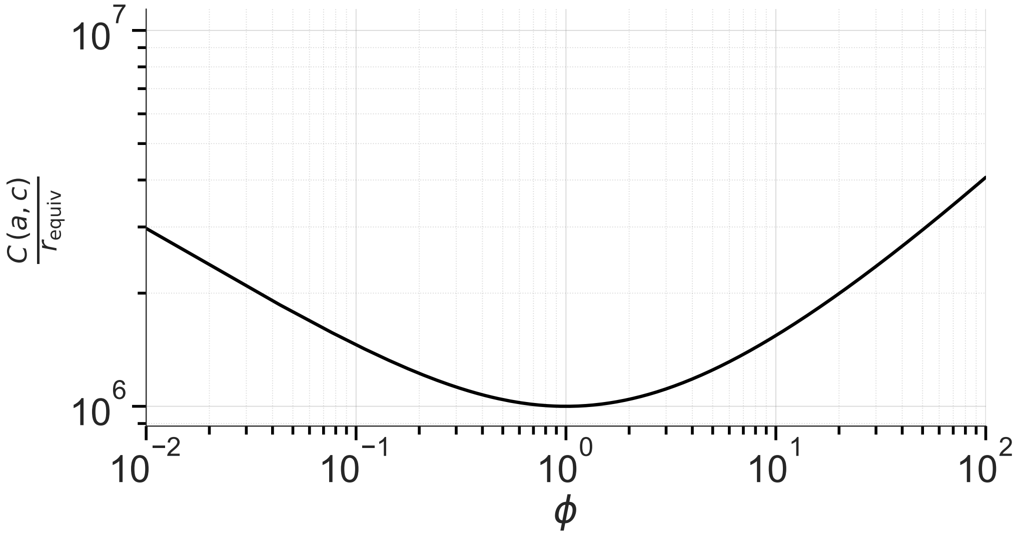

Figure 2.2: Spheroid capacitance $C(a, c)$ as an universal function of aspect ratio relative to the volume equivalent radius r_0.

Still, Westbrook et al. (2008) show that the actual capacitance might depend on the internal structure of the hydrometeor, eventually causing an overestimation of capacitance for hydrometeors of reduced density when using the original formulation of CL94. For snow aggregates, they find a capacitance of $C_{\mathrm{unr}} = D/4$ which will be used for unrimed aggregates. In case of riming, we apply a linear interpolation between the capacitance of an unrimed particle $C = D/4$ (Westbrook et al., 2008) and that of a sphere $C_{\mathrm{sph}} = D/2$, depending on the degree of riming (F_r) defined with the critical volume (V_{crit})

$$V_{\mathrm{crit}} = \frac{\pi}{6} D^3 - V_i \,, \tag{2.21}$$

$$F_r = \frac{(V_f + \max(V_r, m_r\,\rho_i^{-1} + m_w\,\rho_l^{-1}))}{V_{\mathrm{crit}}} \,, \qquad V_{\mathrm{crit}} > 0 \,, \tag{2.22}$$

$$C = D\,\left((1 - F_r)\,C_{\mathrm{unr}} + F_r\,C_{\mathrm{sph}}\right) \,. \tag{2.23}$$

For the volume of frozen water we simply assume ice density $V_f = m_f\,\rho_i^{-1}$.

INHERENT GROWTH FUNCTION AND DEPOSITION DENSITY Kobayashi (1961) shows that the evolution of primary habits (planar or columnar) depends mainly on ambient temperature, while that of secondary habits (branching and hollowing) depends on supersaturation. To quantify the temperature regimes favoring certain geometries, CL94 derive an Inherent Growth Function (Γ) by collecting laboratory and in-situ measurements for the temperature range between 0 ° and −30 °C (respectively $243 - 273$ K) by relating individual growth along the two major axes

$$\Gamma(T) = \frac{d \ln c}{d \ln a} \,. \tag{2.24}$$

The original IGF of CL94 is shown in Figure 2.3. It should be pointed out that the

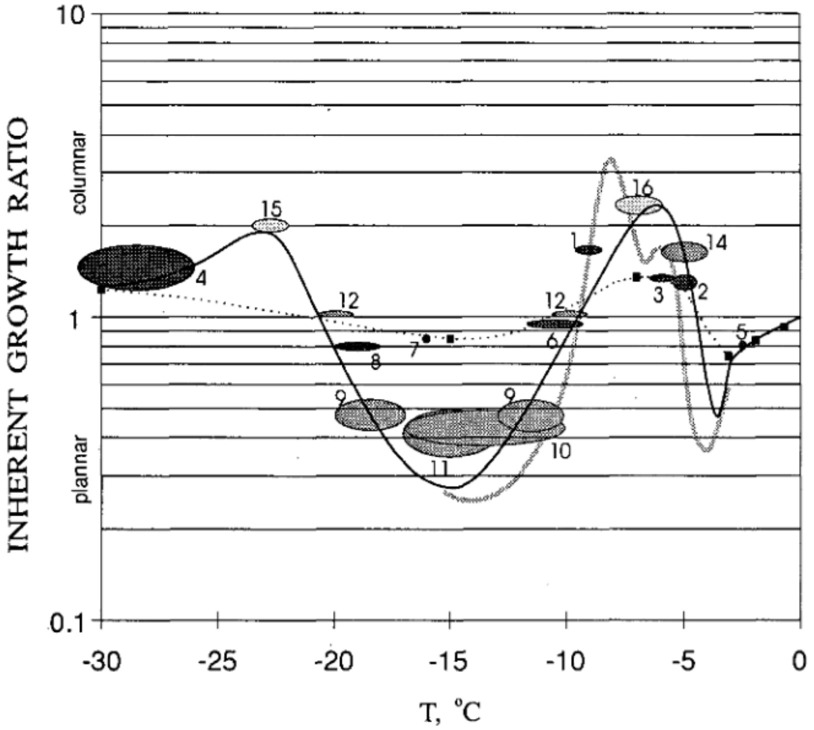

Figure 2.3: Original IGF from CL94 (Chen and Lamb, 1994b, Fig. 3 within, thin solid line) as a function of temperature T, compared to other fits, experimental, and observational data. For details on each data source, the reader is referred to the original paper. ©American Meteorological Society. Used with permission.

IGF is defined for water saturation and it is not clear, how growth tendencies change for lower supersaturation. Takahashi (2014) e. g.shows that the form of branching crystals depends on the LWC for some temperatures while at others it increases ice mass without influencing the shape. Harrington et al. (2019) and Harrington and Pokrifka (2021) propose a reformulation of the CL94 model that is independent of the IGF using the facet-based hypothesis. This reformulation has some conceptual advantages in other environmental conditions than supersaturation. For now, we will stick with the simpler formulation similar to Shima et al. (2020) and Hoffmann (2020), but future work could focus on increasing the complexity.
The spheroid shape does not explicitly allow for secondary habits. To describe the internal structure of the accumulated ice mass, we introduce the ice volume ice volume (V_i) and the apparent density (ρ_{app})

$$V_i = \frac{4}{3}\pi a^3 \phi = \frac{4}{3}\pi a^2 c \,, \tag{2.25}$$

$$\rho_{app} = \frac{m_i}{V_i} \,. \tag{2.26}$$

The change in crystal mass causes an ice volume change

$$dV_i = \frac{1}{\rho_{depo.}} dm_i \,, \tag{2.27}$$

with the deposition density ($\rho_{depo.}$). To capture branching and hollowing, the volume of the circumscribing spheroid is modified. Physically, the air inside the spheroid lowers the apparent density below ice density. Chen and Lamb (1994b) use an empirical formulation for the deposition density based on experimental results of Fukuta (1969). We prefer the direct parameterization of the deposition density using the IGF and density of solid ice (ρ_i) proposed by Jensen and Harrington (2015, JH15)

$$\rho_{\text{depo}} = \begin{cases} \rho_i\,\Gamma(T)\,, & \Gamma < 1\,, \\ \rho_i\,\Gamma^{-1}(T)\,, & \Gamma \geqslant 1\,. \end{cases} \tag{2.28}$$

since it is straightforward, has less degrees of freedom, and shows better agreement in test against laboratory and observational data (Sec. 4.2). For oblate growth ($\Gamma < 1$), branching happens only if $\nu\,a^2 > \pi\,D_v\,c$ (JH15), otherwise $\rho_{\text{depo}} = \rho_i$. For columnar growth, hollowing happens immediately independent of ϕ.

Using the same deposition density of branching/hollowing for sublimation may lead to unphysical apparent densities because the IGF is only valid for temperature and supersaturation during the deposition process. Laboratory measurements suggest that ice particles preserve their shape during sublimation, maintaining a constant aspect ratio Harrington et al., 2019; Nelson, 1998; Shima et al., 2020. We use the apparent density for particles undergoing sublimation ($\rho_{\text{depo}} = \rho_{\text{app}}$).

Following CL94, we can predict the change in aspect ratio using the IGF

$$d\ln\phi = \frac{\Gamma - 1}{\Gamma + 2}\, d\ln V_i\,. \tag{2.29}$$

The evolution of V_i follows from Eqs. (2.18) and (2.27). As in previous work (Baran, 2012; Korolev and Isaac, 2003; Lawson et al., 2008), we restrict habit development for now to occur only for particles larger than $D \geqslant 10\,\mu\text{m}$, since observations suggest that crystals up to this size are approximately spherical. Based on the results of Nelson (1998) and Harrington et al. (2019), we assume that the aspect ratio (AR) remains unchanged during sublimation.

VENTILATION The ice habit also affects the airflow around the particle and ventilation. The parts of the crystal surface that extend farthest into the flow experience the greatest effect due to increased water vapor advection (Chen and Lamb, 1994b). Hall and Pruppacher (1976) suggest a description of the ventilation coefficient by

$$f_v = b_1 + b_2\, X_{v,eq}^{\gamma}\,, \tag{2.30}$$

the constants b_1, b_2, and γ have been generalized from observations for spheres and plates as

$$\begin{aligned} &b_1 = 1.0, && b_2 = 0.14, && \gamma = 2 && \text{for } X_{v,eq} \leqslant 1\,, \\ &b_1 = 0.86, && b_2 = 0.28, && \gamma = 1 && \text{for } X_{v,eq} > 1\,. \end{aligned}$$

The proposed ventilation coefficient f_v is a function of Schmidt number N_{Sc} and Reynolds number $N_{Re,eq}$

$$X_{v,eq} = N_{Sc}^{\frac{1}{3}}\, N_{Re,eq}^{\frac{1}{2}}\,, \tag{2.31}$$

$$N_{Sc} = \frac{\mu_a}{\rho_a\, D_v}\,, \tag{2.32}$$

$$N_{Re,eq} = \frac{D_{eq,v}\, v_t\, \rho_a}{\mu_a}\,. \tag{2.33}$$

The dynamic viscosity μ_a can be described by Sutherland's Law (Sutherland, 1893)

$$\mu_a(T) = \mu_0 \frac{T_0 + T_S}{T + T_S} \left(\frac{T}{T_0} \right)^{3/2} , \tag{2.34}$$

with $\mu_0 = 1.716 \times 10^{-5}$, the melting/freezing point $T_0 = 273.15\,\mathrm{K}$, and the Sutherland temperature $T_S = 110.4\,\mathrm{K}$. The other variables are the air density ρ_a, the volume-equivalent diameter of a sphere $D_{eq,v}$, and the terminal velocity v_t. Pruppacher and Klett (1997) collected habit-specific solutions for selected N_{Re}-regimes, but no continuous description for all habits is known to the authors. We propose a habit-dependent formulation based on several numerical studies in Section 4.1.

Ventilation affects the geometric evolution by favoring the edges of the crystals. To account for this effect, we replace the IGF of Eq. (2.29) by the ventilation-influenced growth habit Γ^* as proposed by CL94

$$\Gamma^* = \Gamma\, f^* , \tag{2.35}$$

where the ratio of the local ventilation coefficients f^* of the respective axis (f_c, f_a)

$$f^* = \frac{f_c}{f_a} \approx \frac{b_1 + b_2\, X^\gamma\, (\frac{c}{r_0})^{1/2}}{b_1 + b_2\, X^\gamma\, (\frac{a}{r_0})^{1/2}} , \tag{2.36}$$

is used. The local ventilation coefficient compares the local axis dimension to the radius of a sphere $r_0 = \frac{D_{eq,v}}{2}$ with the same total volume.

POROSITY Particles that are not solid ice present the challenge of distinguishing between the cross-sectional area of the circumscribing ellipse, which is critical for determining the swept volume in collision events, and the hydrodynamic area for determining flow resistance. The latter must take into account the porosity of the particle. JH15 suggest a linear dependency on ϕ and ρ_{app} to link the degree of branching to the thickness of a plate

$$\begin{aligned} \widetilde{A} &= \xi_p\, A \\ \xi_p &= (1 - \phi) \left(\frac{\rho_{app}}{\rho_i} \right) + \phi \qquad && \text{for oblates,} \\ \xi_p &= 1 && \text{for prolates.} \end{aligned} \tag{2.37}$$

A decrease in cross-sectional area represents flow through the porous structures of the particle, which in turn reduces flow resistance. Prolates are assumed to be hollow inwards, so the cross-sectional area is effectively unaffected ($A = \widetilde{A}$).

In terms of collision probability, we will see that the theory of Böhm uses Boundary Layer Theory (BLT), explicitly considering the difference between geometric and cross-sectional area via the area ratio q (cf. Eq. 2.80), which is similar to the porosity based on shape (ξ_p) above. For prognostic aggregates (cf. Sec. 2.2.6), the definition of ξ_p is not adequate to describe fairly porous structures while being at or close to sphericity. From a dimensional analysis, Shima et al. (2020) propose a general formulation for ξ_p as follows

$$\xi_p = \left(\frac{\rho_{app}}{\rho_i} \right)^{\exp(-\phi)} , \tag{2.38}$$

resulting in a similar behavior to Jensen and Harrington (2015) for all aspect ratios but also consider porosity effects at sphericity. We will discuss this approach in Section 5.3.2 in more detail.

2.2.4 *Riming*

McSnow includes two descriptions of the riming process, a continuous and a stochastic riming approach. The continuous riming approach of Cober and List (1993) uses a bulk collision efficiency derived from measurements and solves the mass growth equation for riming for the average over the cloud droplet distribution. The drawback is that the collision efficiency is derived from measurements of conical graupel, so using it is an extrapolation to a wider range of ice particle habits. von Blohn et al. (2009) argue that the bulk approach of Cober and List underestimates the collision efficiency by up to 25 % for spherical graupel.

The stochastic approach is based on the collision efficiency of Böhm (cf. Sec. 2.3.2), which takes into account particle properties such as shape, density, and fall velocity, but relies partly on semi-empirical assumptions. We decide to focus on stochastic riming, since its dependence on particle properties should lead to a better representation of the riming behavior for particles with developed habit.

The basic assumption of stochastic riming is an equal probability of finding a water droplet for a given volume, which is valid for a locally well mixed cloud. The number of droplets N_d collected along the vertical offset is calculated from the swept volume

$$N_d = \frac{\pi}{4} N_{LWC} \, (D + 2\, r_d)^2 \, |v_t - v_d| \, \Delta t \, , \tag{2.39}$$

where the number of droplets for a specific LWC (N_{LWC}) is given by m_d, the mean cloud droplet mass

$$N_{LWC} = LWC/(6\, md) \, , \tag{2.40}$$

assuming an exponential distribution. The resulting number is scaled by a droplet multiplicity (ξ_d) and the droplets are drawn from an exponential drop size distribution. Depending on the distribution type, the size range can be 1-40 µm. We calculate the collision efficiency (E_c) of Böhm (cf. Sec. 2.3 for details) for a collision between the particle and each of the droplets and update rime mass and volume

$$m_r(t + \Delta t) = m_r(t) + m_d \, E_c \, \xi_d \, , \tag{2.41}$$

$$V_r(t + \Delta t) = V_r(t) + \frac{m_d}{\rho_{rime}} \, E_c \, \xi_d \, . \tag{2.42}$$

We choose to use the empirical relation for the rime density of Cober and List (1993) which provides information about the density of newly formed rime (ρ_{rime}) added to the existing particle

$$\rho_{rime} = 78 + 184\, R_{imp} - 15\, R_{imp}^2 \, . \tag{2.43}$$

The parameterization uses the impact parameter (R_{imp})

$$R_{imp} = -\frac{r_{d\, v_{imp}}}{T_s} \, , \tag{2.44}$$

with the impact velocity (ν_{imp}) of Rasmussen and Heymsfield (1985), the droplet radius (r_d) (in µm), and the surface temperature of the ice particle (T_s) (in degree Celsius).

Depending on the ice habit the added rime may not be evenly distributed over the particles' surface but preferential zones can develop (Wang and Ji, 2000), resulting in different geometries that typically are expressed by the fractal dimension of mass-size and mass-area relations (Erfani and Mitchell, 2017; Seifert et al., 2019). The distribution of rime along the two major axes in the spheroidal model is a critical factor in the prediction of ice crystal habit. We assume that particles fall with their largest cross-sectional area perpendicular to the flow, so that rime is always added to the minor axis while preserving the maximum dimension, transforming the habit of the particle towards a quasi-spherical shape. Jensen and Harrington (2015) refer to the work of Heymsfield (1978) for observations of the aspect ratio of graupel and propose that this quasi-spherical shape translates into an aspect ratio of $\phi = 0.8$ for plates or equivalently $\phi = 1/0.8 = 1.25$ for columns. For prolates with an aspect ratio between $1 < \phi \leqslant 1.25$, the updated equatorial radius a can be described as

$$a = \sqrt{\frac{V_{\mathrm{tot}} + \frac{\Delta m_{\mathrm{rime}}}{\rho_{\mathrm{rime}}}}{\frac{4\pi}{3} c}} , \tag{2.45}$$

with V_{tot} the total volume before riming. Analogous, for oblate particles with $0.8 < \phi \leqslant 1$

$$c = \frac{V_{\mathrm{tot}} + \frac{\Delta m_{\mathrm{rime}}}{\rho_{\mathrm{rime}}}}{\frac{4\pi}{3} a^2} . \tag{2.46}$$

The choice of a quasi-spherical aspect ratio threshold can lead to an oscillation around these values if simultaneous depositional growth supports the development of a more pronounced habit. These oscillations can be interpreted as a tumbling of the graupel particle, whereby the newly added mass is randomly deposited onto one of the axes.

We combine habit prediction with the stochastic riming approach of *McSnow*, introduced by Brdar and Seifert (2018), since it incorporates the shape properties of the particle into the collision probability using the theory of Böhm via the Stokes number (cf. Sec. 2.3.2). To better understand the feedback between habit information and collision probability, we will take a closer look at the implications of the shape dependence of the collision kernel.

2.2.5 *Melting/Freezing*

The change in latent heat $\frac{dQ}{dt}$

$$\begin{aligned}\left(\frac{dm_w}{dt}\right)_{\mathrm{melt}} = -\Bigg(\left(\frac{dQ}{dt}\right)_{\mathrm{depo}} + \left(\frac{dQ}{dt}\right)_{\mathrm{diff}}\Bigg) L_{\mathrm{depo}}(T)^{-1} + \\ \left(\frac{dQ}{dt}\right)_{\mathrm{rime}} L_{\mathrm{melt}}(T)^{-1} ,\end{aligned} \tag{2.47}$$

is defined by three components: deposition, diffusion of heat, and riming.

$$\left(\frac{dQ}{dt}\right)_{depo} = \left(\frac{dm}{dt}\right)_{depo} L_{depo}(T_0)\ , \tag{2.48}$$

$$\left(\frac{dQ}{dt}\right)_{diff} = -4\,\pi\,C\,f_v\,K_a(T)\,(T-T_0)\ , \tag{2.49}$$

$$\left(\frac{dQ}{dt}\right)_{rime} = -\left(\frac{dm}{dt}\right)_{rime} (c_{p,w}\,(T-T_0) - L_{melt}(T))\ , \tag{2.50}$$

$$\tag{2.51}$$

where $K_a(T)$ is the thermal conductivity of dry air, $c_{p,w}$ is the specific heat capacity of water, and $L(T)$ is the latent heat of fusion.

When freezing, drops are assumed to maintain their shape/aspect ratio. Mitra et al. (1990) and Kintea et al. (2015) suggest that the geometry of an ice crystal remains unchanged until it collapses into a water droplet, but the question remains whether water fills the gaps revealed by branched or rimed structures, possibly changing the density of the particles but not necessarily their shape. In *McSnow*, we assume that the gaps are filled, following Rasmussen and Heymsfield (1987) Due to the lack of knowledge, we point out that this potentially changes the behavior of melting particles.

2.2.6 *Aggregation*

Parallel to processes happening on an individual particle level, the interaction between them range from collisions that can cause the original particle to (partly) break (Chapter 7) or even adhere to one another, forming aggregates. To determine, if two ice particles successfully aggregate, we evaluate the quasi-stochastic collision equation for well-mixed clouds. This probabilistic approach follows the work of Gillespie (1972) and Gillespie (1976) for the coalescence process of cloud droplets and defines the collision kernel (K) as

$$K = \pi\,\mathcal{G}\,S_i\,E_c\,|v_1 - v_2|\ , \tag{2.52}$$

where $\mathcal{G}$ describes the geometric collision cross section of two particles (discussed later), and v_1 and v_2 are the individual particle velocities. Böhm's theory of the collision efficiency E_c is explained in detail in Section 2.3.2 and here will only be introduced as a measure for the likelihood of collision. The aggregation process additionally depends on the sticking efficency of ice (S_i) which describes the probability of the two solid bodies sticking together. While the formation of ice bonds is essential to cause adhesion between ice particles (Lamb and Verlinde, 2011), temperatures below the freezing point and short interaction times strongly complicate the process. The two main mechanisms used to explain the increased likelihood of adhesion are the quasi-liquid layer (QLL) (Slater and Michaelides, 2019) and the mechanical interlocking of dendritic features (Pruppacher and Klett, 1997). The theory of the QLL has been postulated by Faraday (1850) and assumes that a frozen water has a thin, quasi-liquid thin layer at its surface even well below the freezing point. This layer consist of only weakly bound water molecules and its thickness increases with increasing temperature. In case of a collision these molecules can form ice bonds

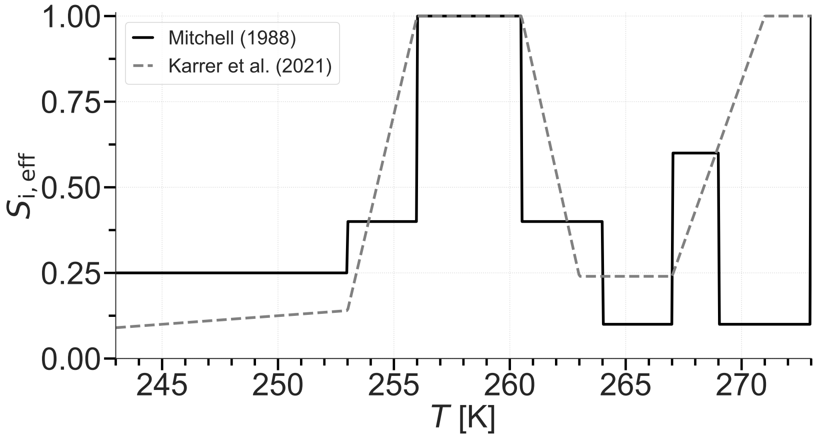

Figure 2.4: Sticking efficiency as a function of temperature as found by Mitchell (1988, solid) and Karrer et al. (2021, dashed line).

that cause the particles to adhere. To date, Asakawa et al. (2016) demonstrated that two distinct types of QLLs exist.

The adhesion or sticking efficiency tries to parameterize this two mechanisms of increases likelihood of adhesion after collision which can be expressed as a function of temperature. Several descriptions are available (e. g. Connolly et al., 2012; Lin et al., 1983) but we decide to use the piece-wise constant formulation of Mitchell (1988)

$$S_i = \begin{cases} 0.1\,, & T \geqslant 4^\circ\,C \\ 0.6\,, & -4^\circ\,C > T \geqslant -6^\circ\,C \\ 0.1\,, & -6^\circ\,C > T \geqslant -9^\circ\,C \\ 0.4\,, & -9^\circ\,C > T \geqslant -12.5^\circ\,C \\ 1.0\,, & -12.5^\circ\,C > T \geqslant -17^\circ\,C \\ 0.4\,, & -17^\circ\,C > T \geqslant -20^\circ\,C \\ 0.25\,, & -20^\circ\,C > T\,. \end{cases} \tag{2.53}$$

as the standard. A comprehensive discussion about the effect of the sticking efficiency can be found in Karrer et al. (2021). In turn, we implemented their updated formulation that on average increases the probability for aggregation in the oblate-favoring regime as well as for temperatures approaching the melting point. This formulation will be used in Chapter 6 to improve the models ability to reproduce IMP fingerprints based on polarimetric radar observations. Figure 2.4 visualizes the differences between the description of Mitchell (1988) and Karrer et al. (2021). Note that Phillips et al. (2015) propose a parameterized sticking efficiency based on the CKE which is also available in *McSnow*.

If two ice particles successfully aggregate, the resulting particle has the attributes

$$\mathcal{P}_{12} = \mathcal{P}_1 + \mathcal{P}_2 = (m_{i,1} + m_{i,2}, m_{r,1} + m_{r,2}, V_{r,1} + V_{r,2}, \ldots)\,. \tag{2.54}$$

It is essential to address the issue of ice volume and aspect ratio in a manner that ensures the creation of a coherent and intelligible new geometry, as both are not inherently additive. In Section 5.3, we will first rely on the diagnostic geometry introduced by Brdar and Seifert (2018) following the empirical power laws for the mass-size relation of aggregates (Mitchell, 1996, S3: Aggregates of Side Planes, Columns, and Bullets). The corresponding aspect ratio of the aggregate is set to $\phi_{agg} = 1$. The approach does not describe the transition from aggregates defined by the shape of a few individual monomer habits to those consisting of many particles. For small numbers of monomers ($N_m < 10$), we expect that this rather simple empirical approach may lead to errors in the estimation of particle properties. Even in the case of relatively large values of N_m, the aggregate shapes do not become self-similar and depend on the properties of the monomers out of which the aggregate is built, as demonstrated by Karrer et al. (2021).

When relying on a mass-size relation for the aggregate geometry, the ice volume can be derived by assuming a spherical shape of the aggregates, consistent with the assumed AR of $\phi_{agg} = 1$.

Another approach is to predict the shape of aggregates with the spheroidal approach as originally introduced by Chen and Lamb (1994a). Shima et al. (2020) points out that the parameterization of Chen and Lamb (1994a) tends to produce aggregates with apparent densities lighter than water vapor, and therefore propose a new model based on snow compaction. For particles with volume weighted apparent densities $\overline{\rho}_{12}$ close to ice density

$$\overline{\rho}_{12} = \frac{(m_1 + m_2)}{(V_1 + V_2)} , \tag{2.55}$$

it is assumed that the shapes of the individual crystals do not change and that the spheroidal approximation of the resulting aggregate reduces the apparent density due to the inclusion of voids between the crystals. As the volume-weighted apparent density becomes smaller, the voids between the individual crystals can be filled by smaller ice crystals, causing effective compaction. With this argument, Shima et al. (2020) assume a minimum apparent density $\rho_{app,min}$ based on observations (Magono and Nakamura, 1965) and determine the resulting particles' apparent density $\rho_{app,res}$ by weighted averaging

$$\rho_{app,res} = \frac{(\rho_i - \overline{\rho}_{12})\, \rho_{12,max} + (\overline{\rho}_{12} - \overline{\rho}_{app,min})\, \rho_{12,min}}{\rho_i - \rho_{app,min}} , \tag{2.56}$$

where the minimum possible apparent density is defined by the maximum volume assuming maximum overlap, while the maximum dimension is preserved

$$\rho_{12,min} = \frac{m_1 + m_2}{V_{max}} . \tag{2.57}$$

Note the additional assumption of $\rho_{12,max} = \overline{\rho}_{12}$. The maximum volume for a pair of particles with $D_1 \geqslant D_2$ is

$$\begin{aligned} V_{max,o} &= \frac{4}{3}\pi a_1^2 \left[c_1 + \min(a_2, c_2)\right] && \text{for oblates,} \\ V_{max,p} &= \frac{4}{3}\pi c_1 \left[a_1 + \min(a_2, c_2)\right] \max(a_1, a_2, c_2) && \text{for prolates.} \end{aligned} \tag{2.58}$$

From the resulting averaged density the minor dimension is updated

$$\begin{aligned} c_{12} &= \frac{m_1 + m_2}{\frac{4}{3}\,\pi\,\rho_{\mathrm{app,res}}\,a_{12}^2} && \text{for oblates,} \\ a_{12} &= \sqrt{\frac{m_1 + m_2}{\frac{4}{3}\,\pi\,\rho_{\mathrm{app,res}}\,c_{12}^2}} && \text{for prolates.} \end{aligned} \tag{2.59}$$

Section 5.3.2 will compare this simplified approach with the prognostic aggregation scheme of Shima et al. (2020).

COLLISION KERNEL GEOMETRY When using an explicit habit prediction, the assumption about the geometry term ($\mathcal{G}$) of the collision kernel K must be taken into account. In classical m-D- and m-A-relations, the maximum dimension D is used to estimate the geometry term (D-Kernel)

$$K_D = \pi \left(\frac{D_1}{2} + \frac{D_1}{2}\right)^2 S_i\, E_c\, |v_1 - v_2| = \pi\, (r_1 + r_2)^2\, S_i\, E_c\, |v_1 - v_2|\,. \tag{2.60}$$

The formulation is neutral for the treatment of oblates, but may overestimate the actual collision cross section of a prolate. An alternative is the A-Kernel Böhm, 1994; Connolly et al., 2012; Karrer et al., 2021

$$K_A = \pi \left(\sqrt{A_1\,\pi^{-1}} + \sqrt{A_2\,\pi^{-1}}\right)^2 S\, E_c\, |v_1 - v_2|\,. \tag{2.61}$$

The overestimation can be determined by the ratio of the maximum dimension of the prolates D_{max} to the area equivalent diameter $D_{\mathrm{eq,a}}$ and is proportional to

$$\frac{D_{\mathrm{max}}}{D_{\mathrm{eq,a}}} = \frac{2\,c}{2\,\sqrt{A_n\,\pi^{-1}}} = \frac{c}{\sqrt{a\,c}} = \sqrt{\frac{c}{a}} = \sqrt{\phi}\,. \tag{2.62}$$

Based on the results of Karrer et al. (2021), we favor the use of the A-kernel when using the habit prediction scheme as it is neutral for oblates and reduces the effect of the long axis for prolates.

The aggregation process is special in the sense that it directly interferes with the assumptions of the super-particle approach. Section 2.4.1 will explain explain how the aggregation is handled numerically and explains the role of the multiplicity ξ.

2.2.7 *Secondary Ice Production*

Several secondary ice production mechanisms have been proposed to explain the difference between the observed INP and IPNC. Korolev and Leisner (2020) review experimental studies from the last 70 years on six SIP mechanisms, shown in Figure 2.5: (a) fragmentation of freezing drops, (b) rime splintering (Hallett–Mossop process), (c) fragmentation due to ice–ice collision, (d) fragmentation due to thermal shock, (e) fragmentation of sublimating ice particles, and (f) activation of INPs in transient supersaturation around freezing drops. In summary, all processes are either poorly understood or experiments give conflicting results, and the effectiveness of IPNC enhancement for the different processes cannot be precisely identified. With respect to the atmospheric regimes within the scope of this thesis, two of the six processes are likely to occur, namely rime splitting and fragmentation during ice-ice collision (hereafter simply referred to as fragmentation).

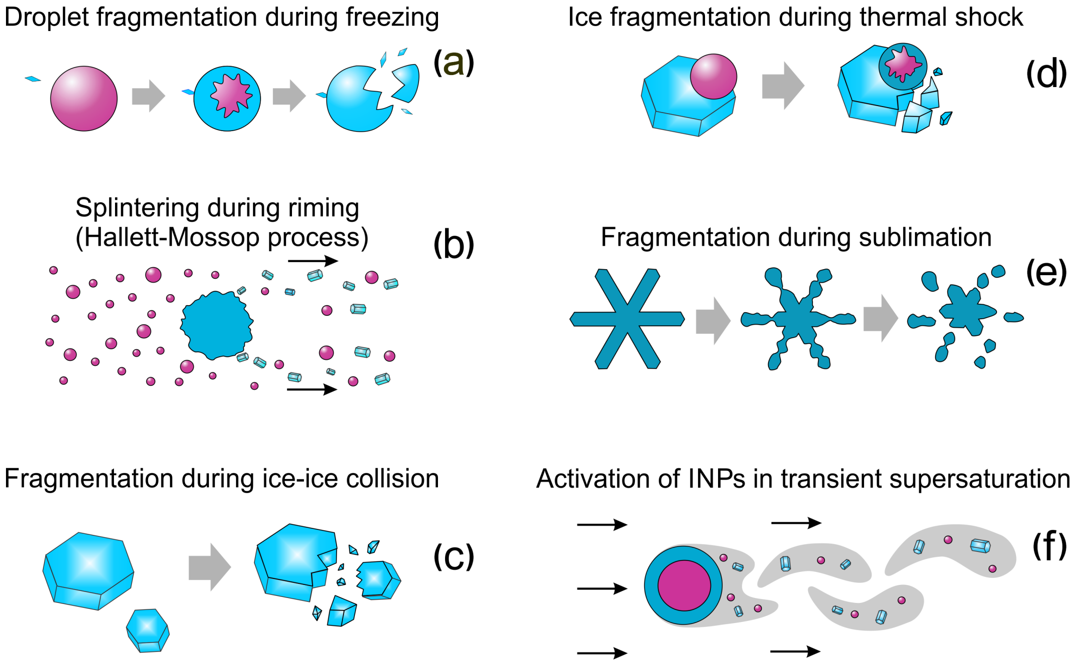

Figure 2.5: Conceptual diagram of SIP mechanisms: (a) fragmentation of freezing drops, (b) rime splintering (Hallett–Mossop process), (c) fragmentation due to ice–ice collision, (d) fragmentation due to thermal shock, (e) fragmentation of sublimating ice particles, and (f) activation of INPs in transient supersaturation around freezing drops. The ice phase is depicted by blue, the liquid phase by red colors. This figure was taken from (Korolev and Leisner, 2020) is redistributed under the creative commons attribution 4.0 License.

2.2.7.1 *Rime splintering*

In clouds containing water in the liquid and ice phase, and at temperatures between −3°C and −8°C, collisions between liquid droplets and large ice crystals can cause droplets to freeze and shatter, producing an abundance of small ice splinters. Several studies have examined the physical mechanisms involved in splinter formation. Mossop (1976) proposes four possible mechanisms, including the formation of an ice shell around accreted droplets followed by fragmentation during freezing, detachment of droplets in contact with the rime, growth and detachment of fragile ice needles, and detachment of rimed ice by evaporation. Choularton et al. (1980, 1978) suggest that accreted droplets with specific characteristics could minimize heat transfer, leading to the formation of an ice shell around the droplet and subsequent shell fractures with protuberance formation. Dong and Hallett (1989) suggest that stress buildup within accreted droplets caused by a temperature gradient during freezing may contribute to fragment formation. In a study by Emersic and Connolly (2017), they propose that the rime spikes formed by ongoing droplet accretion have the potential to detach during particle tumbling or due to the influence of small droplets. While the mechanism behind the production of rime splinters is not fully understood, studies have attempted to include the rate of ice crystals produced by rime splintering (P_{HM}) as a function of the added accreted rime mass and temperature (Pruppacher and Klett, 1997, Eqs. 16-70 & 16-71),

$$P_{\mathrm{HM}} = 350 \times 10^6 \, \frac{dm_r}{dt} \, f(T) \, , \tag{2.63}$$

$$f(T) = \begin{cases} \dfrac{(270.16 - T)}{2} \, , & 270.16 \geqslant T \geqslant \ 268.16\,\mathrm{K} \\ \dfrac{(T - 265.16)}{3} \, , & 286.16 \geqslant T \geqslant \ 265.16\,\mathrm{K} \\ \qquad 0 \, , \ \text{otherwise} \, . \end{cases} \tag{2.64}$$

While this formulation is used in for the continuous riming, the number of splinters for the stochastic riming is relative to the number of drops with a radius greater than $r_{\mathrm{crit}} > 12\,\mu\mathrm{m}$

$$P_{\mathrm{HM}} = \frac{1}{250} \, \frac{\pi \, d^2_{\mathrm{graupel}}}{4} \, v_{\mathrm{graupel}} \, E_{\mathrm{coll}} \, N_{r > r_{\mathrm{crit}}} \, f(T) \, . \tag{2.65}$$

Here, $N_{r>r_{\mathrm{crit}}}$ is the number of cloud drops greater than r_{crit}. Both equations are based on observations where the first assumes 350 shards per 10^{-3} g of rime accreted while the second finds one shard per 250 drops (larger than the threshold). Unless otherwise noted, we will use Eq. 2.65 as it depends on the graupel characteristics as well as the collision efficiency.

2.2.7.2 *Fragmentation*

Descriptions of the production of fragments from ice-ice collisions are rare due to a lack of observational data. The idea of the fragmentation scheme of Phillips et al. (2017a) is based on the principle of energy conservation in the case of mechanical breakup in collisions of ice particles. During collisions, new cloud ice particles are initiated without the need for INP. While rime splintering (Hallett-Mossop process, Hallett and Mossop, 1974) is limited to a narrow temperature range and can only explain the high concentrations of ice for clouds with a warm base, fragmentation can occur for any collision event of solid hydrometeors.

Although measurements are scarce, Phillips et al. (2017a) use the principle of energy conservation combined with fits to observations by Takahashi et al. (1995) and Vardiman (1978) to propose a physical formulation of fragmentation. The key property, the initial collision kinetic energy (K_0), is defined as

$$K_0 = \frac{1}{2} \, \frac{m_1 \, m_2}{m_1 + m_2} \, (v_1 - v_2)^2 \, , \tag{2.66}$$

with the masses of the colliding particles m_n and their terminal velocities v_n. The conservation of CKE for a rebounding collision is

$$K_0 = K_{\mathbf{fin}} + \Delta S + K_{\mathrm{th}} \, . \tag{2.67}$$

Here $K_{\mathbf{fin}}$ is the final CKE of the system after the collision as the sum of the energies of the colliding particles and their change in rotation. The final collision kinetic energy ($K_{\mathbf{fin}}$) also includes the kinetic energy of all the fragments and the air. The change in surface adhesion energy (ΔS) describes the change in potential energy after the collision as the particles separate, and K_{th} is the kinetic energy lost due to inelastic deformation, heat, and noise. It is assumed that a b_2 is the energy available to create fragments by breaking asperities (including branches, accreted rime, or parts of aggregated crystals) and is evenly distributed over all asperities in the contact area.

$$\delta K_{th} = b_2 K_{th} \approx b_2 K_0 (1 - q_{res}^2) < K_{th} \ . \tag{2.68}$$

For this assumption to be valid, it must also be assumed that the fractional energy lost (K_{th}/K_0) is constant even for collisions where $\Delta S \neq 0$ (as shown by Wall et al., 1990). Therefore, the coefficient of restitution (q_{res}) is universally applicable.

$$q_{res} = \sqrt{1 - \frac{K_{th}}{K_0}} \ . \tag{2.69}$$

The number of fragments (N_{frag}) is the product of the number of breakable asperities at the point of contact ($N_{contact}$) and the probability that such an asperity will be broken by the impact P

$$N_{frag} = N_{contact} \, P \left(\frac{\delta K_{th}}{N_{contact}} \geqslant G_{break} \right) \ . \tag{2.70}$$

The number of breakable asperities $N_{contact}$ for a collision type $\mathbf{M}$

$$N_{contact}(\mathbf{M}) = \alpha_{equiv} \, b_1 \, n_{branch}(\mathbf{M}) \ , \tag{2.71}$$

can be defined by the number density of breakable asperities ($n_{branch}(\mathbf{M})$), a fractional constant b_1, and the equivalent spherical area (α_{equiv})

$$\alpha_{equiv} = \pi \, D_{equiv,small}^2 \ , \tag{2.72}$$

where $D_{equiv,small}$ is the equivalent spherical diameter of the smaller or more fragile particle. For simplicity, $A(\mathbf{M}) = b_1 \, n_{branch}(\mathbf{M})$ is used as a measure of the number density (per unit area) of breakable asperities. The quantities are specific to the collision type $\mathbf{M}(T, D, RH_i, ...)$, which in turn depends on the atmospheric conditions, the particle size, the degree of riming, and possibly other factors such as the impact angle. For the full explicit derivation of the probability function, the reader is referred to the original paper by Phillips et al. (2017a). A summary is given here. The arguments of the probability function are the total energy available for breaking δK_{th} distributed over all breakable branches and the work needed to break a single asperity (G_{break}). The work required to break an asperity of a given width is approximately proportional to its cross-sectional area $G_{break} \propto \widetilde{A}$. By assuming an exponential distribution for the width of asperities (Polycarpou and Etsion, 1999) and thus for G_{break}, the probability distribution $g(G_{break})$ can be approximated by a Weibull distribution

$$g \propto G_{break}^{\gamma-1} \exp\left[- \left(\frac{G_{break}}{G_c} \right)^{\gamma} \right] \ , \tag{2.73}$$

where fracture energy (G_c) is the scale parameter of the Weibull distribution of G_{break} and γ is the shape parameter. The probability to break an asperity (Ξ) of a given width is that which is less than the CKE-dependent limit Ξ_0

$$P\left(G_{break} \leqslant \frac{\delta K_{th}}{N_{contact}} \right) = P(\Xi \leqslant \Xi_0) = ... = 1 - \exp\left[-\Omega \, \lambda \left(\frac{K_0}{\alpha_{equiv}} \right)^{\gamma} \right] \ , \tag{2.74}$$

with

$$\Omega(\mathbf{M}) = b_3 \left(\frac{b_2(1-q^2)}{n_{\mathrm{branch}}\, b_1} \right)^{\gamma} . \tag{2.75}$$

Equation 2.74 relates how the probability of an asperity being broken is determined by collision kinetic energy (K_0). In the interest of a generalized formulation, the work required to break an asperity averaged over size and strength $\langle G_{\mathrm{break}} \rangle$ can be found as the mean of the Weibull function

$$\langle G_{\mathrm{break}} \rangle = G_c\, \Gamma_f \left(1 + \frac{1}{\gamma} \right) , \tag{2.76}$$

with the Gamma function (Γ_f). Phillips et al. (2017a) introduce a measure inversely proportional to $\langle G_{\mathrm{break}} \rangle$ called the asperity-fragility coefficient (C_f)

$$C_f = \frac{b_2(1-q_{\mathrm{res}}^2)\Gamma_f(1+\frac{1}{\gamma})}{\langle G_{\mathrm{break}} \rangle} . \tag{2.77}$$

This results in the general formula for the number of fragments $N \in \mathbb{N}$ created by a collision of type $\mathbf{M}$

$$\begin{aligned} N_{\mathrm{frag}} &= \alpha_{\mathrm{equiv}}\, A(\mathbf{M})\, P\left(\frac{\delta K_{\mathrm{th}}}{N_{\mathrm{contact}}} \geqslant G_{\mathrm{break}} \right) \\ &\propto 1 - \exp\left\{ - \left[\frac{C_f K_0}{\alpha_{\mathrm{equiv}} A(\mathbf{M})} \right]^{\gamma} \right\} , \end{aligned} \tag{2.78}$$

$$\Rightarrow N_{\mathrm{frag}} = \alpha_{\mathrm{equiv}}\, A(\mathbf{M}) \left(1 - \exp\left\{ - \left[\frac{C_f K_0}{\alpha_{\mathrm{equiv}} A(\mathbf{M})} \right]^{\gamma} \right\} \right) . \tag{2.79}$$

In general, there are three broad types of ice collisions:

1. type : graupel or hail with other graupel/hail,
2. type : crystal or snow with graupel/hail
3. type : crystal or snow with other crystals/snow

The specifics of the categories found in the original paper are not used because for *McSnow* there is individual particle information. Particles with a degree of riming $F_r > 0.5$ are considered graupel without size information. If a particle has a fraction of frozen water m_f greater than 80 % of the total mass and there is water on the surface, it is classified as hail. All other particles are (pristine) ice or snow, distinguished by the monomer number.

When particles are of the same species, the smaller particle is assumed to be more fragile. Otherwise, the particle that is not graupel/hail is the more fragile, basically assuming that cloud ice and snow have a more fragile structure. Unlike the bulk microphysics, the individual information of the particles allows the fragility to be determined by evaluating their total density.

The resulting fragments are initiated with an average mass, which is assumed to be a small, constant mass fraction of the more fragile particles (ζ). The total number of fragments produced by a collision is limited by an upper bound of N_{limit} depending on the collision type. When evaluating $A(M)$, the polynomial fits are only valid for

the size range $0.5\,\mathrm{mm} < D < 5\,\mathrm{mm}$ and $F_r \leqslant 0.5$. Values exceeding these limits are set to the nearest limit. The specifics of the various parameters used for different collision types can be found in the appendix (Tab. A.2).
For application in a model, the dependence of ice morphology on relative humidity and growth history is neglected. The morphological habit can only be characterized by temperature and rime fraction $\mathbf{M} \approx (T, D, F_r)$. Observations show that $A(\mathbf{M})$ is at least partly temperature dependent. The C_f has only an average characteristic empirical value depending on the morphology, because the lack of observations prevents stronger dependencies on temperature, humidity, rimed fraction, size, or similar. Phillips et al. (2017a) are well aware that the empirical results derived from observations have some major caveats. Therefore, they have made some corrections for possible sublimation effects. Similarly, the observations only measure head-on collisions, which could have increased the number of fragments. Overall, they estimate that the number of fragments may have an error of at least a factor of 2. For further reference, we will abbreviate this scheme as the Phillips fragmentation scheme (PFS).

2.3 REVIEW OF BÖHM'S TERMINAL VELOCITY AND COLLISION EFFICIENCY PARAMETERIZATION

The work of Böhm comprises several publications, making it difficult to extract the parameterizations for terminal velocity and collision efficiency from his original work (Böhm, 1989, 1992a,b,c, 1994, 1999). Therefore, we review and summarize his work and its application to habit prediction. Since Böhm (2004) advised to use the original equations because they compare better with numerical simulations and field observations, we exclude the revision of Posselt et al. (2004).

2.3.1 *Terminal Velocity*

The terminal velocity scheme is important for particles with different shapes and directly affects the depositional growth and the collision kernel. Concurrently, the terminal velocity determines the residence time of a particle, which is frequently employed in NWP models as a tuning parameter.
Böhm's parameterization is a generalized and complete framework that makes the following necessary assumptions

- The maximum dimension is oriented in the horizontal plane, as shown for example by Westbrook and Sephton (2017) for all simple geometries studied.
- The porosity p in the theory of Böhm is related to the ratio of the cross-sectional area $\tilde{A}$ (Eq. (2.37)) to the area of the circumscribing ellipsis A_{ce} (Eq. (2.6)). It represents the internal structure of ice crystals caused by secondary habits (cf. Fig. 2.6)

  $$p = 1 - q, \qquad q = \frac{\tilde{A}}{A_{ce}} \,. \tag{2.80}$$

  The ratio q is not to be confused with the area ratio $A_r = \tilde{A}\, A_{cc}^{-1}$ which Heymsfield and Westbrook (2010) and McCorquodale and Westbrook (2021a)

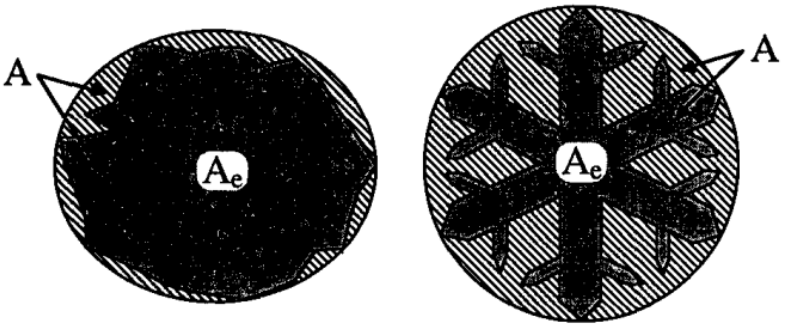

Figure 2.6: Definitions of cross-sectional area A_e ($= \widetilde{A}$) and circumscribing ellipsis area A ($= A_{ce}$) from Böhm (1989). ©American Meteorological Society. Used with permission.

define as the ratio of the cross-sectional area to the circumscribing circle A_{cc} (Eq. (3.1)).

- While fall velocities based on prolate or cylindrical geometries are realistic, Böhm (1992a) argues that hexagonal columns are better represented by cylinders and suggest using them for $\phi > 1$.

  $$q = \frac{4}{\pi} \qquad \text{for } \phi > 1 \ .$$

  This approximation is discussed in detail in Section 3.1.

- We add the assumption that all particles accelerate immediately to their terminal velocity. See, e. g., Naumann and Seifert (2015) for an alternative approach that attempts to account for deviations from the terminal fall velocity.

Böhm's parameterization is valid for solid and liquid hydrometeors and is based on a functional dependence of the drag coefficient on the Reynolds number derived from BLT. The terminal velocity follows the definition of the Reynolds number. Both the Reynolds number and the drag coefficient are modified by the aspect ratio via the Best number (see Eq. 2.81). Böhm defines the characteristic length scale as the equatorial diameter $D_{char} = 2\,a$ instead of the maximum dimension (also mentioned by Shima et al., 2020). For columnar particles, we determine the equatorial diameter by using the total particle mass and assuming the particle has the volume of a cylinder. The used variables are the Best number (X), the turbulence modified Best number (X'), the dynamic viscosity (μ), the air density (ρ_a), the viscous shape parameter (k), a function regarding the aspect ratio (Γ_ϕ), the drag coefficient ($C_{DP,S}$), the drag coefficient fitted for prolates (C_{DP}), the Oseen drag coefficient (C_{DO}), the inertial drag coefficient (C_{DI}), and some helper variables β, γ. The minimum and maximum functions are used to constrain transitions from very oblate over quasi-spherical to very prolate particles. For more details on the derivation, the reader is referred to Böhm (1989) and Böhm (1992a).

$$
\begin{aligned}
X(m,\phi,q) &= \frac{8\, m_i\, g\, \rho_a}{\pi\, \mu^2\, \max(\phi;1)\, \max(q^{1/4};q)}\,, && \text{(2.81a)}\\
k(\phi) &= \min\Bigg(\max(0.82+0.18\,\phi\,;0.85)\,;\left(0.37+\frac{0.63}{\phi}\right)\,; && \\
&\qquad \frac{1.33}{\max(\log\phi\,;0)+1.19}\Bigg)\,, && \text{(2.81b)}\\
\Gamma_\phi &= \max\left(1\,;\min(1.98\,;3.76-8.41\phi+9.18\phi^2-3.53\phi^3)\right)\,, && \text{(2.81c)}\\
C_{DP,S} &= \max\left(0.292\,k\,\Gamma_\phi\,;0.492-\frac{0.2}{\sqrt{\phi}}\right)\,, && \text{(2.81d)}\\
C_{DP} &= \max\left(1;q(1.46q-0.46)\right)\, C_{DP,S}\,, && \text{(2.81e)}\\
C'_{DP} &= C_{DP}\,\frac{X'}{X} = C_{DP}\,\frac{1+(X/X_o)^2}{1+1.6(X/X_o)^2}, && \\
&\text{with } X_o = \begin{cases} 2.8\times 10^6, & \text{ice particles,}\\ 6.7\times 10^6, & \text{water particles,}\end{cases} && \text{(2.81f)}\\
C_{Do} &= 4.5\,k^2\,\max(\phi\,;1)\,, && \text{(2.81g)}\\
\beta &= \left[1+\frac{C_{DP}}{6\,k}\left(\frac{X'}{C'_{DP}}\right)^{1/2}\right]^{1/2} - 1\,, && \text{(2.81h)}\\
\gamma &= \frac{C_{Do}-C_{DP}}{4\,C_{DP}}\,, && \text{(2.81i)}\\
N_{Re} &= \frac{6\,k}{C'_{DP}}\,\beta^2\left[1+\frac{2\,\beta\, e^{-\beta\,\gamma}}{(2+\beta)(1+\beta)}\right]\,, && \text{(2.81j)}\\
C_{DI} &= \frac{X}{N_{Re}^2} - \frac{24\,k}{N_{Re}}\,, && \text{(2.81k)}\\
v_t &= \frac{\mu\, N_{Re}}{\rho_a\, d_{char}}\,. && \text{(2.81l)}
\end{aligned}
$$

The middle term of equation 2.81 c is found with and without the square root of the aspect ratio in the denominator (see Eq. 13 in Böhm, 1992a and Eq. 9 in Böhm, 1999). Analysis indicates that for a consistent transition the version from Böhm (1992a) should be correct while differences are marginal.

Böhm (1992a) showed that the formula is consistent with viscous theory, and by matching the results from BLT with Oseen's theory (Oseen, 1927), there is good agreement of inertial drag at low Reynolds numbers. Böhm (1992a) claims that the errors are generally on the order of $\epsilon \leqslant 10\,\%$ for $0 < N_{Re} < 5 \times 10^5$ for the hydrometeor types studied (raindrops, columnar and planar ice crystals, rimed and unrimed aggregates, various types of graupel, and hail).

2.3.2 *Collision Efficiency*

Independently of the state of the collision particles (i.e. water-water/coalescence, water-ice/riming, or ice-ice/aggregation), the collision efficiency E_c is defined as the ratio of the actual collision cross section to the geometric one (Pruppacher and Klett, 1997)

$$E_c = \frac{x_c^2}{(r_1 + r_2)^2} = \frac{y_s}{\delta} , \tag{2.82}$$

where x_c is the critical initial horizontal offset and r_n is the radius of the interacting particles. Böhm (1992b) states that the collision efficiency for axisymmetric particles can be described by the ratio of the stop distance of the collected particle (y_s) and the boundary layer thickness (δ) of the collecting particle . For non-axisymmetric particles, the collision efficiency derivation is extended to a generalized form (Böhm, 1992c)

$$E_c = \left(\frac{y_s}{\delta}\right)^{2/j} , \tag{2.83}$$

with $j = 1$ for a two-dimensional flow (around the prolate) and $j = 2$ for the axisymmetric case. The boundary layer thickness δ can be calculated by

$$\delta = \delta_0 \, \frac{r}{\sqrt{N_{Re}\, \Gamma_\phi}} , \tag{2.84}$$

with $\delta_0 = 3.60$ for oblates and $\delta_0 = 4.54$ for prolates The habit specific function Γ_ϕ can be found in Eq. 2.81c.

By replacing the individual boundary layer by the sum of the boundary layers of the colliding particles and integrating the differential equation from the initial velocity (detailed analysis in the dissertation of Böhm, 1990), Böhm finds the collision efficiency for the resulting two-body system as

$$E_c = \begin{cases} \left[H \ln\left(\cosh \frac{F}{H} + \frac{1+G}{F} \sinh \frac{F}{H}\right) - G\right]^{2/j}, & \left(\frac{F}{H} < 10\right) , \\ H \ln\left(\frac{F+G}{2F}\right) + F - G, & \left(\frac{F}{H} \geqslant 10\right) . \end{cases} \tag{2.85}$$

The variables used are defined as follows

$$F = \sqrt{G^2 + \frac{C_{I,1}\, v_{I1}^2}{C_{DI}^* \, |v_1 - v_2|^2}} , \tag{2.86a}$$

$$G = \frac{6\, \mu_a}{\rho_a \, r^* \, |v_1 - v_2| \, C_{DI}^*} , \tag{2.86b}$$

$$H = \frac{2\, m^*}{\rho_a \, \pi \, r^{*2} \, C_{DI}^* \, \delta} , \tag{2.86c}$$

$$v_{I1} = \frac{2+j}{4} v_1 . \tag{2.86d}$$

with the inertial drag coefficient with respect to r^* (C_{DI}^*) and the initial velocity while $C_{I,1}$ refers to the bigger particle properties. While the latter is determined by Eq. 2.81l, C_{DI}^* is found by Eq. 2.81f-g and

$$C_{DI}^* = C'_{DP} \left(1 + \frac{4}{\beta}\left(1 - e^{-\gamma\, \beta}\right)\right) , \tag{2.87}$$

to match the value of C_{DI} with the value from Oseen theory at low Reynolds numbers.

The two-body system is characterized by the radius r^*, mass m^*, area of intersection A^*, initial velocity v^*, and boundary layer thickness δ_s^*

$$r^* = \frac{r_1\, r_2}{r_1 + r_2} = \sqrt{A^*/\pi}\,, \tag{2.88a}$$

$$m^* = \frac{m_1\, m_2}{m_1 + m_2}\,, \tag{2.88b}$$

$$A^* = \pi\, r^{*2} = \frac{A_1\, A_2}{\pi\,(r_{e1} + r_{e2})}\,, \tag{2.88c}$$

$$v^* = \max\left(|v_1 - v_2|; v_{\min}\right)\,, \tag{2.88d}$$

$$\delta_s^* = \delta_{s1}\sqrt{v_1/v^*} + \delta_{s2}\sqrt{v_2/v^*}\,. \tag{2.88e}$$

For v^*, a minimum value is assumed ($v_{\min} = 10^{-10}\,\mathrm{m\,s^{-1}}$) because for equally fast particles the difference would approach zero, leading to a division by zero in Eq. 2.86 a and 2.86 b.

In the case of an oblate particle, the equivalent circular radius r_e is the equatorial radius r but for prolate particles the definition changes to

$$r_e = \left(\frac{4\,\phi}{\pi}\right)^{1/2} r_1\,, \tag{2.89}$$

following the special assumptions of columns to be better approximated by a cylindrical shape. In Böhm (1999), Böhm especially mentions that in case of columns or irregularly shaped aggregates the equivalent circular definition shall be used. In a generalized form for all particle shapes they can be written as

$$r_e = \sqrt{A/\pi}\,, \tag{2.90a}$$

$$\phi_e = \min(\phi; 1)\,\frac{r}{r_e}\,, \tag{2.90b}$$

$$q_e = \begin{cases} \pi\, q/4, & q > 1, \\ q, & q \leqslant 1, \end{cases} = q\left[1 - \frac{\max(q-1;0)}{q-1}\left(1 - \frac{\pi}{4}\right)\right]\,. \tag{2.90c}$$

To fully define the shape characteristics of the two-body system, we additionally need to give definitions of the equivalent aspect ratio and porosity. Simple averaging of these quantities might lead to strong over- or underestimation. Hence, we use the radius weighted mean of those characteristics (Böhm, 1999)

$$\xi^* = r^*\left(\frac{\xi_1}{r_{e1}} + \frac{\xi_2}{r_{e2}}\right) \quad (\xi = q, \phi)\,, \tag{2.91}$$

where the indices refer to the corresponding particle.

For anisotropic particles, the velocity v_1 has to be replaced by a characteristic velocity

$$v_1' = \begin{cases} \phi_1\, v_1 & \text{, for plates,} \\ \frac{3}{4}\, v_1 & \text{, for columns.} \end{cases} \tag{2.92}$$

To account for the contribution of the surrounding non-frictional flow, Böhm added an approximate analytical solution based on potential flow theory (cf. Böhm, 1994).

This extension aims at improving the asymptotic behavior for low Reynolds numbers $N_{Re} \lesssim 1$. With this modification, the total collision efficiency E is the product of the collision efficiency according to BLT E_c (from above) and the contribution from potential flow theory E_p.

$$E = E_c\,E_p = \begin{cases} E_c \left[\left(\cosh \frac{\Delta_x t_\delta}{c_x} + \frac{1}{\Delta_x} \sinh \frac{\Delta_x t_\delta}{c_x}\, e^{-t_\delta/c_x}\right)\right]^{-j}, & (b\,c_y \geqslant 1)\,, \\ E_c \left[\left(\frac{2\,\Delta_x}{1+\Delta_x}\, e^{-(\Delta_x-1)\,t_\delta/c_x}\right)\right]^{j}, & (b\,c_y \leqslant 1)\,. \end{cases} \tag{2.93}$$

The variables used in the flow correction for potential flow are defined as

$$t_\delta = \begin{cases} \frac{c_y}{\Delta_y} \arctan \frac{\Delta_y}{b\,c_y - 1}, & (b\,c_y \geqslant 1)\,, \\ \frac{c_y}{\Delta_y} (\pi - \arctan \frac{\Delta_y}{1 - b\,c_y}), & (\frac{1}{2} < b\,c_y < 1)\,, \end{cases} \tag{2.94a}$$

$$c_i = \frac{m_2}{3\,k_{2,i}\,\pi\,r_2\,\eta_a} \quad (i = x, y)\,, \tag{2.94b}$$

$$b = \frac{3\,\nu}{r_{e,1}\,\delta_1}\,, \tag{2.94c}$$

$$\Delta_x = \sqrt{2\,b\,c_x/j + 1}\,, \tag{2.94d}$$

$$\Delta_y = \sqrt{2\,b\,c_y - 1}\,. \tag{2.94e}$$

For the remainder of the thesis, we will refer to the total collision efficiency E as E_c and use it for all collision events of aggregation, riming, and coalescence (Bringi et al., 2020).

As an additional and important modification, Böhm incorporated the variation of hydrometeors' fall velocity into the collision efficiency, which allows for self-collection of particles of similar velocity. With this addition, the framework accounts for the fact that all solid hydrometeors are irregular and their geometry varies, where both effects cannot be captured by the spheroidal geometry. The full integration and details can be found in the original paper by Böhm (1992c). Here we note the result that the difference of the actual fall velocities of irregular hydrometeors (marked by the bar) changes the collision efficiency by

$$E\,|\bar{v}_1 - \bar{v}_2| = v_{t,1}\, f\left(\frac{v_{t,1}}{v_{t,2}}\right) + v_{t,2}\, f\left(\frac{v_{t,2}}{v_{t,1}}\right)\,, \tag{2.95}$$

where

$$f(z) = \Phi\left(\frac{\ln z + \sigma^2}{2\,\sigma}\right)\,, \tag{2.96}$$

and where Σ is the error function. Böhm (1992c) assumes that the fall speed of a population of ice crystals and snowflakes is statistically distributed, and assumes that the distribution is log-normal because the growth processes are multiplicative and the standard deviation is defined as

$$\sigma = v_{t,i}\,\sqrt{e^{\sigma^2/2} - 1} \approx \sigma\, v_{t,i} \qquad (\sigma \ll 1)\,. \tag{2.97}$$

Assuming an equal mean fall velocity and a standard deviation of $\sigma = 0.25$, this results in an expected value of the fall velocity difference of

$$E\,|\bar{v}_1 - \bar{v}_2| = 0.281\, v_{t,1}\,. \tag{2.98}$$

This modification is critical to collision efficiency because it affects particles with similar fall speeds, effectively increasing the probability of collision.

2.4 NUMERICAL ASPECTS

Beside the microphysical details, the most important numerical aspects need further elaboration. We limit this section to the Monte-Carlo approach for aggregation and the interpolation of the atmospheric state to the particle position.
The use of different numerical time steps for the different processes is possible in *McSnow* to increase efficiency. Brdar and Seifert (2018) rate the differences due to the sub-stepping as negligible, we therefore just assume a constant time step for all processes and integration (see e. g.Eq. 2.39).

2.4.1 *Monte-Carlo Aggregation*

Monte-Carlo aggregation is a critical part of particle modeling for an efficient approximation of the aggregation process of hydrometeors (same is true for coalescence). When considering particle aggregation, it becomes necessary to determine which super-particles are close enough to interact. To address this issue, we divide the vertical domain into a set of n_z height levels and restrict aggregation to particles within the same height level. This requires the assumption that particles within a height level are well mixed. As aggregation is treated as a stochastic process, the number of super-particles per grid box should not be below 10 and rather in the order of 100 (Brdar and Seifert, 2018). In an analysis of collection/aggregation algorithms, Unterstrasser et al. (2017) find similar numbers for numerical convergence.
Each super-particle represents an ensemble of particles expressed by its' multiplicity. When two super-particles $\mathcal{S}_1$ and $\mathcal{S}_2$ aggregate, they are replaced by two new super-particles ($\mathcal{S}_1', \mathcal{S}_2'$) with the updated attributes (marked by the prime). We distinguish two cases, either the multiplicity of one particle is greater than that of the other ($\xi_1 > \xi_2$) or they are equal ($\xi_1 = \xi_2$). In the first case, the attributes of $\mathcal{S}_1$ remain unchanged, but its' multiplicity is reduced. The remaining particle $\mathcal{S}_1'$ contains the particles that do not interact with the collision partner $\mathcal{S}_2$. In case of equal multiplicity we keep both super-particles if $\xi_1 = \xi_2 > 1$, otherwise we remove one. Regarding this special case, $[\xi_2/2]$ particles are transferred to $\mathcal{S}_1$ and aggregate, while the other half aggregates with the particles of $\mathcal{S}_2$. Here, the largest integer less than or equal to x is indicated by the [x] Gauss brackets. In programming languages, this is often called the `FLOOR` function. For a set of particles $\mathcal{I} = (\mathcal{S}_1, ..., \mathcal{S}_n)$ inside a grid box, we apply the Monte Carlo aggregation of Shima et al. (2009) in three steps:

1. generating an perturbed array of the set of particles $\mathcal{Q}$ defining the potential collision partner without overlap .
2. the probability of collision p_{coll} for each pair $(\mathcal{S}_j, \mathcal{S}_k)$ is calculated using the collision kernel K from Equation 2.52

$$p_{\text{coll}} = \max(\xi_j, \xi_k)\, K \,\frac{N_S\,(N_S - 1)}{\frac{2}{\frac{N_S}{2}}}\,. \tag{2.99}$$

   The number of collisions is determined with a random number that is drawn from a uniform distribution $\varphi \in (0, 1)$

$$\gamma_j = \begin{cases} [p_{\text{coll}}] + 1 & \text{, if } \varphi < p_{\text{coll}} - [p_{\text{coll}}] \\ [p_{\text{coll}}] & \text{, otherwise.} \end{cases} \tag{2.100}$$

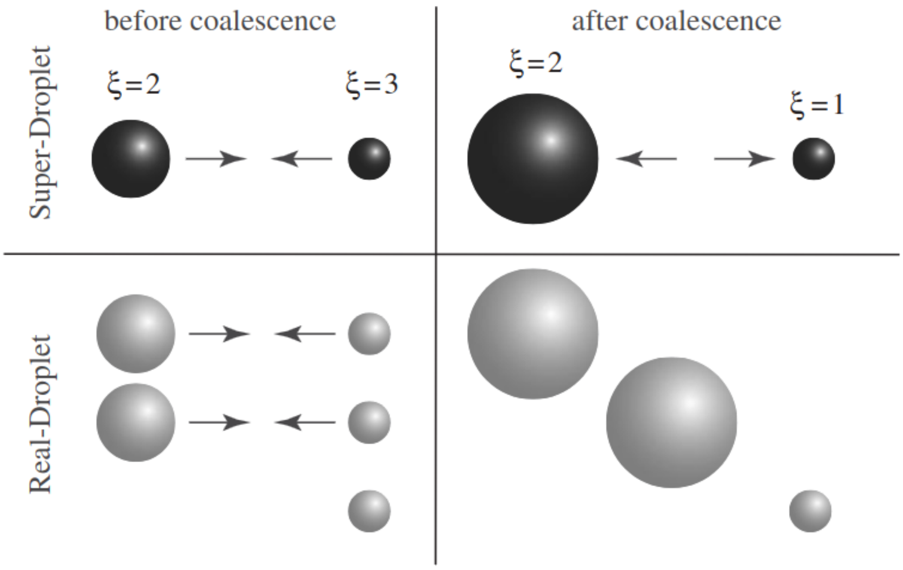

Figure 2.7: Schematic of Shima et al. (2009), visualizing the coalescence process with super-particles (upper row) compared to real droplets (bottom row). The number of real droplets represented by one super-particle is given by its' multiplicity (ξ). ©Royal Meteorological Society/John Wiley and Sons. Used with permission.

If $\gamma_j = 0$ the pair $(\mathcal{S}_j, \mathcal{S}_k)$ does not collide.

3. In case of multiple collisions of the two particles we set $\widetilde{\gamma}_j = \min(\gamma_j, [\xi_j/\xi_k])$ and the updated attributes after collision of $(\mathcal{S}_j, \mathcal{S}_k)$ are
   (a) if $\xi_j - \widetilde{\gamma}_j \, \xi_k > 0$:

$$\begin{aligned} \xi_j' &= \xi_j - \widetilde{\gamma}_j \, \xi_k \,, \\ \Psi_k' &= \Psi_k + \widetilde{\gamma}_j \, \Psi_j \quad \text{for } \Psi \in \mathcal{P} = (m_i, m_r, \ldots) \,. \end{aligned} \tag{2.101}$$

   (b) if $\xi_j = \widetilde{\gamma}_j \, \xi_k$:

$$\begin{aligned} &\xi_j' = [\xi_k/2] \,, \qquad \xi_k' = \xi_k - [\xi_k/2] \,, \\ &\Psi_j' = \Psi_k' = \Psi_k + \widetilde{\gamma}_j \, \Psi_j \quad \text{for } \Psi \in \mathcal{P} = (m_i, m_r, \ldots) \,, \end{aligned} \tag{2.102}$$

   conserving the total number of super-particles.

To illustrate the super-particle approach, Figure 2.7 from Shima et al. (2009, Fig. 1) provides a schematic view on the process. The coalescence of two super-particles of multiplicity $\xi_1 = 2$ and $\xi_2 = 3$ (upper row) represents the collection of three smaller by two larger droplets (bottom row). We see that the total number of super-particles is constant while their size and multiplicity changes accordingly.

2.4.2 *Interpolation of the Atmospheric State*

Sheridan et al. (2009) shows that habit development is strongly controlled by (atmospheric) conditions shortly after nucleation, when relative changes in mass and shape are most pronounced. Numerical models of the atmosphere typically assume uniform thermodynamic conditions within a grid cell. Especially in regions where the IGF shows strong gradients, the uniform treatment leads to different habits than if the actual thermodynamic conditions at the position of the particles were assumed. In LES and NWP models, the vertical spacing inside clouds can easily exceed $\Delta z = 50\,\mathrm{m}$ (Dziekan et al., 2019; Shima et al., 2020), which already results in a temperature difference between the lower and upper edge of the cell of $\Delta T \geqslant 0.3\,\mathrm{K}$, assuming a temperature gradient of $\gamma = 0.0062\,\mathrm{Km}^{-1}$. Numerical techniques such as a vertically stretched grid, as used in models like ICON, can lead to vertical grid spacings exceeding $\Delta z > 100, \mathrm{m}$. This resolution amplifies the impact of temperature inconsistencies on habit development, especially in critical regions near cloud tops. As discussed in the previous section, the choice of vertical spacing can have a significant effect on the aggregation process if chosen too fine. To assess the influence of vertical grid resolution on particle shape and mass, sample simulations assuming constant temperature within individual grid cells have been conducted; the results are presented in Figure 2.8. A particle with starting diameter $D_{\mathrm{start}} = 10\,\mu\mathrm{m}$ falls through an idealized atmosphere with linear temperature gradient and constant supersaturation. Aspect ratio and mass have been normalized with the interpolated solution, marked by the hat ($\widehat{\phi}$). At a fine vertical resolution (e.g., $\Delta z = 10, \mathrm{m}$), the numerical impact is minimal. However, coarser resolutions, typical of LES or NWP models, introduce significant numerical effects that can lead to markedly different particle shapes and masses. These differences not only affect individual particle properties but also alter the initial growth pathways, which in turn influence subsequent feedback processes. Additionally, the resulting variations impact aggregation and riming probabilities, as particles with larger cross-sectional areas are more likely to undergo these processes, and vice versa.

A natural choice is therefore to interpolate the atmospheric state to the particle position. In *McSnow*, Equation 2.104 can be used to interpolate atmospheric variables that are assumed to be approximately linear between two height levels (e. g.T), while

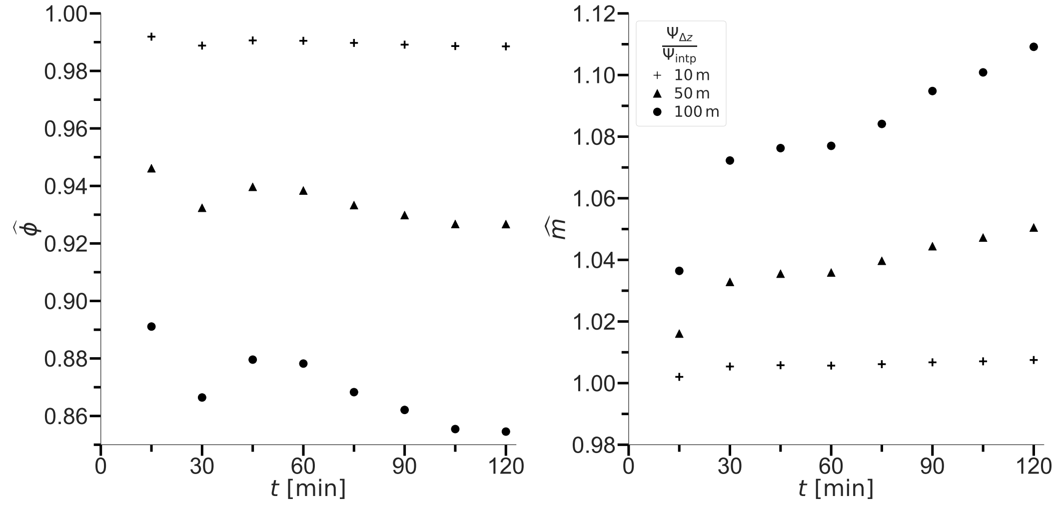

Figure 2.8: Time evolution of the normalized aspect ratio $\widehat{\phi}$ and mass $\widehat{m}$ of a falling particle, as a function of vertical resolution. The particle has a starting diameter of $D_{\mathrm{start}} = 10\,\mu\mathrm{m}$ and falls through a simplified atmosphere (similar to the setup in Section 5.1) with a constant 5% supersaturation over ice.

the Equation 2.105 must be used for exponentially scaling variables such as pressure p

$$\Delta z = \frac{z - z_0}{z_1 - z_0}\,, \tag{2.103}$$

$$\Psi(z) = \Psi(z_0) + (\Psi(z_1) - \Psi(z_0))\,\Delta z\,, \tag{2.104}$$

$$\psi(z) = \psi(z_0)\left(\frac{\psi(z_1)}{\psi(z_0)}\right)^{\Delta z}\,. \tag{2.105}$$

We recommend to interpolate the atmospheric state to the particle position to ensure that habit evolution remains independent of the atmospheric grid resolution. The associated increase in computational cost is justified by the resulting improvements in accuracy and model consistency.

2.5 RADAR REMOTE SENSING

The concurrent existence of hydrometeors of different size, shape and density results in complex in-cloud interactions that are difficult to understand. The integration of various radar techniques can offer insight into different aspects of ice microphysics which can serve as a guideline or an "atmospheric truth" which can be used to constrain model simulations. Polarimetric radars provide variables such as specific differential phase (K_{DP}) and differential reflectivity (Z_{DR}) that are crucial for identifying specific microphysical processes. K_{DP} is highly sensitive to dense concentrations of non-spherical particles, making it effective for detecting SIP signatures in slanted radar measurements. Furthermore, Z_{DR} is independent of total particle concentration, allowing its combined analysis with K_{DP} to help separate the effects of particle shape and concentration. Combining different methods of radar retrievals, IMP fingerprints (Kumjian et al., 2022) can be isolated and the conditions necessary to produce them can be investigated by simulations as a "numerical laboratory". In the first part, this sections introduces a subset of the important radar variables helpful to compare and understand the fingerprints of microphysical processes.
The second part will focus on the forward modeling method necessary to compare modeled microphysics and observations.

2.5.1 *Radar Quantities*

In general, radars observe an integrated signal that includes the entire particle population in its path. The combination of retrieval methods and physical relations can help to entangle the in-cloud state and determine process fingerprints. In this subsection, we introduce some important radar variables that are essential to understand ice microphysical processes from radar observations.

RADAR REFLECTIVITY FACTOR To describe the population, we can use particle size distributions that, depending on the hydrometeor type, are similar to an exponential size distribution. A widely used form to describe the raindrop spectrum is the Marshall-Palmer (MP) distribution (Marshall and Palmer, 1948)

$$n(D) = n_0 \exp\left(-\Lambda D\right)\,, \tag{2.106}$$

where $\Lambda = 4.1\,\mathrm{RR}^{-0.21}\,\mathrm{mm}^{-1} = 1/D_0$, the precipitation rate (RR), and the number of particles at the mean diameter $n_0 = n(D_0)$. To extend the description to all hydrometeors, the so-called generalized γ-distribution can be used (Seifert and Beheng, 2006)

$$n(D) = N_0\, D^{\nu}\, \exp\left(-\Lambda\, D^{\mu}\right) . \tag{2.107}$$

This form reduces to the exponential distribution with $\nu = 0$ and $\mu = 1$, to the classical γ distribution with $\mu = 1$, and to the Weibull distribution with $\nu = \mu - 1$. Given the PSD, the radar reflectivity factor (Z) per unit volume can be written as

$$Z \equiv \int_0^{\infty} n(D)\, D^6\, dD\ , \tag{2.108}$$

and is commonly expressed in logarithmic units of dBZ. The radar reflectivity factor is proportional to the power backscattered from all hydrometeors within the sampled volume and therefore depends on the number per unit volume, size, shape, state (water or ice), and aspect ratio of the hydrometeors. For more details on the radar equation and scattering, the reader is referred to the literature on radar meteorology (e. g. Raghavan, 2003).

To account for the different states of the hydrometeors, we introduce the equivalent radar reflectivity factor (Z_e), which compares the radar reflectivity factor of the water droplets with the radar wavelength (λ) that would produce the same reflectivity if the target properties were unknown.

$$Z_e(\lambda) = \frac{\lambda^4}{\pi^5\, |K_\lambda|^2} \int_0^{\infty} n(D)\, \sigma_b(D, \lambda)\, dD\ . \tag{2.109}$$

The dielectric properties at wavelength λ ($|K_\lambda|$) depends on the hydrometeor mixture and the backscattering cross section (σ_b) is defined as the fraction of the incident radiation that is scattered directly back to the radar. The latter depends on the size of an individual particle and the radar wavelength. For small water droplets, where Rayleigh scattering can be assumed, it is $Ze = Z$. Figure 2.9 illustrates how ice particle growth processes in mixed-phase clouds are represented by the spheroidal geometry model and how they cause an increase in reflectivity.

DOPPLER VELOCITY The use of Doppler radars allows the velocity of hydrometeors to be measured by interpreting the Doppler effect caused by the change in phase shift (Fabry, 2015). The Doppler velocity (ν_D) depends on the hydrometeor characteristics of size, shape and state via the terminal velocity of the investigated particles, modified by the wind field. By applying a Fourier transform to the power spectrum, we can derive the Doppler spectrum, which can be interpreted as the reflectivity weighted radial velocity distribution of the scatterers in that region

$$S_\lambda(\nu_D) = \frac{\lambda^4}{\pi^5\, |K_\lambda|^2}\, n(D)\, \sigma_b(D, \lambda)\, \frac{dD}{d\nu_D}\ . \tag{2.110}$$

If simultaneous measurements allow both air motion and turbulence to be removed, the Doppler spectrum can be used to estimate the PSD (Barrett et al., 2019; Moisseev and Chandrasekar, 2007; Mróz et al., 2020) if the shape characteristics are known. While this may be comparatively simple for raindrops, ice particles may have more

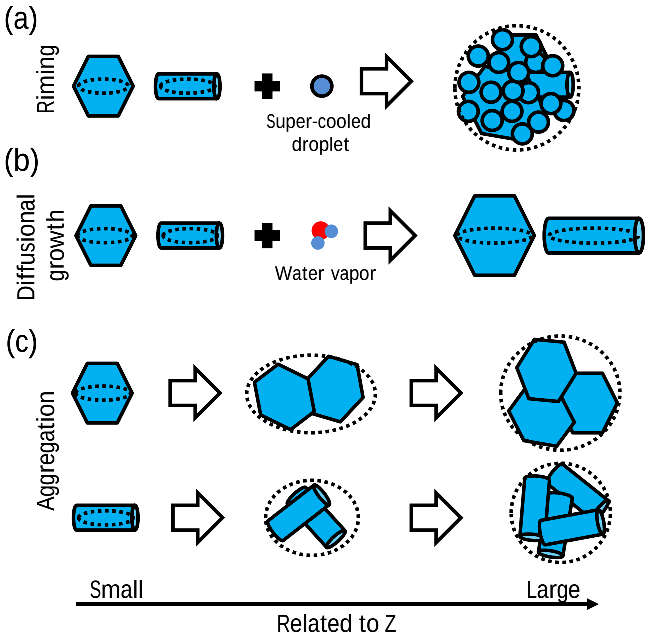

Figure 2.9: Drawing of ice particle growth processes in mixed-phase clouds. Ice crystal riming is shown in panel (a), diffusional growth of ice crystals and aggregation of ice crystals are shown in panel (b) and (c), respectively. The hexagonal plates and cylindrical columns represent either the plate and dendrite form or the needle and column form, respectively. In the drawing, the increase in size is indicated by larger particles. In the measurements, as indicated by the arrow at the bottom, an increase in particle size is associated with an increase in Z values. The shapes of the particles are indicated by the dotted ellipses since particles are modeled as spheroids. This figure was taken from Pfitzenmaier et al., 2018 and redistributed under the creative commons attribution 4.0 License.

complex geometries that are difficult to estimate correctly. The mean Doppler velocity (MDV) is the first moment of the Doppler spectrum, divided by the zeroth moment

$$\mathrm{MDV}(\lambda) = \frac{\int_0^\infty v^1 S_\lambda(v_D) dv_D}{\int_0^\infty S_\lambda(v_D) dv_D}, \tag{2.111}$$

and represents the mean particle motion within the sample volume. We define that negative MDV values correspond to a particle moving towards the ground.
The spectral dissection of quantities into velocity bins allows to analyze the radar quantities for different ranges of the size spectrum and can yield information about ongoing ice microphysical processes. This spectral approach can e. g.be used to identify particles modes indicating the occurrence of certain IMPs (von Terzi et al., 2022). In Chapter 6, we will use the spectral reflectivity (sZ_e) and spectral differential reflectivity (sZ_{DR}) for in-depth process analysis.

DUAL-WAVELENGTH RATIO The multi-frequency approach can help determine the evolution by aggregation or riming by combining observations from two or more radars at different operating frequencies. For growing particles, the backscattering cross section becomes comparable to the wavelength, causing destructive interference effects (Kumjian, 2018). Combining two radars of different wavelength, this effect can be used to gather information about the particle size, depending on the onset of interference. The difference in equivalent radar reflectivity factor for two different wavelength is called dual-wavelength ratio (DWR) and calculated as the ratio in reflectivity

$$\mathrm{DWR}_{\lambda_1,\lambda_2} = \frac{Z_e(\lambda_1)}{Z_e(\lambda_2)}\,, \quad \lambda_1 > \lambda_2\,, \tag{2.112}$$

expressed in dB. The second wavelength should be chosen so that the hydrometeors are outside the Rayleigh scattering regime, so that for frozen hydrometeors Z_e is smaller than for pure Rayleigh scattering (Kneifel et al., 2020). If properly chosen, the size dependence of the transition between scattering regimes can be exploited, as the DWR increases for large particles in the PSD. An illustration of this effect can be found in Figure 1 of Ori et al. (2020).

DIFFERENTIAL REFLECTIVITY Polarimetric radar observations are primarily sensitive to the shape and concentration of hydrometeors. Nonspherical particles scatter radiation differently when targeted by polarized radiation. Here we distinguish between horizontal and vertical polarization, which are indicated by corresponding subscripts (e. g.$Z_{e,h}$ and $Z_{e,v}$). Seliga and Bringi (1976) define the Z_{DR} as

$$Z_{DR} = \frac{Z_{e,h}}{Z_{e,v}}\,. \tag{2.113}$$

We can use Z_{DR} to identify the shape of particles that scatter radiation relative to their mass distribution. While nearly spherical particles produce $Z_{DR} \approx 0$, while Kumjian (2018) report that thin oblate particles such as dendrites can produce $Z_{DR} > 6\,\mathrm{dB}$. The caveat to interpreting Z_{DR} is that even when asymmetric particles are present, single large particles with low density and shapes close to sphericity can drastically reduce the signal. High concentrations of asymmetric particles are required to contribute meaningfully to the integrated Z_{DR}. Therefore, the sZ_{DR} can be used to decompose the signal and attribute the effect of asymmetric particles versus aggregates.

SPECIFIC DIFFERENTIAL PHASE SHIFT An electromagnetic wave acquires a differential phase shift (Φ_{DP}) relative to a wave propagating the same distance in a vacuum when it travels through a dielectric medium such as liquid or ice. This is due to the fact that the phase velocity decreases for a wave propagating through liquid or ice compared to a wave propagating in a vacuum. Wave velocities are not expected to differ between horizontal and vertical polarization. However, interference between the radar transmitted wave and the scattered wave results in a different phase shift because the amplitudes of the scattered waves for asymmetric particles are different for horizontally and vertically polarized waves. Often the range derivative of Φ_{DP} is used, known as the specific differential phase (K_{DP}), which gives the phase shift per unit radial distance

$$K_{DP} = \frac{1}{2}\frac{\mathrm{d}\,\Phi_{DP}}{\mathrm{d}\,r_{\mathbf{dis}}}\,. \tag{2.114}$$

The K_{DP} can be thought of as a measure of the amount and/or size of non-spherical particles in the sample volume.

2.6 FORWARD MODELING

The main obstacle to comparison between microphysical models and observations is the use of different quantities to describe the observed state. The use of *McSnow* provides individual particle information and allows the derivation of characteristic PSDs, but to transfer the information to the observational space a forward operator is needed. As part of the EN OPTIMice group (Emmy-Noether working group "**O**ptimal combination of **P**olarimetric and **T**riple frequency radar techniques for **I**mproving **Mi**crophysical pro**ce**ss understanding of cold clouds", lead Dr. Stefan Kneifel), which is linked to IMPRINT via Dr. Kneifel, José Dias-Neto and Davide Ori developed a Forward Operator on top of the *PyTMatrix* framework of Leinonen (2014) to handle the rich information of *McSnow*. In her PhD thesis, von Terzi (2023) extended the framework to include look-up tables, based on Discrete Dipole Approximation (DDA) (Purcell and Pennypacker, 1973; Yurkin and Hoekstra, 2011) calculations of a large variety of realistically shaped plate-like and columnar ice crystals as well as aggregates. Furthermore, noise convolution and turbulence broadening (Maahn, 2015) have been added. While the spheroidal approximation matches with the originally used T-matrix approach (Waterman, 1965), stable solutions for aspect ratios smaller $\phi < 0.01$ or $D > 5\,\mathrm{mm}$ can not always be found. Due to the soft spherodial approximation performed in the T-matrix, the polarimetric signal is expected to be underestimated, especially for highly asymmetric branched particles (i.e. dendrites) as well as low density particles such as aggregates (Kneifel et al., 2020). To take full advantage of the information provided by a habit prediction scheme, the polarimetric radar signal must be represented as realistically as possible, hence the need for DDA.

3

DISCUSSION OF BÖHM'S THEORY FOR HABIT PREDICTION

3.1 SHAPE ASSUMPTIONS FOR COLUMNS

Böhm's theory is valid for porous spheroids, however, he recommends to use cylinders for $\phi > 1$ to approximate hexagonal columns (see Sec. 2.3.1). For particles that change habit, the hydrodynamic assumption in Böhm's theory changes from a symmetric flow around an oblate to an asymmetric flow around a cylinder which can lead to an abrupt change in terminal velocity (cf. solid versus dashed lines in Fig. 3.3). This change in morphology between primary habits may not be fully transferable to natural ice geometries, where complex crystalline features such as capped columns may evolve instead of complete habit changes. It is unclear if and how the spheroidal approach could capture these effects.

In an effort to reconcile Böhm's theory for cylindrical particles with the data for cylinders according to Jayaweera and Cottis (1969), in Figure 3.1 we compare the C_d-N_{Re} relation for cylinders and prolates according to Böhm (1992a) with the mentioned data as well as more recent results for prolates of Sanjeevi et al. (2022, only valid for $1 \leqslant \phi \leqslant 8$). The latter uses equivalent diameter and the corresponding cross-section and has to be transformed to the cross-sectional area $\tilde{A}$ by multiplying C_d with $\phi^{-1/3}$.

To match the solution for cylinders with the data of Jayaweera and Cottis (1969) (as shown in Fig. 3 of Böhm, 1992a), we found that for the Best number X the case distinction of q for columns has to be removed as written in Eq. (2.81a) (the original formulation can be found at Eqs. (17) & (18) in Böhm, 1992a or Eq. (7) in Böhm, 1999). This treatment additionally allows the consideration of porosity for columnar particles which becomes especially relevant when riming happens.

The **T**rajectory **R**econstruction **A**lgorithm implemented through Image ana**L**ysis (TRAIL) is a recent laboratory measurement conducted by McCorquodale and Westbrook (2021b), which provides data for over 80 realistic particle geometries at different aspect ratios. McCorquodale and Westbrook (2021a) evaluate the performance of Böhm's original work (Böhm, 1989, B89) and criticize a general overestimation of the drag coefficient. We expect the modifications from Böhm (1992a) to Böhm (1999) including the dependency on the shape of the spheroid to significantly improve the agreement with the lab data.

The C_d-N_{Re} relation of the latest formulation from Böhm (including above modification) is compared with the TRAIL results (colored markers) and the data points for a columnar particle near sphericity (*CO1*, $\phi = 1.2$, black markes) from Westbrook and Sephton (2017) in Figure 3.2. The dashed and dash-dotted lines show the C_d-N_{Re} relation following Böhm for three different aspect ratios (color-coded) representing spherical ($\phi = 1$, black), plate-like ($\phi = 0.1$, red), and columnar/prolate particles ($\phi = 5$, green). We re-scale the drag coefficient by the area ratio $A_r^{1/2}$ to compensate for the effect of A_r and allow comparison between the data and the derived C_d-N_{Re}-relation of Heymsfield and Westbrook (2010). The area ratio A_r needs special

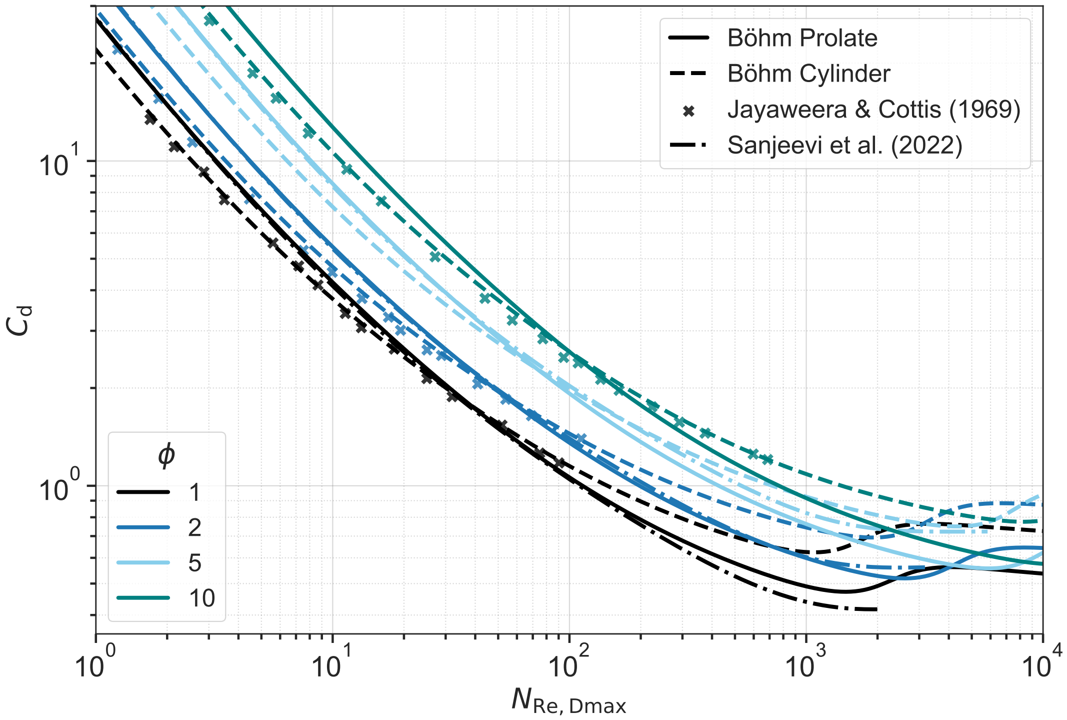

Figure 3.1: Comparison of $N_{\mathrm{Re,Dmax}}$ and C_d of the parameterization of Böhm for a non-porous prolate spheroid (solid) and a cylinder (dashed) geometry with cylinder data of Jayaweera and Cottis (1969, cross markers) and prolate data of Sanjeevi et al. (2022, dash-dotted) for different ϕ (color-coded). Note that all N_{Re} are transformed to use D_{max} and all C_d use $\tilde{A}$.

attention when the scheme of Böhm is used for columnar particles, because the definition varies from that of q (Eq. (2.80)). McCorquodale and Westbrook (2021a) define the area ratio A_r as

$$\begin{aligned} A_r &= \tilde{A}\, A_{cc}^{-1}\,, \\ A_r &= q\,\phi^{-1}\,, \qquad \text{for } \phi > 1. \end{aligned} \tag{3.1}$$

The curves following Böhm in Figure 3.2 depict solid/non-porous particles with $q = 1$ (plate-like, sphere and prolate) and $q = 4\,\pi^{-1}$ for cylinders, respectively.
The laboratory data and the parameterization agree well and the explicit dependence on the aspect ratio of the hydrometeors can capture the geometric effect of the different particle types. The drag coefficient of columnar particles differs between the cylindrical and the prolate. At low $N_{\mathrm{Re,Dmax}}$, the curves overlap and seem to be able to reproduce the drag coefficient. However, as $N_{\mathrm{Re,Dmax}}$ increases, the formulations diverge, with laboratory data lying between the two lines. Using the original data from McCorquodale and Westbrook (2021a) and the points for $\phi = 1.2$ (Westbrook and Sephton, 2017), we fit a N_{Re}-C_d relation only for hexagonal columns (HCs) that accounts for the ice particle geometry (as proposed by Böhm, 1989 and Heymsfield and Westbrook, 2010), assuming that they do not tilt and fall with maximum drag at an area ratio $A_r = \frac{4}{\pi\,\phi}$

$$C_d = A_r^n C_0 (1 + d_0 N_{\mathrm{Re,Dmax}}^{-1/2})^2\,. \tag{3.2}$$

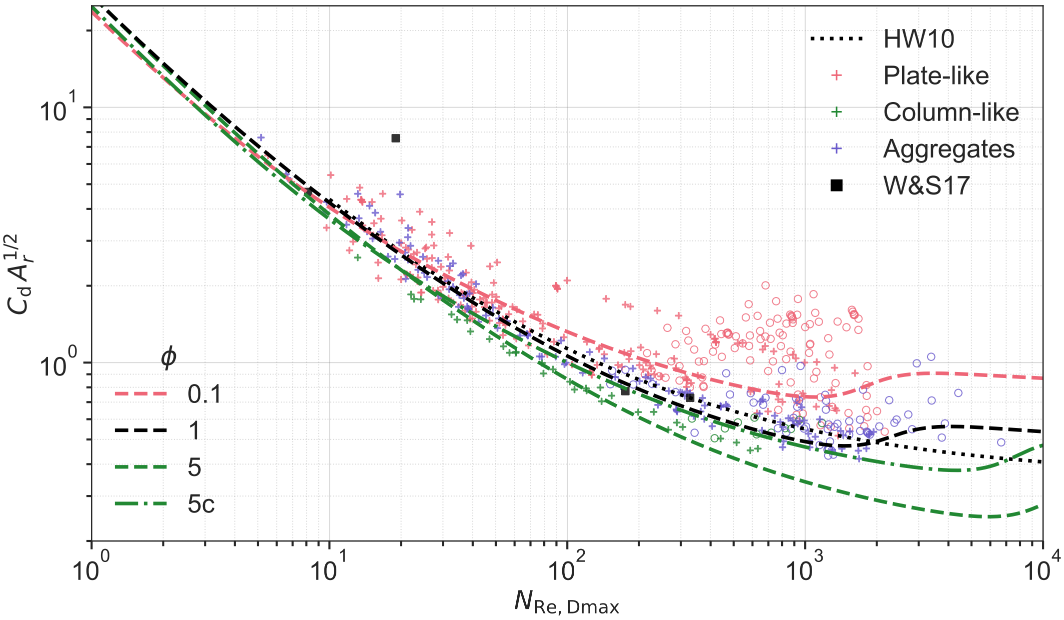

Figure 3.2: Comparison of measurements of $N_{Re,Dmax}$ and compensated drag coefficient $C_d A_r^{1/2}$ for ice particle analogues (McCorquodale and Westbrook, 2021a, colored '+'/'∘' for steady/unsteady regimes) against the parameterization of Böhm. Black squares mark the data from Westbrook and Sephton (2017, W&S17) for a cylinder with $\phi = 1.2$. The black dotted line marks the results from Heymsfield and Westbrook (2010), while the dashed colored lines show the results using the parameterization from Böhm for solid spheroids at the corresponding ϕ. The green dash-dotted line (5c) represents a cylindrical particle with $\phi = 5$. Data points for rosettes are omitted for visual clarity.

The empirical values found are $n = -0.4$, $C_0 = 0.4$, and $d_0 = 7.1$, which naturally improves the agreement for hexagonal columns (HCs) over the generalized models of Heymsfield and Westbrook (2010) and McCorquodale and Westbrook (2021a). As the Best number X only depends on ambient conditions and particle characteristics, we choose the atmospheric state ($T = 258\,\mathrm{K}$ and $\rho_a = 1\,\mathrm{kg\,m^{-3}}$) to resemble the typical conditions.

Based on the solid hexagonal columns from McCorquodale and Westbrook (2021a) with an aspect ratio of $\phi = 5$ and the atmospheric state, we dimensionalized the particles and determined the masses to be $m = [3.95 \times 10^{-9}, 1.49 \times 10^{-8}, 5.25 \times 10^{-8}, 1.81 \times 10^{-7}]\,\mathrm{kg}$. Combined with the use of the empirical values obtained for Eq. (3.2), we can extrapolate the behavior to other aspect ratios and find corresponding terminal velocities.

Figure 3.3 shows the fall speed as a function of aspect ratio $v_t(\phi)$ for four particles of increasing mass. The dark blue line is representative for $N_{Re,Dmax} < 100$ and the light blue, teal, and grey line for particles with $100 < N_{Re,Dmax} < 1000$. Comparing the results from Böhm's scheme for the prolate (solid) and the cylindrical assumption (dashed), shows the aforementioned deceleration at $\phi = 1$. The fall velocity behavior derived from the data of McCorquodale and Westbrook (2021a) suggests a more subtle transition from a prolate to a cylindrical geometry, especially when particles become heavier. The cylindrical geometry prescribes an edge at the basal surface, but physically the representation of this edge in the hydrodynamic properties is at

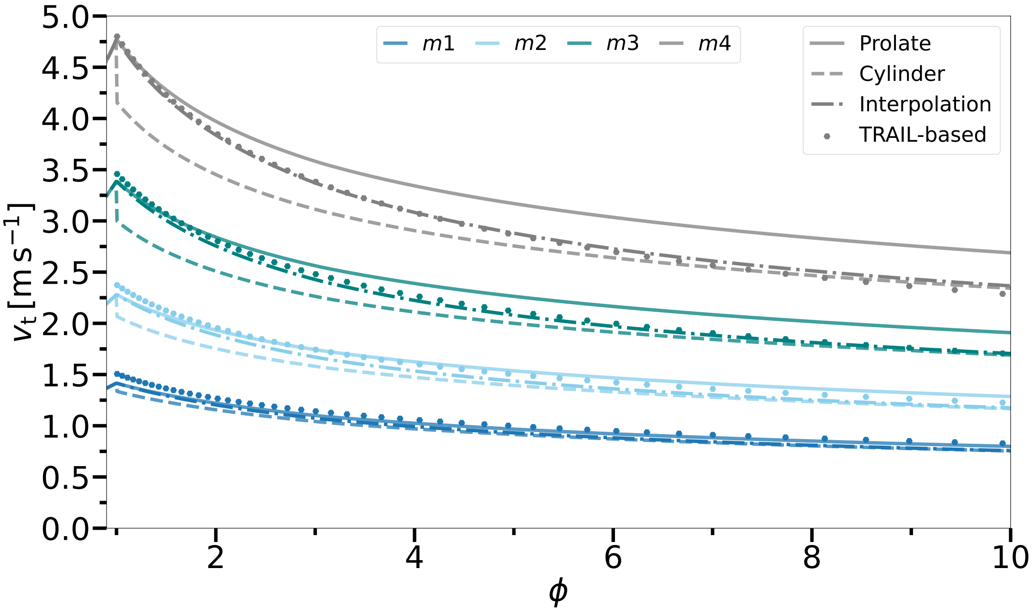

Figure 3.3: Terminal fall speed v_t dependency on the aspect ratio ϕ for particles with different mass (color-coded), treated as a prolate (solid) or a cylindrical spheroid (dashed), for TRAIL-based data (points), and for an interpolated approach (dash-dotted line, Eq. (3.3)).

least questionable in the spheroidal framework of habits. We therefore advocate an interpolation between the two fall velocities v_{pro} and v_{cyl} using the form

$$v(\phi) = f(\phi)\, v_{\text{pro}} + (1 - f(\phi))\, v_{\text{cyl}}, \tag{3.3}$$

$$f(\phi) = e^{-0.3\,(\phi - 1)} \tag{3.4}$$

This simple function helps to account for the relatively steep decrease in v_t with increasing ϕ, while matching the asymptotic behavior for the cylindrical approach. Figure 3.3 already includes the interpolated fall speed as dash-dotted lines that match the TRAIL results fairly well. The interpolation overcomes the need to choose between cylinder and prolate geometry, providing a smooth transition from prolate to cylinder-like behavior of ice columns.

3.2 RESPONSE TO ATMOSPHERIC CONDITIONS

The terminal fall velocity and the collision efficiency of Böhm are derived from using the Reynolds and Best numbers. This introduces a dependency on atmospheric conditions since both numbers depend on the air density ρ_a and the temperature via the dynamic viscosity $\mu(T)$ (Eqs. (2.81a) & (2.34)). Therefore, v_t and E_c must also change with height if a realistic atmospheric profile is assumed.
Pinsky et al. (2001) find an increase in collision efficiency of more than a factor of two for a collision of small droplets ($D_1 \approx 30 - 50\,\mu\text{m}$ and $D_2 \approx 10 - 20\,\mu\text{m}$) between the 1000 and 500 hPa levels. The effect of the atmospheric conditions decreases with increasing droplet size. They argue that 90 % of the enhancement is due to the sensitivity of E_c to the relative velocity difference and only 10 % to an increase in

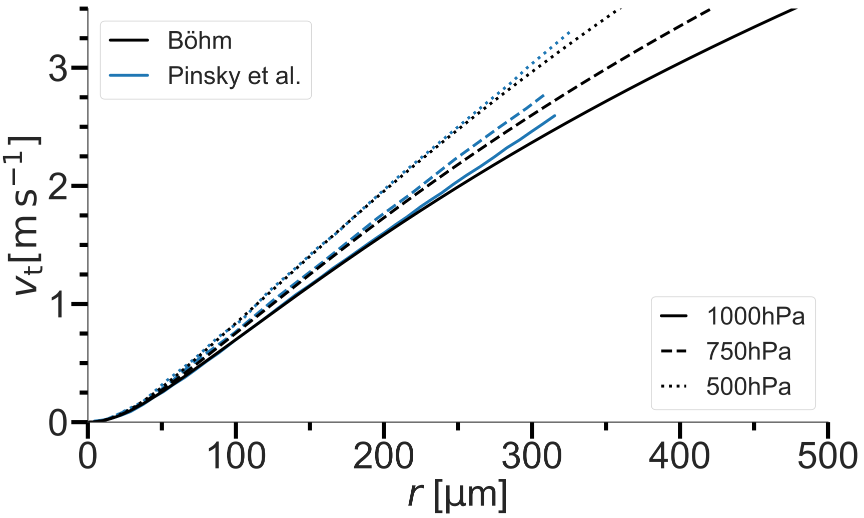

Figure 3.4: Dependency of v_t on the drop radius for the pressure levels 1000 hPa (solid), 750 hPa (long dashed), 500 hPa (short dashed) for Böhm's scheme (black) and from Pinsky et al. (2001) (blue lines).

swept volume. Böhm (1992b) finds an increase in E_c with temperature and pressure on the order of only 10 % for small drops ($r_1 \lesssim 30\,\mu m$) and almost no effect for larger ones. Although we expect the work of Böhm to be generalizable, the contradiction of the two results requires an analysis of the dependence of Böhm's fall velocity and collision efficiency parameterizations on different atmospheric states for droplets and ice particles. Compared to Pinsky et al. (2001), we change the surface temperature to freezing point to have a physically justified setup for ice particles at $p = 1000\,hPa$. While this change could affect the results, we argue that the exponential decrease in pressure with height dominates the effect over the linear dependence of temperature. Fig. 3.4 shows the comparison of terminal velocity by droplet size between the results of Pinsky et al. (2001) and with the scheme of Böhm. Böhm's scheme predicts comparable results for all pressure levels. Both results show that the terminal velocity for a drop with $r = 300\,\mu m$ is about 25 % greater at 500 hPa than at 1000 hPa. Using the adjustment factor of Beard (1980) allows us to compare the pressure dependence as a function of atmospheric conditions

$$f_{\nu_t} = \frac{\nu_t(T, p)}{\nu_{t,o}(T_0, p_0)}\,, \tag{3.5}$$

with the reference value of $\nu_{t,o}$ at $p_0 = 1000\,hPa$ and $T_0 = 273.15\,K$.

We look at four different particle types (drop, oblate w. $\phi = 0.25$, prolate w. $\phi = 4$, and graupel w. $\phi = 1$ and $\rho_r = 800\,kg\,m^{-3}$) and five different masses equal to the mass of a sphere with an volume equivalent diameter of $D_{eq,v} = [20, 50, 100, 200, 500]\,\mu m$. In Figure 3.5 we see that the adjustment factor is proportional to $D_{eq,v}$ and can reach a maximum of about 1.3 at 500 hPa for $D_{eq,v} = 500\,\mu m$. The difference between particle types is small, but becomes more relevant for larger particles.

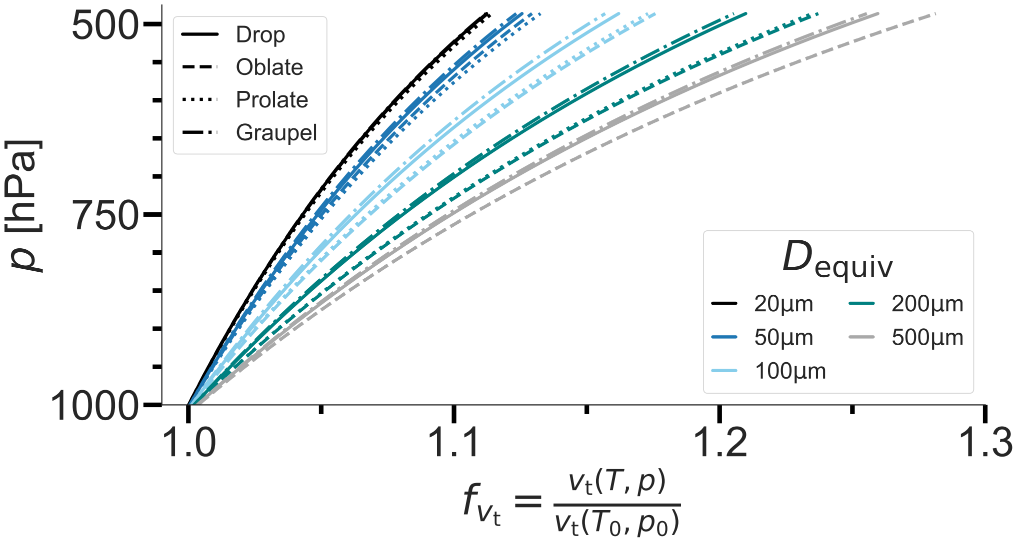

Figure 3.5: p-profiles of f_{v_t} for drops (solid), oblates (dashed), prolates (dotted), and graupel particles (dash-dotted lines). Color-coded is the equivalent diameter.

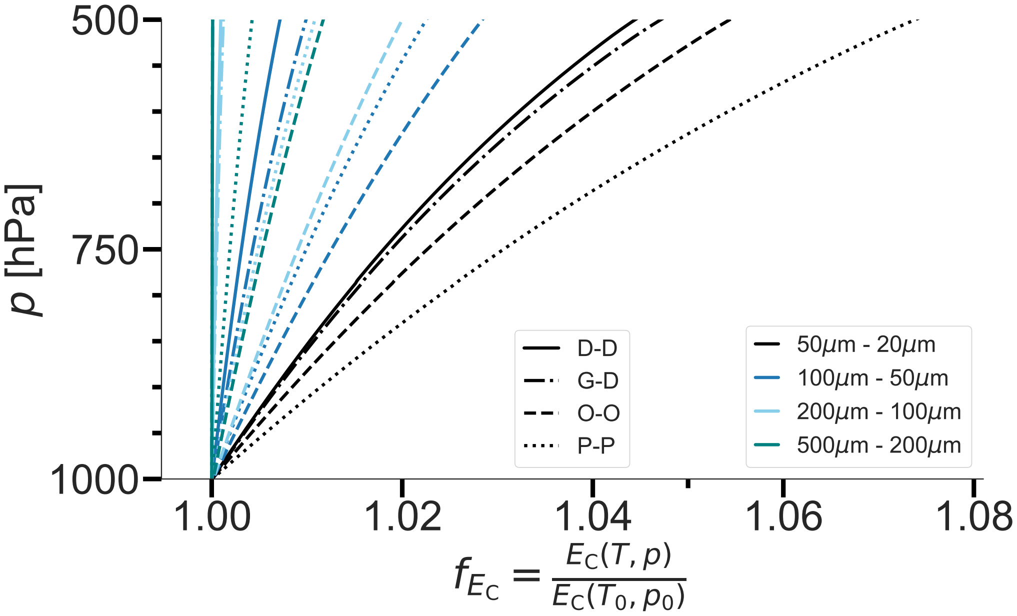

Figure 3.6: p-profiles of f_{E_c} for a drop-drop (D-D, solid), graupel-droplet (G-D, dash-dotted lines), an oblate-oblate (O-O, dashed), and a prolate-prolate collision (P-P, dotted).

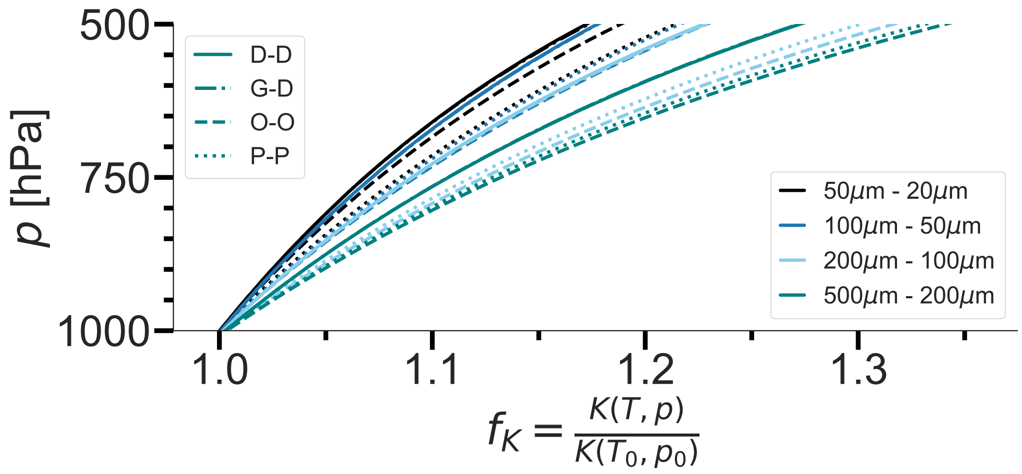

Figure 3.7: p-profiles of f_K for a drop-drop (D-D, solid), graupel-droplet (G-D, dash-dotted lines), an oblate-oblate (O-O, dashed), and a prolate-prolate collision (P-P, dotted).

In Figure 3.6 we analyze the effect of the changing thermodynamic state on the collision efficiency for four different collision pairs: drop-drop (D-D, solid lines), graupel-drop (G-D, dash-dotted lines), oblate-oblate (O-O, dashed lines), and prolate-prolate (P-P, dotted lines) collisions. The equivalent diameters of the particles involved are color-coded and include the size range used for the terminal velocity. The impact is inversely proportional to the mass/size and much smaller than that for v_t, not exceeding $f_{E_c} < 1.12$. We can therefore specify the statement of Pinsky et al. (2001): for small particles, the change in collision efficiency itself dominates the collision behavior. The impact is higher for large particles ($\leqslant 30\,\%$), where the change in terminal velocity dominates the atmospheric dependence of the collision kernel. Looking at pairs with similar fall velocities, where the collision efficiency rapidly approaches zero, we observe adjustment factors greater than two, as observed by Pinsky et al. (2001) (not shown).
The combined effect of atmospheric conditions on terminal velocity and collision efficiency is shown in Figure 3.7 via the adjustment factor of the collision kernel f_K. For small particle collisions, the onset of effective collisions results in a significant difference in the collision efficiency, which dominates the rather small change in the terminal velocity. Conversely, for larger particle collisions, atmospheric conditions have a larger impact on the individual terminal fall speed when compared to collision efficiency. The latter, however, directly affects the collision kernel as well as the collision efficiency.

3.3 HABIT IMPACT ON RIMING EFFICIENCY

While Böhm compares and calibrates his theory for the collision efficiency with results of Schlamp et al. (1975), Martin et al. (1981) and Reinking (1979), more recent results of Wang and Ji (e. g. 2000) are available. These are improved with respect to the shape of the particles investigated and the accuracy of the flow field. Therefore, their results are suitable to evaluate the validity of Böhm (1992a)'s theory for collision events of porous spheroids with spherical droplets up to radii of $r = 100\,\mu m$. In

Figure 3.8, the analytical collision efficiencies of Böhm are plotted against the simulation of Wang and Ji (2000) for given geometries of plates, cylinders, and broadly branched crystals. The cylindrical shape is the most difficult to compare due to the mismatch between the actual and spheroidal shape, combined with the asymmetry of the flow.

The results for the oblates are in good agreement with respect to the onset, maxima and cut-offs of all eight particles (Fig. 3.8 a). The direct comparison for the cylinder (Fig. 3.8 b) shows a slightly delayed onset and higher maxima for curves following the theory of Böhm. The cut-offs are shifted to higher collected droplet radii compared to Wang and Ji (2000). Note that terminal velocity interpolation is applied. For branched crystals (Fig. 3.8 c) the onset and maximum are quite close. Only the cut-off radii differ, especially for larger crystals. The overall accuracy for small radii is quite limited anyway, as Homann et al. (2016) note that the collision probability can be significantly altered by turbulent air motion.

While there are some differences in general, the formulation provides a reasonable parameterization of the qualitative behavior given the theoretical assumptions. The assumed porous spheroidal model cannot represent the complex geometries found in Wang and Ji (2000) as effectively as more specialized fits like those presented in Erfani and Mitchell (2017). However, this parameterization enables the formulation of a collision efficiency that is independent of whether the particle is solid or liquid. We conclude that the theory of Böhm provides a suitable framework for parameterizing the collision efficiency of primary habits even when compared to (more recent) numerical simulations.

3.4 HABIT IMPACT ON AGGREGATION EFFICIENCY

A comparison of habit effects on riming efficiency indicates that the framework is also suitable for the aggregation process. There is a limited body of experimental research examining the collision efficiency of ice particles colliding with fixed targets (e. g. Hallgren and Hosler, 1960; Hosler and Hallgren, 1960; Keith and Saunders, 1989). It is common for these experiments to be conducted with the objective of studying graupel-collecting ice crystals, rather than the aggregation process that forms snow. In their study, Wang (2013) present experimental results that demonstrate the average collision efficiency as a function of temperature $E_c(T)$. Nevertheless, the author is unaware of any theoretical study that examines the aggregation efficiency. For this reason, we have elected to analyze the dependence of the collision efficiency on the aspect ratio using the framework of Böhm for the collision of two ice crystals of diameter $D = 100\ \mu m$ at ice density. Figure 3.9 depicts the collision efficiency E_c as a function of the aspect ratio of the two particles. In this context, a comparison is made between the original scheme, as previously outlined (a), and the results obtained through the use of interpolation for prolate particles (b). It should be noted that the plots do not take into account the variance applied to the terminal fall speed; they merely illustrate the original collision efficiency. All four plots exhibit a discernible pattern of quadrants that can be classified as oblate-oblate (O-O, lower left), prolate-prolate (P-P, upper right), and prolate-oblate and vice versa (P-O, upper left and lower right).

The distinct lines between the quadrants can be explained by the sudden change in

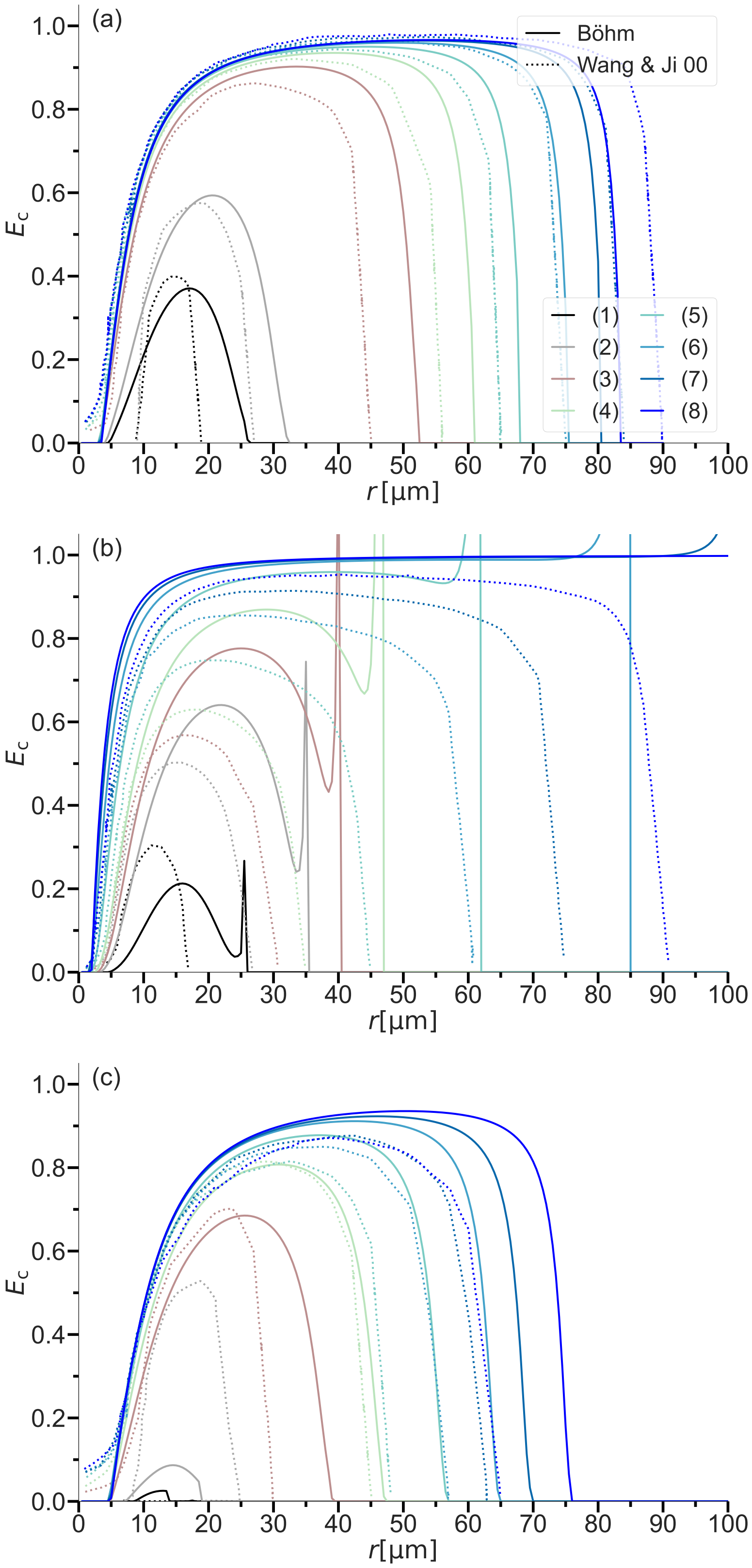

Figure 3.8: Collision efficiencies of (a) thin oblates, (b) cylinders, and (c) broadly branched crystals with spheres. Particle dimensions (color-coded) and reference numerical simulations of Wang and Ji (2000). Note that the eight lines describe different particle geometries depending on the case.

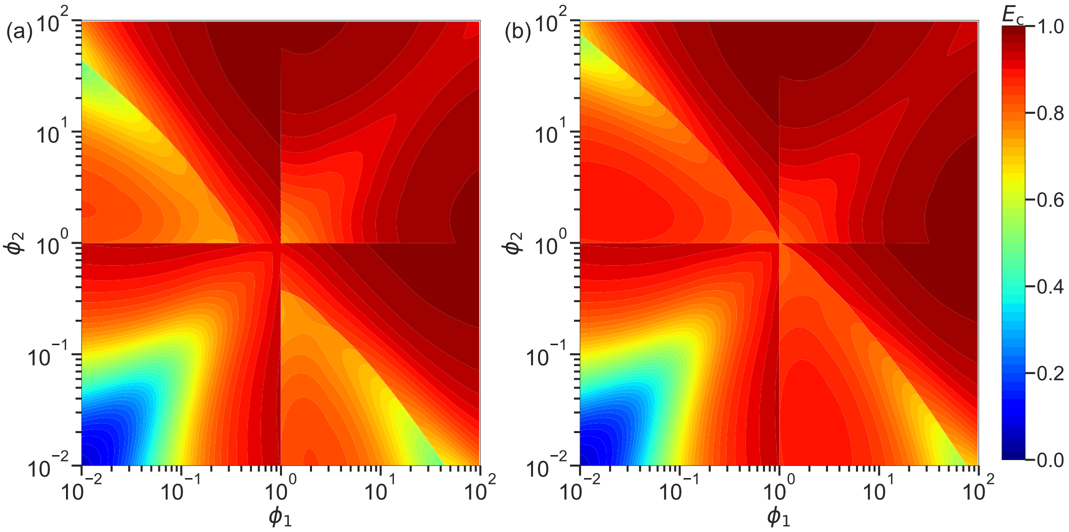

Figure 3.9: Collision efficiency as a function of aspect ratios of the two ice crystals with a diameter of $D = 100\,\mu m$. Plots show the collision efficiency (a) without and (b) with interpolation of the fall velocity between cylinder and prolate.

the particle characteristics, namely the abrupt change in the flow symmetry and the sudden deceleration due to the cylindrical assumption (see Sec. 3.1). The collision efficiency (top row) of O-O collisions is symmetric about the diagonal and is lowest when both particles have strongly developed ARs, where the fall velocity saturates and the difference approaches zero. The saturation effect is observed to become less pronounced as the particles approach sphericity.
The P-P collision demonstrates a similar symmetry around the diagonal; however, the asymmetry in the flow field around the prolate bodies markedly enhances the collision efficiency. In the case of collisions between particles of different shapes (P-O, O-P), the resulting pattern is the most complex, exhibiting a degree of blending between the semi-empirical assumptions made by Böhm. The line-like feature indicates the combination of aspect ratios at which the terminal velocity of prolate and oblate particles is identical. It is evident that this feature does not extend in a linear fashion towards the center. Rather, the distinct shape assumptions are canceled out at the point where $\phi = 1$. The offset can be addressed through the application of interpolation for prolate particles, thereby enhancing the shape transition to achieve a more spherical configuration. It is generally only possible to achieve high values of collision efficiency for particles of the same mass when the particles have opposite habits or when prolates have very different ARs. It is important to note that the highest collision efficiencies with prolates involved can only occur when $\phi > 20$, which is rarely observed in nature.

In this chapter, we put forth an interpolation between prolate and cylindrical shape assumptions that enhances the terminal velocity projected by Böhm's theory when benchmarked against laboratory data. We were able to clarify the influence of atmospheric conditions on terminal velocity, collision efficiency, and the collision kernel. The ice habit has a significant impact on both riming and aggregation efficiencies, influencing their onset and eventual decline to zero. A favorable alignment between the hydrodynamic theory proposed by Böhm and the recent theoretical investigations conducted by Wang and Ji (2000) can be attained. However, due to the absence of a comprehensive theory governing aggregation, our investigation is constrained to examining the sensitivity of collision efficiency to aspect ratio.

4

REVISION OF THEORY

The theoretical descriptions given in Chapter 2, while being extensive, still include several assumptions that can alter the sensitivity of one or more ice microphysical studies. We found that recent studies regarding ventilation of non-spherical particles give reason to revise the formulations and find a generalized solution suitable for explicit habit prediction schemes. The second important area of revision will be the cornerstone of the habit prediction itself, the inherent growth function (IGF). We do not only want to show that the original formulation does provide a generally good description but use observational results to propose some updates that can improve the capability to reflect the habit development as a function of temperature.

4.1 SHAPE-DEPENDENT VENTILATION

Several studies present formulations for habit-specific ventilation coefficients based on the underlying geometry, which may differ substantially from Hall and Pruppacher (1976, HP76) (Prolate: Wang and Ji (2000, W&J00), Ke et al. (2018, Ke18), Kiwitt et al. (2022, K22), Chen et al. (2021), Oblates: Pitter et al. (1974, P74), Ji and Wang (1999, J99), Wang (2021, W21), Nettesheim and Wang (2018, NW17) , spheres: Woo and Hamielec (1971, WH71), Whitaker, 1972).

The left side of Figure 4.1 shows a collection of these datasets as well as three proposed fits of the dependence of ventilation on X_v for spheres (Hall and Pruppacher, 1976, solid), dendrites (Nettesheim and Wang, 2018, NW17, long dashed), and columns (Ji and Wang, 1999, JW99, short dashed). The formulation of Hall and Pruppacher (1976) shows reasonable behavior for (nearly) spherical particles, but especially for prolate particles, large underestimations of the ventilation coefficient are given (up to 3 for a given X_v).

Using the collected dataset, we modify the formulation of Hall and Pruppacher

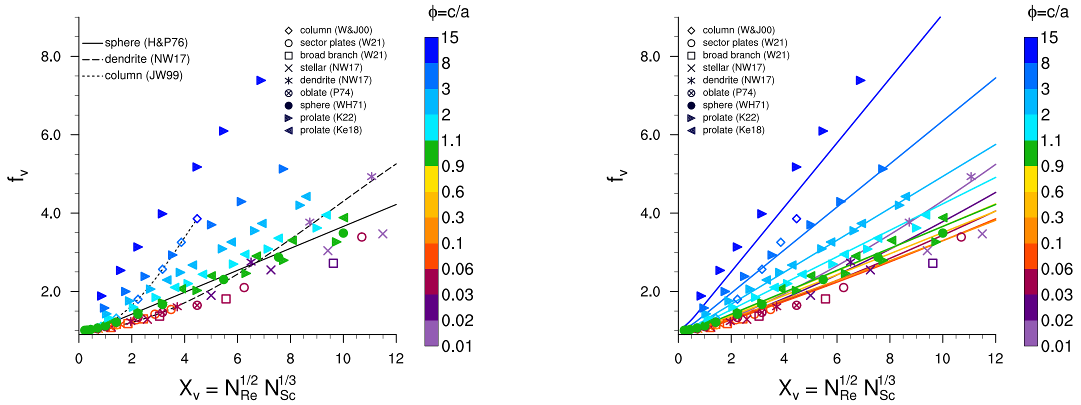

Figure 4.1: Left: Data points and functional dependencies of $f_v(X_v)$ for several studies. Right: Proposed functional habit-dependent description $f_v(\phi)$. The aspect ratio of the assumed particles is color-coded.

(1976, cf. Eq. (2.30)) by adding a ϕ-dependent term to the ventilation coefficient

$$\begin{aligned} f_{v,\mathrm{prolate}} &= f_v + c_1\, X_{v,\mathrm{eq}} \quad \phi, && \text{for } \phi > 1, \quad c_1 = 2.8 \times 10^{-2}\,, \\ f_{v,\mathrm{oblate}} &= f_v + c_2\, X_{v,\mathrm{eq}}^{3/2} \quad \phi^{-1}, && \text{for } \phi < 1, \quad c_2 = 2.8 \times 10^{-3}\,. \end{aligned} \tag{4.1}$$

Good agreement with the data can be found for all geometries (right side of Figure 4.1). The shape-dependent ventilation introduced here is utilized in Eq. 2.18. It is important to note that we added this shape-dependence only for the (overall) ventilation coefficient (Eq. (2.30)) but do not modify the effect of ventilation on the inherent growth function (Eq. (2.36)). The latter only uses the generalized form of Hall and Pruppacher (1976, Eq. (2.30)) and considers the habit effect by comparing the local axis dimension with the radius of a sphere with the same total volume (at ice density).

4.2 INHERENT GROWTH FUNCTION

The IGF, as introduced by CL94, paired with a parameterization of the deposition density can describe primary and secondary habit development in the spheroidal framework (e. g. Jensen and Harrington, 2015; Shima et al., 2020; Sulia and Harrington, 2011). While providing a fundamental physical description of the growth ratio of the a- to c-axis, the original fit of observational and laboratory results has some inconsistencies when compared with more recent laboratory (Connolly et al., 2012) or modeling studies (Hashino and Tripoli, 2007; Sheridan et al., 2009) for certain temperature regimes.

In this section, we will evaluate the results using the original IGF, point out its deficiencies, and propose another version of the IGF based on observational evidence that corrects some of the shortcomings. Table 4.1 gives an overview about the model configurations that are used to exhibit the microphysical sensitivities both in this section and in the Sec. 5.

Table 4.1: Description of the model configuration identifiers used throughout Sec. 4 & 5.

Identifier	**Monomer Geom.**	**ϕ-dep. vent.**	**v_t interpolation**	**IGF**
diag.	diagnostic	-	-	-
HP	spheroid	no	no	CL94
HP + vent	spheroid	yes	no	CL94
IGF1	spheroid	yes	yes	CL94
IGF2	spheroid	yes	yes	upd. + no size constraint
IGF2+	spheroid	yes	yes	upd. + no size constraint mod. branching

4.2.1 *Original Version of Chen & Lamb*

Takahashi et al. (1991, TH91) provide a set of laboratory measurements that quantify the depositional growth of ice crystals at constant temperature ($T \in [250\,\mathrm{K}, 270\,\mathrm{K}]$) and water saturation. Because of the high quality measurements of the mass, density, and geometry of individual ice crystals, Chen and Lamb (1994b) use the TH91 experiments as a benchmark to validate their habit prediction scheme. Figure 4.2 reproduces Figures 7 to 9 of Chen and Lamb (1994b) using results from the habit prediction (HP) scheme without (black) and with the new habit-dependent ventilation coefficient (green lines). It also includes the result with a diagnostic geometry for monomers using the empirical m-D relation of Mitchell (1996) for aggregates of side planes, columns, and bullets (S3, long dashed lines) and a strictly spherical geometry (short dashed lines). In the lab experiment, the particles freeze from a droplet distribution and the size/weight shows slight variations. In the simulations, an initial radius similar to the maximum of the droplet distribution of $r_{\mathrm{start}} = 2\,\mu\mathrm{m}$ (Takahashi and Fukuta, 1988) shows overall good agreement with the laboratory data and compares significantly better than the m-D-relation of Mitchell. The difference in the initial radius is considered small compared to the uncertainties of the measurements and the model assumptions.

For the limiting case of spherical development at $\Gamma = 1$ for temperatures $T \approx 253$ or $263\,\mathrm{K}$, the habit prediction is in agreement with the results for spherical particles, and the laboratory results show slightly lighter crystals. In the columnar regime, $T \in [248\,\mathrm{K}, 252\,\mathrm{K}]$ (cold) and $T \in [263\,\mathrm{K}, 268\,\mathrm{K}]$ (warm), the prolates are heavier than the crystals grown by TH91. For the oblate maximum around $T = 258\,\mathrm{K}$ they are lighter than laboratory data suggest. Since $X_{v,eq}$ does not exceed 1.5 for all particles studied, we see only a slight enhancement of the deposited mass for all non-spherical growth regimes when the habit-dependent ventilation coefficient is included. As expected, prolates are more influenced than oblates, but not enough to change the geometry or density significantly (Fig. 4.2 b & c). From here on, all results will include the habit-dependent ventilation coefficient.

The differences between our model and the laboratory data for particle mass are due to the predicted geometry, too high/low apparent density, or a combination of both. Therefore, Figure 4.2 (b) and (c) show that within the warm columnar regime, prolates tend to grow to larger aspect ratios than suggested by the laboratory data. Nevertheless, the eventual hollowing captured by the deposition density parameterization is representative. The axis length of oblate growing particles follows the results for the a axis, while showing an inability to represent strongly branched, thin dendritic crystals. This feature is due to the spheroidal assumption and the initial spherical growth up to $D \geqslant 10\,\mu\mathrm{m}$, leading to an overestimation of the c axis size.

If all particles were allowed to grow habit-specifically immediately after nucleation it would reduce the differences observed for the oblate geometry, but leads to unnatural aspect ratios in the columnar regime. The coupling of IGF and deposition density leads to branching for the entire oblate regime and does not reproduce the sharp density minimum for branching particles observed by TH91.

Particles within the cold columnar regime ($T < 253\,\mathrm{K}$) evolve prolate features with a secondary maximum, while TH91 observe nearly spherical or only slightly prolate particles. The habit description becomes ambiguous for the temperature range due to the increased occurrence of polycrystals (based on field observations Um

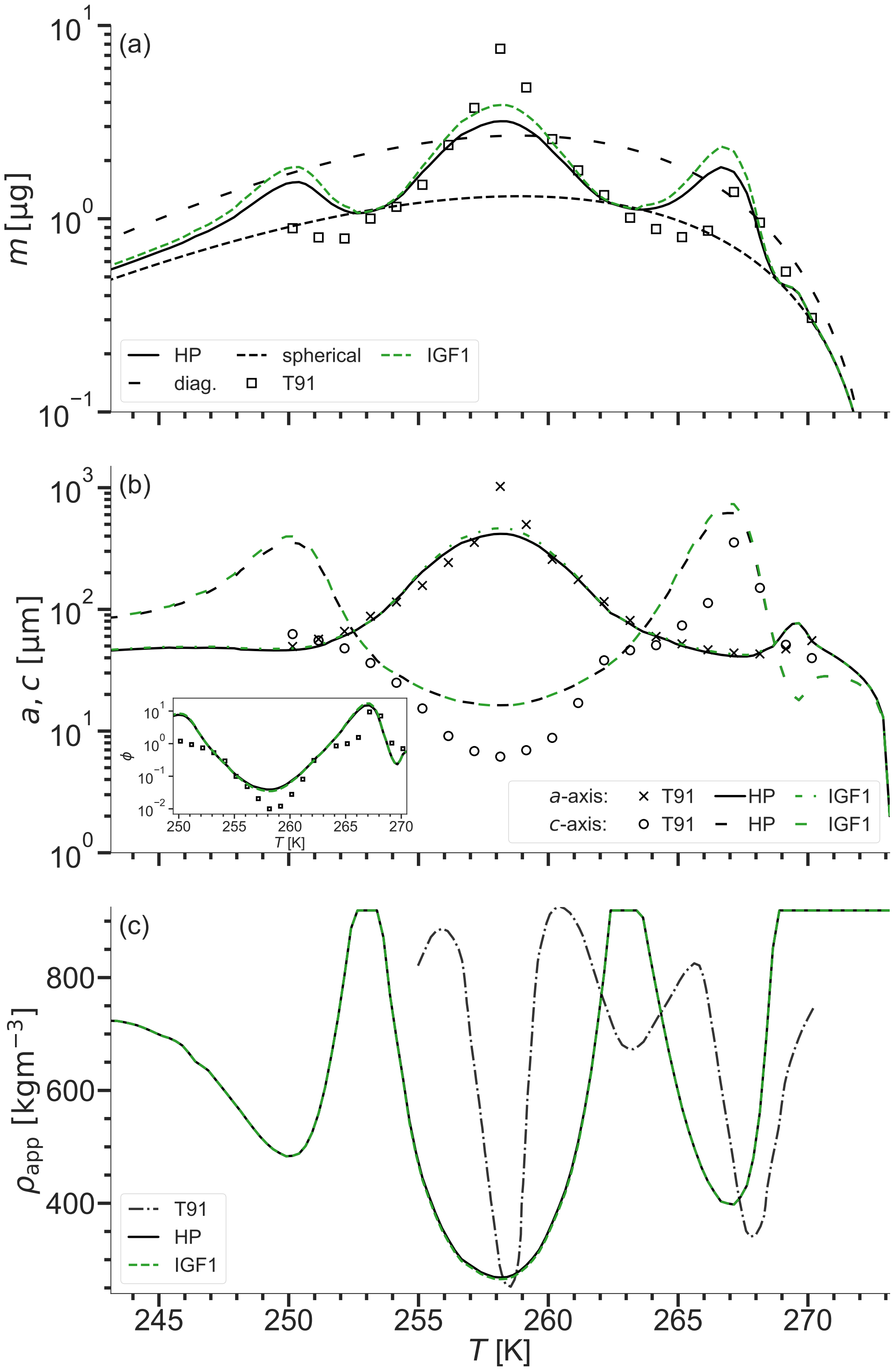

Figure 4.2: T-dependence of (a) m, (b) geometry ($a-$, $c-$axis, ϕ), and (c) $\rho_{\mathbf{app}}$ after 10 min of vapor deposition. The black line shows results for the baseline HP, green lines include the habit-dependent ventilation coefficient and terminal velocity interpolation (IGF1), and the markers show results of Takahashi et al. (1991, TH91). (a) includes a line for a particle with a diagnostic geometry (diag., long dashed) and that for a spherical crystal (short dashed).

et al. (e. g. 2015). The complex shape of polycrystals and their density cannot be adequately captured by the spheroidal approach. However, model agreement with laboratory data on ice mass deposition is improved by the explicit habit prediction and habit-dependent ventilation.

4.2.2 *Polarimetric Signal of Model Results*

To further analyze the modeled results, we use the methods proposed by Myagkov et al. (2016b) to calculate the polarizability ratio (PR) for the different temperature regimes. Myagkov et al. (2016a) combines the methods of Melnikov and Straka (2013) and Matrosov et al. (2012) to obtain the polarizability ratio $\rho_e(\phi, \rho_{app})$ from a 35 GHz cloud radar with a hybrid polarimetric configuration. The PR is based on the particle shape and its dielectric properties and can be used to retrieve information about the environmental conditions under which particles develop certain habits and apparent densities. For their analysis, only particles near cloud top are considered since these observed characteristics developed in local conditions and particle mixtures are unlikely. Myagkov et al. (2016b) show that observed PRs are similar to those obtained from the free fall chamber of Takahashi et al. (1991) within the uncertainties of the (temperature) measurements. The PR analysis provides insight into the functional coupling between geometry and density via the IGF (Eq. (2.28)). The qualitative behavior of the PR is similar to that of the aspect ratio, where oblate particles have $\rho_e(\phi < 1) < 1$ and vice versa for prolate particles $\rho_e(\phi > 1) > 1$. It is important to note that the sensitivity of the PR to a change in geometry is higher for high particle densities (see Fig. 2 of Myagkov et al., 2016b).

Figure 4.3 compares the PRs of TH91 (open grey triangles, all growth times), observations near cloud tops (Myagkov et al., 2016b, black circles), and the results after three and ten minutes of simulated growth with HP (pluses/circles, color indicates app. density). We show two different time steps of the HP to distinguish between primary and secondary habit effects of oblates: after three minutes, only primary habits develop, so that particles reach a maximum PR before branching. The qualitative results of the HP compare well with TH91 and observations. Particles with the most extreme PRs do not develop when using the HP, and their transition between regimes appears to be shifted.

For the maximum in the warm prolate regime, the particles appear to have the correct aspect ratio (Fig. 4.2(b)) with a slightly lower PR than the observations. This finding suggests that the warm prolate maximum of the IGF may cause excessive hollowing. In addition, the maximum may be too broad, causing an offset in the transition regime.

Oblates that turn out not to be thin enough (cf. Fig. 4.2 b) result in a PR that (after three minutes) is not as low as suggested by the observations, but is qualitatively consistent. The strong branching of the particles throughout the oblate-favoring regime leads to an overestimated reduction of the PR for the simulated particles. According to this analysis, it seems necessary to postpone branching to later stages of particle evolution.

Warm oblates ($269 < T < 273$ K) and the cold prolate maximum ($T < 252$ K) cannot be fully evaluated due to a lack of observational data points. However, existing laboratory measurements suggest that these maxima may be overestimated. Due to

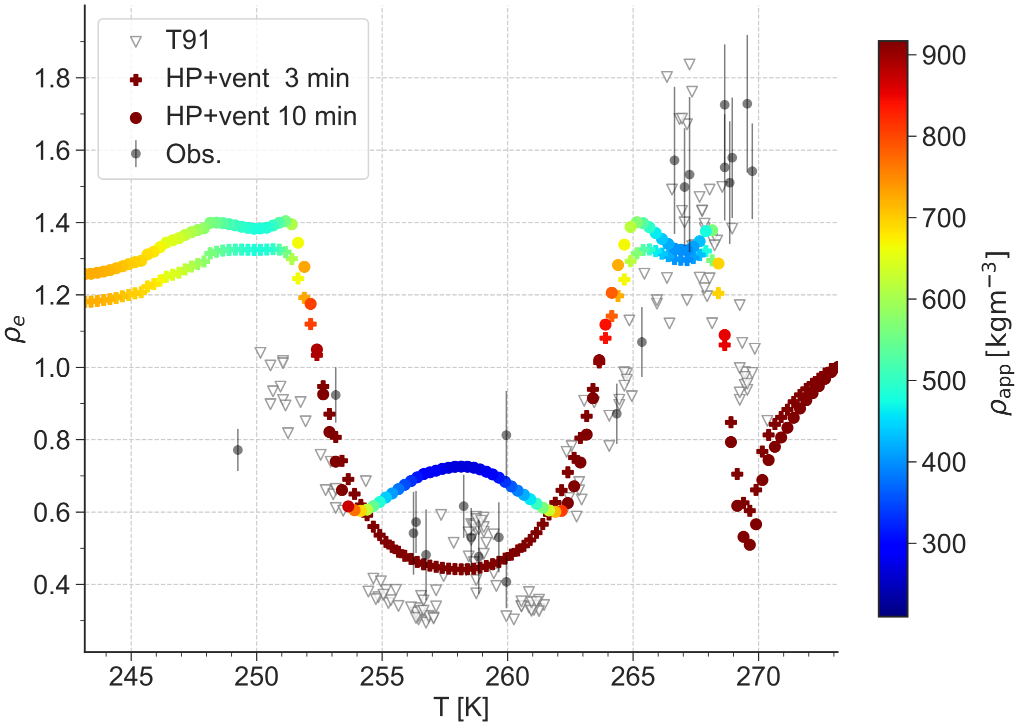

Figure 4.3: T-dependence of the polarizability ratios ρ_e for ice crystals grown in the free-fall chamber (open grey triangles), with HP + habit dependent ventilation ([+] for $t = 3\,\text{min}$, [•] for $t = 10\,\text{min}$), and observed near cloud tops (black squares, error bars represent ±1 standard deviation). Color-coded is the particle's apparent density ρ_{app}.

the limitations of the spheroidal framework we cannot describe the development of polycrystals, but the original IGF classifies these particles as prolate. The above deficiencies for the specific regimes are:

1. oblate minimum around $T = 269\,\text{K}$ is too low,
2. prolate maximum around $T = 267\,\text{K}$ too high m with too low ρ_{app},
3. crystals around $T = 258\,\text{K}$ not thin enough ,
4. cold prolate/polycrystal regime exhibits has too high m and ϕ.

4.2.3 *Updated Inherent Growth Function*

To overcome the above deficiencies, we propose a modification of the IGF and related assumptions to improve the habit-dependent particle growth. Starting from point one, there is no clear evidence for a strong oblate minimum at $T = 269\,\text{K}$, either from the observations shown above or from other sources such as Bailey and Hallett (2009). We therefore use the values suggested by Sei and Gonda (1989). Future retrievals may be useful to evaluate this change.

Point two can be addressed by reducing the IGF maximum around $T = 267\,K$ by 25% and fitting the curve to $\Gamma = 1$ at the appropriate temperatures. This change should result in slightly shorter, lighter, but denser columns that better match the TH91 data. For PR, the geometric change is (partially) offset by an increase in density.

In the oblate growth regime, the IGF initially produces the correct geometries (cf. 3 min results), but branching seems to occur too early and for a relatively wide range of planar particles. Comparing the simulated density with the wind tunnel results (Fig. 4.2c), we see that particles branch only for a narrow temperature range. So instead of changing the IGF, we change the branching criterion to better resemble the onset of branching. In the formulation of JH15 (see Eq. (2.28)), branching does not occur before $\nu\, a^2 > \pi\, D_v\, c \Rightarrow a \geqslant 100\,\mu m$. Here, we modify the JH15 criterion and propose that particles grow through deposition at bulk ice density until they branch when $a \geqslant 200\,\mu m$, effectively delaying the onset of branching.

For the final point, we merge the time-dependent growth rates of TH91 (Tab. 2 of Takahashi et al., 1991) with the results of Sheridan (2008) and Sheridan et al. (2009). Connolly et al. (2012) also report a discrepancy between observed and modeled crystals for the regime around $T = 253\,K$ using CL94's IGF, but they assume oblate growth for colder temperatures. Due to the dominance of polycrystals, it becomes difficult to generalize these habits to either prolate or oblate spheroids. The advantage of assumed columnar growth is the immediate hollowing, which effectively reduces the apparent density, whereas if oblate growth is assumed, the branching criterion of JH15 is not met because the particles remain nearly spherical.

Figure 4.4 shows the original IGF (black) and our proposed version (blue line) combining the above modifications, together with the diagnosed Inherent Growth Ratios of Takahashi et al. (1991) for short (red) and long growth times (black dots). In Figure 4.5, results of the depositional growth experiment using the new IGF (blue lines) are compared with the original results (black lines) for mass, axis measure, and apparent density. Using the new IGF, the accumulated mass is decreased for the warm prolate peak as well as in the polycrystalline regime, removing the secondary peak (colder $T = 253\,K$) (Fig. 4.5 a).

In terms of geometry, the changes induced by the modified IGF are suitable for both prolate regimes. There is no modification of the IGF in the oblate regime around $T = 258\,K$. The reduction of the warm oblate minimum is in good agreement with the laboratory results. The resulting changes in particle density are negligible.

A second experiment includes the modified IGF, combined with the modified branching criterion of $a \geqslant 200\,\mu m$ introduced above (IGF2+, red lines). The lower limit of $D > 10\,\mu m$ for habit development can be physically justified by the studies mentioned above (cf. Sec. 2.2.3), but at the same time it prevents the development of very thin oblates observed by Takahashi et al. (1991). In this setup we therefore remove the limiter and allow free evolution after nucleation (with $r_{start} = 2\,\mu m$ and $\phi = 1$), which gives the best agreement with TH91. The modifications result in more mass being deposited around $T = 258\,K$, bringing the results closer to the TH91 measurements.

In terms of geometry, the transition from the oblate to the polycrystalline regime as well as the shape of the oblates are very similar to the measurements. The coupling of the IGF and the deposition density leads to subsequent changes in the apparent density. It seems difficult to assess the change in apparent density, but the narrowed oblate minimum seems justified, while the warm prolate minimum might overesti-

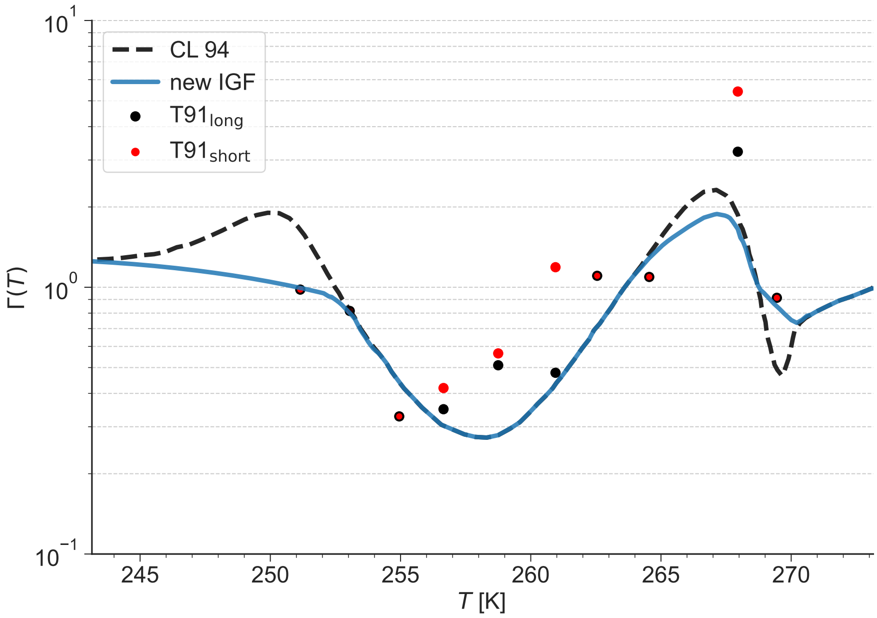

Figure 4.4: IGF of CL94 and our new formulation as a function of temperature. Explicit values calculated from the empirical relations for short and long growth period of Takahashi et al. (1991) are marked as red and black dots.

mate the particle density.

To evaluate the combined effect of shape and density, we analyze the PR with the updated IGF including the additional modifications. Figure 4.6 confirms that this setup can remove the major deficiencies between the laboratory measurements and the simulation. The warm oblate regime shows higher PRs, while the warm prolate maximum is slightly closer to the majority of observational data due to the interplay of geometry and density (less hollowing). Nevertheless, the highest PRs cannot be matched. This discrepancy can be attributed to the parameterization of the hollowing, since the AR is well matched.

In the cold oblate regime, delayed branching significantly improves the agreement of the PR with the observational and T91 results. The evolution of particles with very low PRs ($\rho_e < 0.4$) can be observed after three minutes, as suggested by the measurements. The same is true for the increase in PR due to strong branching around $T = 258\,\text{K}$. Finally, the transition from oblate to polycrystals seems to agree better with the results of T91 and Myagkov et al. (2016b).

For possible further modifications of this version of the IGF, more retrieved observational or laboratory data is needed. In particular, the regimes that are sparsely populated by measurements (such as the polycrystalline region) could be of great benefit to such a detrimental function as the IGF.

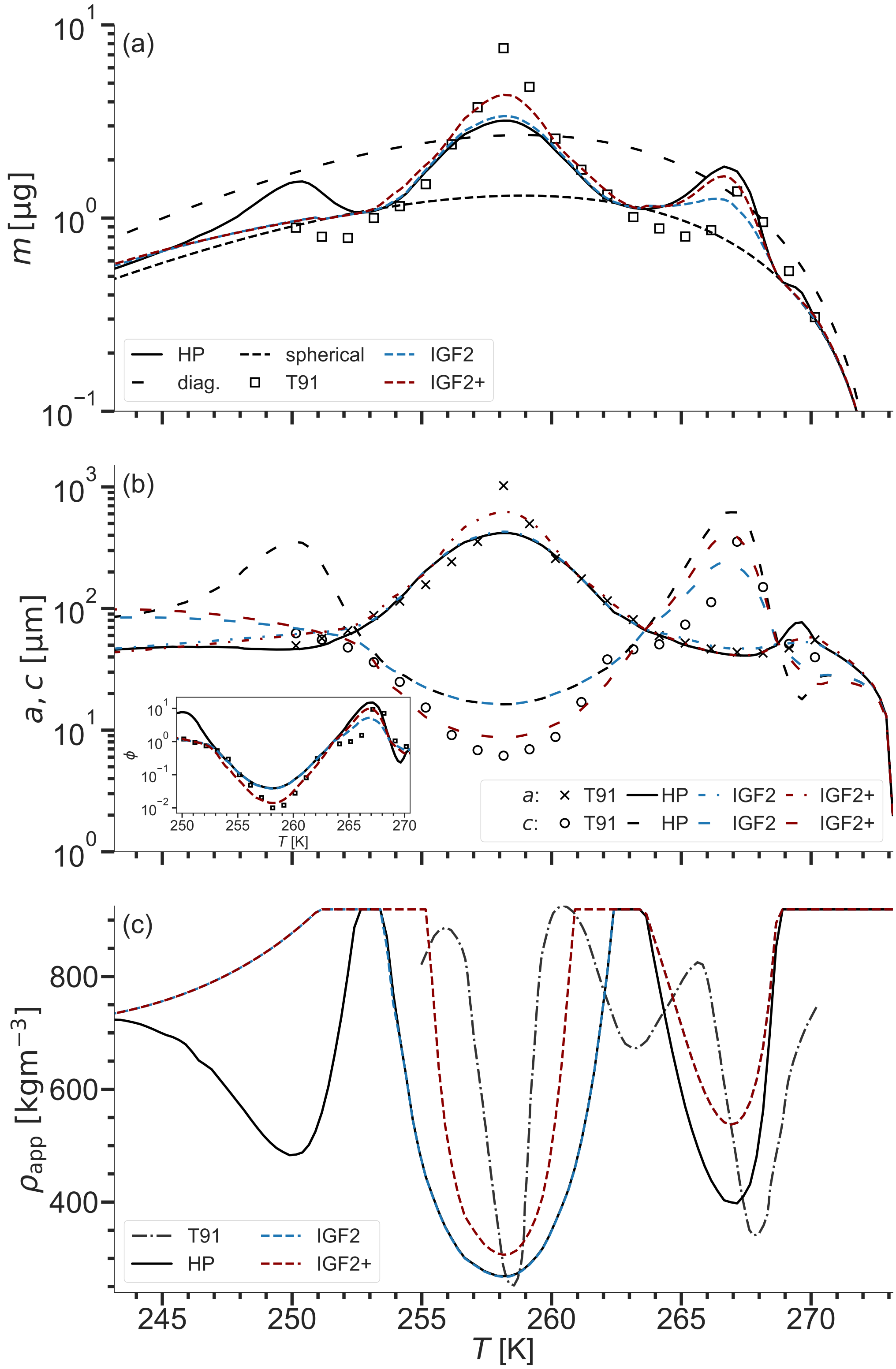

Figure 4.5: As Fig. 4.2 but also compared with the results of the updated IGF (blue) and of the updated IGF including branching modification (IGF2+, red).

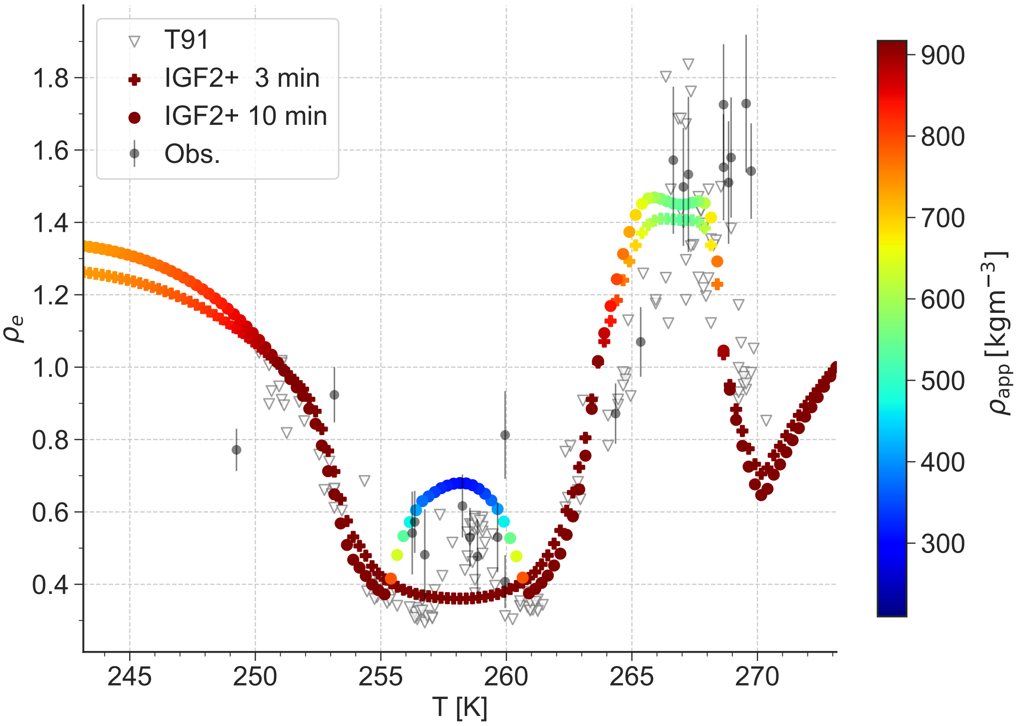

Figure 4.6: As Fig. 4.3 but with the new IGF and altered branching criterion.

5

IDEALIZED CASE STUDY EXHIBITING SENSITIVITIES

Habit prediction has a pronounced impact on many microphysical processes and can introduce variability among particles by abandoning static m-D and v_t-relations. *McSnow* is unique in the sense that it combines the habit prediction scheme of Chen and Lamb (1994b) and Jensen and Harrington (2015) with the full set of parameterizations of Böhm. Using Böhm's framework for the parameterization of particle properties allows a physically consistent and mathematically continuous description of the habit dependency of most microphysical processes. The effect of habit prediction on particles at constant temperature has been shown in Figure 4.2, but this setup can only serve as a limiting case. In real clouds, hydrometeors experience different thermodynamic conditions and change the conditions themselves by absorbing/releasing water and latent heat. We soften the constraints implied by the laboratory setting by focusing on a setup where particles fall through a one-dimensional column (rain/snow shaft) with a prescribed atmospheric profile. The model setup (Fig. 5.1) is defined to mimic different sections inside a cloud where certain relevant ice microphysical processes dominate. In the upper part, depositional growth of small particles should govern the evolution. The ice mass accumulated by deposition changes the shape and fall velocity. Both terminal velocity and geometry are linked to the likelihood of collision events and change the onset of aggregation and how effective it is. In the lower part of the profile, both monomers and aggregates encounter a liquid water zone (LWZ) where the impact of the ice habit on the effectiveness of riming is examined.

5.1 SETUP

Similar as in Brdar and Seifert (2018), the temperature profile is constructed using the surface temperature of $T_{surf} = 273\,K$ and a constant lapse rate of $\gamma = 0.0062\,Km^{-1}$. The domain height is case specific with $z_{top} = 5000\,m$ ($T_{top} = 242\,K$) for a prolate and $z_{top} = 3000\,m$ ($T_{top} = 254.4\,K$) for an oblate favoring regime. Water vapor, liquid water, and temperature are assumed to be constant and not increased or decreased by any microphysical process.

In the upper 80 % of the (case-specific) domain, particles grow solely by vapor depositional growth and aggregation at a supersaturation of 5 % with respect to water. In the lower 20 %, the regime is dominated by riming due to a liquid water zone (LWZ) ($LWC = 0.2\,gm^{-3}$), which enhances particle growth and in turn increases the probability of aggregation. We do not impose a subsaturated regime because the habit-specific effect is small and possible aggregation events become unlikely due to decreasing particle size. The initial properties (mass and size) of the ice crystals are drawn from a gamma distribution in mass with a shape parameter of two and with a mean mass equal to the mass of a spherical ice particle with a diameter of $D_{eq,v} = 10\,\mu m$, the initial aspect ratio is set to $\phi = 1$. Particles are generated at a constant nucleation rate within a nucleation zone that spans 10 % of

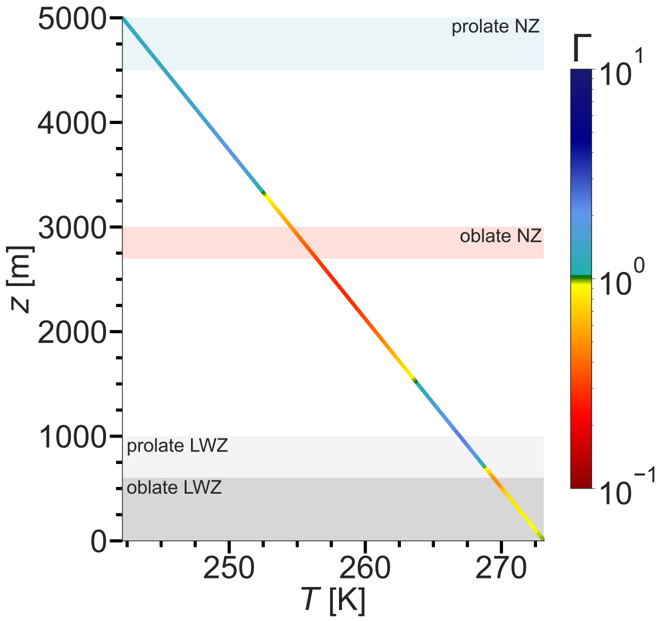

Figure 5.1: Background atmosphere for the one-dimensional model simulations incl. the vertical profiles of temperature and corresponding IGF. The nucleation zones (NZs) and liquid water zones (LWZs) are situated in the shaded regions for the respective cases.

the total domain height. A random initialization height has a positive effect on the variance of the developed particle habits due to the different atmospheric conditions compared to constant nucleation at the domain top. Particles larger than $D > 10\,\mu\mathrm{m}$ are initialized with an apparent density derived from empirical mass-area relations to avoid underestimating the actual particle geometry and overestimating the fall velocity.

We integrate the model over 10 h to reach a steady state, and all statistical quantities are averaged over the last 5 h. We checked for enough super-particles per cell to ensure numerical convergence. Riming is treated by the stochastic riming scheme (cf. Brdar and Seifert, 2018; Bringi et al., 2020) which makes use of the theory of Böhm for terminal velocity and collision efficiency. Droplets are drawn from an exponential drop size distribution with a mean cloud droplet radius of $r_d = 10\,\mu\mathrm{m}$.

Sheridan et al. (2009) shows that habit development is strongly controlled by conditions shortly after nucleation, when relative changes in mass and shape are most pronounced. Numerical models of the atmosphere typically assume uniform thermodynamic conditions within a grid cell. Especially in regions where the IGF shows strong gradients, the uniform treatment leads to the same initial habit development for all particles within that cell and underestimates the habit variability as if the actual thermodynamic conditions at the particle position were assumed. In Large Eddy Simulation (LES) and Numerical Weather Prediction (NWP) models the vertical spacing inside clouds can easily exceed $\Delta z = 50\,\mathrm{m}$ Dziekan et al., 2019; Shima et al., 2020, which already results in a temperature difference between the lower and upper edge of the cell of $\Delta T \geqslant 0.3\,\mathrm{K}$ (assuming the above temperature gradient). Hence, we strongly recommend an interpolation of the atmospheric state to the particle position, making the habit evolution independent of the resolution of the atmospheric grid.

5.2 DEPOSITION

The results in Figure 4.2 imply a change in deposition rate due to the habit prediction and the preceding dependencies on capacitance, ventilation, and fall velocity. To study the effect of particle habits without the complex feedback between ice microphysical processes, we suppress aggregation and remove the liquid water layer for the time being. We focus on a prolate and an oblate favoring initial growth scenario as archetypes for typically observed monomer cases and show why it is important to consider ice habits.

5.2.1 *Prognostic Geometry vs. Mass-Size Relation*

Figure 5.2 illustrates the diversity of particle properties induced by the temperature dependence (original IGF of CL94) of the habit evolution of the mass, velocity, and density of individual crystals relative to their maximum dimension. Since there is no complete set of empirical formulations, we use individual relations for the variables: mass-size of Mitchell (1996), velocity of Heymsfield (1972, Tab. 3), and apparent density from Pruppacher and Klett (1997) for comparison.
We compare the results of the explicit habit prediction in different configurations (specified in Tab. 4.1) with those of simulations using the diagnostic geometry as introduced by Brdar and Seifert (2018) based on the power law of Mitchell (1996) for aggregates of side planes, columns, and bullets.
Like Shima et al. (2020), we use the normalized mass of the ice particles

$$\overline{m} = \frac{m}{\rho_i \frac{\pi}{6} D^3}, \qquad D = 2\ \max(a, c)\ . \tag{5.1}$$

The terminal velocity has been normalized to surface conditions $v_{t,0}$ to remove the direct atmospheric effect (see Sec. 3.2) and ease comparison with the empirical equations of Heymsfield (1972) that assume a reference pressure of $p = 1000\,\text{hPa}$.
The empirical mass-size-relations for aggregates, plates, columns, or broadly branched crystals of M96 may be able to estimate an average behavior of the mass-size spectrum for certain diameter ranges, but the variations caused by local temperature and supersaturation effects seem impossible to describe with prescribed thresholds or a mixture of static relations. Depending on the nucleation conditions prescribed by the initialization height and mass, the particles develop different characteristics for the same maximum dimension. For larger maximum dimensions, we see that the diagnostic geometry tends to underestimate the prolate and overestimate the oblate particle mass, demonstrating the weakness of using the diagnostic approach for the different regimes. Habit-specific relations are not sufficient to represent the dynamic evolution of habits, and additional thresholds based on particle properties would have to be defined to use them. This strongly emphasizes the importance of the HP for predicting ice growth in clouds.
Specifically for the mass of prolate particles, a sharp increase around $D = 0.4\,\text{mm}$ can be observed, accompanied by an increase in velocity and apparent density. This behavior cannot be matched by the slope of any empirical relation and exhibits

a caveat of the deposition density description for secondary habits as formulated by JH15: the deposition density is a function depending solely on the surrounding temperature and is assumed to approach ice density for the transition from prolate-favoring to oblate-favoring conditions (and vice versa) ($\Gamma \to 1 \Rightarrow \rho_{\mathrm{app}} \to \rho_{\mathrm{i}}$, cf. Eq. (2.28)). Because the columns cannot satisfy the branching criterion of JH15, they grow with ice density not only when in regions that mandate spherical growth, but also when falling in oblate-favoring conditions where the addition of high-density mass causes acceleration (Fig. 5.2 b). Coupled with the comparatively short residence times in habit-forming regimes due to high fall velocities, columns do not substantially change the habit they initially formed under conditions close to their nucleation height. The deposition density for habits growing in unfavorable conditions is unknown. Comparison with the empirical relation for apparent density suggests that the assumption of secondary habits (immediate onset and subsequent degree of hollowing) may be overstated.

Particles nucleated under oblate-favoring conditions can form relatively small ARs once they begin to branch. The development of a large area presented to the flow increases the drag, leading to an almost constant terminal velocity at large diameters. This feedback positively supports habit development in the local atmospheric conditions. Compared with the empirical relation of the apparent density of dendrites, the onset of branching seems premature and further motivates our changes to the branching criterion. Oblates that fall into conditions of higher deposition density experience an increase in apparent density. It is unclear whether this behavior is physically reasonable or if it is an artifact of the coupling between IGF and the deposition density. Hashino and Tripoli (2007) hypothesize that dendritic arms grow under prolate-favoring conditions due to an increased ventilation effect along the tips, while there is no current theory for columns. Future laboratory experiments may help to better understand this behavior and motivate a modified treatment of the modeled particles, but for now, we stick with the secondary habit treatment proposed by JH15.

To get a quantitative impression of the average effect of the habit prediction, Figure 5.3 shows the vertical profiles of mass flux, deposition rate, and mass-weighted terminal velocity $\overline{v}_t$. A comparison of particles following the m-D-relation of Mitchell (1996, solid lines) with the original formulation of cylindrical hydrodynamic behavior of Böhm (1992a, long-dashed, HP+vent) shows that the habit prediction significantly reduces mass flux (precipitation rate, Fig 5.3 a). The diagnostic geometry predicts larger areas for particles of a certain maximum dimension than those of prolate spheroids of the habit prediction. This drastically increases the deposition rate (Fig. 5.3 b) via the increased capacitance, while leading to lower fall velocities for the same mass (Fig. 5.3 c). Slower particles prolong the residence time, leading to even more depositional growth that cannot be compensated for by the increased ventilation effect for the fast columnar particles. In turn, particles that follow the fixed m-D-relation can develop up to twice the mass flux of particles that develop a habit.

Using the interpolation for the velocity of columnar particles increases the terminal velocity slightly for large particles (Sec. 3.1). Still, the resulting mass flux is robust and does not change notably. Upcoming results will only use the interpolated fall velocity for prolates due to consistency with laboratory results.

The behavior of particles nucleated under oblate-favoring conditions qualifies the

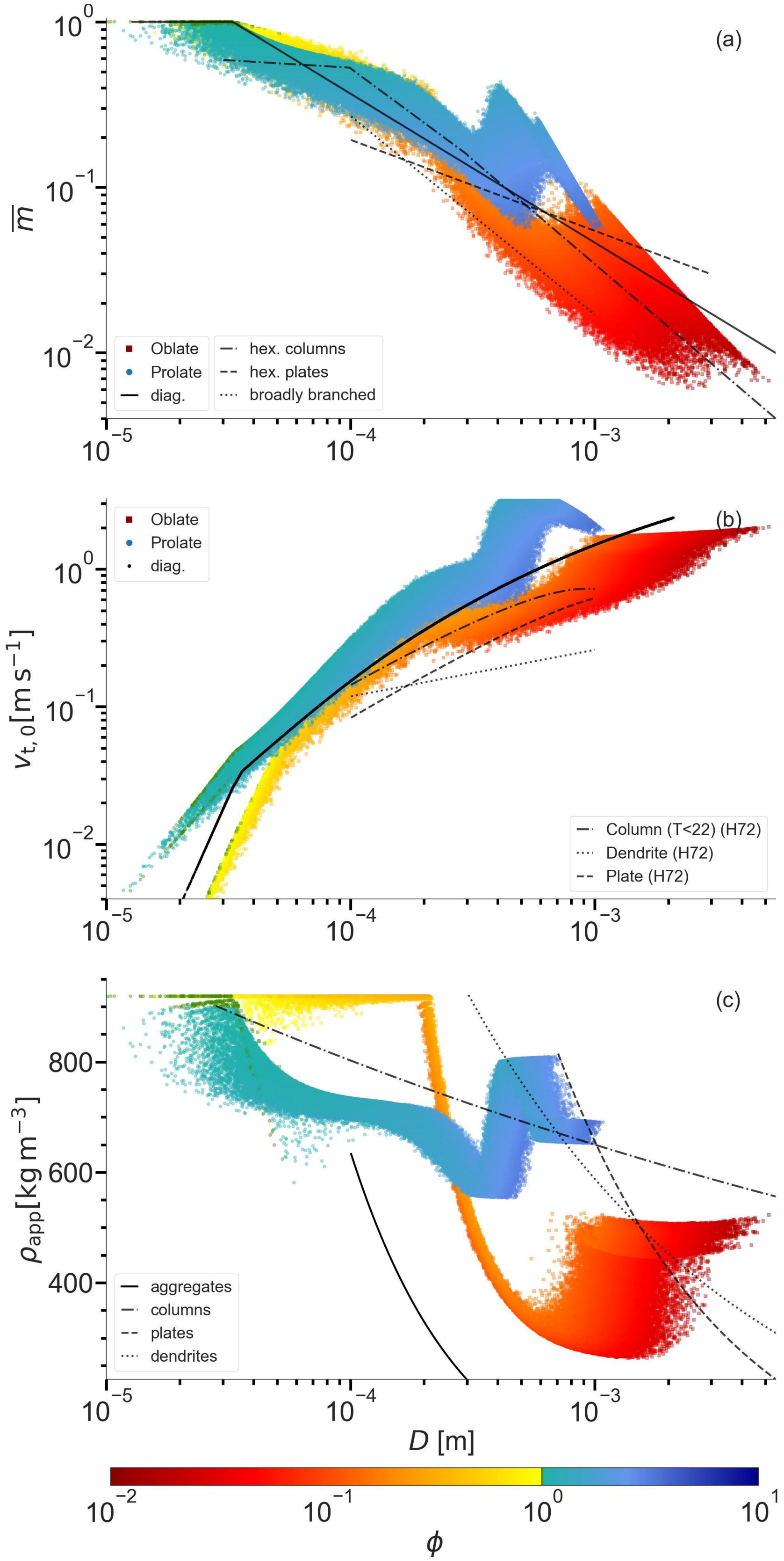

Figure 5.2: $\overline{m}$-D (a), $v_{t,0}$-D (b), and ρ_{app}-D relations (c) for the steady state of the simulation. Markers represent the simulations using a diagnostic geometry and an explicit habit prediction. The particles AR ϕ is color-coded. Lines in (a) are empirical relations of Mitchell (1996), in (b) of Heymsfield (1972), and in (c) from Pruppacher and Klett (1997).

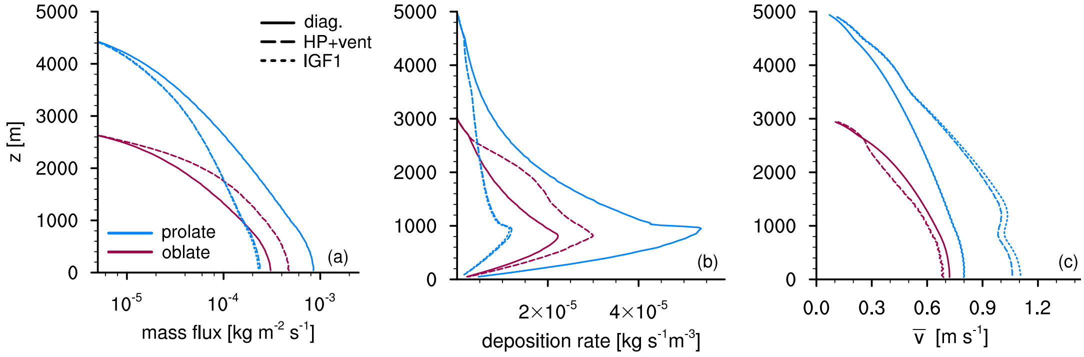

Figure 5.3: Comparison of vertical profiles of (a) mass flux, (b) deposition rate, and (c) mass-weighted velocity $\bar{v}$ for particles nucleated in a prolate (blue, $\Delta z_{\mathrm{nuc}} = 4500 - 5000\,\mathrm{m}$) and an oblate (red, $\Delta z_{\mathrm{nuc}} = 2700 - 3000\,\mathrm{m}$) regime using a diagnostic geometry (solid), habit prediction with ventilation (HP+vent, long-dashed), and habit prediction with interpolated velocity for columns (IGF1, short-dashed).

results of the simplified experimental setup of Takahashi et al.: Plates generate more mass than particles with a diagnostic geometry, but the effect is less pronounced than for prolates. Even at higher masses, oblates have a slightly longer residence time than particles without a habit. The development of thin plates or dendritic structures increases the surface area, causing a positive feedback on capacitance and ventilation, amplified by habit-dependent ventilation, increasing the deposition rate. An opposite effect on the accumulated mass of the two categories of habits can be observed: the HP effectively causes an increase in precipitation mass for oblate particles and a decrease for prolate particles (such as the mass flux/precipitation).

5.2.2 *Updated IGF*

While we do not expect the effect of the updated habit scheme (IGF2 and IGF2+) to be nearly as pronounced as in the isolated laboratory setup of Takahashi et al., the changes may initialize altered habit developments. In particular, particles nucleated in the cold prolate regime remain more spherical and are therefore more prone to primary habit change. Figure 5.4 shows the changes in both growth regimes caused by the modifications of the IGF, including the branching criterion. The flattening of the prolate maximum in the cold regime ($T < 253\,\mathrm{K}$) leads to the evolution of fast falling crystals because their AR remains close to sphericity and their apparent density is comparatively high, improving the agreement with the empirical relation of the apparent density of columns. These crystals short residence times result in reduced total depositional growth and maximum dimension, and ultimately shorter lifetimes as they fall out as precipitation.

The change in branching criterion delays the development of porous structures for plates, and the more compact shape results in an initially increased terminal fall velocity. As soon as strong branching sets in, v_t reaches lower velocities as for the original branching criterion closer to the empirical relation for dendrites of Heymsfield (1972). The delayed onset of branching agrees well with the empirical relation for the apparent density of dendrites.

Generally, the modifications to the IGF and branching criterion have the desired effect on mass and apparent density, while the terminal velocities of the columnar

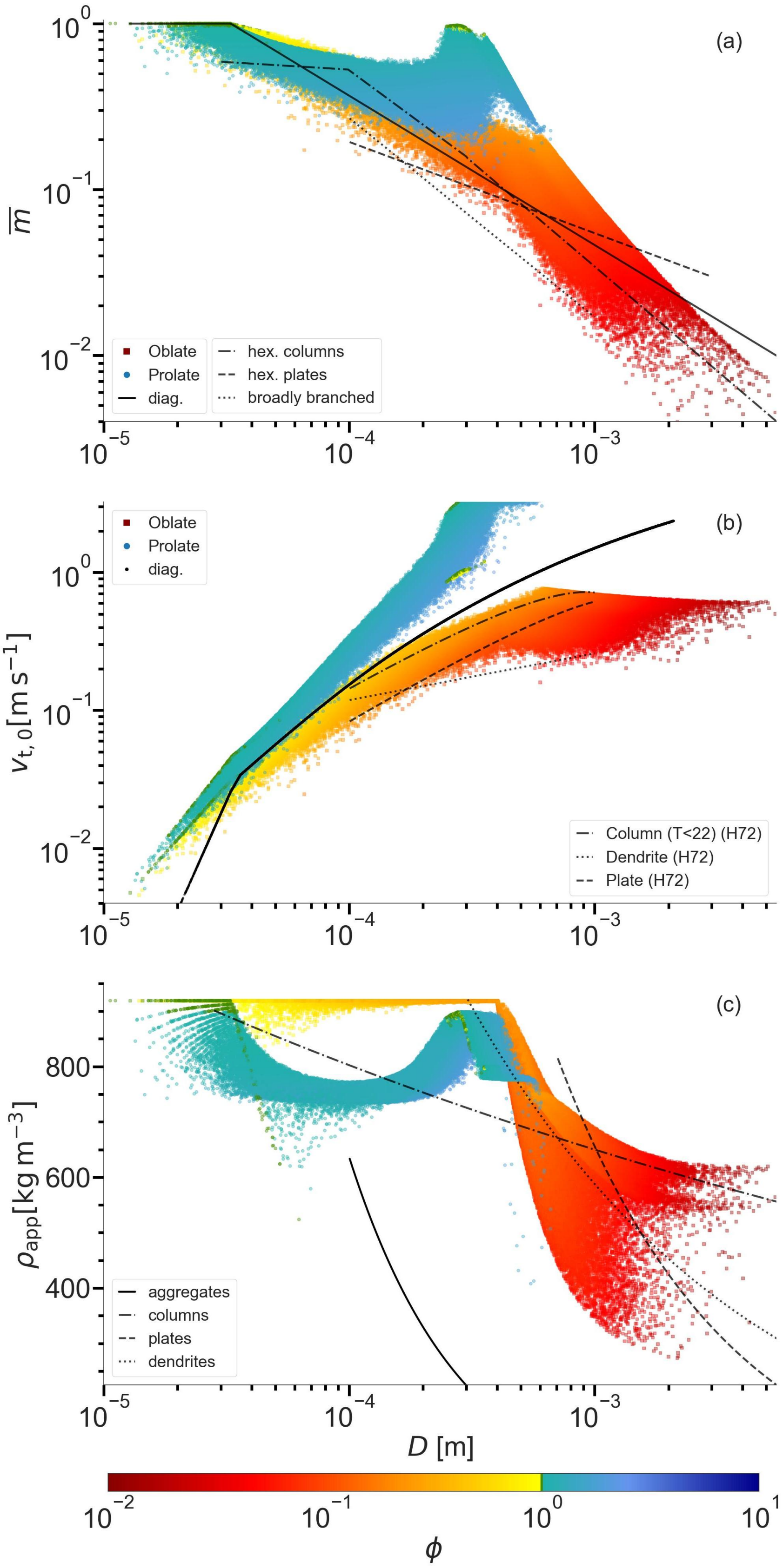

Figure 5.4: Same as Fig. 5.2 but using the updated IGF configuration *IGF2+*. Lines in (a) are empirical relations of Mitchell (1996), in (b) of Heymsfield (1972), and in (c) from Pruppacher and Klett (1997).

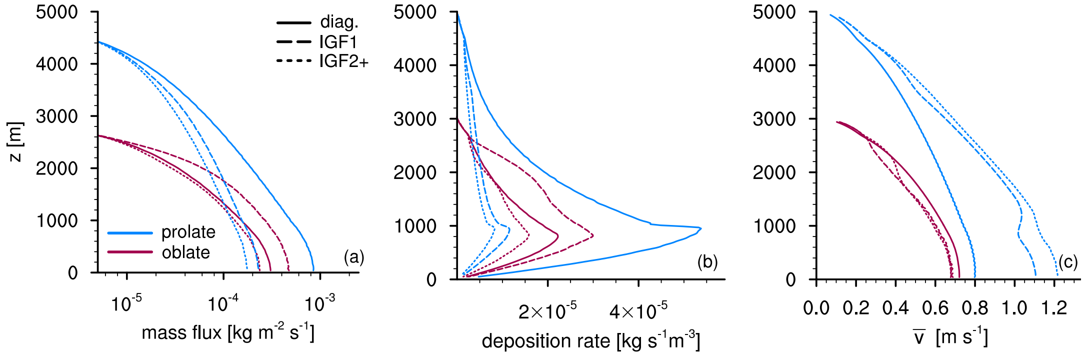

Figure 5.5: Comparison of vertical profiles of (a) mass flux, (b) deposition rate, and (c) mass-weighted velocity $\overline{v}$ for particles nucleated in a prolate regime (blue, $\Delta z_{\text{nuc}} = 4500 - 5000\,\text{m}$) and an oblate regime (red, $\Delta z_{\text{nuc}} = 2700 - 3000\,\text{m}$) using a diagnostic geometry (diag., solid), HP with original IGF, ventilation and v_t-interpolation (IGF1, dashed), and HP with updated IGF and modified branching criterion (IGF2, short-dashed).

particles remain quite high.

The average vertical profiles in Figure 5.5 allow to summarize the quantitative behavior: The mass flux for plates following the original IGF is significantly increased compared to the diagnostic counterpart. For the updated formulation, the mass flux is similar to that of particles without explicit habits. This highlights the importance of the initial growth phase, where the exact onset of branching significantly affects the particle characteristics. The new IGF causes a decrease in mass flux for both the oblate and prolate cases compared to the original IGF configuration for similar reasons: While prolates remain more spherical and less hollow, oblates branch later and the more compact geometry shortens the residence time. This can only be seen by comparing Figures 5.2 and 5.4 because the mass-weighted velocity (Fig 5.5 c) does not show the effect of the lighter particles. The effect of the two IGF versions on habit development is visualized in Figure 5.6. For reference, lines are plotted for ϕ-D-relations from Auer and Veal (1970), assuming the corresponding nucleation temperature (columnar (dash-dotted) $T < 253\,\text{K}$, P1e (dashed): $256\,\text{K} < T < 260\,\text{K}$). The ARs of the prolates (blue) developed for IGF1 are similar to those expected from the empirical relations in the corresponding temperature range.

Using the IGF2+ instead, columnar particles develop similar ARs for lower D due to the removal of the size constraint on habit development, but for larger D their ARs are less pronounced and some particles even change their habit (highlighted in light blue). The classification of these particles is difficult, but they could be interpreted as complex polycrystals like capped columns. If they are polycrystals, this raises the question of the apparent density treatment. It seems unlikely that Eq. (2.28) can describe the development of secondary habits for polycrystalline structures, since the dependence of Eq. (2.29) on Γ makes it difficult to produce low-density spherical ice crystals.

By removing the size constraint on habit development, planar particles (red) are able to develop strong aspect ratios close to $\phi = 10^{-2}$ (lower right corner) for IGF2+. For very large D, the aspect ratios are similar to those expected from the empirical relation for dendrites.

We can conclude that the changes to the IGF and the branching criterion reduce the

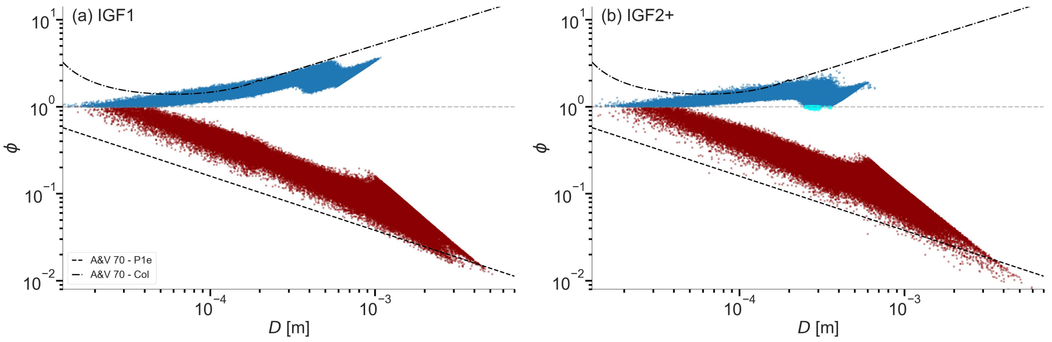

Figure 5.6: ϕ-D relations of the two cases for the original IGF (a) and the updated version with modifications (b). The black lines are empirical relations from Auer and Veal (1970).

mass flux for both scenarios while allowing the development of very thin plates. It remains an open question how to deal with particles that change their habit, since the spheroidal approach is limited to simple geometries.

5.3 AGGREGATION

The three main factors influencing the aggregation process are the geometric area A, the fall velocity difference $\Delta v = |v_1 - v_2|$, and the collision efficiency E_c, which depends on the difference in v_t.

5.3.1 *Diagnostic Aggregate Geometry*

The reader should note that in the current model state, the HP is solely intended for monomers. Following the first collision, particles adhere to the diagnostic geometry. The three main factors influencing the aggregation process are the geometric area A, the fall velocity difference $\Delta v = |v_{t,1} - v_{t,2}|$, and the collision efficiency E_c, which itself depends on the difference Δv. The habit prediction scheme affects all of the above factors by introducing variability in particle shape and density, broadening the velocity spectrum, and potentially changing the cross sectional area. Here, we use the formulation from Mitchell (1988) for sticking efficiency, which prescribes piecewise linear values for temperature ranges. Intuitively, the habit prediction is expected to lead to altered, habit-specific aggregation rates that feedback on depositional growth. Figure 5.7 shows the vertical profiles of number density (left column) and mass flux (right column) for the oblate (top row) and prolate (bottom row) cases, separated into monomers and aggregates. The vertical number density profiles show that the different descriptions of depositional growth and geometry have critical effects on aggregation. The development of dendritic crystals causes an earlier and stronger initial aggregation rate compared to particles without HP and is strongest for the original IGF (crystals branch earlier). Both IGF configurations show a reduction in monomer number density, but the earlier branching critically influences the onset of aggregation and the additional collection of both monomers and aggregates further down. This causes the mass flux for the original IGF to be dominated by aggregates. The number of aggregates for the modified IGF is almost independent of height,

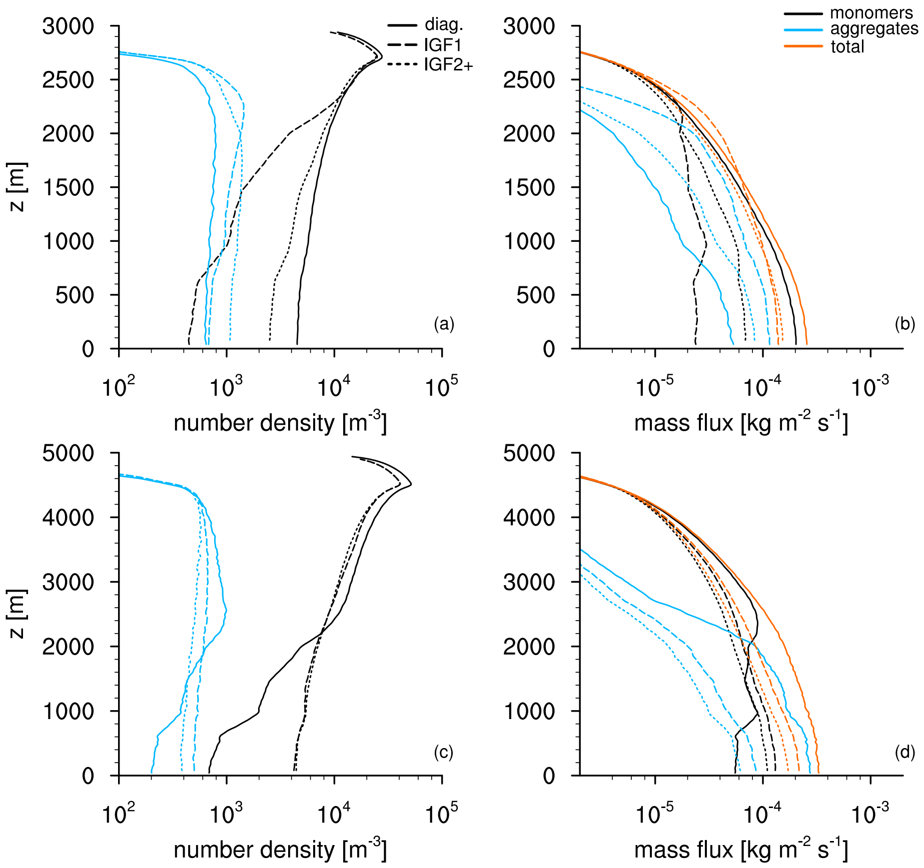

Figure 5.7: Vertical profiles of number density (a & c) and mass flux (b & d) for monomers (black) and aggregates (blue) for the oblate (top row) and prolate (bottom row) nucleation regimes using a diagnostic geometry (solid), using IGF1 (dashed), and IGF2+ (short-dashed) with deposition and aggregation enabled.

indicating that aggregates mainly collect other monomers rather than self-collection of monomers or aggregates. Analysis of the number of monomers per aggregate confirms that mostly large monomers are collected, while smaller crystals rarely aggregate (not shown).

Oblate particles grow efficiently by vapor growth and their collection by aggregation does not transfer its positive effects to the aggregates because we assume that their geometry is reduced to the m-D power law. This leads to a reduction in the total mass flux when the HP is compared to the classical m-D-relation, indicating the effect of the simplified aggregation geometry that immediately forgets the monomer information. A difference between the two IGF configurations for the composition of the total mass flux at the surface is present: for the original IGF, the mass flux is dominated by aggregates and close to equality for the new configuration. The higher total number density leads to more depositional growth because the supersaturation is fixed. If there would be an interactive feedback between hydrometeors and the atmosphere, higher number densities would lead to a faster depletion of the supersaturation.

The prolate case shows the opposite behavior: the reduced depositional growth compared to particles without explicit habit, caused by shorter residence times, leads to smaller cross sectional areas, which in turn decreases the aggregation rates. Particles with a diagnostic geometry, on the other hand, start to aggregate efficiently in the lower half of the domain, where the sticking efficiency is high, so that the number densities of monomers and aggregates constantly decrease and large aggregates form. Aggregates dominate the mass flux when no habits can develop, while for the HP the mass flux is defined by that of the monomers.

The prediction of habits significantly impacts the studied cases' aggregation. The strength of the impact depends on the dominant primary habit, but it may be overestimated in deep or multi-layer cloud where the development of alternative habits could result in potentially high aggregation rates.

5.3.2 *Prognostic Aggregate Geometry*

The implementation of a prognostic geometry for aggregates in the context of explicit habit prediction will have a cascading effect on all microphysical processes, given that all habit specifications are now also applicable to aggregates. In both case studies, the effect on number densities is nearly inconsequential (Fig. 5.8 a & c). However, a reduction and alteration in the partitioning of the mass flux can be observed for either setup, as illustrated in Figure 5.8 b & d.

In the oblate case, the mass flux for aggregates exhibits only slight variation when the geometry treatment is altered. In contrast, for prolates, the mass flux of aggregates is reduced, with an increase in the flux of monomers. This modification can be attributed to a combination of assumptions that affect the terminal velocity: The application of the prognostic geometry results in an update to the aspect ratio, whereby only the minor dimension is modified. This effectively causes a rounding effect, but it may also lead to a change in the habit of the particles, from prolate to oblate or vice versa. This effect can be interpreted as a form of tumbling, and due to the interpolation for prolate particles, no artificial deceleration or acceleration is expected.

Figure 5.9 illustrates that if we assume a diagnostic aggregate geometry and $\mathtt{phi} = 1$, the maximum dimension increases steadily. In contrast, for the prognostic aggregate geometry, the particles first become more spherical (with a fairly constant maximum dimension) up to the point where they might change habit (light blue/light red markers). The reduction in maximum dimension results in a corresponding decrease in collision cross-section, which in turn diminishes the efficiency of aggregates in collecting particles along their trajectories. Nevertheless, the effective area of prognostic aggregate geometries is derived from the formulations for spheroids, including an estimation of the ratio of the projected area to the ellipse area q (see Eq. 2.38), which is aspect ratio dependent.

Here, we introduce the term *lacunarity* which is defined by Dunnavan et al. (2019) as "a measure of porosity or density, where higher values of lacunarity represent more gaps overall" (Dunnavan et al., 2019, p.3921). In their study, Dunnavan et al. (2019) employ observations from a Multi-Angle Snowflake Camera (MASC) (Garrett et al., 2015) and simulations to ascertain the shape and density evolution of snow aggregates. Their findings indicate that the lacunarity increases almost constantly with increasing monomer number for aggregates of oblates, prolates, or habit mixes. Upon analysis of the formulation presented by Shima et al. (2020, Eq. 2.38), it can be observed that the lacunarity is proportional to ξ_p^{-1}, which rapidly approaches

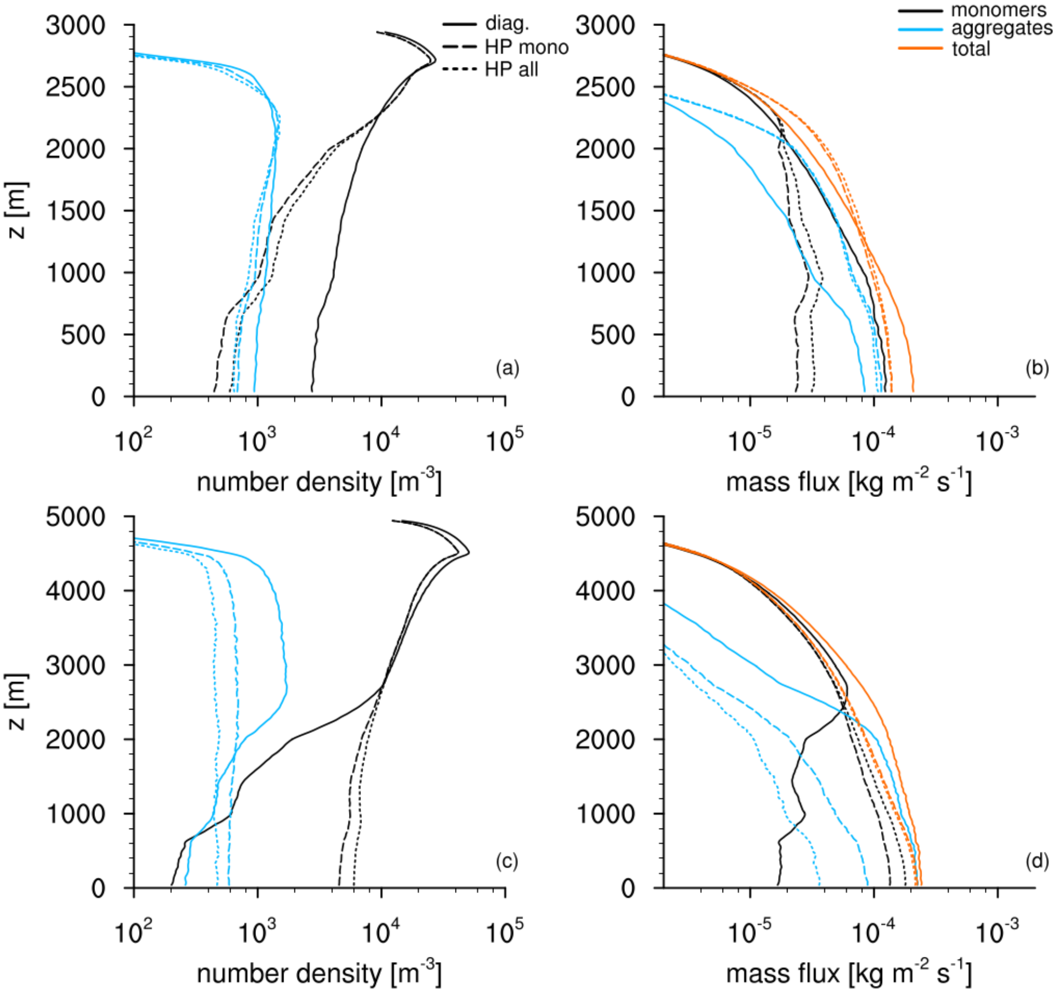

Figure 5.8: Same as Fig. 5.7 but comparing a diagnostic geometry for all particles (solid), HP for monomers only (dashed), and HP for all ice particles (short-dashed). Results use the original IGF.

unity for particles that are nearly spherical or prolate, even at relatively low densities (see Fig. 5.10). The formulation is inconsistent with the findings of Dunnavan et al.

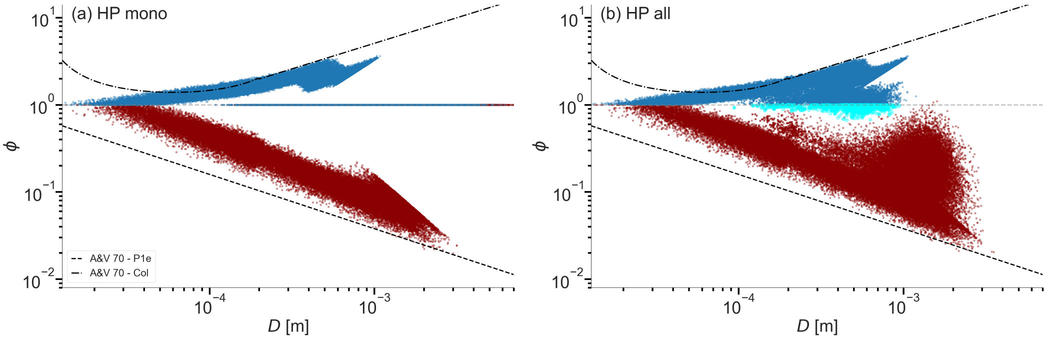

Figure 5.9: ϕ-D relations of the two cases for a diagnostic aggregate geometry (a) and a prognostic aggregate geometry (b). The black lines are empirical relations from Auer and Veal (1970).

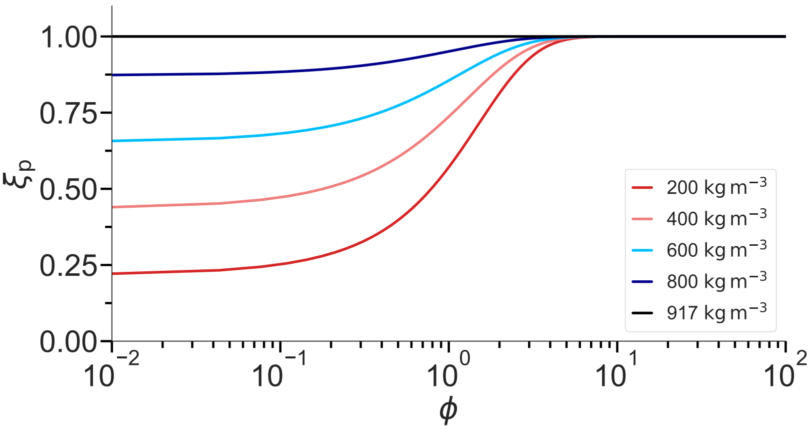

Figure 5.10: ξ_p as a function of ϕ for different apparent densities.

(2019) as it underestimates the lacunarity associated with a reduction in apparent density resulting from an increase in the number of monomers. The aggregation of particles results in a significant change in lacunarity, which in turn increases the terminal velocity. The shortened residence time results in reduced depositional growth and a decreased likelihood of aggregation, as the terminal velocity difference with the relatively fast prolate particles is diminished. Consequently, the mass flux of aggregates is reduced, with the total mass flux dominated by the mass flux of monomers. It is observed that the description of the parameter ξ_p may result in an underestimation of the gaps present in aggregates composed of prolates, which in turn may lead to a modification of their terminal fall velocity.

This effect becomes evident examining the PSDs stratified by the number of monomers per aggregate for the two cases in relation to the habit consideration in Figure 5.11. In the oblate case, the highest number of monomers per aggregate is observed when the HP is applied to monomers only (Fig. 5.11 b), as the slow, plate-like or dendritic crystals have the largest collision cross section and are thus most likely to be collected by the porous spherical aggregates. The application of the HP to all particles (Fig. 5.11 c) results in the formation of only small aggregates, whose maximum dimension does not increase significantly until the particles are close to sphericity. In the prolate case, two additional effects are observed. First, the large fall distance results in particles encountering a greater number of collision partners, leading to an increase in the number of aggregates and the monomer concentration when the diagnostic geometry is employed (Fig. 5.11 d). Secondly, narrow prolate spheroids maintain a robust monomer mode due to their geometry, which markedly diminishes the collision kernel. When the HP is applied to all particles, this effect also extends to aggregates that have already formed, thereby further reducing the probability of collision. The impact of the HP on the PSD illustrated here represents a particularly pronounced instance of geometric influence, given that the crystals that develop a habit engage with crystals of the same or analogous habit (see Fig. 3.9).

The prognostic aggregate geometry has a relatively minor impact on the number densities and total mass flux. However, it does give rise to certain side effects, including those associated with the porosity treatment for prolate aggregates and a notable reduction in aggregation events due to the geometry itself. Further studies

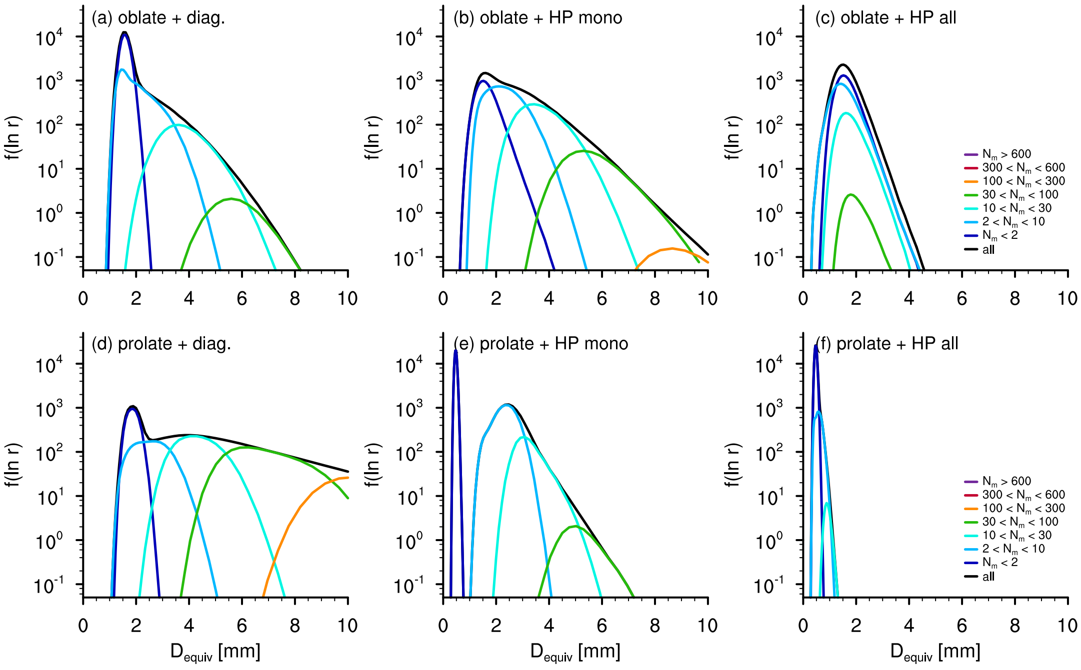

Figure 5.11: Particle size distributions for the different HP considerations in relation to monomer number per super-particle (color-coded) for the two case studies (upper row: oblate, bottom row: prolate) between surface and domain top. The left column shows results with the diagnostic geometry for all particles, the middle column for HP only for monomers and the right column for HP for all ice crystals.

and refinements may enhance the representation of aggregate properties within the spheroidal framework. However, for the remainder of this thesis, we will utilize the explicit HP for monomers only and apply the diagnostic aggregate geometry.

5.4 RIMING

Finally, we enable riming by specifying a liquid water zone in the bottom 20% of the domain (Fig. 5.12). Particles are classified as rimed as soon as they contain rime mass. While the knowledge about the sticking efficiency of rimed particles can be considered limited, we stick to the temperature dependent parameterization of Mitchell (1988). For low LWCs, the transition from prolate/oblate monomers may be slow, and habit effects caused by deposition may persist, but high LWCs lead to effective rounding of particles, which can then be described by m-D-relations for rimed particles or graupel (as shown by Jensen and Harrington, 2015). For the monomers, we will continue to utilize the prognostic deposition approach in conjunction with the fill-in model, which was introduced in Section 2.2.4.

For the chosen conditions, all particles are large enough to rime immediately upon reaching the LWZ, regardless of configuration (cf. onset of riming in Fig. 3.8). Riming increases the mass and area of the particles while accelerating them, increasing the rate of aggregation and leading to a further decrease in number density. The immediate effect of the added rime mass is to fill the porous structures before effectively increasing the maximum dimension. For particles that do not develop a habit, this effect is especially strong due to the low apparent density prescribed by

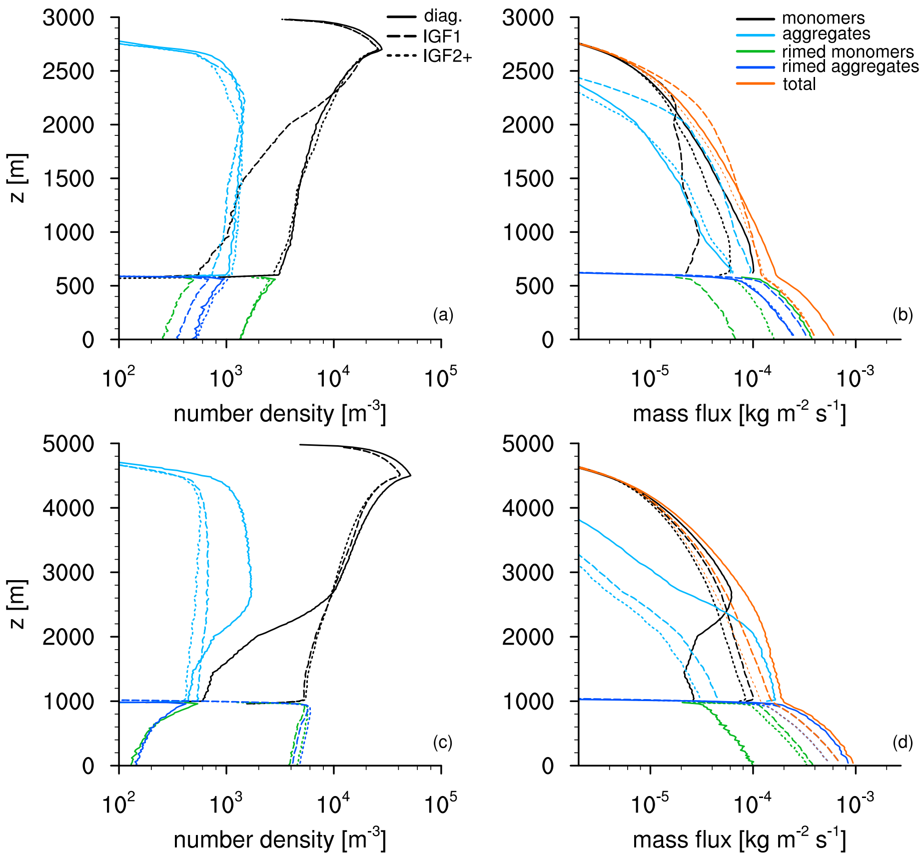

Figure 5.12: Vertical profiles of number density (a & c) and mass flux (b & d) for monomers (black), aggregates (black), rimed monomers (green), and rimed aggregates (dark blue) for the oblate (top row) and prolate nucleation regimes (bottom row) using a diagnostic geometry (solid), HP with original IGF (dashed), and HP with updated IGF and modified branching criterion (short-dashed) with all processes enabled.

the empirical relation (cf. Fig. 5.2 c).

Regardless of the primary habit, particles that are allowed to evolve habits are effectively dragged toward sphericity by the assumption that riming only increases the minor dimension (see Eq. (2.45) & (2.46)). Therefore, riming accelerates the most pronounced evolved habit through mass growth and rounding. The IGF configuration has a weak effect on riming compared to deposition and aggregation. Only for prolates following the original IGF can a more pronounced decrease in number density in the LWZ be observed, because the cross-sectional area is more effectively changed by rounding when more pronounced ARs have developed.

6

INVESTIGATION OF ICE MICROPHYSICAL PROCESS FINGERPRINTS

After characterizing the sensitivities of *McSnow* including the identification of uncertainties in the microphysical process description, we want to use the capabilities of the model to investigate IMP fingerprints. While *McSnow* can be used as an optional microphysical scheme for two- or three-dimensional simulations using the ICON model (Zängl et al., 2015), the complexity imposed by the many unknown observables such as the initial size and shape distribution of particles, coupled with the significant computational resources required to ensure stochastic convergence, makes it very difficult to perform IMP fingerprint studies based on the model configuration.

To overcome this problem, we will therefore search for weather situations where the radar signal persists for a time span that allows to derive meaningful average profiles which allows us to try to recreate the state using a one-dimensional simulation and is not as dependent on dynamical processes. The decision to use a one-dimensional setup introduces several simplifications that make comparison with real cases challenging. Dynamic effects caused by latent heat release, mixing effects due to turbulence, and horizontal advection cannot be adequately represented. The lack of feedback between the microphysics and the prescribed atmospheric state does not allow for natural evolution of the latter, such as temperature changes or depletion of supersaturation. Despite these limitations of the one-dimensional setup, we want to prove that the introduction of an explicit habit prediction in the current form still allows good representation of the ice microphysical processes and leads to plausible synthetic polarimetric observations.

In the first part of this chapter, we review the available observations from both in situ and remote sensing instruments to describe the state of the atmosphere that we were trying to model. We explain how we configured the simulation setup based on the observations and how unknown or weakly constrained variables are handled. The last part compares the synthetic observations resulting from the best setup identified with the observations to identify processes where *McSnow* is able to correctly predict the evolution of the hydrometeor spectrum and where process descriptions and the forward model are unable to reproduce IMP fingerprints.

6.1 AVAILABLE OBSERVATIONS

The data base of observations was collected during the TRIPEx-pol-scan campaign between December 2021 and February 2022 at the Jülich ObservatorY for Cloud Evolution Core Facility (JOYCE-CF) (Löhnert et al., 2015). The campaign is the successor of the successful TRIPEx-pol (von Terzi et al., 2022). The roof platform of JOYCE-CF was equipped with an X-band, a Ka-band, and a W-band radar, where the Ka-band and W-band radars performed scans at 30 ° elevation while the X-band was pointed vertically (refer to Tab. 6.1). All radars underwent careful calibration

Table 6.1: Technical specifications of the four radars that were deployed during the TRIPEx-pol-scan campaign. The Ka-band radar used linear depolarisation ratio (LDR) spectra, the W-band was operated in Simultaneous Transmit - Simultaneous Receive (STSR) mode.

Specifications	X-band	Ka-band	W-band
Frequency [GHz]	9.4	35.5	94.0
Polarimetry	single-pol	LDR	STSR
Number of spectral averages	10	20	28
Half-power beam width [°]	1.0	0.6	0.6
Range resolution [m]	36.0	36.0	35.8
Temporal resolution [s]	2	2	7
Sensitivity at 1 km [dBz], 2 s int. time	−50	−63	−58
Maximum range [km]	12	15	16
v_D resolution [$\mathrm{m\,s^{-1}}$]	0.038	0.04	0.05
Nyquvist range [$\mathrm{m\,s^{-1}}$]	± 78	± 20	± 6

and a series of processing steps, and corrections for attenuation effects. The setup of the TRIPEx-pol campaign, as described by von Terzi et al. (2022), provides further details on radar-related procedures.

Additionally, the site supplies measurement data on precipitation rates collected by rain gauges, temperature and humidity via microwave radiometers, and wind speed via Doppler wind lidars. During the research campaign, a total of 50 Vaisala RS41 radiosondes were deployed to obtain vertical profiles of temperature, pressure, and relative humidity. Although wind speed and direction could be obtained through the use of Global Positioning System (GPS), it is assumed that the atmosphere was adequately sampled above the site up to approximately 4 km.

It is unfortunate that the meteorological conditions during the course of the campaign were not ideal for the observation of situations characterized by the prevalence of columnar crystals. In one instance, there were indications of the potential presence of columnar particles, albeit in a relatively weak form. However, the relative humidity observed by the radiosonde was insufficient to reproduce the cloud. Accordingly, an attempt will be made to reproduce polarimetric radar observations of a case dominated by plate-like monomers, where IMP fingerprints have been more readily identifiable.

In order to select an appropriate case for the observational campaign, we sought clouds with tops situated at a level slightly above or within the DGL, with the objective of inducing nucleating particles to become oblate. The existence of plate-like and dendritic structures indicates that there should be notable sZ_{DR} signals for monomers of a small to medium size prior to aggregation. The following section will provide further information regarding the atmospheric conditions of the selected day and the radar profiles used to limit the model runs.

6.1.1 *Atmospheric State*

On 31 January 2022, Germany experienced the effects of a low-pressure frontal system named *Odette*. The precipitation caused by the frontal system, especially in central Germany, first fell as snow in the front of the long precipitation band before changing to sleet and rain. The snowline in western Germany was about 1000 m. At the campaign site, the almost continuous precipitation throughout the day (Fig. 6.1, Pfitzenmaier and Löhnert, 2023) accumulated to a daily total of 10.8 mm. The precipitation rates (RRs) showed variability, with peak maximum RRs remaining below $\mathrm{RR} < 3\,\mathrm{mm\,h^{-1}}$. The surface temperature T_{surf} measured at JOYCE-CF remained between $T_{\mathrm{surf}} \in [277 - 278\,\mathrm{K}]$. However, at approximately 20:00 UTC, advection of cold air caused the surface temperature to drop to $T_{\mathrm{surf}} = 275.4\,\mathrm{K}$.

To contextualize the atmospheric state during the radiosonde launch at approximately 11:30 UTC, we first examine the prevailing synoptic situation, including cloud cover and precipitation patterns. Figure,6.2 illustrates this by presenting a visualization of the high resolution visible (HRV) channels from the Spinning Enhanced Visible and Infrared Imager (SEVIRI) instrument on MSG-4 of the European Organisation for the Exploitation of Meteorological Satellites (EUMETSAT). The SEVIRI HRV image reveals an extensive, bright stratiform cloud deck over northern and central Germany, indicative of a stable, thick cloud system. The correlation between the visible cloud shield and the disdrometer data suggests that the JOYCE-CF region was experiencing active frontal precipitation, likely from an occluded front traversing Western Germany. The corresponding synoptic chart of the DWD can be found in the Appendix A.1 (Fig. A.1).

Figure 6.3 shows the vertical temperature and humidity profiles derived from the radiosonde that are crucial for modeling the described atmospheric state. The temperature profile shows a nearly linear decrease with height, with a temperature gradient of $\gamma = 0.0069\,\mathrm{K\,m^{-1}}$. The near surface temperature recorded by the radiosonde was $T_{\mathrm{surf}} = 277.6\,\mathrm{K}$, which is in agreement with the temperature measured at the site. The melting layer is around 630 m, where the supersaturation is around 0 % and negative below. From the melting layer up to about 4200 m the air is supersaturated. The relative humidity, in relation to water saturation, exceeds $\mathrm{RH} > 90\%$ and can even reach $\mathrm{RH} = 100\%$, providing sufficient water vapor for efficient depositional growth.

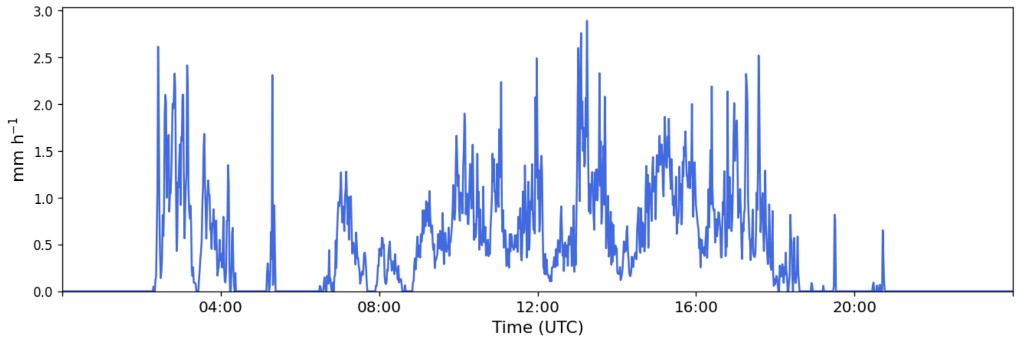

Figure 6.1: Disdrometer data from Jülich on 31. January 2022. This figure was taken from Pfitzenmaier and Löhnert (2023) and redistributed under the *CC-BY 4.0* (2013) license.

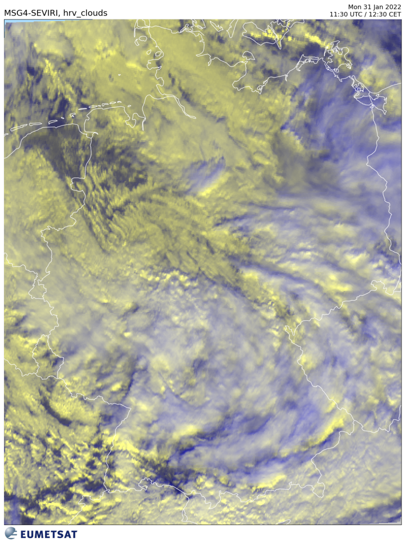

Figure 6.2: Satellite (SEVIRI HRV) imagery captured on 31. January 2022 at 11:30 UTC (EUMETSAT, published under *CC-BY 4.0* 2013).

However, the radiosonde observations alone are insufficient to confirm or deny the presence of supercooled liquid water in regions where the relative humidity reaches $\mathrm{RH} = 100\%$. At this stage of the investigation, optimal utilization of the information provided by polarimetric radar observations can become crucial for further constraining the microphysical and dynamical parameters within the numerical model configuration.

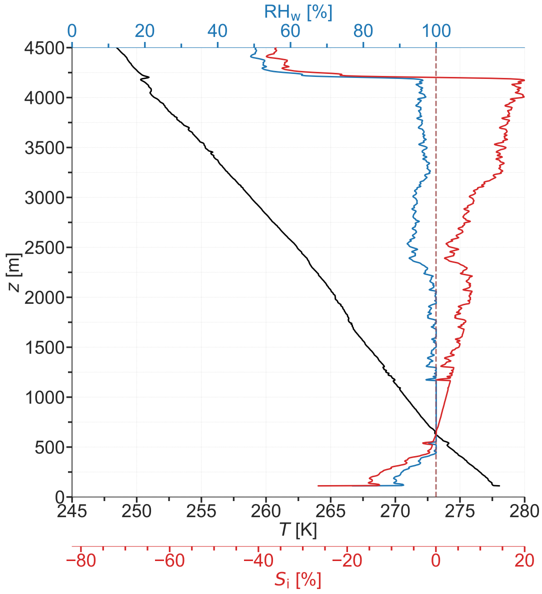

Figure 6.3: Radiosonde profiles (31. January 2022, 11:30 UTC) of temperature T, relative humidity with respect to water RH_w and supersaturation over ice S_i. The dashed line marks the freezing temperature as well as supersaturation of $S_i = 0\,\%$.

6.1.2 *Radar Observations*

The polarimetric radar observations collected during the campaign allow us to search for IMP fingerprints that might help us in obtaining a more comprehensive understanding of the in-cloud microphysical situation.

The in-cloud conditions expressed by the five radar variables can be seen in a time-height diagram in Figure 6.4: (a) equivalent radar reflectivity factor (Z_e), (b) mean Doppler velocity (MDV), (c) dual-wavelength ratio for the Ka-W-bands (DWR_{KaW}), (d) maximum spectral differential reflectivity ($sZ_{\mathbf{DR,max}}$), and (e) specific differential phase (K_{DP}). The results shown have undergone attenuation correction, negative MDV refer to particles falling towards the surface.

The highest reflectivity Z_e (Fig. 6.4 a) during the day can be found beneath the melting layer, owing to the existence of large raindrops formed by coalescence. Higher reflectivity values above the melting layer are related to the presence of large particles due to aggregation or riming, to the presence of high concentrations of ice particles, or to a combination of the two effects.

Over the course of the day, the MDV (Fig. 6.4 b) varies between 0 to $-1.5\,\mathrm{m\,s^{-1}}$, suggesting the prevalence of predominantly unrimed or lightly rimed crystals. Between 06:00 and 13:00 UTC, there is evidence for the presence of an updraft at a height of about $1.5-2$ km, indicated by a relatively large Z_e, while the MDV is quite low (Fig. 6.4 a & b). For higher cloud tops, observing high Z_e and DWR_{KaW} signals indicate that aggregation occurs throughout the day (Fig. 6.4 a & c).

We posit that in the later periods of the day when DWR values are already substantial at the top of the cloud, liquid water's presence results in amplified attenuation in the W-band in contrast to the Ka-band radar. Through the combination of DWR and MDV observations, there is strong evidence of a riming event occurring around 14:00 UTC, characterized by significantly increased MDV.

The presence of particles with small aspect ratios (for plate-like particles) and large apparent densities can be identified by high values of sZ_{DR} as seen in Figure 6.4 d. Therefore, if $sZ_{\mathbf{DR,max}}$ is increased, it indicates the presence of asymmetric or fairly solid ice crystals. As the cloud top temperature drops below $T < 253$ K (between 07:00 and 11:00 UTC), $sZ_{\mathbf{DR,max}}$ shows enhanced values even at temperatures colder than $T < 263$ K, indicating significant dendritic particle growth. The sustained enhancement of $sZ_{\mathbf{DR,max}}$ down to the melting layer in most cases suggests a continuous presence of pristine plate-like ice crystals throughout the observation period. During the day, especially after 12:00 UTC, a distinct layer of increased $sZ_{\mathbf{DR,max}}$ is observed starting at temperatures around $T = 265$ K.

High values of K_{DP} can reflect an increase in particle concentration as well as size, especially for asymmetric ice particles (Fig 6.4 e), while there is an ongoing debate about the specific types of ice particles responsible for an enhanced K_{DP}. Although it has been argued that only pristine ice crystals contribute to K_{DP}, simulations using DDA indicate that aggregates also produce K_{DP}, albeit to a significantly lesser extent than dendrites (von Terzi et al., 2022, Fig. C1 within).

Throughout the day, distinct "pockets" of enhanced K_{DP} are observed, indicating localized regions with higher concentrations of ice particles. These pockets are predominantly found at temperatures above $T > -10°\mathrm{C}$, particularly in the latter half of the day, when they coincide with regions of enhanced $sZ_{\mathbf{DR,max}}$. One possible explanation for the observed enhancements in both K_{DP} and $sZ_{\mathbf{DR,max}}$ is a SIP. In the

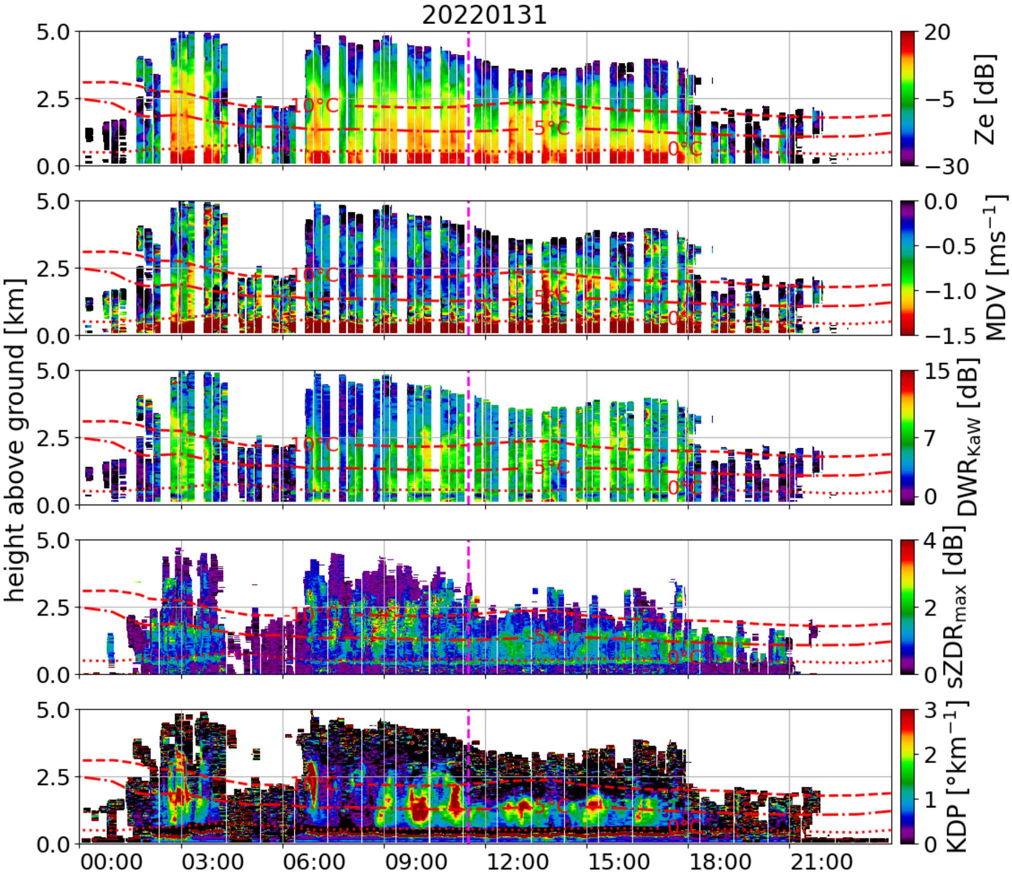

Figure 6.4: Dendrite event on 31. Jan 2022 at JOYCE-CF. The time-height plots show the (a) Ze, (b) MDV, (c) $\mathrm{DWR_{KaW}}$, (d) $\mathrm{sZ_{DR,max}}$, and (e) $\mathrm{K_{DP}}$. The red lines depict isotherms while the magenta lines mark the launch of radiosondes. Figure used with courtesy of L. von Terzi.

observed regions, dendritic particles may collide with other hydrometeors, resulting in the ejection of small fragments (fragmentation/ice-ice collision). An alternative hypothesis is based on the increase in MDV near the melting layer, which indicates possible riming. This scenario could be associated with ongoing rime splintering, as proposed by Hallett and Mossop (1974).

The above mentioned radiosonde, launched at about 11:30 UTC, sampled the atmosphere near the time when elevated $\mathrm{sZ_{DR,max}}$ and $\mathrm{K_{DP}}$ were observed (magenta line in Fig. 6.4). Therefore, we apply temporal averaging to the observed radar variables around this time to further analyze the atmospheric state.

The radar profiles from the 30-minute interval surrounding the radiosonde launch (Fig. 6.5) are instrumental in identifying the cloud process fingerprints and serve as a benchmark for our simulations. The MDV profile (red line in Fig. 6.5 a) shows that the mean fall velocity of the particles is slower than $v_t < -1.5\,\mathrm{m\,s^{-1}}$, again indicating unrimed or lightly rimed snow. A slowdown in MDV between $T = -15$ and $T = -10°\mathrm{C}$ can be observed, which is consistent with the statistics of von Terzi et al. (2022). von Terzi et al. (2022) hypothesize that this effect could be related to the existence of an updraft caused by latent heat release due to strong dendritic growth. Except for the slowdown, the MDV increases in principle continuously as it approaches the surface. The radar reflectivity factor Z_e (black line in Fig. 6.5 b) increases steadily from the top of the cloud downward, presumably due to an increase in size or particle concentration. The strong increase in reflectivity between $T = -15$ and $T = -10°C$ could be caused by an increase in number concentration (due to a possible updraft caused by latent heat release) as well as an increase due to size changes resulting in an increasing DWR (Fig. 6.5 b).

It can be seen that the initial enhancement occurs even at colder temperatures ($T < -12°C$) where the DWR does not show significant changes, so the increase in number concentration may be dominant here. The DWR of both the Ka-W bands (red) and the X-Ka bands (black line) show significant increases starting at $T \geqslant -12°C$, indicating the onset of aggregation due to depositional growth of sufficiently large dendritic particles. Z_{DR} (Fig. 6.5 c) also shows a peak at $T = -12°C$, indicating the presence of growing dendrites in this region. The decrease in Z_{DR} between $T = -12°C$ and $T = -5°C$ may be related to the decrease in total particle number caused by ongoing aggregation. Interestingly, both the DWR of the Ka-W- and the X-Ka-band show similar increasing trends for $T > -5°C$, suggesting the possibility of light riming due to the presence of liquid water. Both variables could be dominated by SIP around this temperature, resulting in higher particle concentrations that could potentially explain the observed increase. It should be noted that the DWRs can become negative for colder temperatures. This is an artifact of the attenuation correction, where the time intervals chosen have to be relatively long to ensure a sufficient number of measured points. Additionally, the attenuation correction method is susceptible to the presence of supercooled liquid layers. In the event that either of the two aforementioned effects is present, it is possible that the correction may overestimate the true attenuation, resulting in negative DWR values. Readers interested in further details on the attenuation correction method are directed to von Terzi et al. (2022).

Utilizing the spectral information provided by sZ_{DR}, one only sees a notable increase for slow and therefore small particles around $T = –4°C$ (Fig. 6.5 d). For faster particles, one can observe a high variability in the sZ_{DR} signal for $T > –5°C$. The peak of Z_{DR} and $sZ_{\mathbf{DR,max}}$ at $T = –4°C$ also coincides with a maximum of K_{DP} (Fig. 6.5 e), supporting the theory of increased particle concentration. For temperatures colder than $T \leqslant -10°C$, K_{DP} is noisy and shows narrow peaks that are difficult to interpret. The strength of sZ_e (Fig. 6.5 f) is quite low for the whole profile, reaching a maximum just above 0 dB. However, the steady increase towards the bottom indicates that the particle spectrum is shifting towards more reflective particles, whether large monomers or aggregates that may eventually be rimed. The increase in turbulence broadens the sZ_e spectrum towards the melting layer, while the diversification of particle properties may exaggerate this observation.

Based on the time-averaged vertical profiles, it is possible to identify the following relations between observations and IMP fingerprints (see Tab. 6.2). These relations are then tested in an appropriate model configuration in order to gain a deeper understanding of them.

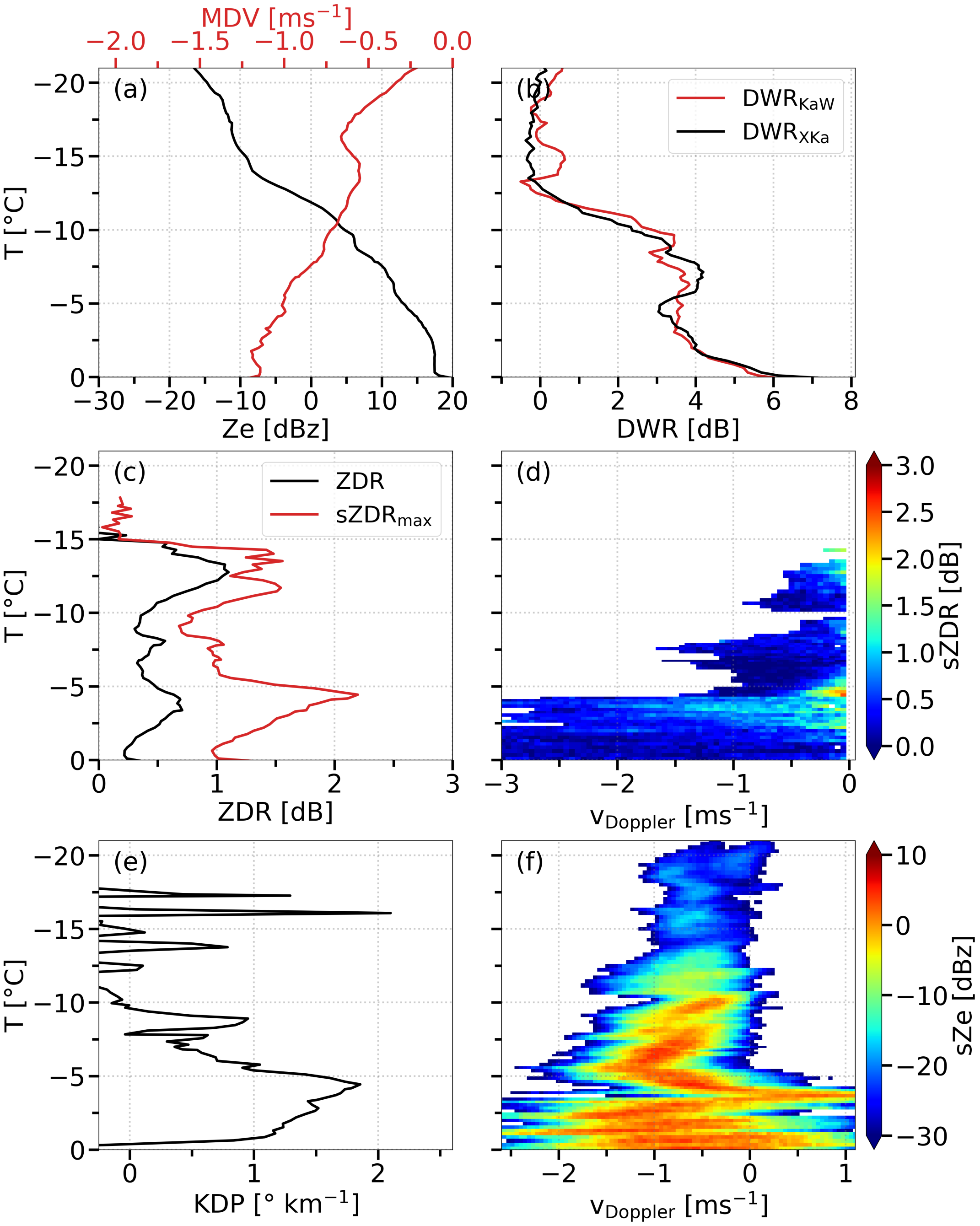

Figure 6.5: Radar profiles of the dendrite event on 31. Jan 2022 at 11:30 UTC. Vertical profiles of (a) Z_e and MDV, (b) DWR, (c) Z_{DR}, and (e) K_{DP}. Spectrograms are shown for (d) sZ_{DR} and $sZ_{\mathbf{DR,max}}$, (f) and sZ_e. The profiles are averaged over a 30-minute period around the radiosonde launch, while the spectrograms have been selected to correspond with the launch time. Figure used with courtesy of L. von Terzi.

Table 6.2: Radar observations and the ice microphysical process associated with them.

Observation	**ice microphysical process**
1. increasing Z_e and MDV profile towards the melting layer with a distinct slowdown in MDV around $T = -15°C$	depositional growth and onset of branching
2. increase in DWR	onset of aggregation in the DGL
3. local maxima of Z_{DR}, sZ_{DR}, and K_{DP}	increase in particle concentration
4. spectral broadening of sZ_{DR} and sZ_e	increased turbulence

6.2 NUMERICAL EXPERIMENT

Most of the in-cloud conditions are unknown, but we attempt to constrain the simulation setup to physically appropriate conditions based on the above observations. This can be seen as a proof of concept: the combination of the IMP polarimetric fingerprints with the process sensitivities found in Chapter 4 and 5 can serve as a tool to gain information about the in-cloud processes and thus rule out certain scenarios. In the next segment, the set of assumptions for the construction of the model setup for the dendritic case study will be shown.

6.2.1 *Model Configuration*

The vertical structure of the atmosphere can be prescribed by the radiosonde, but we can only estimate the nucleation conditions. While empirical formulations about the relation between reflectivity and IWC exist, it is difficult to retrieve information about the PSD from the observations without the knowledge of particle properties. This information can be critical since the shape of the PSD is defining for the initial ice crystal size and shape and in turn the terminal velocity and initial habit development (cf. Sheridan et al., 2009, regarding relative habit growth). Crystals larger than a certain size thresholds cannot be assumed to be spherical anymore and certain habits might lead to a reduced apparent density like columnar particles that start to hollow. Since we want the shape or apparent density to evolve as freely as possible, *McSnow* samples the crystal mass from a PSD with a mean crystal diameter of $D_{\text{init}} = 10\,\mu\text{m}$ and $\nu_{\text{Gamma}} = \mu_{\text{Gamma}} = 1$ and assume that almost all particles are still relatively close to sphericity ($\phi_{\text{init}} = 1$) and ice density ($\rho_{\text{app,init}} = \rho_i$). As we do not know where particles initially are originated, we choose to nucleate particles at a constant rate of $24\,\text{L}^{-1}\text{s}^{-1}$ in the region of supersaturation between $z_{\text{nucl},1} = 1000\,\text{m} \cong 270\,\text{K}$ to $z_{\text{nucl},2} = 4100\,\text{m} \cong 250\,\text{K}$. This rate results in an INP concentration of about $4\,\text{l}^{-1}$. The initial multiplicity is $\xi = 800$ real particles per super-particle.
The relative humidity of close to $\text{RH} = 100\,\%$ in the height range between $z_{r,1} = 500\,\text{m}$ and $z_{r,2} \approx 2000\,\text{m}$ (Fig. 6.3) indicates the presence of a LWZ and the increase in MDV around $T \approx 265\,\text{K} = -8°C$, as seen in Figure 6.5, supports the argument that particles are subject to riming. Due to the moderate increase in MDV, we expect only low to

moderate values of liquid water content in the order of LWC $< 0.5\,\mathrm{g m^{-3}}$. We tested different values to match the increase in mean Doppler velocity in a comparable way and found a value of LWC $= 0.3\,\mathrm{g m^{-3}}$ to be physically sensible. As in Chapter 5, droplets are drawn from an exponential drop size distribution with a mean cloud droplet radius of $r_d = 10\,\mu\mathrm{m}$.
The choice of microphysical parameterizations can strongly influence the mass and number fluxes as Chapter 5 has shown before. In light of the considerable uncertainty surrounding the nucleation rates, we have selected the configuration that demonstrated the most promising performance when benchmarked against the polarizability ratios (PRs) of observational and laboratory data, as detailed in Chapter 5:

- to be independent of grid resolution, the atmospheric state is interpolated to the particle positions;
- the theory of Böhm for terminal velocity and collision efficiency is applied, including the interpolation of terminal velocity for prolates;
- as discussed in Sec. 5, we use the HP scheme for monomers only and treat aggregates with an empirical m-D relation;
- the updated IGF with modifications to the branching criterion is applied;
- the ventilation coefficient is calculated using the AR-dependent formulation;
- the riming process is modeled with the stochastic riming scheme;
- aggregation and riming events use the A-kernel.

Given the assumption of LWC and the significance of accurately representing the aggregation process, it is also necessary to

- test whether the rime splintering assumed by the increase in K_{DP} found in the vertical radar profile is in effect;
- investigate the dependence of the results on the sticking efficiency using the descriptions of Mitchell (1988, configuration name **S1**) and of Karrer et al. (2021, configuration name **S2**).

During the experimental phase of identifying an optimal configuration, the extent of aggregation was found to be underestimated. Böhm (1992c) suggests that irregularities in geometry exert an influence on both monomers and aggregates, within the confines of statistical limitations. In order to emulate this phenomenon, a variance is applied to the terminal velocities of each hydrometeor involved in a collision event. In this study, in particular, aggregates that follow the static geometric formulation are underrepresented in their geometric variability, given the numerous possibilities for mass distribution. While Böhm (1992c) estimates the standard deviation of a log-normal distribution, we similarly perturb the terminal velocity of each hydrometeor, ν_i, only for the collision kernel (Eq. 2.52) by an artificial turbulence modifier (σ_{kern})

$$\nu_{*,i} = \nu_i + \left((R - 0.5)\, \sigma_{\mathrm{kern}} \right) , \tag{6.1}$$

where $0 \leqslant R < 1$ is a randomly drawn number. If not stated otherwise, $\sigma_{\mathrm{kern}} = 0.25$. Similar ideas have been used in (experimental) NWP microphysics schemes to account for the under-representation of particle variability (Böhm, 1990; Seifert and Beheng, 2006).

6.2.2 *Model Results and Synthetic Observations*

The initial step is to ascertain the correlation between the average precipitation rate generated by the model and the actual rainfall intensity as measured by the disdrometer (Fig. 6.1). This step serves to validate the assumptions made regarding the configuration while simultaneously confirming that the model is in a quasi-steady state, suitable for averaging (with the exception of stochastic variance). After 2 hours, the simulation reached a quasi-steady state at a precipitation rate of $RR = 0.3\,\mathrm{mmh}^{-1}$. Although the precipitation rate may be slightly lower than the minimum rate observed, it is possible to obtain reasonable results within the scope of the simplifications.
A more detailed understanding of the model's performance can be gained by comparing the vertical profiles of the radar and the model (synthetic signal from forward modeling with *McRadar* to ascertain whether the precipitation originates from hydrometeors that are developing similarly within the clouds.

Configuration S1

We begin with the aforementioned configuration S1, utilising the previously described setup with the sticking efficiency as outlined in the work of Mitchell (1988) and with the rime splintering parameterisation disabled. Figure 6.6 shows the comparison of the radar (solid) and forward simulated observations (dashed lines) of (a) Z_e and MDV, (b) DWR, (c) Z_{DR}, and (d) K_{DP}. The radar observations(Fig. 6.6 a, black solid line) indicate a gradual increase in reflectivity at the cloud top, beginning at $T = -20°C$. In the temperature range of $T \leqslant -15°C$, the signal of the modeled hydrometeors (black dashed line) increases steadily due to the constant nucleation and sedimentation of particles from the layers above, which is paired with the onset of depositional growth. The discrepancy in initial growth may be attributed to the assumption of constant water vapor in the model, which underscores the challenge of accurately representing the initial state of the particle size and shape distribution. In natural conditions, the prevalence of small ice crystals competes with the water vapor, resulting in its eventual depletion over time. A potential side effect may be attributed to the phenomenon of radiosonde drift. This could have resulted in the radiosonde drifting with the cloud while sampling air close to $RH = 100\,\%$. However, the 30-minute averaged radar profiles may also sample less humid air. In order to counteract the depletion theory as well as the radiosonde drift, the observation time span is limited to a period where the cloud observations remain relatively stable.
Lastly, the number of super-particles in the vicinity of the cloud top can subceed 100 particles per cell which can impact the statistical interpretation of the assumed stochasticity.
In the region between $-15°C \leqslant T \leqslant -10°C$, the expected substantial increase in Z_e due to the onset of aggregation observed in the radar data may be less pronounced than anticipated. In the vicinity of the LWZ, and in the immediate vicinity of the melting layer, the reflectivities both reach approximately $Z_e \approx 20\,\mathrm{dB}$.
The MDV profiles (Fig. 6.6 a, red lines) are quantitatively similar and the qualitative

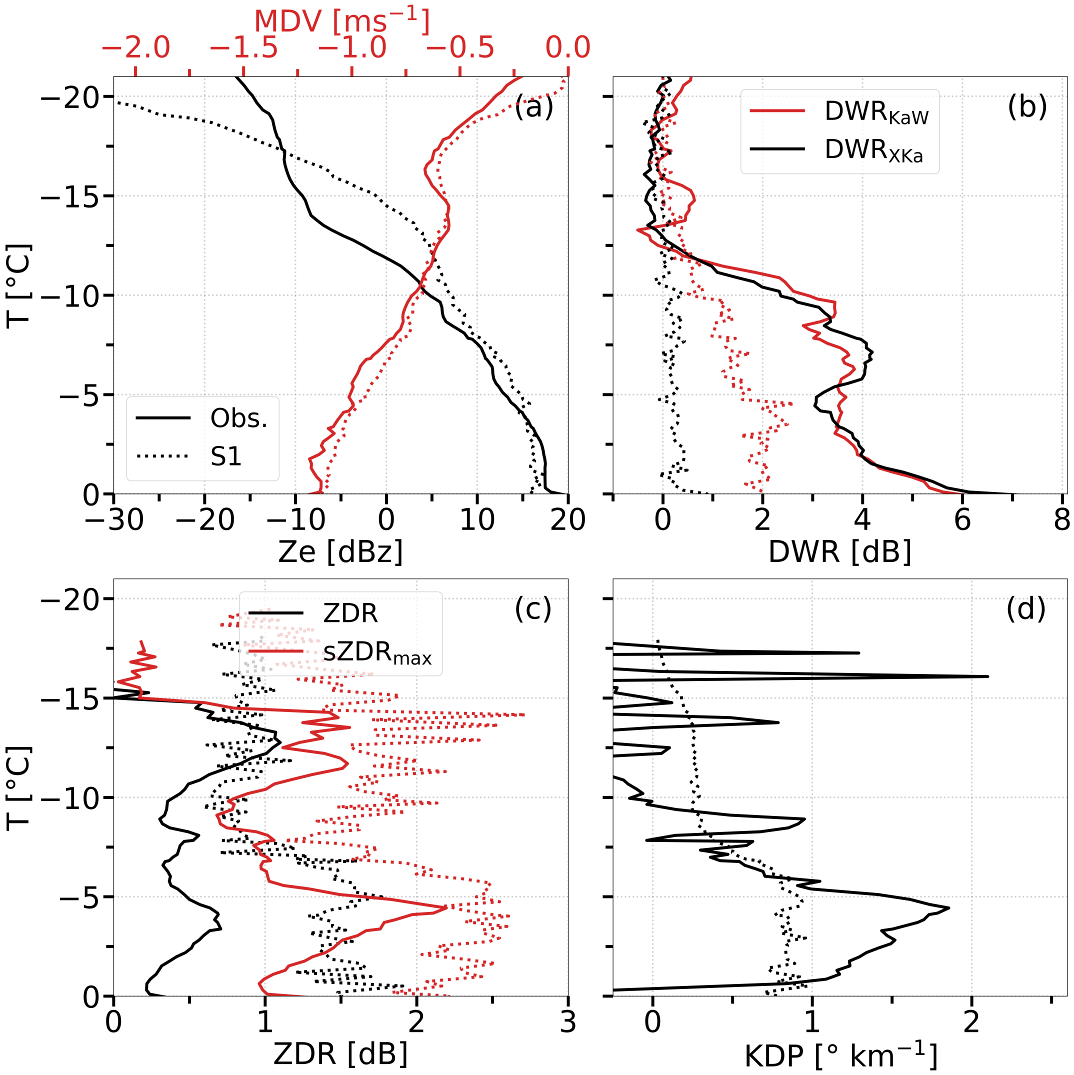

Figure 6.6: Comparison between radar (obs., solid lines) and synthetic profiles (S1, dashed lines) of the configuration S1 for the dendrite event. Vertical profiles of (a) Z_e and MDV, (b) DWR, (c) Z_{DR} and $sZ_{\mathbf{DR,max}}$, and (d) K_{DP}.

behavior is almost identical to the observed ones. In particular, the capture of the slowdown when the DGL is approached is captured remarkably given the basic assumptions made. In light of the fact that *McSnow* does not permit the formation of an updraft as a consequence of latent heat release, as theorized by von Terzi et al. (2022), it can be inferred that the deceleration is a result of the emergence of branching, which rapidly enlarges the cross-sectional area and consequently increases the aerodynamic drag. In the temperature range of $-10°C \leqslant T \leqslant 0°C$, the rise in MDV with a moderate increase in Z_e aligns with observations, lending support to the hypothesis that the elevated relative humidity in combination with the observed MDVs can be regarded as an indicator of riming resulting from a LWZ. In general, the MDV profile is well matched with regard to the absence of dynamic processes, including up- and downdrafts, as well as turbulence.

The representation of aggregates is investigated through an analysis of the DWR profiles illustrated in Figure 6.6 b. The initial onset of aggregation within the DGL is evident from the increase in DWRs in both the radar and synthetic observations.

Both observed and simulated $\mathrm{DWR}_{\mathrm{KaW}}$ (red lines) exhibit a slight increase as they enter the DGL, indicating the deposition process may be responsible for the onset of aggregation. The synthetic profile shows a slightly different behavior than the observed one: medium sized aggregates driving $\mathrm{DWR}_{\mathrm{XKa}}$ (black lines) are either strongly underrepresented or do not contribute strongly enough to the synthetic signal to match the observed one. The profile of $\mathrm{DWR}_{\mathrm{KaW}}$ is stronger, but still shows a significant underestimation of the observed signal by up to 2 to 4 dB. Given that both signals exhibit an underestimation, two potential explanations may be considered. Firstly, the setup may not be producing aggregates of sufficient magnitude to drive the signal. Secondly, it may be necessary to consider the modeled aggregate shapes, as this could affect their influence on the DWR. While the latter requires substantial advancement of the forward model, the quantity and magnitude of aggregates could be augmented by parameterizing the adhesion efficiency with the parameterization of Karrer et al. (2021) (cf. Sec. 2.4), which provides greater probabilities for adhesion within the observed temperature range. Prior to undertaking an analysis of the second configuration, which incorporates an adhesion efficiency parameterization, it is first appropriate to complete a comparison of configuration S1 in relation to Z_{DR}, K_{DP}, and the spectrograms.

A more detailed examination of Z_{DR}, $sZ_{\mathbf{DR,max}}$, and K_{DP} allows for a more rigorous evaluation of the model's capacity to predict the evolving monomer characteristics. With regard to Z_{DR}, the synthetic signal is noisy and reaches magnitudes comparable to, or in the lower section even higher than, those of the observed profile. The overall resemblance of $sZ_{\mathbf{DR,max}}$ is qualitatively very well met, but quantitatively, an over-assessment of the synthetic signal is present. For Z_{DR}, $sZ_{\mathbf{DR,max}}$, and K_{DP} it should be noted that the forward simulations assume a perfectly horizontal alignment of the particles, similar to the fall velocity parameterization. This caveat may be partly responsible for *McRadar* producing Z_{DR} signals that are too high.

For the observed cold peak around $T = -13°\mathrm{C}$, the signal from dendrites developing in the simulated setup is sufficient to produce a signal that is similar to the observations. Around the warm peak at $T = -4°\mathrm{C}$, the synthetic signal grows to substantially overestimate Z_{DR} compared to the observation. Paired with the large $sZ_{\mathbf{DR,max}}$, this is an indication that the strongly pronounced monomer habits are dominating the signal over the aggregates. It may be due to insufficient removal of large dendritic crystals by aggregation that the signal is stronger than the observations suggest. The effects of the different particles categorized by Doppler bins will be investigated in a later part of this section, where the spectrograms of sZ_{DR} are analyzed.

Finally, the simulated particles are compared to the observed profile of K_{DP} as seen in Figure 6.6 d. While for colder temperatures an average non-zero signal is produced by the signal, caused by the underlying concentration of ice particles, the observational signal is noisy and therefore difficult to interpret. For temperatures above $T > -7°\mathrm{C} K_{\mathrm{DP}}$, the concentration of K_{DP} rises above $0.5°\ \mathrm{km}^{-1}$. However, the simulation is unable to reproduce the signal of the natural hydrometeors due to an underestimation of ice crystal concentration or the number of aggregates. In light of our assumption of a perfect horizontal orientation of the ice crystals, which amplifies the signal produced by the forward model, further investigation into the potential for more accurate reproduction of the distinctive K_{DP} could be undertaken in the future.

The comparison of the mean vertical profiles is encouraging, given the simplifications

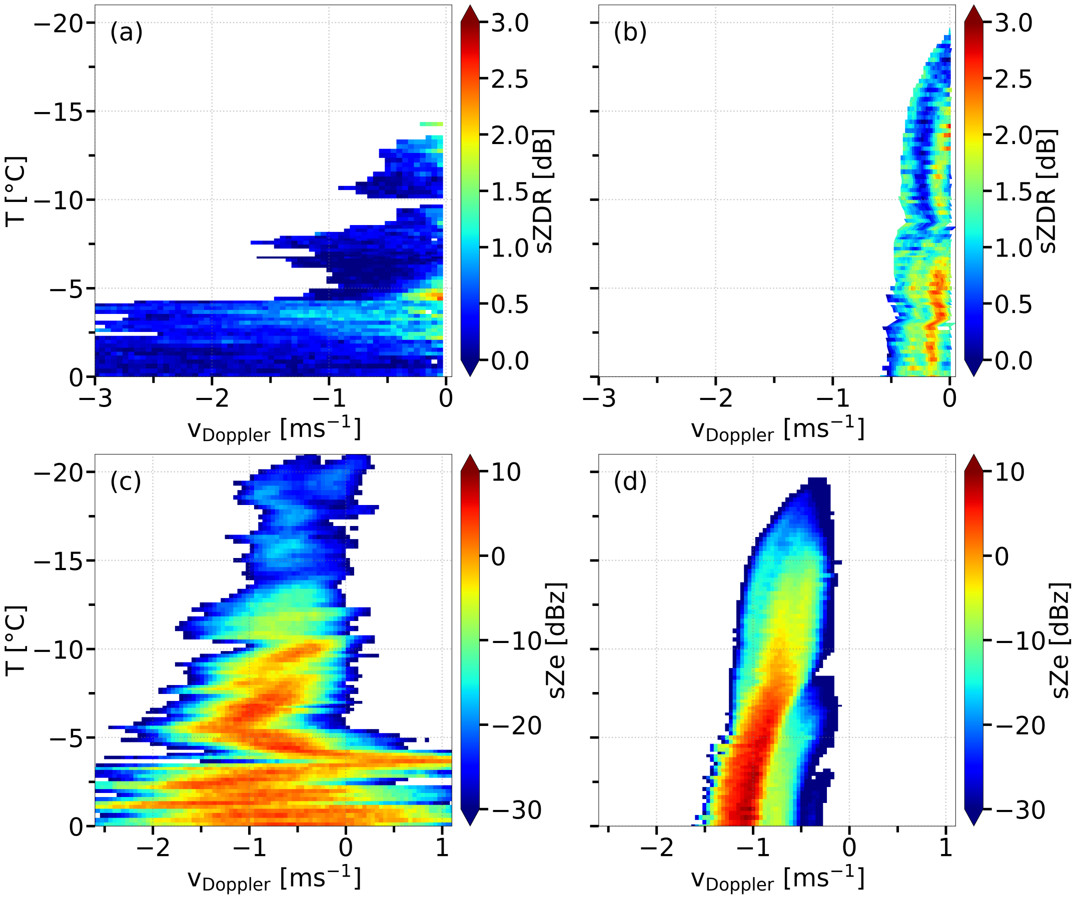

Figure 6.7: Comparison between radar and synthetic spectrograms of (a) observed and (b) simulated sZ_{DR}, as well as (c) observed and (d) simulated sZ_{e} of configuration S1 for the dendrite event.

made in the parameterizations of both *McSnow* and *McRadar* and in the assumptions made for the setup. However, the time averaging affects the comparison by smoothing out signals while at the same time compensating for radiosonde drift.

Furthermore, an additional analysis will be conducted on the spectrograms of sZ_{DR} and sZ_{e}, which are based on the radar scan that occurred in close temporal proximity to the launch of the radiosonde. The aforementioned spectrograms facilitate a more comprehensive understanding of the model's capacity to simulate the ad hoc state and the statistical variance. Figure 6.7 depicts the observed (left column, (a) and (c)) and simulated (right column, (b) and (d)) spectrograms in side-by-side comparison. A fundamental distinction can be observed between the observational and simulation-based spectrograms. The absence of a dynamic atmosphere in the model results in a fairly constant simulated Doppler spectrum with minimal variability in width between different heights. In contrast, the spectrogram of the radar signal exhibits a less uniform profile with height, with only minor particles demonstrating a notable sZ_{DR}, which are aligned with the simulated spectrum.

It is crucial to discuss the role of turbulence at this point in the discussion. Firstly, turbulent air motions are likely to result in the mixing of hydrometeors, which may increase the probability of collision and aggregation. Secondly, the mixing of monomers that could cause a high sZ_{DR} with aggregates with low sZ_{DR} results in the masking of ice crystals due to the inherent size-dependence of sZDR. In essence, turbulent motions serve to broaden the spectrum, thereby spreading the total sZ_{DR} signal over a greater number of Doppler bins. The considerable broadening of the observed spectrum around $T = -5°$ C may be attributed to turbulent motions and wind shear, which exert a notable influence at an elevation of 30°.

At temperatures of approximately $T \geqslant -5°$ C, the observed sZ_{DR} of small, slow-falling particles is significant, while in simulations, larger and faster particles also exhibit a significant signal. It seems probable that these faster particles are plate-like in shape and descend from above. The sZ_{DR} and, consequently, the Z_{DR} profile are, by construction, significantly influenced by the presence of large particles. Large particles may be either aspherical monomers, rimed and therefore relatively spherical particles, or aggregates where the current state of the habit prediction is unable to accurately predict their shape. The observation indicates that these particles are absent at warmer temperatures, which suggests that the model may not aggregate them efficiently enough.

The presence of enhanced turbulence is also signaled in the observed spectrogram of sZ_e where the edges of the spectra fluctuate heavily. In the lower part of the observed spectrogram for temperatures above $T > -5°$ C, updrafts are present, indicated by positive Doppler velocities reaching up to $1\,\mathrm{m\,s^{-1}}$, which cause the lifting of hydrometeors. The absence of updrafts in the simulated atmosphere is clearly evident in the altered spectrogram, which shows a narrow band of higher sZ_e. Despite the more homogeneous signal, the intensification of sZ_e from higher to lower altitudes is generally similar, and the mean value of the v_D-spectrum is approximately the same, although the widths of the ranges differ.

In conclusion, the simulation is capable of reproducing both the mean Z_e signal (as shown in Fig. 6.6 a) and the evolution of variance in Doppler velocity, which is attributable to a combination of different developing monomer habits, rimed particles, and aggregates. In addition to the quantitative discrepancy resulting from the methodology and the static atmosphere, the qualitative characteristics of the spectrograms are comparable. This indicates that the simulated spectrum adequately represents the variability of in-cloud processes.

Configuration S2

While the above synthetic observations underline the potential of *McSnow* to reproduce IMP fingerprints, the shortcomings with respect to DWR will be addressed and emphasize how important the choice of parameterizations is for this potential. We change the sticking efficiency to the description of Karrer et al. (2021) (see Fig. 2.4) and leave the rest of the configuration untouched (configuration name **S2**). On average, this description should increase the probability of aggregation and produce larger aggregates while removing monomers.

Figure 6.8 a shows that there is little effect on the quality of the reflectivity profile, but the MDV increases to values larger than those observed. From the DWR profiles we can see that the increase comes from larger particles that may have been formed by riming or aggregation. The onset of the increase in DWR is well matched for the Ka-W bands, and the maximum strength is comparable. For the simulation, the first aggregates that form begin to collect more particles rapidly due to the increase in size, matching the observed signal of DWR_{XKa} until about $T = -7°$C. Here, they

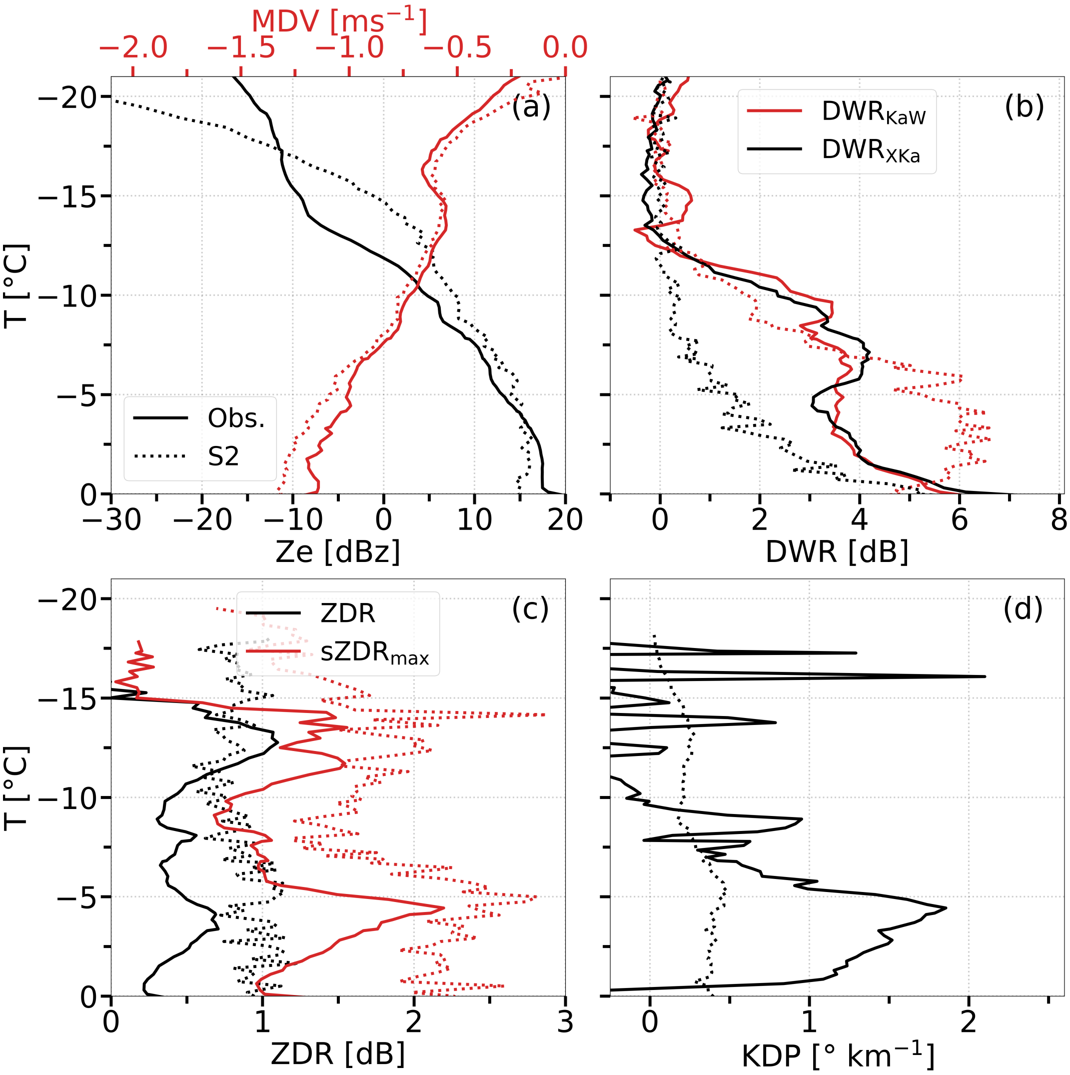

Figure 6.8: Comparison between radar (obs., solid lines) and synthetic profiles (S2, dashed lines) of the configuration S2 for the dendrite event. Vertical profiles of (a) Z_e and MDV, (b) DWR, (c) Z_{DR} and $sZ_{\mathbf{DR,max}}$, and (d) K_{DP}.

reach up to 6 dB due to the collection of particles along their paths.

The decrease in DWR_{KaW} around $T = -5°C$ in the observed signal may indicate that the large aggregates are decreasing in size, possibly due to SIP effects. Alternatively, an increase in small particle concentration could shift the mean mass diameter to smaller particles, also reducingDWR. The DWR_{XKa} configuration exhibits a slower rate of increase, yet it differs from the original configuration in that it produces a meaningful signal that exceeds 5 dB.

Concurrently, it is evident that the enhancement in DWR exerts a beneficial influence on the profiles of Z_{DR} and $sZ_{\mathbf{DR,max}}$. However, although this positive impact is achieved, it is at the cost of a reduction in the degree of agreement observed in K_{DP}, where the maximum for $T > -5°C$ is diminished. The enhanced sticking efficiency effectively removes a greater proportion of the asymmetric monomers that drive Z_{DR} and $sZ_{\mathbf{DR,max}}$, while the reduction in number concentration dampens the signal of K_{DP}. It is important to recall that the assumed horizontal alignment of particles leads to an overestimation, which would improve the agreement of signals for Z_{DR}

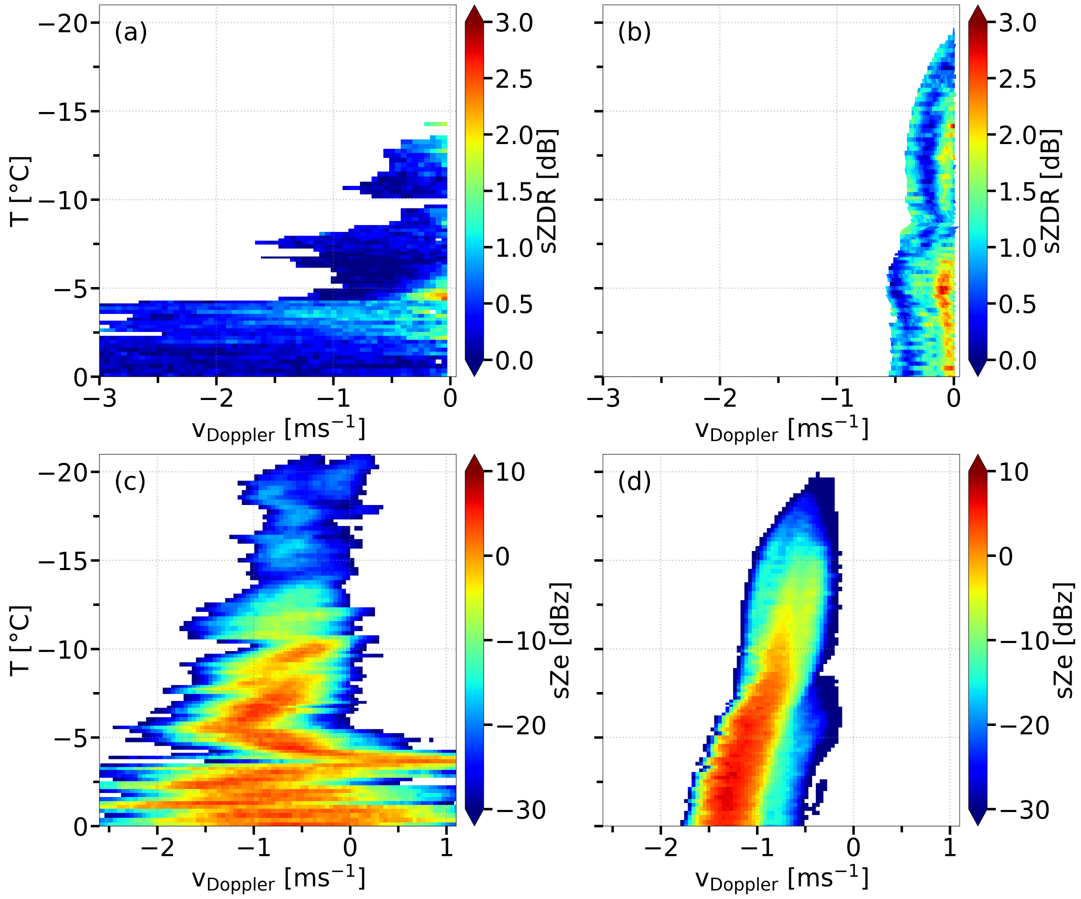

Figure 6.9: Comparison between radar and synthetic spectrograms of (a) observed and (b) simulated sZ_{DR}, as well as (c) observed and (d) simulated sZ_{e} of configuration S2 for the dendrite event.

and $sZ_{\mathbf{DR,max}}$ between observation and model.

For the sake of completeness, Figure 6.9 shows how the change in sticking efficiency reduces the sZ_{DR} for particles on the faster edge of the spectrum collected by aggregation. Both the spectrum of sZ_{DR} and sZ_{e} indicate higher maximum Doppler velocities of the heavier and faster aggregates, which have been inferred by the increased MDV compared to configuration S1. Therefore, the tilt of the spectrum is slightly stronger due to the acceleration caused by the mass increase of the aggregates, stronger riming, and coupled with the resulting rounding of the particles.

6.2.3 *Integrating Ice Microphysical Insights*

The objective of this experiment has been to assess the capacity to represent ice microphysical processes in one-dimensional simulations. The numerical experiments show that the current state of *McSnow* can reproduce IMP fingerprints in a promising way. Based on simple assumptions, a one-dimensional simulation is not only able to reproduce mean polarimetric radar signals, but also allows the development of quantitatively similar spectrograms. We are able to simulate the observed MDV profile including the pronounced slowing in the DGL paired with realistic reflectivities.

A simple estimation of the LWC shows to result in a realistic riming behavior. We can confirm that the increase in DWR signals is caused by the onset of aggregation triggered by strong depositional growth. The agreement in quality between Z_{DR} and $sZ_{\mathbf{DR,max}}$ indicates that *McSnow* treats monomer habits in a sensible manner when run in the habit prediction mode, despite the assumption of perfect horizontal alignment of particles in the forward model, which causes an overestimation of both signals. Improvements in both the habit geometry of the aggregates and further refinement of the assumptions of the forward model could improve the simulated radar signals to help better understand the sensitivities and processes driving these measures.

However, there are difficulties with a more sensitive variable such as K_{DP}, where it has been difficult to identify distinct maxima. This may indicate that a process causing increased number concentrations is not active when simulating the case. While the presence of a LWZ is necessary to correctly capture the increase in fall velocity, the relatively weak riming, along with the implemented description of the Hallett-Mossop process (cf. Sec. 2.2.7), does not effectively cause rime splintering.

It has been suggested that incorporating feedback between (ice) microphysical and thermodynamic processes has the potential to provide further insight into in-cloud processes. Therefore, future studies could either include a dynamic coupling of ice microphysics and atmosphere in one-dimensional simulations or increase the complexity by performing two- or three-dimensional simulations.

7

FRAGMENTATION DUE TO ICE-ICE COLLISION

The scientific community extensively debates the significance of different SIPs to explain the discrepancies between the number of INP and IPNC (e. g. Field et al., 2017; Korolev et al., 2020, and others). While primary ice nucleation is expected to decrease at elevated temperatures, secondary ice processes emerge as a plausible rationale for an increased ice particle number density. Empirical laboratory studies of Takahashi et al. (1995), Griggs and Choularton (1986), and Vardiman (1974) strongly suggest that collisional fragmentation of ice is a viable mechanism for the generation of new particles.

In addition, the existence of an updraft within the DGL favourable to maximum depositional growth may imply a significant positive feedback loop between ice microphysics and dynamics, potentially amplifying ice particle growth. von Terzi et al. (2022) find a concurrent increase in aggregation and particle number density within the DGL and formulate the need for a mechanism to generate new ice crystals. Inside the DGL, the significant difference between the saturation vapor pressure of water and that of ice (Fig. 7.1, grey shading) causes effective growth of plate-like particles which eventually begin to branch and develop fragile structures (cf. Sec. 4.2). The newly formed structures may undergo further mechanical interlocking, which is thought to be the primary mechanism for aggregation within the above temperature range. Both these newly formed delicate structures and aggregates (which comprise of branched structures) have an increased potential to fracture when colliding with solid hydrometeors.

The objective of this chapter is to elaborate on the potential for ice-ice collisions, particularly for fragile particles, in order to address the discrepancies between the number of INP and IPNC observed in previous studies. We thus commence by employing the fragmentation model of Phillips et al. (2017a), as introduced in Section 2.2.7.2, which we will henceforth refer to as the *Phillips fragmentation scheme* (PFS). In this section, we will focus on the key variables determining how particles are fragmented in collisional events. To categorize the collision type, the PFS employs the

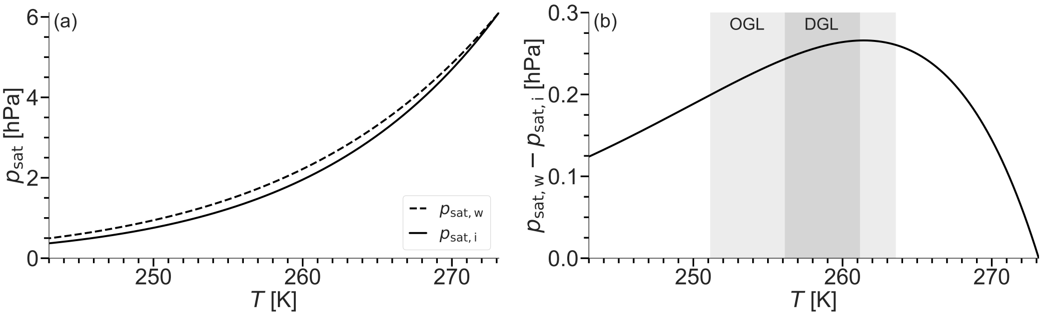

Figure 7.1: (a) Saturation vapor pressure of water and ice, based on the Magnus equation. (b) The difference in saturation vapor pressure is shown on the right. The shaded regions mark the oblate growth layer (OGL) and the dendritic growth layer (DGL).

degree of riming and ambient temperature. The particles that fragment are classified as either graupel, dendritic (with high potential for fragmentation), or non-dendritic (with low potential for fragmentation). The validity of the concept of temperature as a proxy for the collision type as well as the assumption that the smaller particle is always the one that breaks will be examined in more detail from here on. The temperature argument is only applicable if the particles involved in a collision are situated in proximity to regions where specific atmospheric conditions are more favorable for the development of certain properties like shape or density. This is because particles originating from other atmospheric regions may exhibit distinctive individual characteristics.

For example, one could hypothesize that non-dendritic particles could be transported into the DGL, which would result in a re-categorization based on ambient temperature. This, in turn, would increase the expected fragility of the particle as well as the likelihood that these particles will eject numerous fragments. Conversely, dendritic crystals that are outside of their typical growth regime would likely lose the potential to fracture into numerous fragments. However, this assumption is subject to an obvious caveat. Moreover, we anticipate that fragmentation will be particularly effective for particles that form under diverse conditions, resulting in significant differences in terminal fall velocity and consequently in the CKE.

In their analysis, Phillips et al. (2017a) propose that the smaller of the two particles may undergo a breakage event. However, it is plausible that fluffy aggregates and extended dendrites may attain considerable proportions at low aparent densities, thereby exposing their delicate structures to the potential for impact-induced breakage. Conversely, graupel and hail particles can be relatively heavy in relation to their maximum dimension and offer fewer breakable asperities.

This chapter begins with the presentation of an updated framework, which is based on the physical principles proposed by Phillips et al. (2017a) and is informed by a new and different set of data on the material properties of ice. However, rather than relying on the assumptions previously discussed, the updated framework gives priority to the unique properties of individual particles based on their growth history. The resulting generalized framework is based on assumptions about physical concepts that can serve as a source of inspiration and guidance for new laboratory experiments, while also allowing for the integration of new knowledge.

The chapter expands upon previous research by proposing a comprehensive fragmentation scheme based on individual particle habit. To assess the efficacy of the proposed schemes, we will utilize the configurations presented in Chapter 5 as a case study for potential SIP. Subsequently, we elaborate further on the scheme's potential to produce an increased IPNC in a more complex setup, which has been presented in Chapter 6.

The chapter concludes with a list of key questions regarding particle characteristics that future research could address to enhance comprehension of the ice-ice collision process. While the authors acknowledge that the level of detail required to utilize the formulation explicitly based on particle properties is limited to models with a high degree of microphysical complexity, it could nevertheless serve as a foundation for understanding and modeling fragmentation.

7.1 UPDATED FRAMEWORK BASED ON FRAGILITY

In order to utilize the comprehensive information offered by a LPM, our objective is to substitute the three types of collisions with customized alternatives and incorporate individual particle characteristics, such as their apparent density ρ_{app}, which can establish the crystal fragility ($\mathcal{F}$)

$$\mathcal{F} = 1 - \frac{\rho_{\mathrm{app}}}{\rho_{\mathrm{i}}} \; . \tag{7.1}$$

In order to test the hypothesis, we have gathered datasets that are readily accessible. Figure 7.2 compares the derived CKE to produce a fragment of Griggs and Choularton (1986, vertical lines, G&C86) with the datasets of Takahashi et al. (1995, black hexagons, T95), Gautam (2022, gray squares, Ga22), Vardiman (1974, blue lines, V74), and Grzegorczyk et al. (2023) and Grzegorczyk (2022, G22).

Grzegorczyk (2022) provides a dataset for graupel-graupel collisions (circles) and for graupel-snowflake collisions (triangles). The dendritic structures, which grew in an aquarium-like growth chamber, were used to manually assemble snowflakes. The resulting snowflakes were separated into two categories based on the type of collision they underwent: central (yellow) and edge (dark blue). In the case of the graupel-graupel collisions, dendritic extensions were grown under constant temperature and water saturation conditions on an ice sphere with a diameter of a few millimeters. Three impact velocities were subjected to testing, each distinguished by a distinct color.

In order to determine the number of fragments ejected by dropping naturally grown aggregates onto a mesh, Vardiman (1974) conducted an experiment in which the aggregates were categorized as unrimed, lightly rimed, and heavily rimed. Gautam (2022) replicates this experiment with a comparable configuration, modifying the mesh to include stationary frozen droplets at the intersections to facilitate more natural collisions. The fragment numbers obtained are consistent with those presented by Vardiman (1974), and both datasets are expected to be reasonably accurate, given that naturally occurring crystals were used. It should be noted that fragments below a certain size may not have been included in their analysis due to the low resolution of the cameras. Furthermore, the estimation by Gautam (2022) may underestimate the error since the cutoff at 200 µm only captures 63 % of the fragments discovered by Grzegorczyk (2022) for graupel-snowflake collisions.

The combined datasets illustrate a typical range for the CKE, with the exception of the experiment conducted by Takahashi et al. (1995). The elevated CKE values observed in the experiments are anomalous for natural collisions, given the substantial mass of the ice spheres with centimeter-sized diameters. The fragments originated from structures formed on the surface of another sphere, exhibiting a growth mechanism that deviates from the typical branching pattern. Information regarding the breakage velocity, aspect ratio, maximum dimension, and presumed temperature range for various monomer types can be found in Griggs and Choularton (1986). In combination with empirical D-ρ relations from Pruppacher and Klett (1997) for given temperature regimes, this allows for the estimation of the CKE required to produce a single fragment.

A comparison of the fragmentation energies of different monomers, as illustrated in Figure 7.2, indicates that dendrites require approximately one order of magnitude

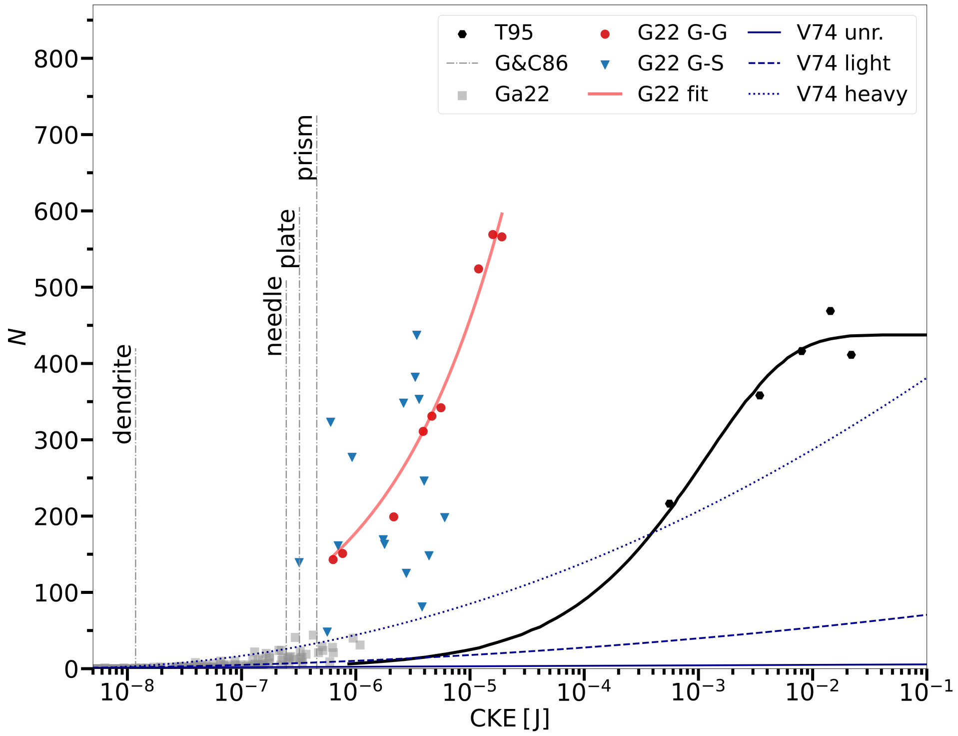

Figure 7.2: Number of fragments N produced relative to the CKE for different observational datasets.

less energy to fragment in collisions, which lends support to the fragility argument. Columns, plates, and prisms require a similar CKE, and their ordering is determined by the apparent density from the empirical formulations. For the time being, prisms and needles are grouped into the category of columns to eliminate an additional threshold based on the aspect ratio. Here, it is hypothesised that particles exhibiting long columnar morphology may require a reduced critical CKE in order to undergo fracture, due to the formation of secondary habits (hollowing). In light of the available datasets, we aim to propose a correlation between fragility and the anticipated number of fragments resulting from a collision based on the available CKE. The two central quantities that must be considered in order to ascertain the properties of the crystal in question are, firstly, the estimated asperity number density (A_n) and secondly, the asperity-fragility coefficient (C_f). These quantities are provided by the equation Eq. 2.79

$$N_{\text{frag}} = \alpha_{\text{equiv}}\, A(\mathbf{M}) \left(1 - \exp\left\{-\left[\frac{C_f K_0}{\alpha_{\text{equiv}} A(\mathbf{M})}\right]^{\gamma}\right\}\right) .$$

The following two subsections will attempt to derive general descriptions for these quantities based on the available data.

7.1.1 *Asperity-Fragility-Coefficient*

Although the number density of asperities may be determined by the specific particle type, the asperity-fragility coefficient is assumed to be related to the particle's fragility via the width distribution of the asperities Γ_f (originally as Eq. 2.77)

$$C_f = \frac{b_2(1-q_{res}^2)\Gamma_f(1+\frac{1}{\gamma})}{\langle G_{break}\rangle} \; .$$

We adhere to the description of the maximum number of breakable asperities as outlined in Eq. 2.71. Nevertheless, the quantities employed to determine the C_f are redefined as a function of the apparent density of the particle to be fragmented. The mean energy needed to fracture an asperity $\langle G_{break}\rangle$ is inherently linked to the width distribution of the asperities Γ_f. Since the latter is unknown, we rewrite the average energy required to break an asperity in terms of fracture mechanics (Anderson, 2017)

$$\langle G_{break}\rangle = G_c\, A_{branch} \; , \tag{7.2}$$

by G_c and the fracture area (A_{branch}). If it is assumed that fractures always comprise of solid ice accumulated through riming or vapor deposition, the density effect can only be explained by the average width of the breakable asperities. Although this is also unknown and expected to vary depending on particle characteristics, it can be approximated by a simplified geometry. Laboratory measurements conducted by Grzegorczyk (2022) indicate that only the fragile dendritic structures growing on the surface of graupel particles are damaged, while the inner core remains intact. Each asperity, regardless of habit classification, is assumed to be columnar and uses the lateral radius of an asperity (r_{asp}) to calculate the lateral area of an asperity (A_{asp})

$$A_{asp} = \pi\, r_{asp}^2 \; . \tag{7.3}$$

The ratio of the total ice area ($A_i = n\, A_{asp}$) to the area of the circumscribing circle (A_c) is roughly equivalent to the ratio of apparent density to ice density (cf. definition of porosity in Fig. 2.6). Therefore, the asperity's radius can be calculated as

$$\frac{A_i}{A_c} \approx \frac{\rho_{app}}{\rho_{ice}} \Longleftrightarrow A_i \approx \frac{\rho_{app}}{\rho_{ice}} A_c \; , \tag{7.4a}$$

$$A_i = N_c\,(\pi\, r_{asp}^2) \approx \frac{\rho_{app}}{\rho_{ice}}\, \pi\, r_c^2 \; , \tag{7.4b}$$

$$r_{asp} \approx r_c \sqrt{\frac{\frac{\rho_{app}}{\rho_{ice}}}{\alpha_{equiv}\, A(M)}} \; . \tag{7.4c}$$

The expression can be interpreted as follows: for the same apparent density, the average width of the asperities must decrease as their number increases, and vice versa. For planar structures with branchings or fragile structures, one can apply this approach by assuming an unfragmented, solid circular (or hexagonal) core

$$r_{asp} = (r_c - r_{core}) \sqrt{\frac{\frac{\rho_{app}}{\rho_{ice}}}{\alpha_{equiv}\, A(M)}} \; . \tag{7.5}$$

The radius of the core $r_{\text{core}} = 100\,\mu\text{m}$ is chosen to resemble the value for the branching criterion of Jensen and Harrington (2015) (cf. Sec. 2.2.3). In the absence of a prognostic equation for the aggregate geometry in *McSnow*, the treatment of the apparent density is de facto dependent on the choice of an empiric relation. Given that the different volumes are treated additively for aggregation (cf. Eq. 2.54), one can circumvent this choice through a straightforward approach for the total volume of an aggregate $V_{\text{tot,agg}}$, where rime can fill in open spaces

$$V_{\text{tot,agg}} = \begin{cases} V_i \,, & \text{, if } V_i - m_i\,\rho_i > m_f\,\rho_i^{-1} + V_r \\ V_r + (m_i + m_f)\,\rho_i^{-1} \,, & \text{else .} \end{cases} \tag{7.6}$$

The energy to break an ice structure G_c of a certain area can be calculated by

$$G_c = K_c^2/E, \tag{7.7}$$

with the ice fracture toughness (K_c) and the effective modulus of elasticity (E). Marinescu and Pruteanu (2015) find that fracture toughness decreases with increasing porosity because porosity effectively reduces the cross-sectional area to be fractured. Although Kirchner et al. (2000) provide data showing a relation between K_c and ice density, we assume that fractures will occur in solid ice structures, and we account for density effects through the asperity width. The fracture toughness and Young's modulus measurements are $K_c = 100\,\text{kPa}\,\text{m}^{-2}$ and $E = 9.38\,\text{GPa}$, respectively (Tippmann et al., 2013).

The coefficient of restitution (q_{res}) is the only yet undefined determinant of the asperity-fragility coefficient. According to Vardiman (1974), the average value of $q_{\text{res}} = 0.37$ is found during collisions between graupel and a fixed plate. However, individual results exhibit high variability, ranging from $q_{\text{res}} = [0.08 - 0.96]$. Higa et al. (1998) note a significant reduction in q_{res} for ice at impact speeds ranging from 0.4 to $1.24\,\text{m}\,\text{s}^{-1}$ (see their Fig. 4), which is within the typical range for hydrometeors colliding.

A more general formulation that includes the properties of the colliding objects is proposed by Jackson et al. (2010). They find that the coefficient of restitution for a ball dropped on a surface of the same material can be calculated by

$$q_{\text{res}} = 3.1 \left(\frac{S_y}{E'}\right)^{5/8} \left(\frac{R_s}{R}\right)^{3/8} \left(\sqrt{\frac{E'}{\rho_{\text{app}}}}\frac{1}{v_{\text{imp}}}\right)^{1/4} , \tag{7.8a}$$

$$E' = \frac{E}{1 - \mu_{\text{Poisson}}^2} , \tag{7.8b}$$

$$R = \frac{1}{r_1} + \frac{1}{r_2} . \tag{7.8c}$$

Equation 7.8a depends on the dynamic yield strength (S_y), the smaller of the two radii R_s, the impact velocity v_{imp}, and the Poisson's ratio $\mu_{\text{Poisson}} = 0.33$ (from Tippmann et al., 2013). For the expected strain rates, we can assume that the dynamic yield strength is quasi-static at $S_y = 5.2\,\text{MPa}$ (Petrovic, 2003; Tippmann et al., 2013). Jackson et al. (2010) state that the equation overestimates the true COR and that it is only valid for $0.001 < \frac{\rho v^2}{S_y}$, but the results found are similar to those of Higa et al. (1998).

7.1.2 *Number Density of Asperities*

Having a method to describe how the fragility of individual asperities affects the energy required to break them leaves only the number of asperities per unit area $A_n(M)$ unknown. The authors are not aware of a comprehensive study that enables the determination of the number of asperities $A(M)$, so we decide to estimate it using simple geometric arguments

$$A(M) = \frac{N_c(M)}{A_{\text{char}}(M)}\,, \tag{7.9}$$

using the data from Griggs and Choularton (1986) and Takahashi et al. (1991). Motivated by their observations, we have classified particles into four categories based on their apparent density ρ_{app}, aspect ratio ϕ, and monomer number N_m (see Tab. 7.1). Columns and plates are relatively sturdy particles that are likely to produce minimal crystal ejections during fragmentation events. Griggs and Choularton (1986) demonstrate that the energy required to produce a fragment (when bombarded with glass beads) is significantly greater for these two species than for delicate dendrites (refer to Fig. 7.2 and their Tables 1 & 3). It is improbable that a collision involving typical CKEs would result in numerous fragments from plates and columns. Even if plates or columns are the more fragile particle, imagine a hollow column or thin plate, we assume that the number of fragments is somewhere on the order of $N_c = [10^0 - 10^1]$. Dendrites, by comparison, are more delicate in structure and thus more prone to breakage. It is unclear which sections of the crystal arms are broken, but the fragment distributions collected by Grzegorczyk (2022) and Gautam (2022) suggest that the average fragment size is in the range of 10 % of the parent particle size. A potential preference for particular types of breakage can be illustrated by envisioning a tree struck by a powerful gust. Neither the slender leafy twigs nor the sturdy limbs attached to the trunk would typically be fractured, however, there exists a crucial size that would be affected. For an exemplary illustration, one may refer to the works of Francis and Gillespie (1993) and Francis (2000), wherein a correlation is identified between crown loss and stem failure in relation to the branch resistance to flexing. Prospective studies may offer insights into whether there exists a critical dimension and what it could be.

A laboratory-grown dendrite, developed in great detail by Takahashi et al. (1991, Fig. 3, bottom left), is employed to calculate the number of asperities with a size of 10 % as $N_c = 30$. For details regarding the estimated values of asperity number density $A(M)$ for distinct monomer types, we kindly refer to Table 7.1.

Aggregates may comprise different monomers, making them challenging to generalize. Our proposed approach is to define the properties of an aggregate based on the properties of the dominant monomer species present within it. The total number of asperities of an aggregate is proportional to the number of asperities within each monomer it contains, as derived from the habit-specific $A_n(M)$ and the monomers surface area (S_{mono}), scaled by the aggregates surface area (S_{agg}).

Table 7.1: Type categorization defined by apparent density ρ_{app}, aspect ratio, ϕ, monomer number N_m, the A_n, and the fraction of energy available to break asperities b_2.
** Only observations for aggregates consisting of dendrites are available. The value can serve as an upper limit.*

Type	ϕ	ρ_{app}	N_m	$A_n(M)$ [m^{-2}]	b_2
Column	$\geqslant 1$	$\leqslant \rho_{\mathrm{ice}}$	1	3.40×10^6	2.731×10^{-1}
Plate	< 1	$\approx \rho_{\mathrm{ice}}$	1	6.37×10^7	1.092×10^{-4}
Dendrite	< 1	$< \rho_{\mathrm{ice}}$	1	3.12×10^6	1.448
Aggregate	any	$\ll \rho_{\mathrm{ice}}$	>1	Eq. 7.11	2.973×10^{-4} *

The surface area of a spheroid is a function of the aspect ratio and can be defined by the two semi-axes a and c

$$S_{\mathrm{oblate}} = 2\pi a^2 + \frac{\pi c^2}{\epsilon_1} \ln\left(\frac{1+\epsilon_1}{1-\epsilon_1}\right), \qquad \epsilon_1 = \sqrt{1-\frac{c^2}{a^2}}, \tag{7.10a}$$

$$S_{\mathrm{prolate}} = 2\pi a^2 + 2\pi \frac{a\,c}{\epsilon_2} \sin^{-1} \epsilon_2, \qquad \epsilon_2 = \sqrt{1-\frac{a^2}{c^2}}. \tag{7.10b}$$

We introduce a term that is proportional to the links between crystals. These links are affected by leverage effects and are considered to behave like additional asperities. Although multiple particles may be mechanically interlocked, we assume that these links only exist between two particles, and the total number of links is $N_m - 1$. The number density of asperities of the aggregate is therefore

$$A_{n,\mathrm{agg}} = \frac{(N_m - 1) + N_m\, S_{\mathrm{mono}}\, A_{n,\mathrm{mono}}}{S_{\mathrm{agg}}}. \tag{7.11}$$

The energy required to break an asperity is assumed as an average quantity characterized by the fragility and therefore we do not define a specific internal bond strength. Determining individual fraction of the energy available to break asperities (b_2) values can be challenging as aggregates formed from different habits have not been explored yet. Hence, we will use the value obtained from dendrite aggregates detected by Gautam (2022). Since dendrites are regarded as the most fragile, the calculated value can be treated as an upper limit for the expected N.

The derived values of b_2 from above laboratory and observational data are presented in Tab 7.1. For dendrites, a fraction b_2 greater than one is observed. According to Griggs and Choularton (1986), dendrites can become so fragile that they fragment by air alone, in the absence of an ice collision. This adds another fragmentation mechanism if delicate structures are present. Furthermore, the simplified asperity approach is a limitation for the intricate dendritic structures formed. Future laboratory studies may enable the parameter to be readjusted. Section 7.3 will present some of the necessary information that could help to improve the scheme and may inspire potential laboratory studies.

Nevertheless, it can be concluded that this approach yields accurate dependencies within the generalized framework, without requiring knowledge of habit-specific surface and asperity structures. In this thesis, the described process is referred to as the *Updated fragmentation scheme* (UFS).

7.1.3 *Characterization of Particles after the Collision*

Irrespective of the fragmentation parameterization, following a collision event, three super-particles are generated: the fragmented particle, the "collider" particle, and a new super-particle containing the fragments. In the event that the collider remains intact, it is the fragmented particle that will experience mass loss, which may result in a potential change in shape. The amount of mass lost can be calculated by multiplying the number of fragments by the mass fraction, which is approximately 10^{-3}. This assumption is based on the concept that the typical fragment size is approximately 10 % of the largest dimension, even if the outer portion may have a lower apparent density. For simplicity, we will reduce individual ice mass categories based on their relative fraction of the total mass. However, we anticipate a more significant decrease in total volume due to the fracturing of the porous structures and a rounding. In nature, collisions between particles may result in irregular or incomplete shapes (Hobbs and Farber, 1972; Schwarzenboeck et al., 2009), but these details cannot be considered within the context of the spheroidal framework. Thus, our approach is to generalize the shape change for the two spheroidal habits. It can be anticipated that for a prolate particle, the fragmentation will result in a reduction in particle length. Consequently, the maximum dimension should be reduced by 10 % to reflect this change in the aspect ratio. An oblate particle, on the other hand, may only be affected on the side where the collision takes place, and the ejection of e. g.individual dendritic arms or just parts of them is more likely. As a result, we have decided to reduce the total area by 10 % by decreasing the major axis of the particle by about 5 % ($A_{\text{reduced}} \propto \sqrt{0.9\, a^2} \approx 0.95\, a$). It is important to note that a change in habit is assumed only when the particles are fairly asymmetric. The habit is not updated through fragmentation if $0.8 < \phi < 1.25$.

The updated habit is used to diagnose the volume of the fragmented particle. We propose a formulation that interpolates between the ice volume of the particle before the collision, $V_{\text{i,before}}$, and the ice volume when reduced by the same fraction as the mass, $V_{\text{i,c}}$. We assume ice density for a spheroid with a critical volume $V_{\text{i,crit}}$ and a critical radius of approximately $r_{\text{crit}} \approx 100\mu\text{m}$ (for a plate or solid column) with the updated aspect ratio

$$\rho_{\text{i,after}} = \frac{\left((V_{\text{i,before}} - V_{\text{i,c}})\, \rho_{\text{crit}} + (V_{\text{i,c}} - V_{\text{i,crit}})\, \rho_{\text{i,before}}\right)}{(V_{\text{i,before}} - V_{\text{i,crit}})}\,, \tag{7.12a}$$

$$V_{\text{i,c}} = V_{\text{i,before}}\,(1 - N_{\text{frag}}\,\zeta)\,, \tag{7.12b}$$

$$V_{\text{crit}} = \begin{cases} \frac{4}{\pi}\,\frac{r_{\text{crit}}^3}{\phi_{\text{upd}}^2}, & \text{if } \phi \geqslant 1\,, \\ \frac{4}{\pi}\, r_{\text{crit}}^3\, \phi_{\text{upd}}, & \text{if } \phi < 1\,. \end{cases} \tag{7.12c}$$

$$V_{\text{i,after}} = \frac{m_{\text{i,after}}}{\rho_{\text{i,after}}}\,. \tag{7.12d}$$

The shape of the typical fragment is even more difficult to determine. Due to the lack of observations, we stick to the assumption that the typical fragment size is about 10 % of the parent's maximum dimension. The two-dimensional analysis of the fragment size distributions of Grzegorczyk (2022) and Gautam (2022) includes an aspect ratio distribution, but the fragment aspect ratio $\hat{\phi}$ is defined as fragment length to width. Both studies show an aspect ratio around $\hat{\phi} \in [0.25 - 0.9]$, but no

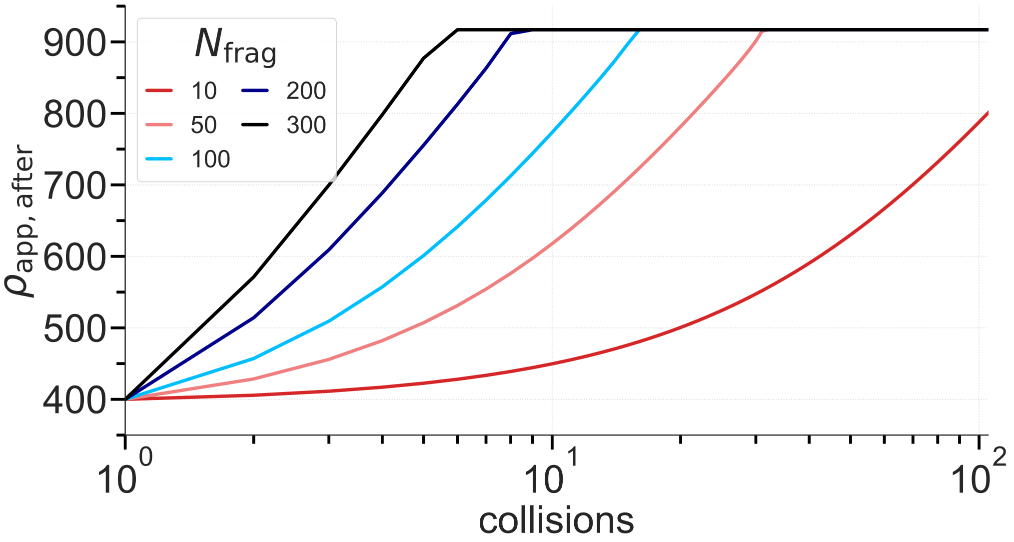

Figure 7.3: Apparent density of parent particle after a number of collision following Eq. 7.12a. The colored lines mark the number of particles ejected by each collision.

information on fragment thickness is available. Therefore, it is not clear how to characterize the average aspect ratio and also the apparent density of the fragments. Until more information is available, we randomly choose an initial fragment aspect ratio within $\phi_{\text{init}} \in [0.8 - 1.25]$ with the same apparent density as the parent particle before collision.

For aggregates with larger monomer numbers, we hypothesize that a fragmentation event could eject whole monomers by breaking linkage. Depending on the aggregate composition either interlocking or frozen structures formed by a QLL are broken, making the process difficult to characterize. Hence, we opted to propose a straightforward description, postulating that for each ten monomers present in an aggregate, one is ejected (equivalent to the floor function)

$$\lfloor n \rfloor = n, \qquad \text{where} \qquad n \leqslant x < n+1\,, \tag{7.13}$$

with n representing an integer.

The application of the super-particle approach may result in a secondary effect, which we term *partial fragmentation*. In cases where the smaller or more fragile particle displays a multiplicity that exceeds that of the collision partner, a portion, represented by the multiplicity, remains unfragmented. Consequently, it is necessary to introduce a supplementary super-particle that contains the information of the particles that did not participate in the collision.

7.2 POTENTIAL SECONDARY ICE PRODUCTION BY FRAGMENTATION

To understand the full potential of ice-ice collisions as a SIP, we first investigate isolated collision between two particles regarding their fragmentation potential. Prior to applying the parameterizations to a complex one-dimensional simulation, we demonstrate how the effectiveness of the fragmentation schemes is dependent upon the assumed particle type. Accordingly, we re-facilitate the setups for an oblate- and

Table 7.2: Categorization of the different monomers used to test the efficiencies of the fragmentation schemes. Particles are categorized by aspect ratio (ϕ), apparent density (ρ_{app}), and temperature (T).

Type	ϕ	ρ_{app} [$\mathrm{kg\,m^{-3}}$]	T [K]
Column	3	700	255
Plate	0.2	900	263
Dendrite	0.02	400	258
Graupel ($F_r = 0.95$)	0.8	480	267

a prolate-dominated configuration, as presented in Chapter 5. It is hypothesised that the UFS will produce a greater number of fragments than the PFS due to the formation of structures with a lower apparent density. Dendritic structures may cause collisions with the potential for the production of a significant number of fragments. The outcome is less clear for prolate structures where collisions that have the necessary CKE to shatter the fairly sturdy columns and/or needles should be rare or even impossible when applying the UFS. The PFS does not categorize particles according to habit, but rather according to temperature. Consequently, it may prove more effective in fragmenting prolate particles, as particles that sediment into the DGL are classified as "dendritic particles" due to the temperature-dependent categorization.

The application of both fragmentation schemes to the real case scenario serves to conclude the chapter by answering the questions of whether the given conditions are favorable for fragmentation to occur and whether the ejected particles are a potential cause for the strong K_{DP} signal observed at temperatures warmer than $T > -7°$ C.

7.2.1 *Sensitivity of the Parameterizations to Individual Particle Habit*

Prior to examining the comprehensive impact of ice collisions on a snow shaft experiment, it is reasonable to investigate the efficiency and initiation of fragmentation in an idealized collision between a large, heavy hail particle and a particle symbolizing the diverse habits. All particles are assumed to be pristine, and their characteristics are detailed in Table 7.2. The temperature is utilized to differentiate between dendritic and non-dendritic particles in the PFS, and is indicative of the region in which these particles typically develop following the IGF. The CKE is proportionally scaled by increasing the size of the monomer, while keeping the apparent density and aspect ratio constant. Figure 7.4 depicts the number of fragments ejected in a collision between a hail particle of diameter $D = 1$ cm and three distinct monomer types whose size increases monotonically. The UFS scheme (dashed lines) produces a greater number of fragments than the PFS for the same CKE, irrespective of particle habit. The results demonstrate that plate-like and columnar particles produce up to eight times more particles for the fragility-based method in comparison to the PFS. It is evident that the fragmentation onset occurs somewhat earlier for the fragility-based method. In the PFS, the number of fragments ejected from columns and plates is comparable, as both are classified as collision type II or III (see Tab. A.2

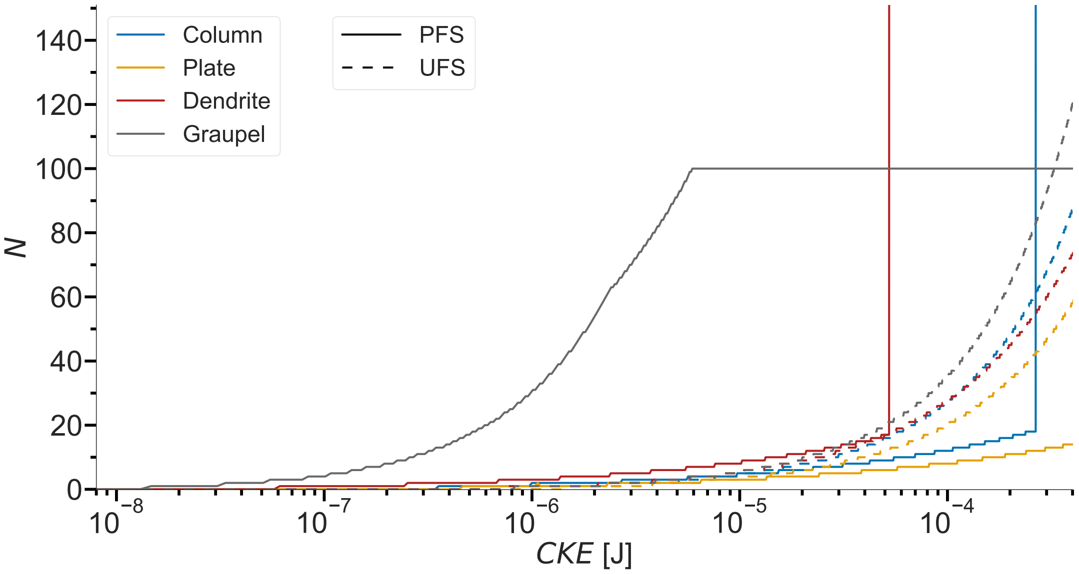

Figure 7.4: Number of fragments N as a function of CKE for columns (blue), plates (yellow), dendrites (red), and graupel (grey) with hail of $D = 1\,\mathrm{cm}$. The two fragmentation schemes are indicated by solid lines for the PFS and long-dashed lines for the UFS.

in the Appendix). Employing habit-specific parameterization yields a higher value of N for the plate collision than for the columns collision due to the increased surface area coupled with a higher asperity density A_n. It can be seen that both schemes will result in a significant alteration to the IPNC of those cases which are plate- and columnar-dominated, particularly when collisions occur with high CKE. However, in cases which are dendrite-dominated, the updated formulation will result in fragmentation at low CKE, due to the fragile structures evolving. As CKE increases, more asperities break, resulting in a steady increase in the number of ejected particles. For large particles and high CKE, the large number of asperities (dendritic arms) leads to up to 15 times more fragments compared to the PFS. The introduced fragility and habit dependence enable collisions with low to medium CKE to make a significant contribution to the IPNC, which in turn can cause a positive feedback on the mass flux and the aggregation probability. It should be noted that the sudden increase in the number of fragments for dendrites in the PFS is caused by extrapolation and associated limiters (Tab. A.2).

The collision between graupel and hail is examined independently as collision type I in the PFS, allowing for comparable onset and slope results with updated dendrite formulation. Fragmentation is limited to a maximum of $N_{max} = 100$, as noted by Phillips et al. (2017a). In the updated formulation, there is no explicit differentiation between ice and rime. This is because their combination of apparent density and almost spherical shape produces a collision outcome similar to that of the investigated plate-like crystal This test of individual monomers indicates that the simulation results greatly vary depending on the fragmentation scheme used, which is heavily influenced by particle shape.

The description of aggregate fragmentation behavior is based on theoretical analysis of aggregate geometry and the most prevalent habit. In the case where two monomers form an aggregate, the majority of the asperities are external and breakable, with only one link serving as an additional target for breaking. As the N_m increases, the number of links grows linearly, yet the ratio of the monomers' surface area to the aggregate's surface area determines the quantity of breakable asperities. How the ratio changes for certain monomer habits or with increasing monomer numbers depends heavily on the underlying assumption of the aggregate geometry. It is expected that the simplified approach of instantaneously transitioning from spheroidal monomers to a porous sphere will lead to an overestimation of the resulting aggregate volume and surface area, causing an underestimation of the aggregate's estimated asperity number density. The prognostic geometry model for aggregates can enhance the representation of the actual number of asperities by refining the volume and surface area estimate. As the number of monomers per aggregate increases, the two solutions would yield comparable results, since for $N_m \gg 1 \to \phi \approx 1$, the surface area ratio is governed by the aggregate due to the entrapment of air.

7.2.2 *Fragmentation in a One-Dimensional Snow Shaft Experiment*

Prior to the application of the fragmentation schemes to the complex situation discussed in Chapter 6, a simple comparison based on the plate-like and columnar test case experiments presented in Chapter 5 will be utilized to investigate the SIP potential of the two fragmentation schemes described. The full setup, which includes aggregation and riming, will be employed to see the full effect of the fragmentation parameterizations, based on three configurations

1. without habit prediction and using the PFS;
2. with habit prediction and using the PFS;
3. with habit prediction and using the UFS;

The initialization of the fragments and the update to the fragmented particles are treated equally, irrespective of the fragmentation scheme employed. In all configurations, particles are only generated if their resulting mass is at least as big as that of a pristine ice crystal of radius $r_{min} = 1\,\mu$m.

7.2.2.1 *Fragmentation in the Idealized Case Study*

Figure 7.5 illustrates the proportion of the total particle population generated by fragmentation. For the oblate case, all three configurations exhibit an active fragmentation process, resulting in fragments comprising 0.8 %, 3.7 %, and 2.7 % of the total super-particle count, respectively. It is important to note that the shares should not be confused with the total real particle count. The multiplicity is the result of the fragmentation schemes and therefore highly variable. For all simulations, only P_2 exceeds 1 % real particle share. The discrepancy between O_1 and O_2 can be attributed to the evolution of particles with larger maximum dimensions due to enhanced depositional growth, in addition to an increase in aggregation, caused by the habit prediction (cf. Chapter 5). In the case of O_3 using the UFS, the formation of ice particles with reduced apparent density (higher fragility), regardless of whether it is caused by branching or aggregation, results in a comparable super-particle share compared with the PFS.

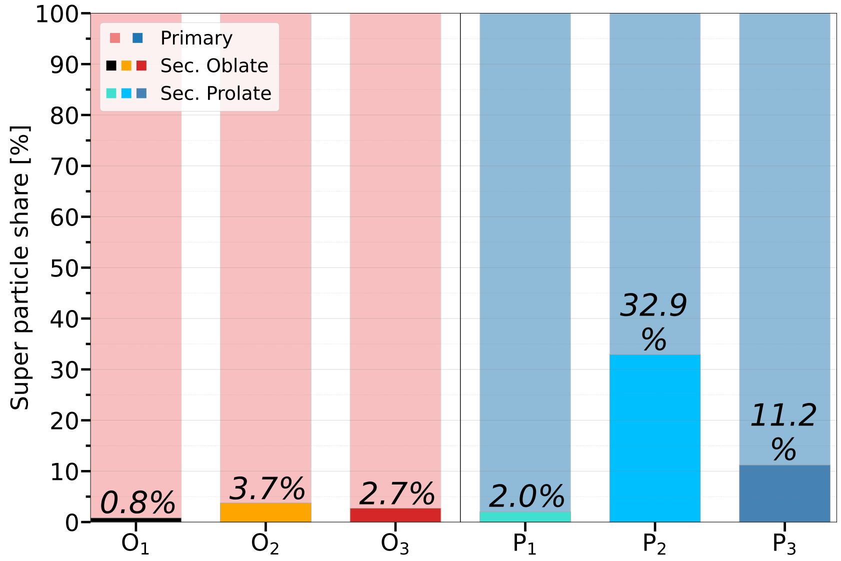

Figure 7.5: Particle shares for the fragmentation schemes employed in the three configurations, for the oblate (left, **O**) and prolate test case (right, **P**).

In the prolate case, the picture is markedly different. Configuration P_1 (without habit prediction) results in the production of fragments that account for 2 % of the total super-particle number. In contrast, configurations P_2 and P_3 exhibit particle shares of 32.9 % and 11.2 % respectively. As a consequence of the development of explicit monomer habits, particles with higher maximum dimensions form, which is a determining variable in the PFS. At the same time, habit prediction leads to particles with high terminal velocities (cf. Fig. 5.4 and 5.5), increasing the potentially available CKE in collision events. It is surprising that the PFS is so active for the prolate dominated case compared to the UFS. The prolate case sees particles with a substantial sedimentation distance and a larger total LWZ compared to the oblate case, which permits growth to substantial maximum dimensions. The PFS methodology exclusively considers the maximum dimension, which exhibits accelerated growth for prolate particles in the spheroidal framework due to the fact that all mass add in prolate-favoring conditions is concentrated on the polar axis c, rather than distributed along the two equatorial axes a. Furthermore, we find that the combination of the high terminal velocities of columnar particles, coupled with the categorization based on temperature and degree of riming in the PFS, results in the ejection of many super-particles. In contrast, the CKE required to break the relatively stable columns in the UFS is difficult to achieve.

In order to gain an understanding of the height interval where fragmentation is active, it is helpful to examine the histograms presented in Figure 7.6. These histograms show the number of fragments initialized per bin with a bin width of 50 m. In both cases, and for all configurations, it is only in the lower half of the domain that pairs of particles have the necessary CKE to break effectively. This is logical, since the heavy and fast particles that drive the CKE need time to develop. At the same time, the variation in terminal fall velocities is most pronounced during ongoing riming and aggregation processes. We can see that for the UFS (O_3 and P_3) there is also fragmentation outside the LWZs, so without riming. In particular, the formation of

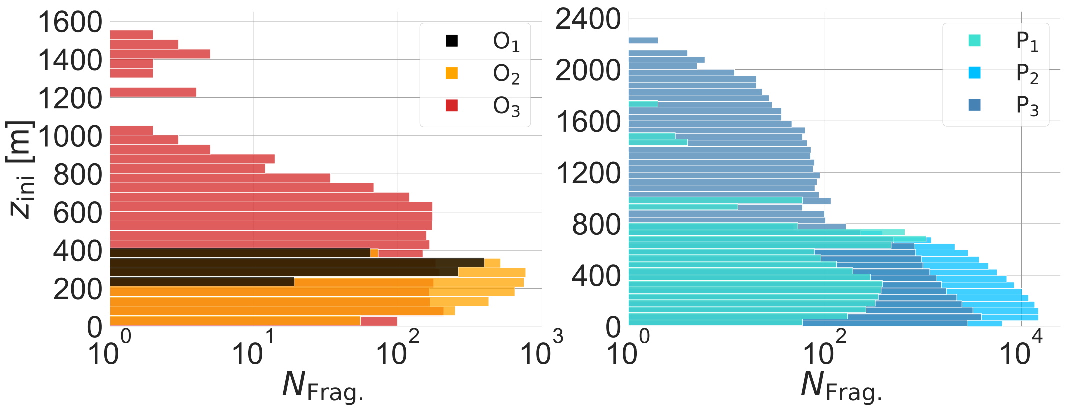

Figure 7.6: Initialization height z_{ini} of the fragments produced by the fragmentation schemes employed in the three configurations, for the oblate (left, **O**) and prolate test case (right, **P**).

secondary habits and aggregates causes an increase in fragility, which increases the potential for fragmentation. For the PFS, we see that, in addition to a few single events outside the LWZ, riming is necessary to cause the ejection of particles.
This brief section illustrates that fragmentation is a viable SIP mechanism. This outcome is encouraging when considering the application of the fragmentation parameterizations to the observed case presented in Chapter 6, which will be discussed in the subsequent section.

7.2.2.2 *Fragmentation in the Real Case Study*

As demonstrated in Chapter 6, it is possible to identify configurations of *McSnow* that are capable of reproducing polarimetric radar observations based on one-dimensional snow-shaft experiments. Nevertheless, achieving consensus between the simulated and observed K_{DP} remains a significant challenge. To test the hypothesis of an IPNC not high enough to drive K_{DP}, possibly due to a lack of a SIP mechanism, the simulation is repeated with the two different fragmentation schemes enabled. We do not vary the sticking efficiency for the setup since it shows to be have less impact compared to the activation of the fragmentation scheme. One might anticipate that the depositional growth inside the DGL paired with the potential for riming in the LWZ could produce particles breakable monomers as well as aggregates. We start with the PFS. Based on the same variables as before, Figure 7.7 illustrates how the PFS changes the simulated profiles by fragmenting particles. As can be observed, the PFS has essentially no impact on the simulation. It is reasonable to posit that the UFS will exhibit a greater potential for fragmentation due to the incorporated habit sensitivity. To test this hypothesis, the experiment will be repeated with the UFS. Figure 7.8 shows that the simulations using the UFS do not substantially differ from those presented in the Figure 7.7. All variables show similar characteristic profiles that are not substantially influenced by the activation of the fragmentation scheme. Although the UFS may categorize specific particles as delicate dendrites or fluffy aggregates, the number of such particles is insufficient to produce a meaningful signal that could be identified as an IMP fingerprint. While they do not provide additional insight about the effectiveness of the fragmentation schemes, the spectrograms have

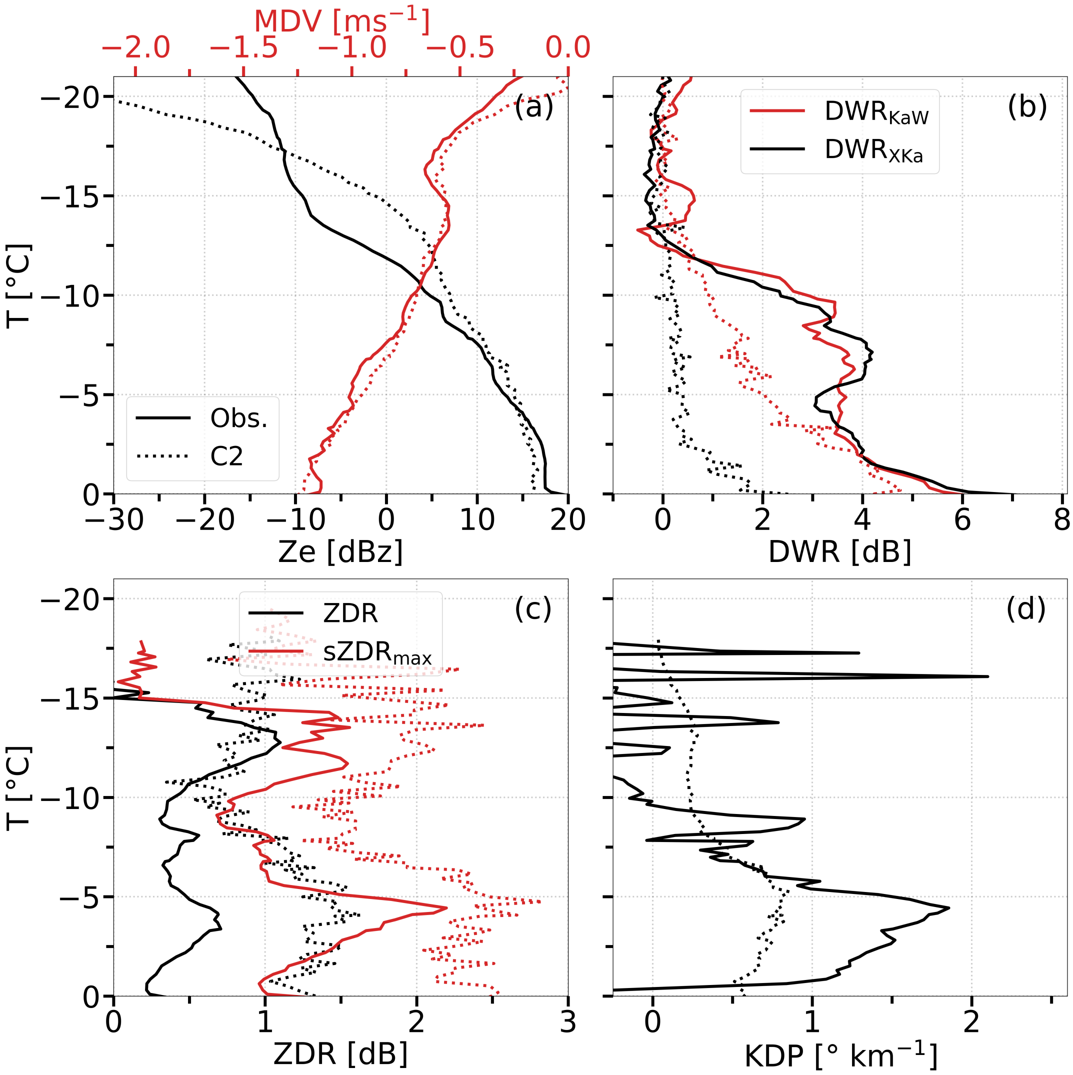

Figure 7.7: Comparison between radar (obs., solid lines) and synthetic profiles (C2, dashed lines) of the configuration using the PFS for the dendrite event. Vertical profiles of (a) Z_e and MDV, (b) DWR, (c) Z_{DR} and $sZ_{\mathbf{DR,max}}$, and (d) K_{DP}.

been added to the Appendix A.2 (Fig. A.3i and A.3ii).

To gain further insight into the impact of the two fragmentation schemes on the simulations, we present the PSDs for the setup without fragmentation (left column), with the PFS (middle) and the UFS (right column) in Figure 7.9. The black lines represent the overall PSD, while the colored lines provide information about the PSD for individual particle types. These include liquid drops (dark red), unrimed crystals (dark blue), unrimed aggregates (light blue), rimed aggregates (dark green), rimed monomers (light green), graupel-like particles (red), and fragments (yellow). A examination of the full height range depicted in the top row of Figure 7.9 (a)-(c) reveals that both fragmentation schemes exert a marginal influence on the overall PSDs as well as on the particle-specific ones. All setups show that particles with maximum dimension larger than $D_{max} > 4$ mm are rimed aggregates which are the heaviest particles and important for collisions to have sufficient CKE. The simulation with the UFS shows the presence of fragments with a small maximum dimension, while in the cases without active fragmentation or with the PFS no fragments are

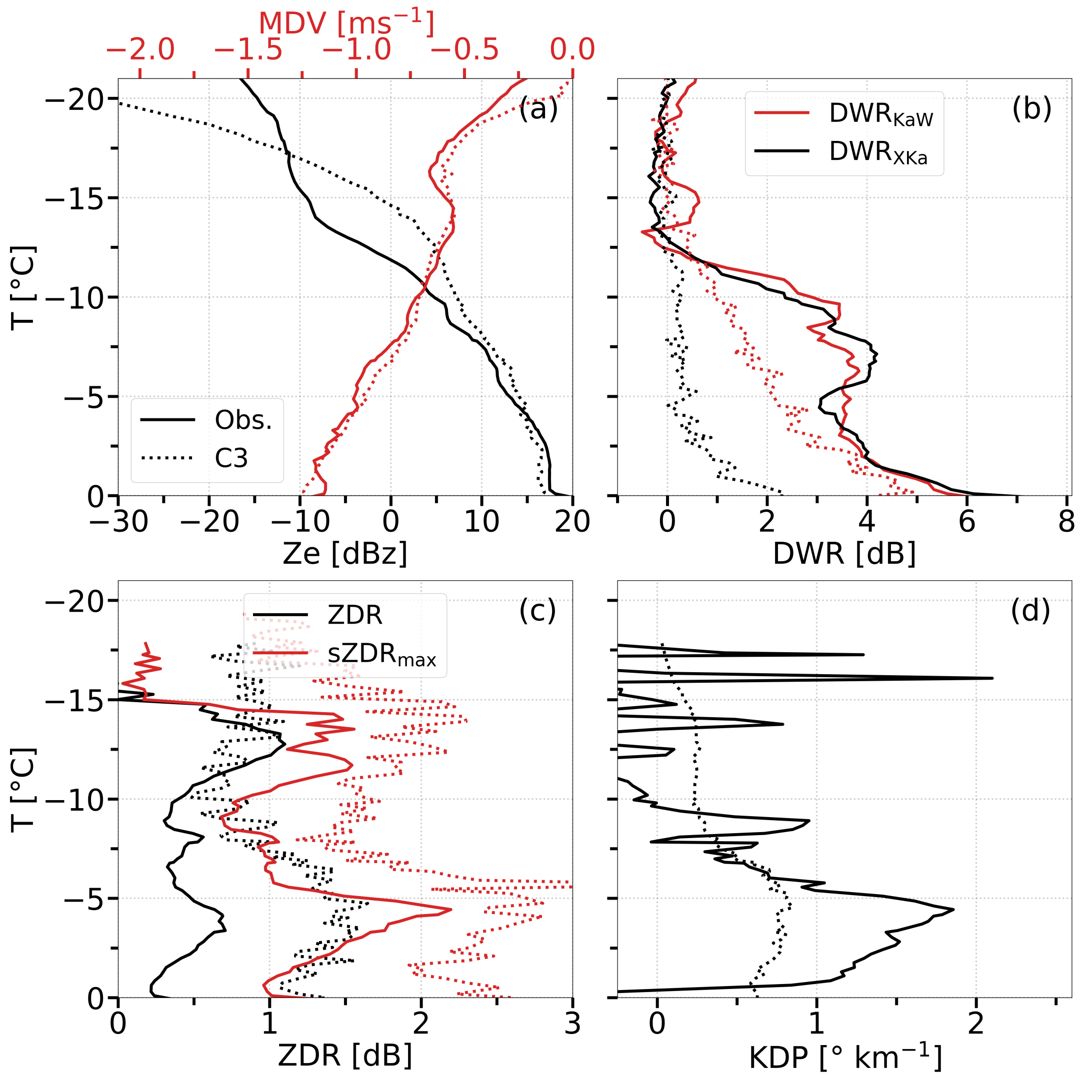

Figure 7.8: Comparison between radar (obs., solid lines) and synthetic profiles (C3, dashed lines) of the configuration using the UFS for the dendrite event. Vertical profiles of (a) Z_e and MDV, (b) DWR, (c) Z_{DR} and $sZ_{\mathbf{DR,max}}$, and (d) K_{DP}.

present.

To find the origin of the fragments, we split the analysis into two different regions: the interval above the LWZ (Fig. 7.9 (d)-(f), $1960\,\mathrm{m} \leqslant z \leqslant 4400\,\mathrm{m}$) and the one covering the LWZ (Fig. 7.9 (h)-(i), $400\,\mathrm{m} \leqslant z < 1960\,\mathrm{m}$).

Starting with the region above the LWZ in the second row, we can isolate how the fragmentation schemes affect all the unrimed particles. Here, pairs of particles either do not reach the necessary CKE to fracture the smaller or more fragile one.

Entering the LWZ, riming becomes the dominant process for particles. The increase in particle mass and velocity is enough to produce fragments when applying the UFS.

Stratifying the PSD by monomer number in Figure 7.10 provides insight into whether either low apparent density monomer crystals are being broken by heavier edge particles, or whether aggregates are the primary target due to the greater number of breakable asperities and their contribution to the pair's CKE. The black lines show the overall PSD while the colored lines give information about the PSDs stratified

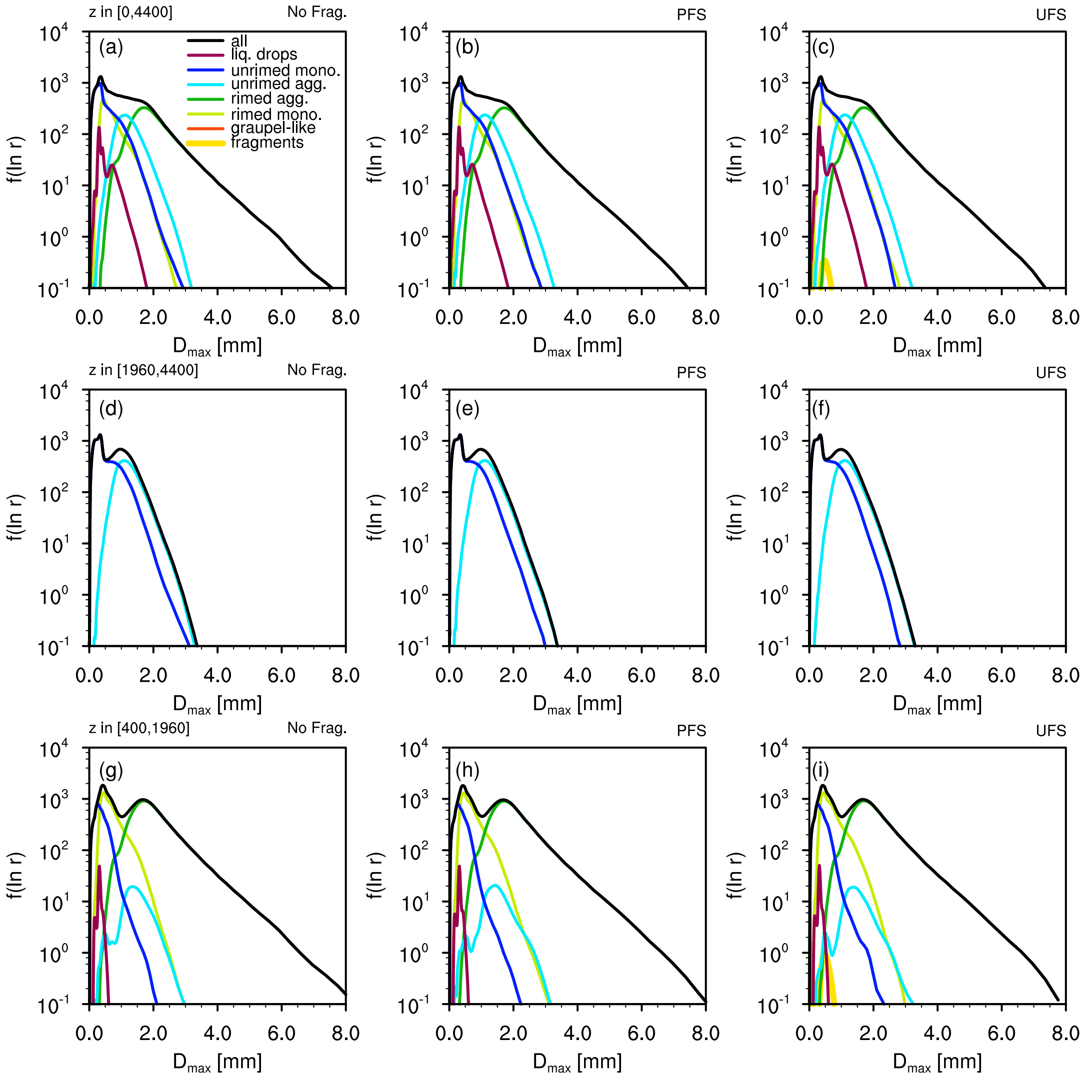

Figure 7.9: PSDs stratified by particle type (according to the legend) for the whole domain (between 0 and 4000 m height, top row), above the LWZ (between 1960 and 4000 m), and inside the LWZ (between 400 and 1960 m height). The leftmost column shows the PSDs without fragmentation, the middle column for the PFS and the right for the UFS.

by monomer number: $N_m < 2$ (dark blue), $2 < N_m < 10$ (light blue), $10 < N_m < 30$ (green), $30 < N_m < 100$ (dark red). Again, we split the different regions and find that the UFS changes the size distributions of aggregates with $10 < N_m < 30$ and $30 < N_m < 100$ within the LWZ. The total number of aggregates with a monomer number between $30 < N_m < 100$ is decreased for maximum dimensions greater than $D_{max} > 4$ mm in favor of the aggregates with a monomer number between $10 < N_m < 30$. The particles with a large number of monomers provide more breakable links between each other, effectively increasing the fragmenting potential. When fragmented, we introduced a reduction in the monomer number of the aggregate in the order of 10 %, which causes particles with monomer numbers slightly above $30 < N_m$ to change classification. While this is an artifact caused by the chosen categorization, it shows a core feature of the UFS: despite being a particle with a large maximum dimension, it can still be the emitter of fragments, since fragility is

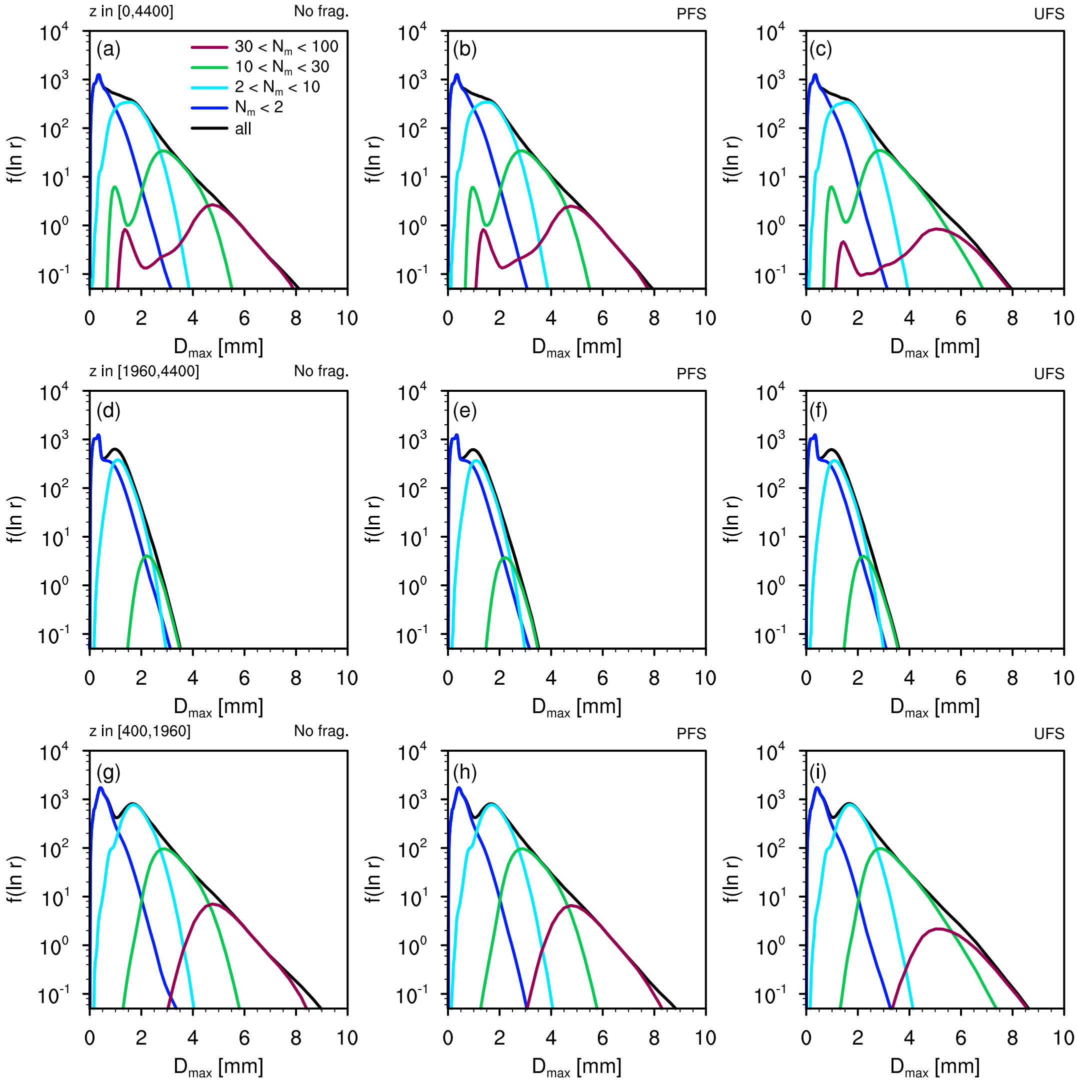

Figure 7.10: As Fig. 7.9 but stratified by monomer number N_m (according to the legend). The leftmost column shows the PSDs without fragmentation, the middle column for the PFS and the right for the UFS.

the determining factor for the identification of the fragmented particle.

The application of the fragmentation schemes to the real case configuration shows that ice-ice collisions are an effective SIP mechanism that should be further investigated in the effort to explain the mismatch between IPNC and INP. The presented updated approach allows new laboratory or observational results which help understanding the underlying process to be implemented. Following the implementation of a more sophisticated methodology for the prediction of aggregate morphology, it would be advisable to repeat this experiment in order to gain a deeper understanding of the significance of aggregate shape, as well as the impact of the presence of unrimed compared to rimed aggregates. In order to conclude this section, we present a list of potential information which we believe will enhance the updated, generalized framework.

7.3 NECESSARY INFORMATION TO IMPROVE THE GENERALIZED FRAMEWORK

In terms of empirical evidence and control of the underlying physical assumptions, the revised framework shows promising results. However, there remain critical gaps in the overall understanding of the process that need to be addressed in order to understand the significance of the multiplicative potential of fragmentation. We have compiled a list of open questions that we believe are worth investigating in order to clarify key unknown aspects.

- *How does fragmentation depend on ambient conditions, such as temperature and supersaturation?* This question covers various crucial factors that could be instrumental in fragmentation, including whether dendrites alter their crispness depending on environmental conditions. Moreover, the influence of LWC on structures (as demonstrated by Takahashi, 2014), or the presence of a QLL, may impact the particle's fragility or collision effectiveness. The question of how habits grow under adverse conditions (prolate particles in oblate-favoring conditions and vice versa) is closely related, and according to Grzegorczyk (2022), dendritic structures can develop on rough surfaces of rimed particles. However, it is uncertain whether and which structures could form under atmospheric conditions outside the DGL regime.

- *What do fragments of different habits typically look like?* Information about the mass and/or size distribution of such fragments, similar to that collected by Grzegorczyk (2022) for a wider range of variables like mass, density, and habit, would be valuable for estimating the appearance of fragments. Currently, no observations exist to establish any correlation between the monomer number of an aggregate and the ejected fragments. This topic is closely related to the following open question.

- *Are there specific asperities that tend to break?* The analogy we use is that asperities resemble the branches of a tree, with structures of a typical size breaking when struck. It is uncertain whether there is a critical size and this could be addressed by experiments focusing on the size to mass ratio of the fragmented particle in relation to the shapes of the mass and the size distribution of the fragments.

- *How do surface and shape characteristics of fragmented particles change?* Experiments conducted at the cold chamber laboratory in Mainz, Germany reveal that dendritic structure growth on graupel particles inhibits their ability to branch out again after a collision event. While depositional growth largely influences this phenomenon, incomplete dendrites also impact the water vapor field surrounding them, as well as their sedimentation and ultimately, ventilation.

- *What role does riming play in fragmentation?* While riming usually enhances the terminal velocity of particles, potential fill-in effects may reinforce the internal structure of porous, delicate particles. It remains uncertain whether riming directly impacts the fragmentation process or if the inclusion of rime only affects the particle's density.

- *How do the critical fragmentation parameters correlate with the monomers within the aggregates?* The explosive ejection of shattered snowflakes containing fragile dendrites will likely produce the largest number of fragments. However, it is challenging to evaluate the effect on aggregates comprised mainly of columns, needles, plates, and/or mixtures.

The presented list is not exhaustive and provides only a selection of questions that may be considered interesting. Additionally, some of these research questions are either particularly challenging to answer or may even have been the subject of investigation in related fields, as evidenced by the examples found in materials science literature. It is our hope that this work will motivate future scientists to further investigate the fragmentation process, as we believe it has significant potential as a SIP mechanism.

8

CONCLUSIONS AND OUTLOOK

8.1 CONCLUSIONS: MODELING, POLARIMETRIC ANALYSIS, AND SIP MECHANISMS

The knowledge about the impact of the variety in solid hydrometeor characteristics on the in-cloud processes as well as precipitation patterns is one of the areas in microphysical research that needs special attention. In particular, the complex transitions involving all three aggregate states present a challenge to the understanding of microphysical processes and are a major focus of current research. The increase in computational resources allows simulations down to the super-particle level, and state-of-the-art observations allow the identification of microphysical ice footprints. Still, individually both can only aid with answering the questions regarding the interaction inside clouds and the feedback between all of the processes happening simultaneously.

This thesis sought to address three primary objectives: first, to enhance the representation of ice microphysical processes with regard to ice particle habits; second, to ascertain what insights can be drawn about IMP fingerprints when such simulations are integrated with state-of-the-art observations; and third, to determine the role played by SIP process fragmentation.

8.1.1 *Part I: Improved Representation of Ice Microphysical Processes Regarding Ice Habits*

The Lagrangian particle model *McSnow* has been expanded by an extended version of the habit prediction scheme of Jensen and Harrington (2015), based on the work of Chen and Lamb (1994b). The comprehensive hydrodynamic description of porous spheroids by Böhm adds parameterizations regarding terminal velocity and collision efficiency. We propose a ϕ-dependent terminal velocity interpolation between prolate and cylindrical shape assumption based on the laboratory results of McCorquodale and Westbrook (2021a), which overcomes the potential deceleration resulting from the cylindrical assumption of Böhm when transitioning from spherical to columnar or vice versa.

A shape-dependent ventilation coefficient has been introduced that combines the results of a collection of recent studies on ventilation of different geometries. While the effect on depositional growth is found to be in the range of a few percent for small particles, for larger particles the ventilation coefficients can increase by a factor of two compared to spheres. The habit prediction scheme in its original version was shown to be in good agreement with individual particle measurements from Takahashi et al. (1991), but also has deficiencies, including the polycrystalline regime, the warm prolate maximum, and the branching criterion used for oblate particles.

A comparison with an independent method using the polarizability ratio of Myagkov et al. (2016a) confirmed these findings. Hence, we propose a modified version of the IGF combined with a modified branching criterion. These modifications were found to improve the results under constant conditions in an appropriate way. The question of when oblate particles branch remains open, but the proposed approach yielded promising results.

The importance of explicit habit prediction for deposition, aggregation and, in part, riming was demonstrated in a simplified 1-D snow shaft simulation. Columnar particles fall faster than their counterparts without explicit habits, and the shortened residence time leads to less ice mass, independent of the IGF configuration. The reduced mass translates into rather weak aspect ratios and the resulting smaller cross-sectional areas significantly reduce the aggregation rate. However, riming is highly effective and partially enhances aggregation due to the assumed effective rounding, thus, increasing the cross-sectional area. For the original IGF configuration, this effect is most pronounced because of the more pronounced aspect ratios that develop due to the prolate maximum around the nucleation temperature.

The deposition rate of the plates is significantly increased compared to the m-D-particles for the original IGF at lower fall velocities, especially for large particles, resulting in a higher mass flux. The planar geometry has a positive effect on the aggregation rate, with the opposite effect observed for prolates. The habit effect is partially mitigated when using the modified branching criterion: particles branch later, stay denser, accelerate more, and grow slower than for the original IGF. In turn, the aggregation rates decrease, but are still higher than when no habits are formed. It remains an open question when oblate particles branch, but the proposed approach showed reasonable results.

Furthermore, large LWCs rapidly transform planar crystals into rimed particles once they reach the onset of riming. If the threshold is already exceeded when entering the LWZ, we do not find a significant effect of habit prediction on riming rates.

Given the importance of ice microphysical processes in mixed-phase clouds, ice habits are highly influential and affect cloud lifetime. The variability of atmospheric conditions shapes individual particles whose characteristics cannot be generalized by broad classifications. The chosen one-dimensional scenarios can only describe parts of the impact of an explicit habit prediction on process rates, but they already emphasize that it is of first order. By design, the setup does not allow the atmosphere to change dynamically, but these effects should play a role in the competition for water vapor and ultimately alter precipitation rates. By not considering the development of updrafts (as found by e. g. von Terzi et al., 2022) or turbulent motions, some of the effects of habits might be overlooked, as these phenomena can increase the probability of aggregation or trigger secondary ice processes such as ice-ice collisions (Phillips et al., 2017b).

The current implementation of an explicit habit prediction should be subject to continuous development in the future to overcome certain limitations and to reduce uncertainties in the process description. The use of the IGF to describe the growth tendency may adequately capture the primary habit development, but the development of secondary habits and their consideration are still meaningful for a complete picture.

In the current state, the detailed information on particle properties provided by *McSnow* can be used for monomer-dominated case studies based on polarimetric measurements. This demonstrates the ability of the model to reproduce polarimetric process footprints and to serve as a numerical laboratory to study microphysical processes in clouds. For more stationary cloud systems, the one-dimensional setup can already provide important insights into the in-cloud process feedback and help to test observational hypotheses. Modeling the impact of particle-scale ice habits on cold-rain process rates provides valuable information that can serve as a benchmark for the development of parameterizations for NWP (Seifert and Rasp, 2020; Seifert and Siewert, 2024).

8.1.2 *Part II: Investigation of Ice Microphysical Features by Combining Numerical Modeling and Polarimetric Fingerprint Analysis*

The improvements realized in the representation of ice microphysical habits of monomers serve as the starting point for the simulation of more realistic atmospheric situations. We investigate IMP fingerprints using the *McSnow* model after it has been successfully characterized regarding its sensitivities and uncertainties in microphysical processes. However, the complexity and computational requirements make it difficult to perform IMP fingerprint studies in two- or rather three-dimensional setups. To overcome this, a weather situation with persistent radar signals has been chosen from the available TRIPEx-pol-scan observational campaign, allowing for meaningful average profiles to be derived for one-dimensional simulations. The concurrent collection of ground observations and the deployment of radiosondes facilitate the acquisition of a more comprehensive overview of the atmospheric condition. The observations have been evaluated with regard to the identification of persistent ice microphysical characteristics, which serve as distinctive indicators of in-cloud ice microphysical processes. In consideration of the presumed liquid water content and the paramount importance of portraying the aggregation process, the probability of rime splintering and the dependence on the sticking efficiency were identified as additional subjects for investigation.

The general model configuration that demonstrated optimal performance in Chapter 5 was employed, incorporating the revised IGF, modified branching criterion, and terminal velocity interpolation between prolate and cylindrical shape assumptions. This configuration was utilized with the assumption of a static and prescribed atmospheric state, based on a radiosonde profile. The lack of a dynamic atmosphere during the experimental phase resulted in slightly insufficient aggregation, as the static setup hindered the development of increased particle concentrations in possible updrafts and therefore suppressed collision and aggregation events. To partly mitigate these effects, a variance to the terminal velocities of each hydrometeor involved in a collision event was applied, inspired by the approach of varying the terminal velocities for the collision efficiency described by Böhm (1992c).

The capacity of *McSnow* to reproduce a dendrite-dominated meteorological situation chosen from the TRIPEx-pol-scan campaign was evaluated by examining the average precipitation rate and comparing it with the vertical radar profiles. The simulations reached a quasi-steady state at a precipitation rate of $0.3\,\mathrm{mm h^{-1}}$, which is similar to the rates observed at the JOYCE-CF campaign site.

A comparison of the radar variables was conducted using forward simulation techniques, which revealed discrepancies in the initial growth of reflectivity. These inconsistencies can be attributed to the difficulty in accurately representing the initial state of particle size and shape distribution. The simulated MDV profile captured key features, including the slowdown when the DGL is approached and agreed remarkably with the observed ones. The profiles of variables related to the growth of particles, such as the DWRs, exhibited potential for enhancement, particularly with regard to aggregation. Conversely, the qualitative agreement between the observations and the simulations for the sZ_{DR} and $sZ_{\mathbf{DR,max}}$ was satisfactory. The representation of K_{DP} proved to be a challenging aspect of the study. While the simulated profile demonstrated a general increase in response to warmer temperatures, the distinctive maximum, potentially attributable to SIP, was not accurately replicated. The comparison between the mean vertical profiles simulated with those of the observations was encouraging, as were the spectrograms, which highlighted that the lack of atmospheric dynamics and turbulence had a notable impact on the spectral width.

A second experiment was conducted to further extend the study and investigate the impact of a different parameterization for the sticking efficiency, based on the work of Karrer et al. (2021). This configuration demonstrated a positive impact on the quality of the reflectivity profile, encompassing the agreement of the simulated profiles of both DWR profiles. The alteration in sticking efficiency resulted in an increase in aggregation, which in turn led to the profiles reaching similar signal strengths. The Z_{DR} and $sZ_{\mathbf{DR,max}}$ of the second experiment exhibited qualitative similarities in their profiles, yet the quantitative values were not representative of the actual results. In contrast to the aforementioned improvements, the enhanced aggregation of the second configuration resulted in a negative impact with regard to the alignment of the K_{DP} profile with the observations, which already exhibited suboptimal representation.

In light of the prevailing lack of consensus regarding the K_{DP} profile, we postulated the potential absence of a SIP mechanism like rime-splintering, which could be responsible for the generation of a higher IPNC and, consequently, the observed K_{DP} signal. The description of the rime-splintering process implemented (see Sec. 2.2.7.1) proved ineffective in producing particles based on the rime mass produced with the given LWC prescribed in this setup. The chapter concluded with the hypothesis that the fragmentation could be a potential SIP process to explain the some of the discrepancy, which served to advance the third objective.

Although the one-dimensional setup has inherent limitations, including the lack of representation of dynamic effects and feedback between microphysics and atmospheric state, it has demonstrated that *McSnow*, including the explicit habit prediction, can serve as a numerical laboratory for ice microphysical processes. Under the appropriate conditions and with a valid forward model, it yields plausible synthetic polarimetric observations that are valuable for studying IMP fingerprints.

8.1.3 *Part III: Ice-Ice Collisions as a Potential Secondary Ice Production Process*

The significance of different secondary ice productions in explaining the discrepancy between INP and IPNC is a topic of extensive debate within the scientific community. The potential for SIPs, such as fragmentation, to explain the observed increase in ice particle density has been put forth as a hypothesis based on empirical laboratory studies.

The third objective was to examine the potential of ice-ice collisions as a mechanism for producing INP and, thus, to provide a partial explanation for the inconsistency

between the number of INP and the IPNC.
As a preliminary step, the original fragmentation scheme put forth by Phillips et al. (2017a) was initially implemented in the particle-based approach of *McSnow*. The Phillips fragmentation scheme (PFS) categorizes the particle habit and subsequent collision types based on size, the ambient temperature and the degree of riming. Nevertheless, particles undergoing sedimentation may depart from their original ambient conditions, which could lead to a potential re-categorization and a change in fragmentative potential. It is anticipated that the ejection of fragments does not necessary depend on the ambient conditions but on the individual particle conditions, where the fragmentation will be most effective if particles with high fragility are involved in the collision.
In a subsequent step, we elected to modify certain original assumptions in light of the availability of particle data in *McSnow*. The original categorization was abandoned in favor of categories based on particle shape, apparent density, and monomer number. Based on results from the field of material science, the physical concept of fracture toughness was applied to the framework, redefining the asperity-fragility coefficient and effectively increasing the number of controllable variables while eliminating the dependency on some of the empirical fits.
The number density of breakable asperities has been assumed to be habit-dependent: particles with delicate structures have more points of breakage than simple geometries such as sturdy plates or short columns. The groundwork laid out by the experiments of Vardiman (1974), Griggs and Choularton (1986), and Takahashi et al. (1991) has enabled the estimation of the number density of different particle types and has highlighted the question of the role of riming and in how to treat rimed particles. A simplified geometry of the asperities has been proposed that is independent of a priori particle categorization but based on the apparent density. Furthermore, a description of the shapes, apparent densities, and monomer number of the two colliding particles following the collision has been put forth. The description assumes that the fragile parts of a particle are broken off, which increases the apparent density of the remaining hydrometeor while simultaneously causing a rounding of the particle. Collisions can cause larger aggregates to lose around 1 fragment per 10 monomers collected.

With the Updated fragmentation scheme (UFS) in place, both the PFS and UFS have demonstrated to produce reasonable results for idealized collisions of hail stones with different ice particle types. While the PFS demonstrates a pronounced dependence on the degree of riming, the UFS integrates the influence of accreted rime into the notion of particle fragility.
In order to gain insight into the impact of fragmentation on a well-characterized system, the potential consequences of fragmentation were investigated using the one-dimensional snow shaft experiment outlined in Chapter 5. The two schemes exhibited differential behavior in relation to the dominant particle habit. In the oblate-dominated case, the use of the UFS resulted in the ejection of a comparable number of fragments compared to PFS. The prolate-dominated setup demonstrated that categorization of the PFS based on ambient temperature is more effective in causing the ejection of ice crystals compared to using the UFS. In both cases, the activity of the PFS was dependent on the presence of rime, whereas for the UFS, fragmentation events for unrimed particles have been observed.
In a final experiment, both schemes were applied to the model configuration based

on the real case configuration of a dendrite-dominated cloud (Chapter 6) to demonstrate the full potential of the combination of polarimetric observations with a model serving as a numerical laboratory to investigate the new parameterizations. The results indicated that fragmentation is only actively producing secondary ice under the given conditions for the UFS, but does not alter the simulated polarimetric variables notably. The presented PSD demonstrated that fragments are ejected exclusively in the LWZ, which suggests that the supplementary mass introduced by riming is essential for achieving the requisite CKE to break particles.

Chapter 7 closes with a series of key questions that future research could address in order to gain a deeper understanding of the ice-ice collision process. It is proposed that the Updated fragmentation scheme, which is founded upon the characteristics of particles, could function as a foundation for modeling fragmentation at the particle level. This could enable a deeper understanding of the fragmentation as a SIP mechanism.

8.2 OUTLOOK: ADVANCING ICE MICROPHYSICAL UNDERSTANDING

The use of a LPM to model microphysics has the potential to greatly enhance our understanding of the intricate interactions between the atmosphere and the various types of hydrometeors. The process descriptions at the particle level permit the incorporation of the most advanced physical understanding, which in turn allows for the entanglement of the complex feedback introduced by the simultaneity of all ongoing processes.

The objective of the first part of this thesis was to demonstrate the value of incorporating comprehensive physical parameterizations, such as those presented in the work of Böhm, and to suggest modifications or reviews where appropriate. While the piecewise effort may be laborious, the results presented here should motivate scientists to invest the necessary effort. A case in point is the introduction of a shape-dependent ventilation factor, where a number of groups, partly from neighboring fields, have laid the groundwork that is crucial if one is to examine non-spherical particles.

Given the central role of the IGF in numerous recent habit prediction models, it is imperative to devote resources to enhancing our comprehension of growth regimes, particularly with respect to saturation pressures below water saturation. In this regard, the facet-based hypothesis could be a candidate to incorporate the supersaturation dependence and remove the caveat that the IGF is strictly valid only for water saturation. Future laboratory studies could be directed towards elucidating the deposition behavior under unfavorable habit conditions, for instance, the growth of oblate particles in an environment that favors prolate growth.

A key improvement for LPMs like *McSnow* will be a generalized description for spheroids regarding the habit of aggregates with increasing monomer number and crystal type, as this causes strong feedbacks with most microphysical processes. It is unclear whether the extrapolation of the explicit habit prediction used for monomers is adequate for aggregates, given that mechanisms like branching or hollowing might operate in a manner that differs based on the internal structure of aggregates. Furthermore, the formation of more intricate geometries by aggregates requires the development of novel, comprehensive descriptions that account for the composition of the particles included. While our focus was on mixed-phase clouds warmer than $T > 253\,K$, the representation of polycrystalline particles or the inclusion of mixed forms such as capped columns could be realized in an effort to improve an understanding of their origin story.

While the one-dimensional cloud parcel model provides invaluable insights into microphysical process rates, it inherently lacks the complexity of a dynamically evolving atmosphere. Future research should therefore focus on embedding these enhanced microphysical schemes within multi-dimensional models, such as LES or cloud-resolving models, to investigate the intricate feedbacks between cloud dynamics and microphysics. This will allow for a more comprehensive assessment of how improvements in habit representation and SIP processes impact cloud evolution in a more realistic atmospheric context. For this application, *McSnow* has been coupled to the ICON model (Zängl et al., 2015) to serve as a possible microphysics scheme. In such a configuration, the LPM approach of *McSnow* can be employed to simulate the microphysical processes at the particle level, with the resulting process rates subsequently fed back to ICON. Due to the enormous computational resources required to perform such simulations with statistical convergence, only a handful of setups have been tested yet. In particular, the coupled model configuration has been part of the 10th International Cloud Modeling Workshop (*The 10th International Cloud Modeling Workshop* 2024) in an effort to investigate the effects of strong vertical wind shear on different representations of microphysical processes used in numerical models based on the COPE case (Lasher-Trapp et al., 2018; Leon et al., 2016).

The case study presented in Chapters 6 and 7 illustrates the potential of a numerical laboratory comprising cutting-edge polarimetric radar observations and a microphysics model that enables the development of process descriptions at the particle level. Based on such simulations and by exploiting existing and collecting new observation datasets, a broader understanding of the detailed importance of the manifold hydrometeor shapes can be achieved. Future improvements in observational instrumentation, coupled with new retrieval techniques, will facilitate the profiling of the various IMP fingerprints with greater clarity.
High-quality observational campaigns like TRIPEx-pol-scan provide a plethora of such fingerprints, which can be used to further investigate the capabilities of models and to identify flawed or missing process descriptions. With regard to the capabilities, observations indicating the presence of prolate-dominated atmospheric states have proven challenging to reconcile with the information available from radiosondes and radars. This should be investigated in other scenarios with a more favorable radiosonde profiles. Alternatively, reliable models can assist in the retrieval of potential atmospheric conditions through the process of reverse engineering observables, thereby offering insight into the internal characteristics of clouds.

Future research could also concentrate on elucidating the significance of SIP in relation to the correlation between INP and IPNC. The majority of processes identified as potential sources for SIP are only inadequately described, if they are described at all. In this regard, Korolev and Leisner (2020) and Morrison et al. (2020) make a compelling case for a more expansive support of new laboratory studies, coupled with a repetition of existing ones, with the objective of gathering more information across the entire parameter space. In order to gain a deeper understanding of ice-ice collisions and the potential fragmentation of particles, it is essential to address a number of crucial questions, which we outlined in Section 7.3.

Neighboring fields such as material science can assist in comprehending the actual processes occurring within clouds, as illustrated in Chapter 7.

By utilizing LPM simulations, it is feasible to translate the evolving understanding at the particle level into the formulation of bulk parameterizations. It may appear that the transfer of the degree of complexity of individual particle information to bulk or bin microphysical schemes is unfeasible. However, the development of solid process understanding can facilitate the creation of descriptions that capture the crucial information.

An alternative approach is the deployment of machine learning (ML) algorithms to derive process rates from models to generate mathematical process descriptions. As indicated by Seifert and Rasp (2020), neural network models demonstrate proficiency in test data, yet their capacity to resolve ordinary differential equations is inferior to that of traditional parameterizations. This finding implies the necessity for integrating more sophisticated methodologies to address the limitations of existing warm-rain schemes.

The increased complexity of cold-rain microphysics further underscores this need. In this regard, detailed LPMs such as *McSnow* are essential for both benchmark simulations and for generating high-fidelity training data for specified process rates. Recent advancements, as highlighted by Seifert and Siewert (2024), demonstrate the successful application of ML in building complex bulk ice microphysics schemes by coarse-graining the output of LPMs. Their work, which uses *McSnow* simulations as training data, shows that ML can effectively perform a coarse-graining of particle-resolved microphysics to multi-category two-moment bulk equations. Notably, this ML-based P3-like scheme (predicting prognostic particle properties like melt water, rime mass, and rime volume) not only reproduces *McSnow* simulations accurately in a box model setting but also improves the representation of the stratiform region in idealized squall line simulations when compared to classic two-moment bulk schemes. Furthermore, Seifert and Siewert (2024) confirm the stability and meaningful results of their ML-based scheme in three-dimensional real-case simulations, even if significant improvements in such complex scenarios require further investigation. This pioneering work underscores the potential of ML to develop bulk schemes of arbitrary complexity by leveraging detailed super-particle simulations. The successful development of this ML-based P3-like scheme represents a potential stride towards bridging the gap between highly detailed Lagrangian particle models and computationally efficient bulk schemes. This methodology offers a novel pathway to incorporate intricate microphysical processes, otherwise too complex for traditional parameterizations, into operational numerical weather prediction and climate models, thereby enabling more realistic and robust simulations of atmospheric phenomena.

LPMs such as *McSnow* offer invaluable insights into the microphysical processes of clouds, particularly in the cold phase, due to their implementation of advanced and state-of-the-art process descriptions. The advancements made in *McSnow* within this thesis, particularly through the improved habit prediction schemes and the refined understanding of ice-ice collision fragmentation, provide crucial and detailed microphysical information. This enhanced process-level understanding directly contributes to reducing uncertainties in the parameterizations used within LES, NWP, and climate models, ultimately leading to more accurate simulations of cloud properties, precipitation formation, and their broader impacts on Earth's energy budget and hydrological cycle.

A

APPENDIX

A.1 INVESTIGATION OF ICE MICROPHYSICAL PROCESS FINGERPRINTS

The DWD surface weather map for 12:00 UTC provides the synoptic context for the observations presented in Section 6.1.1. The surface analysis clearly depicts a occluding front extending across Western Germany, its associated frontal zone directly encompassing the region of JOYCE-CF and consistently producing stratiform clouds and widespread moderate precipitation. The observed stratiform cloud cover and continuous precipitation from both SEVIRI and radar (not shown) are entirely consistent with the classic signature of an active frontal passage.

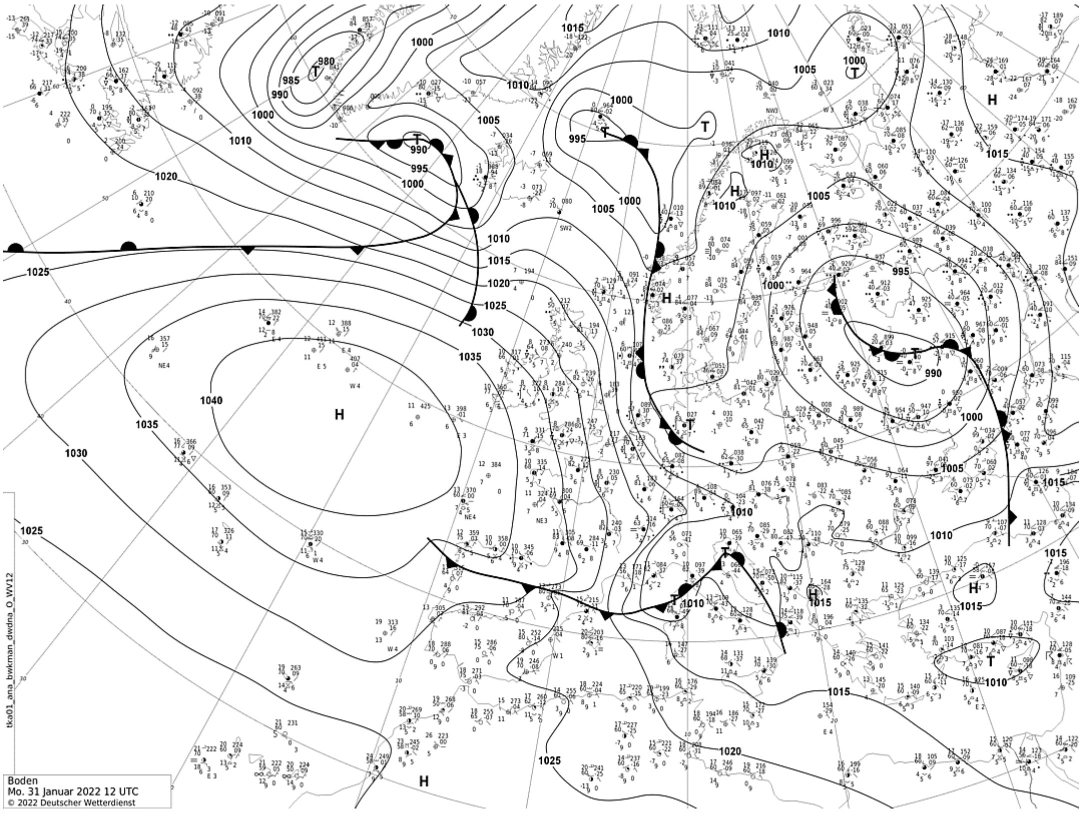

Figure A.1: Synoptic chart of the DWD on 31. January 2022 at 12:00 UTC.

A.2 FRAGMENTATION DUE TO ICE-ICE COLLISION

Table A.2, as detailed in the source text of Phillips et al. (2017a), illustrates the initial parameters and categorizations utilized in Equation 2.79. It should be noted that the variables utilized in the UFS are designated with nomenclature that differs from that employed in the PFS. To avoid confusion, it should be noted that A_n is used in the UFS instead of the variable name A for the estimated asperity number density. The same convention is applied to the asperity-fragility coefficient which is referred to as C_f in the UFS instead of the variable name C. It should be noted that the utilized D is equivalent to the maximum dimension of the particle, D_{max}. The UFS employs a single limiter for $N_{max} = 1000$. All other variables are not represented in the UFS.

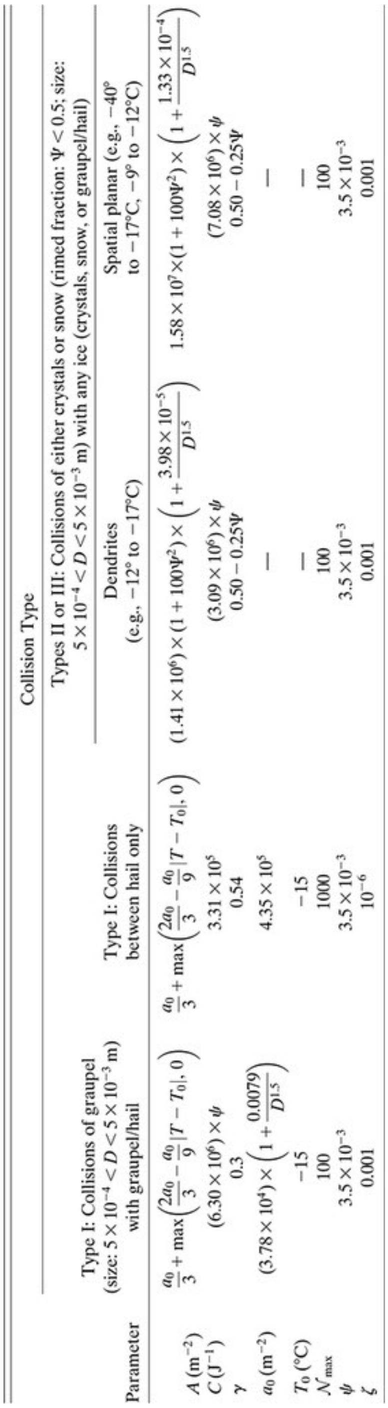

Figure A.2: Parameters of Eq. 2.79 of the PFS for the three collision types (Phillips et al., 2017a). ©American Meteorological Society. Used with permission.

Parameter	Collision Type			
	Type I: Collisions of graupel (size: $5 \times 10^{-4} < D < 5 \times 10^{-3}$ m) with graupel/hail	Type I: Collisions between hail only	Types II or III: Collisions of either crystals or snow (rimed fraction: $\Psi < 0.5$; size: $5 \times 10^{-4} < D < 5 \times 10^{-3}$ m) with any ice (crystals, snow, or graupel/hail): Dendrites (e.g., −12° to −17°C)	Types II or III: Spatial planar (e.g., −40° to −17°C, −9° to −12°C)
A (m^{-2})	$\frac{a_0}{3} + \max\left(\frac{2a_0}{3} - \frac{a_0}{9}\lvert T - T_0\rvert, 0\right)$	$\frac{a_0}{3} + \max\left(\frac{2a_0}{3} - \frac{a_0}{9}\lvert T - T_0\rvert, 0\right)$	$(1.41 \times 10^6) \times (1 + 100\Psi^2) \times \left(1 + \frac{3.98 \times 10^{-5}}{D^{1.5}}\right)$	$1.58 \times 10^7 \times (1 + 100\Psi^2) \times \left(1 + \frac{1.33 \times 10^{-4}}{D^{1.5}}\right)$
C (J^{-1})	$(6.30 \times 10^6) \times \psi$	3.31×10^5	$(3.09 \times 10^6) \times \psi$	$(7.08 \times 10^6) \times \psi$
γ	0.3	0.54	$0.50 - 0.25\Psi$	$0.50 - 0.25\Psi$
a_0 (m^{-2})	$(3.78 \times 10^4) \times \left(1 + \frac{0.0079}{D^{1.5}}\right)$	4.35×10^5	—	—
T_0 (°C)	−15	−15	—	—
$\mathcal{N}_{max}$	100	1000	100	100
ψ	3.5×10^{-3}	3.5×10^{-3}	3.5×10^{-3}	3.5×10^{-3}
ζ	0.001	10^{-6}	0.001	0.001

As demonstrated in Section 7.2.2.2, the fragmentation schemes presented have a relatively minor impact on the synthetic radar profiles. Here, we complete the analysis of the polarimetric variables by adding the spectrograms for both the PFS as well as the UFS in Figures A.3i and A.3ii. Although this type of analysis can be useful for detecting isolated events that are not represented in the combined synthetic radar profile, the fragmentation process does not yield patterns that could be identified as characteristic of the process.

(i) Configuration C2

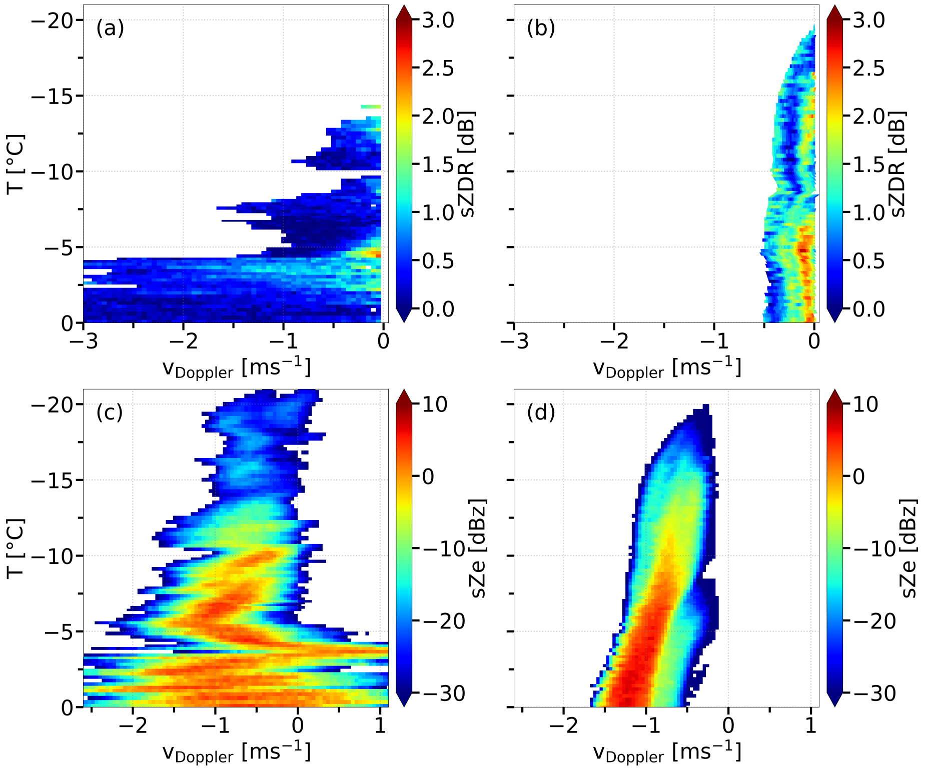

(ii) Configuration C3

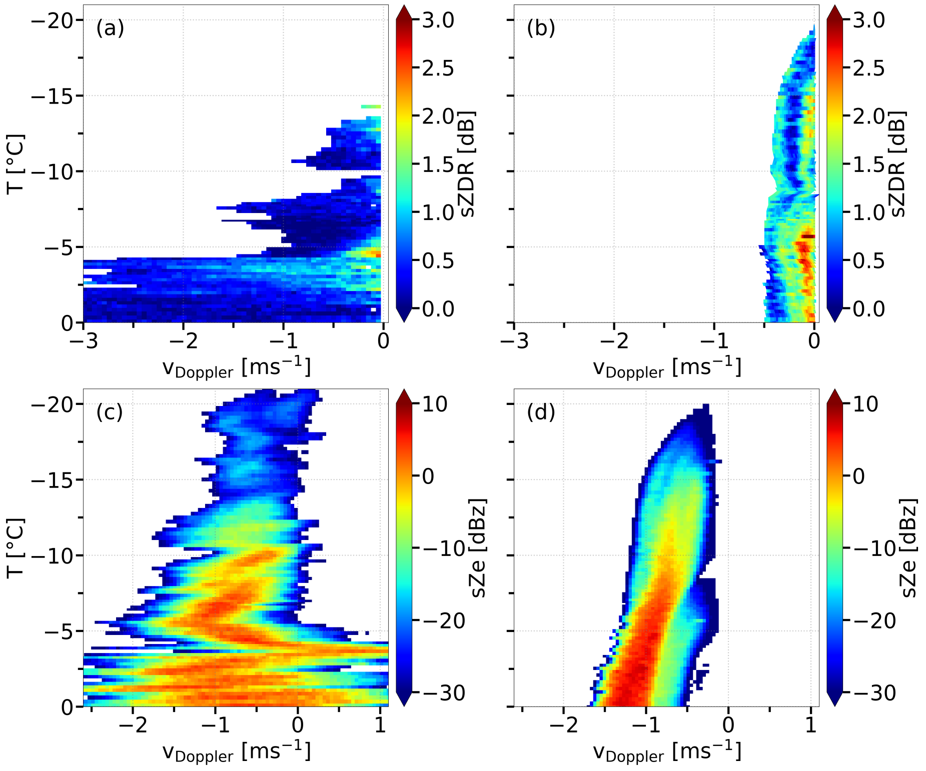

Figure A.3: Comparison between radar and synthetic spectrograms of (a) observed and (b) simulated sZ_{DR}, as well as (c) observed and (d) simulated sZ_e for the configurations C2 ((i), top four plots) and C3 ((ii), bottom four plots) for the dendrite event.

BIBLIOGRAPHY

Abraham, F. F. (1970). "Functional Dependence of Drag Coefficient of a Sphere on Reynolds Number." In: *The Physics of Fluids* 13.8, pp. 2194–2195. DOI: `10.1063/1.1693218`.

Anderson, T. L. (2017). *Fracture Mechanics - Fundamentals and Applications*. Taylor & Francis Inc, p. 688. DOI: `10.1201/9781315370293`.

Andrejczuk, M., J. M. Reisner, B. Henson, M. K. Dubey, and C. A. Jeffery (2008). "The potential impacts of pollution on a nondrizzling stratus deck: Does aerosol number matter more than type?" In: *Journal of Geophysical Research* 113 (D19), p. D19204. DOI: `10.1029/2007JD009445`.

Asakawa, H., G. Sazaki, K. Nagashima, S. Nakatsubo, and Y. Furukawa (2016). "Two types of quasi-liquid layers on ice crystals are formed kinetically." In: *Proceedings of the National Academy of Sciences* 113.7, pp. 1749–1753. DOI: `10.1073/pnas.1521607113`.

Auer, A. H. and D. L. Veal (1970). "The Dimension of Ice Crystals in Natural Clouds." In: *Journal of Atmospheric Sciences* 27.6, pp. 919–926. DOI: `10.1175/1520-0469(1970)027<0919:TDOICI>2.0.CO;2`.

Bailey, M. P. and J. Hallett (2009). "A Comprehensive Habit Diagram for Atmospheric Ice Crystals: Confirmation from the Laboratory, AIRS II, and Other Field Studies." In: *Journal of the Atmospheric Sciences* 66 (9), pp. 2888–2899. DOI: `10.1175/2009JAS2883.1`.

Baran, A. J. (2012). "From the single-scattering properties of ice crystals to climate prediction: A way forward." In: *Atmospheric Research* 112, pp. 45–69. DOI: `10.1016/j.atmosres.2012.04.010`.

Barrett, A. I., C. D. Westbrook, J. C. Nicol, and T. H. Stein (2019). "Rapid ice aggregation process revealed through triple-wavelength Doppler spectrum radar analysis." In: *Atmospheric Chemistry and Physics* 19 (8), pp. 5753–5769. DOI: `10.5194/ACP-19-5753-2019`.

Bauer, P., P. D. Dueben, T. Hoefler, T. Quintino, T. C. Schulthess, and N. P. Wedi (2021). "The digital revolution of Earth-system science." In: *Nature Computational Science* 1.2, pp. 104–113. DOI: `10.1038/s43588-021-00023-0`.

Beard, K. V. (1976). "Terminal Velocity and Shape of Cloud and Precipitation Drops Aloft." In: *Journal of Atmospheric Sciences* 33 (5), pp. 851–864. DOI: `10.1175/1520-0469(1976)033<0851:TVASOC>2.0.CO;2`.

– (1980). "The Effects of Altitude and Electrical Force on the Terminal Velocity of Hydrometeors." In: *Journal of Atmospheric Sciences* 37.6, pp. 1363–1374. DOI: `10.1175/1520-0469(1980)037<1363:TEOAAE>2.0.CO;2`.

Beard, K. V. and S. N. Grover (1974). "Numerical Collision Efficiencies for Small Raindrops Colliding with Micron Size Particles." In: *Journal of Atmospheric Sciences* 31.2, pp. 543–550. DOI: `10.1175/1520-0469(1974)031<0543:NCEFSR>2.0.CO;2`.

Billault-Roux, A.-C., P. Georgakaki, J. Gehring, L. Jaffeux, A. Schwarzenboeck, P. Coutris, A. Nenes, and A. Berne (2023). "Distinct secondary ice production processes observed in radar Doppler spectra: insights from a case study." In: *Atmo-*

spheric Chemistry and Physics 23.17, pp. 10207–10234. DOI: `10.5194/acp-23-10207-2023`.

Bodas-Salcedo, A., J. P. Mulcahy, T. Andrews, K. D. Williams, M. A. Ringer, P. R. Field, and G. S. Elsaesser (2019). "Strong Dependence of Atmospheric Feedbacks on Mixed-Phase Microphysics and AerosolCloud Interactions in HadGEM3." In: *Journal of Advances in Modeling Earth Systems* 11 (6), pp. 1735–1758. DOI: `10.1029/2019MS001688`.

Böhm, J. P. (1989). "A General Equation for the Terminal Fall Speed of Solid Hydrometeors." In: *Journal of the Atmospheric Sciences* 46.15, pp. 2419–2427. DOI: `10.1175/1520-0469(1989)046<2419:AGEFTT>2.0.CO;2`.

– (1990). "On the hydrodynamics of cloud and precipitation particles." PhD thesis. ETH Zurich. DOI: `10.3929/ethz-a-000578177`.

– (1992a). "A general hydrodynamic theory for mixed-phase microphysics. Part I: drag and fall speed of hydrometeors." In: *Atmospheric Research* 27.4, pp. 253–274. DOI: `10.1016/0169-8095(92)90035-9`.

– (1992b). "A general hydrodynamic theory for mixed-phase microphysics. Part II: collision kernels for coalescence." In: *Atmospheric Research* 27.4, pp. 275–290. DOI: `10.1016/0169-8095(92)90036-A`.

– (1992c). "A general hydrodynamic theory for mixed-phase microphysics. Part III: Riming and aggregation." In: *Atmospheric Research* 28.2, pp. 103–123. DOI: `10.1016/0169-8095(92)90023-4`.

– (1994). "Theoretical collision efficiencies for riming and aerosol impaction." In: *Atmospheric Research* 32.1, pp. 171–187. DOI: `10.1016/0169-8095(94)90058-2`.

– (1999). "Revision and clarification of "A general hydrodynamic theory for mixed-phase microphysics"." In: *Atmospheric Research* 52.3, pp. 167–176. DOI: `10.1016/S0169-8095(99)00033-2`.

– (2004). "Reply to Comment on "Revision and clarification of 'A general hydrodynamic theory for mixed-phase microphysics' [Böhm J.P., 1999, Atmos. Res. 52, 167–176]"." In: *Atmospheric Research* 69.3, pp. 289–293. DOI: `10.1016/j.atmosres.2003.10.001`.

Brauer, N. S., P. E. Kirstetter, J. B. Basara, S. Hristova-Veleva, S. Tanelli, and F. Joseph Turk (2024). "Precipitation Microphysics in Tropical Cyclones: A Global Perspective Using the NASA Global Precipitation Measurement Mission Dual-Frequency Precipitation Radar." In: *Journal of Geophysical Research: Atmospheres* 129.1, e2023JD038709. DOI: `10.1029/2023JD038709`.

Brdar, S. and A. Seifert (2018). "McSnow: A Monte-Carlo Particle Model for Riming and Aggregation of Ice Particles in a Multidimensional Microphysical Phase Space." In: *Journal of Advances in Modeling Earth Systems* 10.1, pp. 187–206. DOI: `10.1002/2017MS001167`.

Bringi, V., A. Seifert, W. Wu, M. Thurai, G. J. Huang, and C. Siewert (2020). "Hurricane Dorian Outer Rain Band Observations and 1D Particle Model Simulations: A Case Study." In: *Atmosphere* 11 (8), p. 879. DOI: `10.3390/ATMOS11080879`.

CC-BY 4.0 (2013). (Visited on 08/08/2025).

Chen, J.-P. and D. Lamb (1994a). "Simulation of Cloud Microphysical and Chemical Processes Using a Multicomponent Framework. Part I: Description of the Microphysical Model." In: *Journal of the Atmospheric Sciences* 51.18, pp. 2613–2630. DOI: `10.1175/1520-0469(1994)051<2613:SOCMAC>2.0.CO;2`.

– (1994b). “The Theoretical Basis for the Parameterization of Ice Crystal Habits: Growth by Vapor Deposition.” In: *Journal of the Atmospheric Sciences* 51.9, pp. 1206–1222. DOI: `10.1175/1520-0469(1994)051<1206:TTBFTP>2.0.CO;2`.

Chen, Y., P. Jiang, T. Xiong, W. Wei, Z. Fang, and B. Wang (2021). “Drag and heat transfer coefficients for axisymmetric nonspherical particles: A LBM study.” In: *Chemical Engineering Journal* 424, p. 130391. DOI: `10.1016/J.CEJ.2021.130391`.

Choularton, T. W., D. J. Griggs, B. Y. Humood, and J. Latham (1980). “Laboratory studies of riming, and its relation to ice splinter production.” In: *Quarterly Journal of the Royal Meteorological Society* 106 (448), pp. 367–374. DOI: `10.1002/QJ.49710644809`.

Choularton, T. W., J. Latham, and B. J. Mason (1978). “A possible mechanism of ice splinter production during riming.” In: *Nature* 274 (5673), pp. 791–792. DOI: `10.1038/274791a0`.

Climate Change (IPCC), I. P. on (2023). *Climate Change 2021 – The Physical Science Basis: Working Group I Contribution to the Sixth Assessment Report of the Intergovernmental Panel on Climate Change*. Cambridge University Press. DOI: `10.1017/9781009157896`.

Cober, S. G. and R. List (1993). “Measurements of the Heat and Mass Transfer Parameters Characterizing Conical Graupel Growth.” In: *Journal of the Atmospheric Sciences* 50.11, pp. 1591–1609. DOI: `10.1175/1520-0469(1993)050<1591:MOTHAM>2.0.CO;2`.

Connolly, P. J., C. Emersic, and P. R. Field (2012). “A laboratory investigation into the aggregation efficiency of small ice crystals.” In: *Atmospheric Chemistry and Physics* 12 (4), pp. 2055–2076. DOI: `10.5194/acp-12-2055-2012`.

Dedekind, Z., J. Grazioli, P. H. Austin, and U. Lohmann (2023). “Heavy snowfall event over the Swiss Alps: did wind shear impact secondary ice production?” In: *Atmospheric Chemistry and Physics* 23.4, pp. 2345–2364. DOI: `10.5194/acp-23-2345-2023`.

Dedekind, Z., A. Lauber, S. Ferrachat, and U. Lohmann (2021). “Sensitivity of precipitation formation to secondary ice production in winter orographic mixed-phase clouds.” In: *Atmospheric Chemistry and Physics* 21 (19), pp. 15115–15134. DOI: `10.5194/ACP-21-15115-2021`.

Dias Neto, J., S. Kneifel, D. Ori, S. Trömel, J. Handwerker, B. Bohn, N. Hermes, K. Mühlbauer, M. Lenefer, and C. Simmer (2019). “The TRIple-frequency and Polarimetric radar Experiment for improving process observations of winter precipitation.” In: *Earth System Science Data* 11.2, pp. 845–863. DOI: `10.5194/essd-11-845-2019`.

Dong, Y. Y. and J. Hallett (1989). “Droplet accretion during rime growth and the formation of secondary ice crystals.” In: *Quarterly Journal of the Royal Meteorological Society* 115 (485), pp. 127–142. DOI: `10.1002/QJ.49711548507`.

Dunnavan, E. L., Z. Jiang, J. Y. Harrington, J. Verlinde, K. Fitch, and T. J. Garrett (2019). “The shape and density evolution of snow aggregates.” In: *Journal of the Atmospheric Sciences* 76 (12), pp. 3919–3940. DOI: `10.1175/JAS-D-19-0066.1`.

Dziekan, P., M. Waruszewski, and H. Pawlowska (2019). “University of Warsaw Lagrangian Cloud Model (UWLCM) 1.0: a modern large-eddy simulation tool for warm cloud modeling with Lagrangian microphysics.” In: *Geoscientific Model Development* 12 (6), pp. 2587–2606. DOI: `10.5194/gmd-12-2587-2019`.

Egan, B. A. and J. R. Mahoney (1972). “Numerical Modeling of Advection and Diffusion of Urban Area Source Pollutants.” In: *Journal of Applied Meteorology* 11 (2), pp. 312–322. DOI: `10.1175/1520-0450(1972)011<0312:NMOAAD>2.0.CO;2`.

Emersic, C. and P. J. Connolly (2017). "Microscopic observations of riming on an ice surface using high speed video." In: *Atmospheric Research* 185, pp. 65–72. DOI: `10.1016/J.ATMOSRES.2016.10.014`.

Erfani, E. and D. L. Mitchell (2017). "Growth of ice particle mass and projected area during riming." In: *Atmospheric Chemistry and Physics* 17 (2), pp. 1241–1257. DOI: `10.5194/ACP-17-1241-2017`.

Ervens, B., G. Feingold, K. Sulia, and J. Harrington (2011). "The impact of microphysical parameters, ice nucleation mode, and habit growth on the ice/liquid partitioning in mixed-phase Arctic clouds." In: *Journal of Geophysical Research* 116 (D17), p. D17205. DOI: `10.1029/2011JD015729`.

Fabry, F. (2015). *Radar Meteorology: Principles and Practice*. Cambridge University Press. DOI: `10.1017/CBO9781107707405`.

Fan, J., Y. Wang, D. Rosenfeld, and X. Liu (2016). "Review of AerosolCloud Interactions: Mechanisms, Significance, and Challenges." In: *Journal of the Atmospheric Sciences* 73 (11), pp. 4221–4252. DOI: `10.1175/JAS-D-16-0037.1`.

Faraday, M. R. (1850). "On certain conditions of freezing water." In: *Athenaeum* 1181, pp. 640–641.

Field, P. R. and A. J. Heymsfield (2015). "Importance of snow to global precipitation." In: *Geophysical Research Letters* 42 (21), pp. 9512–9520. DOI: `10.1002/2015GL065497`.

Field, P. R., R. J. Hogan, P. R. A. Brown, A. J. Illingworth, T. W. Choularton, P. H. Kaye, E. Hirst, and R. Greenaway (2004). "Simultaneous radar and aircraft observations of mixed-phase cloud at the 100 m scale." In: *Quarterly Journal of the Royal Meteorological Society* 130.600, pp. 1877–1904. DOI: `10.1256/qj.03.102`.

Field, P. R., R. P. Lawson, P. R. A. Brown, G. Lloyd, C. Westbrook, D. Moisseev, A. Miltenberger, A. Nenes, A. Blyth, T. Choularton, P. Connolly, J. Buehl, J. Crosier, Z. Cui, C. Dearden, P. DeMott, A. Flossmann, A. Heymsfield, Y. Huang, H. Kalesse, Z. A. Kanji, A. Korolev, A. Kirchgaessner, S. Lasher-Trapp, T. Leisner, G. McFarquhar, V. Phillips, J. Stith, and S. Sullivan (2017). "Secondary Ice Production: Current State of the Science and Recommendations for the Future." In: *Meteorological Monographs* 58 (1), pp. 7.1–7.20. DOI: `10.1175/AMSMONOGRAPHS-D-16-0014.1`.

Flossmann, A. I. and W. Wobrock (2010). "A review of our understanding of the aerosol–cloud interaction from the perspective of a bin resolved cloud scale modelling." In: *Atmospheric Research* 97 (4), pp. 478–497. DOI: `10.1016/J.ATMOSRES.2010.05.008`.

Francis, J. K. (2000). "Comparison of Hurricane Damage to Several Species of Urban Trees in San Juan, Puerto Rico." In: *Arboriculture & Urban Forestry (AUF)* 26.4, pp. 189–197. DOI: `10.48044/jauf.2000.022`.

Francis, J. K. and A. J. Gillespie (1993). "Relating Gust Speed to Tree Damage in Hurricane Hugo, 1989." In: *Arboriculture & Urban Forestry (AUF)* 19.6, pp. 368–372. DOI: `10.48044/jauf.1993.057`.

Fukuta, N. (1969). "Experimental Studies on the Growth of Small Ice Crystals." In: *Journal of the Atmospheric Sciences* 26.3, pp. 522–531. DOI: `10.1175/1520-0469(1969)026<0522:ESOTGO>2.0.CO;2`.

Garrett, T. J., S. E. Yuter, C. Fallgatter, K. Shkurko, S. R. Rhodes, and J. L. Endries (2015). "Orientations and aspect ratios of falling snow." In: *Geophysical Research Letters* 42.11, pp. 4617–4622. DOI: `https://doi.org/10.1002/2015GL064040`.

Gaussiat, N., H. Sauvageot, and A. J. Illingworth (2003). "Cloud Liquid Water and Ice Content Retrieval by Multiwavelength Radar." In: *Journal of Atmospheric and*

Oceanic Technology 20.9, pp. 1264–1275. DOI: `10.1175/1520-0426(2003)020<1264:CLWAIC>2.0.CO;2`.

Gautam, M. (2022). “Fragmentation in Graupel-Snow Collisions.” MA thesis. Lund University, pp. 1–48.

Gavze, E. and A. Khain (2022). “Gravitational Collision of Small Nonspherical Particles: Swept Volumes of Prolate and Oblate Spheroids in Calm Air.” In: *Journal of the Atmospheric Sciences* 79.6, pp. 1493–1514. DOI: `10.1175/JAS-D-20-0336.1`.

Georgakaki, P., G. Sotiropoulou, É. Vignon, A. C. Billault-Roux, A. Berne, and A. Nenes (2022). “Secondary ice production processes in wintertime alpine mixed-phase clouds.” In: *Atmospheric Chemistry and Physics* 22 (3), pp. 1965–1988. DOI: `10.5194/ACP-22-1965-2022`.

Gillespie, D. T. (1972). “The Stochastic Coalescence Model for Cloud Droplet Growth.” In: *Journal of Atmospheric Sciences* 29 (8), pp. 1496–1510. DOI: `10.1175/1520-0469(1972)029<1496:TSCMFC>2.0.CO;2`.

– (1976). “A general method for numerically simulating the stochastic time evolution of coupled chemical reactions.” In: *Journal of Computational Physics* 22 (4), pp. 403–434. DOI: `10.1016/0021-9991(76)90041-3`.

Gonda, T. (1980). “The influence of the diffusion of vapor and heat on the morphology of ice crystals grown from the vapor.” In: *Journal of Crystal Growth* 49 (1), pp. 173–181. DOI: `10.1016/0022-0248(80)90079-2`.

Gosset, M. and H. Sauvageot (1992). “A Dual-Wavelength Radar Method for Ice-Water Characterization in Mixed-Phase Clouds.” In: *Journal of Atmospheric and Oceanic Technology* 9.5, pp. 538–547. DOI: `10.1175/1520-0426(1992)009<0538:ADWRMF>2.0.CO;2`.

Grazioli, J., G. Lloyd, L. Panziera, C. R. Hoyle, P. J. Connolly, J. Henneberger, and A. Berne (2015). “Polarimetric radar and in situ observations of riming and snowfall microphysics during CLACE 2014.” In: *Atmospheric Chemistry and Physics* 15.23, pp. 13787–13802. DOI: `10.5194/acp-15-13787-2015`.

Griffin, E. M., T. J. Schuur, and A. V. Ryzhkov (2018). “A Polarimetric Analysis of Ice Microphysical Processes in Snow, Using Quasi-Vertical Profiles.” In: *Journal of Applied Meteorology and Climatology* 57.1, pp. 31–50. DOI: `10.1175/JAMC-D-17-0033.1`.

Griggs, D. J. and T. W. Choularton (1986). “A laboratory study of secondary ice particle production by the fragmentation of rime and vapour-grown ice crystals.” In: *Quarterly Journal of the Royal Meteorological Society* 112.471, pp. 149–163. DOI: `10.1002/qj.49711247109`.

Grzegorczyk, P., S. Yadav, F. Zanger, A. Theis, S. K. Mitra, S. Borrmann, and M. Szakáll (2023). “Fragmentation of ice particles: laboratory experiments on graupel–graupel and graupel–snowflake collisions.” In: *Atmospheric Chemistry and Physics* 23.20, pp. 13505–13521. DOI: `10.5194/acp-23-13505-2023`.

Grzegorczyk, P. (2022). “Exploring the role of fragmentation of ice particles by laboratory studies.” MA thesis. Ecole OPGC, Université Clermont Auvergne, p. 39.

Hall, W. D. and H. R. Pruppacher (1976). “The Survival of Ice Particles Falling from Cirrus Clouds in Subsaturated Air.” In: *Journal of the Atmospheric Sciences* 33.10, pp. 1995–2006. DOI: `10.1175/1520-0469(1976)033<1995:TSOIPF>2.0.CO;2`.

Hallett, J. and S. C. Mossop (1974). “Production of secondary ice particles during the riming process.” In: *Nature* 249.5452, pp. 26–28. DOI: `10.1038/249026a0`.

Hallgren, R. E. and C. L. Hosler (1960). "Preliminary Results on the Aggregation of Ice Crystals." In: *Physics of Precipitation: Proceedings of the Cloud Physics Conference, Woods Hole, Massachusetts, June 3–5, 1959*. American Geophysical Union (AGU), pp. 257–263. DOI: `10.1029/GM005p0257`.

Harrington, J. Y., A. Moyle, L. E. Hanson, and H. Morrison (2019). "On Calculating Deposition Coefficients and Aspect-Ratio Evolution in Approximate Models of Ice Crystal Vapor Growth." In: *Journal of the Atmospheric Sciences* 76.6, pp. 1609–1625. DOI: `10.1175/JAS-D-18-0319.1`.

Harrington, J. Y. and G. F. Pokrifka (2021). "Approximate Models for Lateral Growth on Ice Crystal Surfaces during Vapor Depositional Growth." In: *Journal of the Atmospheric Sciences* 78 (3), pp. 967–981. DOI: `10.1175/JAS-D-20-0228.1`.

Hartmann, S., J. Seidel, A. Keinert, A. Kiselev, T. Leisner, and F. Stratmann (2023). "Secondary ice production - No evidence of a productive rime-splintering mechanisms during dry and wet growth." In: *EGU General Assembly 2023, Vienna, Austria, 24–28 Apr 2023, EGU23-11199*. DOI: `10.5194/egusphere-egu23-11199`.

Hashino, T. and G. J. Tripoli (2007). "The Spectral Ice Habit Prediction System (SHIPS). Part I: Model Description and Simulation of the Vapor Deposition Process." In: *Journal of the Atmospheric Sciences* 64.7, pp. 2210–2237. DOI: `10.1175/JAS3963.1`.

Heymsfield, A. (1972). "Ice Crystal Terminal Velocities." In: *Journal of Atmospheric Sciences* 29 (7), pp. 1348–1357. DOI: `10.1175/1520-0469(1972)029<1348:ICTV>2.0.CO;2`.

Heymsfield, A. J. and C. D. Westbrook (2010). "Advances in the Estimation of Ice Particle Fall Speeds Using Laboratory and Field Measurements." In: *Journal of the Atmospheric Sciences* 67.8, pp. 2469–2482. DOI: `10.1175/2010JAS3379.1`.

Heymsfield, A. J. (1978). "The Characteristics of Graupel Particles in Northeastern Colorado Cumulus Congestus Clouds." In: *Journal of the Atmospheric Sciences* 35.2, pp. 284–295. DOI: `10.1175/1520-0469(1978)035<0284:TCOGPI>2.0.CO;2`.

– (1982). "A Comparative Study of the Rates of Development of Potential Graupel and Hail Embryos in High Plains Storms." In: *Journal of the Atmospheric Sciences* 39.12, pp. 2867–2897. DOI: `10.1175/1520-0469(1982)039<2867:ACSOTR>2.0.CO;2`.

Heymsfield, A. J., C. Schmitt, C. C. J. Chen, A. Bansemer, A. Gettelman, P. R. Field, and C. Liu (2020). "Contributions of the Liquid and Ice Phases to Global Surface Precipitation: Observations and Global Climate Modeling." In: *Journal of the Atmospheric Sciences* 77 (8), pp. 2629–2648. DOI: `10.1175/JAS-D-19-0352.1`.

Higa, M., M. Arakawa, and N. Maeno (1998). "Size Dependence of Restitution Coefficients of Ice in Relation to Collision Strength." In: *Icarus* 133, pp. 310–320. DOI: `10.1006/icar.1998.5938`.

Hobbs, P. V. and R. Farber (1972). "Fragmentation of ice particles in clouds." In: *Journal de Recherches Atmospheriques* 6, pp. 245–258.

Hobbs, P. V., M. K. Politovich, and L. F. Radke (1980). "The Structures of Summer Convective Clouds in Eastern Montana. I: Natural Clouds." In: *Journal of Applied Meteorology and Climatology* 19 (6), pp. 645–663. DOI: `10.1175/1520-0450(1980)019<0645:TSOSCC>2.0.CO;2`.

Hoffmann, F. (2020). "Effects of Entrainment and Mixing on the WegenerBergeron-Findeisen Process." In: *Journal of the Atmospheric Sciences* 77 (6), pp. 2279–2296. DOI: `10.1175/JAS-D-19-0289.1`.

Hogan, R. J., M. P. Mittermaier, and A. J. Illingworth (2006). "The Retrieval of Ice Water Content from Radar Reflectivity Factor and Temperature and Its Use in

Evaluating a Mesoscale Model." In: *Journal of Applied Meteorology and Climatology* 45.2, pp. 301–317. DOI: `10.1175/JAM2340.1`.

Homann, H., T. Guillot, J. Bec, C. W. Ormel, S. Ida, and P. Tanga (2016). "Effect of turbulence on collisions of dust particles with planetesimals in protoplanetary disks." In: *Astronomy & Astrophysics* 589, A129. DOI: `10.1051/0004-6361/201527344`.

Hosler, C. L. and R. E. Hallgren (1960). "The aggregation of small ice crystals." In: *Discussions of the Faraday Society* 30 (0), pp. 200–207. DOI: `10.1039/DF9603000200`.

J, H. and J. Mason (1958). "The influence of temperature and supersaturation on the habit of ice crystals grown from the vapour." In: *Proceedings of the Royal Society of London. Series A. Mathematical and Physical Sciences* 247 (1251), pp. 440–453. DOI: `10.1098/rspa.1958.0199`.

Jackson, R. L., I. Green, and D. B. Marghitu (2010). "Predicting the coefficient of restitution of impacting elastic-perfectly plastic spheres." In: *Nonlinear Dynamics* 60 (3), pp. 217–229. DOI: `10.1007/s11071-009-9591-z`.

Jayaweera, K. O. L. F. and R. E. Cottis (1969). "Fall velocities of plate-like and columnar ice crystals." In: *Quarterly Journal of the Royal Meteorological Society* 95.406, pp. 703–709. DOI: `10.1002/qj.49709540604`.

Jeffreys, H. (1918). "XXX. Some problems of evaporation." In: *The London, Edinburgh, and Dublin Philosophical Magazine and Journal of Science* 35 (207), pp. 270–280. DOI: `10.1080/14786440308635761`.

Jensen, A. A. and J. Y. Harrington (2015). "Modeling Ice Crystal Aspect Ratio Evolution during Riming: A Single-Particle Growth Model." In: *Journal of the Atmospheric Sciences* 72.7, pp. 2569–2590. DOI: `10.1175/JAS-D-14-0297.1`.

Jensen, A. A., J. Y. Harrington, H. Morrison, and J. A. Milbrandt (2017). "Predicting Ice Shape Evolution in a Bulk Microphysics Model." In: *Journal of the Atmospheric Sciences* 74 (6), pp. 2081–2104. DOI: `10.1175/JAS-D-16-0350.1`.

Ji, W. and P. K. Wang (1999). "Ventilation Coefficients for Falling Ice Crystals in the Atmosphere at LowIntermediate Reynolds Numbers." In: *Journal of the Atmospheric Sciences* 56 (6), pp. 829–836. DOI: `10.1175/1520-0469(1999)056<0829:VCFFIC>2.0.CO;2`.

Jiusto, J. E. and H. K. Weickmann (1973). "types of snowfall." In: *Bulletin of the American Meteorological Society* 54 (11), pp. 1148–1162. DOI: `10.1175/1520-0477(1973)054<1148:TOS>2.0.CO;2`.

Kalesse, H., W. Szyrmer, S. Kneifel, P. Kollias, and E. Luke (2016). "Fingerprints of a riming event on cloud radar Doppler spectra: observations and modeling." In: *Atmospheric Chemistry and Physics* 16.5, pp. 2997–3012. DOI: `10.5194/acp-16-2997-2016`.

Kanji, Z. A., L. A. Ladino, H. Wex, Y. Boose, M. Burkert-Kohn, D. J. Cziczo, and M. Krämer (2017). "Overview of Ice Nucleating Particles." In: *Meteorological Monographs* 58, pp. 1.1–1.33. DOI: `10.1175/amsmonographs-d-16-0006.1`.

Karrer, M., A. Seifert, D. Ori, and S. Kneifel (2021). "Improving the representation of aggregation in a two-moment microphysical scheme with statistics of multi-frequency Doppler radar observations." In: *Atmospheric Chemistry and Physics* 21.22, pp. 17133–17166. DOI: `10.5194/acp-21-17133-2021`.

Ke, C., S. Shu, H. Zhang, H. Yuan, and D. Yang (2018). "On the drag coefficient and averaged Nusselt number of an ellipsoidal particle in a fluid." In: *Powder Technology* 325, pp. 134–144. DOI: `10.1016/J.POWTEC.2017.10.049`.

Keith, W. D. and C. P. Saunders (1989). "The collection efficiency of a cylindrical target for ice crystals." In: *Atmospheric Research* 23 (1), pp. 83–95. DOI: `10.1016/0169-8095(89)90059-8`.

Kessler, E. (1969). "On the Distribution and Continuity of Water Substance in Atmospheric Circulations." In: American Meteorological Society, pp. 1–84. DOI: `10.1007/978-1-935704-36-2_1`.

Khain, A. P., N. BenMoshe, and A. Pokrovsky (2008). "Factors Determining the Impact of Aerosols on Surface Precipitation from Clouds: An Attempt at Classification." In: *Journal of the Atmospheric Sciences* 65 (6), pp. 1721–1748. DOI: `10.1175/2007JAS2515.1`.

Khvorostyanov, V. I. and J. A. Curry (2005). "Fall Velocities of Hydrometeors in the Atmosphere: Refinements to a Continuous Analytical Power Law." In: *Journal of the Atmospheric Sciences* 62.12, pp. 4343–4357. DOI: `10.1175/JAS3622.1`.

Kikuchi, K., T. Kameda, K. Higuchi, and A. Yamashita (2013). "A global classification of snow crystals, ice crystals, and solid precipitation based on observations from middle latitudes to polar regions." In: *Atmospheric Research* 132-133, pp. 460–472. DOI: `10.1016/j.atmosres.2013.06.006`.

Kintea, D. M., I. V. Roisman, T. Hauk, and C. Tropea (2015). "Shape evolution of a melting nonspherical particle." In: *Physical Review E - Statistical, Nonlinear, and Soft Matter Physics* 92 (3). DOI: `10.1103/PhysRevE.92.033012`.

Kirchner, H. O. K., G. Michot, and T. Suzuki (2000). "A Fracture toughness of snow in tension." In: *Philosophical Magazine* 80 (5), pp. 1265–1272. DOI: `10.1080/01418610008212114`.

Kiwitt, T., K. Fröhlich, M. Meinke, and W. Schröder (2022). "Nusselt correlation for ellipsoidal particles." In: *International Journal of Multiphase Flow* 149, p. 103941. DOI: `10.1016/J.IJMULTIPHASEFLOW.2021.103941`.

Kneifel, S., J. Leinonen, J. Tyynelä, D. Ori, and A. Battaglia (2020). "Scattering of Hydrometeors." In: *Satellite Precipitation Measurement*. Vol. 1. Springer Cham, pp. 249–276. DOI: `https://doi.org/10.1007/978-3-030-24568-9_15`.

Kobayashi, T. (1961). "The growth of snow crystals at low supersaturations." In: *The Philosophical Magazine: A Journal of Theoretical Experimental and Applied Physics* 6.71, pp. 1363–1370. DOI: `10.1080/14786436108241231`.

Koenig, L. R. and F. W. Murray (1976). "Ice-Bearing Cumulus Cloud Evolution: Numerical Simulation and General Comparison Against Observations." In: *Journal of Applied Meteorology and Climatology* 15.7, pp. 747–762. DOI: `10.1175/1520-0450(1976)015<0747:IBCCEN>2.0.CO;2`.

Korolev, A., I. Heckman, M. Wolde, A. S. Ackerman, A. M. Fridlind, L. A. Ladino, R. P. Lawson, J. Milbrandt, and E. Williams (2020). "A new look at the environmental conditions favorable to secondary ice production." In: *Atmospheric Chemistry and Physics* 20.3, pp. 1391–1429. DOI: `10.5194/acp-20-1391-2020`.

Korolev, A. and G. Isaac (2003). "Roundness and Aspect Ratio of Particles in Ice Clouds." In: *Journal of the Atmospheric Sciences* 60.15, pp. 1795–1808. DOI: `10.1175/1520-0469(2003)060<1795:RAAROP>2.0.CO;2`.

Korolev, A. and T. Leisner (2020). "Review of experimental studies of secondary ice production." In: *Atmospheric Chemistry and Physics* 20 (20), pp. 11767–11797. DOI: `10.5194/acp-20-11767-2020`.

Kumjian, M. R., O. P. Prat, K. J. Reimel, M. V. Lier-Walqui, A. Ryzhkov, M. R. Kumjian, O. P. Prat, K. J. Reimel, M. V. Lier-Walqui, and H. C. Morrison (2022).

"Dual-Polarization Radar Fingerprints of Precipitation Physics: A Review." In: *Remote Sensing* 14 (15), p. 3706. DOI: `10.3390/RS14153706`.

Kumjian, M. R. (2018). "Weather Radars." In: Springer, pp. 15–63. DOI: `10.1007/978-3-319-72583-3_2`.

Kuroda, T. and R. Lacmann (1982). "Growth kinetics of ice from the vapour phase and its growth forms." In: *Journal of Crystal Growth* 56.1, pp. 189–205. DOI: `10.1016/0022-0248(82)90028-8`.

Lagerquist, R., D. Turner, I. Ebert-Uphoff, J. Stewart, and V. Hagerty (2021). "Using Deep Learning to Emulate and Accelerate a Radiative Transfer Model." In: *Journal of Atmospheric and Oceanic Technology* 38.10, pp. 1673–1696. DOI: `10.1175/JTECH-D-21-0007.1`.

Lamb, D. and J. Verlinde (2011). *Physics and Chemistry of Clouds*. Cambridge University Press. DOI: `10.1017/CBO9780511976377`.

Lasher-Trapp, S., S. Kumar, D. H. Moser, A. M. Blyth, J. R. French, R. C. Jackson, D. C. Leon, and D. M. Plummer (2018). "On Different Microphysical Pathways to Convective Rainfall." In: *Journal of Applied Meteorology and Climatology* 57.10, pp. 2399–2417. DOI: `10.1175/JAMC-D-18-0041.1`.

Lauber, A., J. Henneberger, C. Mignani, F. Ramelli, J. T. Pasquier, J. Wieder, M. Hervo, and U. Lohmann (2021). "Continuous secondary-ice production initiated by updrafts through the melting layer in mountainous regions." In: *Atmospheric Chemistry and Physics* 21.5, pp. 3855–3870. DOI: `10.5194/acp-21-3855-2021`.

Lawson, R. P., B. Pilson, B. Baker, Q. Mo, E. Jensen, L. Pfister, and P. Bui (2008). "Aircraft measurements of microphysical properties of subvisible cirrus in the tropical tropopause layer." In: *Atmospheric Chemistry and Physics* 8.6, pp. 1609–1620. DOI: `10.5194/acp-8-1609-2008`.

Leinonen, J. and D. Moisseev (2015). "What do triple-frequency radar signatures reveal about aggregate snowflakes?" In: *Journal of Geophysical Research: Atmospheres* 120 (1), pp. 229–239. DOI: `10.1002/2014JD022072`.

Leinonen, J. (2013). "Impact of the microstructure of precipitation and hydrometeors on multi-frequency radar observations." English. Doctoral thesis. School of Science, 58 + app. 82.

– (2014). "High-level interface to T-matrix scattering calculations: architecture, capabilities and limitations." In: *Optics Express* 22.2, pp. 1655–1660. DOI: `10.1364/OE.22.001655`.

Leinonen, J. and W. Szyrmer (2015). "Radar signatures of snowflake riming: A modeling study." In: *Earth and Space Science* 2 (8), pp. 346–358. DOI: `10.1002/2015EA000102`.

Leon, D. C., J. R. French, S. Lasher-Trapp, A. M. Blyth, S. J. Abel, S. Ballard, A. Barrett, L. J. Bennett, K. Bower, B. Brooks, P. Brown, C. Charlton-Perez, T. Choularton, P. Clark, C. Collier, J. Crosier, Z. Cui, S. Dey, D. Dufton, C. Eagle, M. J. Flynn, M. Gallagher, C. Halliwell, K. Hanley, L. Hawkness-Smith, Y. Huang, G. Kelly, M. Kitchen, A. Korolev, H. Lean, Z. Liu, J. Marsham, D. Moser, J. Nicol, E. G. Norton, D. Plummer, J. Price, H. Ricketts, N. Roberts, P. D. Rosenberg, D. Simonin, J. W. Taylor, R. Warren, P. I. Williams, and G. Young (2016). "The Convective Precipitation Experiment (COPE): Investigating the Origins of Heavy Precipitation in the Southwestern United Kingdom." In: *Bulletin of the American Meteorological Society* 97.6, pp. 1003–1020. DOI: `10.1175/BAMS-D-14-00157.1`.

Libbrecht, K. G. (2023). *Snowcrystals.com*. (Visited on 07/10/2023).

Libbrecht, K. G. (2017). "Physical Dynamics of Ice Crystal Growth." In: *Annual Review of Materials Research* 47 (1), pp. 271–295. DOI: `10.1146/annurev-matsci-070616-124135`.

Lin, Y.-L., R. D. Farley, and H. D. Orville (1983). "Bulk Parameterization of the Snow Field in a Cloud Model." In: *Cover Journal of Applied Meteorology and Climatology Journal of Applied Meteorology and Climatology* 22 (6), pp. 1065–1092. DOI: `10.1175/1520-0450(1983)022<1065:BPOTSF>2.0.CO;2`.

Liu, Y., M.-K. Yau, S.-I. Shima, C. Lu, S. Chen, C. : Liu, M.-K. Yau, S.-I. Shima, C. S. Lu, and S. S. Chen (2023). "Parameterization and Explicit Modeling of Cloud Microphysics: Approaches, Challenges, and Future Directions." In: *Advances in Atmospheric Sciences* 40 (5), pp. 747–790. DOI: `10.1007/S00376-022-2077-3`.

Locatelli, J. D. and P. V. Hobbs (1974). "Fall speeds and masses of solid precipitation particles." In: *Journal of Geophysical Research* 79.15, pp. 2185–2197. DOI: `10.1029/JC079i015p02185`.

Löhnert, U., J. H. Schween, C. Acquistapace, K. Ebell, M. Maahn, M. Barrera-Verdejo, A. Hirsikko, B. Bohn, A. Knaps, E. O'Connor, C. Simmer, A. Wahner, and S. Crewell (2015). "JOYCE: Jülich Observatory for Cloud Evolution." In: *Bulletin of the American Meteorological Society* 96 (7), pp. 1157–1174. DOI: `10.1175/BAMS-D-14-00105.1`.

Maahn, M. (2015). "Exploiting vertically pointing Doppler radar for advancing snow and ice cloud observations." PhD thesis. Universität zu Köln.

Magono, C. and T. Nakamura (1965). "Aerodynamic Studies of Falling Snowflakes." In: *Journal of the Meteorological Society of Japan. Ser. II* 43.3, pp. 139–147. DOI: `10.2151/jmsj1965.43.3_139`.

Marinescu, I. D. and M. Pruteanu (2015). "Chapter 2 - Deformation and Fracture of Ceramic Materials." In: *Handbook of Ceramics Grinding and Polishing*. Ed. by I. D. Marinescu, T. K. Doi, and E. Uhlmann. Boston: William Andrew Publishing, pp. 50–66. DOI: `10.1016/B978-1-4557-7858-4.00002-9`.

Marshall, J. and W. M. K. Palmer (1948). "The Distribution of Raindrops with Size." In: *Journal of the Atmospheric Sciences* 5 (4), pp. 165–166. DOI: `10.1175/1520-0469(1948)005<0165:TDORWS>2.0.CO;2`.

Martin, J. J., P. K. Wang, H. R. Pruppacher, and R. L. Pitter (1981). "Numerical Study of the Effect of Electric Charges on the Efficenciy with which Planar Ice Crystals Collect Supercooled Cloud Drops." In: *Journal of the Atmospheric Sciences* 38.11, pp. 2462–2469. DOI: `10.1175/1520-0469(1981)038<2462:ANSOTE>2.0.CO;2`.

Mason, B. J. and R. Ramanadham (1954). "Modification of the size distribution of falling raindrops by coalescence." In: *Quarterly Journal of the Royal Meteorological Society* 80 (345), pp. 388–394. DOI: `10.1002/qj.49708034508`.

Mason, J. (1971). *The Physics of Clouds*. 2nd ed. Oxford Universtiy Press, pp. 1–671.

Matrosov, S. Y. (1998). "A Dual-Wavelength Radar Method to Measure Snowfall Rate." In: *Journal of Applied Meteorology* 37.11, pp. 1510–1521. DOI: `10.1175/1520-0450(1998)037<1510:ADWRMT>2.0.CO;2`.

Matrosov, S. Y., G. G. Mace, R. Marchand, M. D. Shupe, A. G. Hallar, and I. B. Mccubbin (2012). "Observations of Ice Crystal Habits with a Scanning Polarimetric W-Band Radar at Slant Linear Depolarization Ratio Mode." In: *Journal of Atmospheric and Oceanic Technology* 29 (8), pp. 989–1008. DOI: `10.1175/JTECH-D-11-00131.1`.

McCorquodale, M. W. and C. D. Westbrook (2021a). “TRAIL part 2: A comprehensive assessment of ice particle fall speed parametrisations.” In: *Quarterly Journal of the Royal Meteorological Society* 147.734, pp. 605–626. DOI: `10.1002/qj.3936`.

– (2021b). “TRAIL: A novel approach for studying the aerodynamics of ice particles.” In: *Quarterly Journal of the Royal Meteorological Society* 147.734, pp. 589–604. DOI: `10.1002/qj.3935`.

McDonald, J. (1963). “Use of electrostatic analogy in studies of ice crystal growth.” In: *Zeitschrift für angewandte Mathematik und Physik* 14 (5), pp. 610–620. DOI: `10.1007/BF01601268`.

Melnikov, V. and J. M. Straka (2013). “Axis Ratios and Flutter Angles of Cloud Ice Particles: Retrievals from Radar Data.” In: *Journal of Atmospheric and Oceanic Technology* 30 (8), pp. 1691–1703. DOI: `10.1175/JTECH-D-12-00212.1`.

Meyers, M. P., P. J. DeMott, and W. R. Cotton (1992). “New Primary Ice-Nucleation Parameterizations in an Explicit Cloud Model.” In: *Journal of Applied Meteorology* 31 (7), pp. 708–721. DOI: `10.1175/1520-0450(1992)031<0708:NPINPI>2.0.CO;2`.

Milbrandt, J. A. and H. Morrison (2016). “Parameterization of Cloud Microphysics Based on the Prediction of Bulk Ice Particle Properties. Part III: Introduction of Multiple Free Categories.” In: *Journal of the Atmospheric Sciences* 73.3, pp. 975–995. DOI: `10.1175/JAS-D-15-0204.1`.

Milbrandt, J. A. and M. K. Yau (2005). “A Multimoment Bulk Microphysics Parameterization. Part II: A Proposed Three-Moment Closure and Scheme Description.” In: *Journal of the Atmospheric Sciences* 62.9, pp. 3065–3081. DOI: `10.1175/JAS3535.1`.

Milbrandt, J. A., H. Morrison, D. T. D. II, and M. Paukert (2021). “A Triple-Moment Representation of Ice in the Predicted Particle Properties (P3) Microphysics Scheme.” In: *Journal of the Atmospheric Sciences* 78.2, pp. 439–458. DOI: `10.1175/JAS-D-20-0084.1`.

Mitchell, D. L. (1988). “Evolution of Snow-Size Spectra in Cyclonic Storms. Part I: Snow Growth by Vapor Deposition and Aggregation.” In: *Journal of the Atmospheric Sciences* 45 (22), pp. 3431–3451. DOI: `10.1175/1520-0469(1988)045<3431:EOSSSI>2.0.CO;2`.

– (1996). “Use of Mass- and Area-Dimensional Power Laws for Determining Precipitation Particle Terminal Velocities.” In: *Journal of the Atmospheric Sciences* 53.12, pp. 1710–1723. DOI: `10.1175/1520-0469(1996)053<1710:UOMAAD>2.0.CO;2`.

Mitchell, D. L., R. Zhang, and R. L. Pitter (1990). “Mass-Dimensional Relationships for Ice Particles and the Influence of Riming on Snowfall Rates.” In: *Journal of Applied Meteorology* 29 (2), pp. 153–163. DOI: `10.1175/1520-0450(1990)029<0153:MDRFIP>2.0.CO;2`.

Mitra, S. K., O. Vohl, M. Ahr, and H. R. Pruppacher (1990). “A Wind Tunnel and Theoretical Study of the Melting Behavior of Atmospheric Ice Particles. IV: Experiment and Theory for Snow Flakes.” In: *Journal of Atmospheric Sciences* 47.5, pp. 584–591. DOI: `10.1175/1520-0469(1990)047<0584:AWTATS>2.0.CO;2`.

Moisseev, D. N. and V. Chandrasekar (2007). “Nonparametric Estimation of Raindrop Size Distributions from Dual-Polarization Radar Spectral Observations.” In: *Journal of Atmospheric and Oceanic Technology* 24 (6), pp. 1008–1018. DOI: `10.1175/JTECH2024.1`.

Morrison, H., G. de Boer, G. Feingold, J. Harrington, M. D. Shupe, and K. Sulia (2012). “Resilience of persistent Arctic mixed-phase clouds.” In: *Nature Geoscience* 5 (1), pp. 11–17. DOI: `10.1038/ngeo1332`.

Morrison, H. and W. W. Grabowski (2008). "A Novel Approach for Representing Ice Microphysics in Models: Description and Tests Using a Kinematic Framework." In: *Journal of the Atmospheric Sciences* 65.5, pp. 1528–1548. DOI: `10.1175/2007JAS2491.1`.

Morrison, H., M. van Lier-Walqui, A. M. Fridlind, W. W. Grabowski, J. Y. Harrington, C. Hoose, A. Korolev, M. R. Kumjian, J. A. Milbrandt, H. Pawlowska, D. J. Posselt, O. P. Prat, K. J. Reimel, S.-I. Shima, B. van Diedenhoven, and L. Xue (2020). "Confronting the Challenge of Modeling Cloud and Precipitation Microphysics." In: *Journal of Advances in Modeling Earth Systems* 12.8, e2019MS001689. DOI: `10.1029/2019MS001689`.

Morrison, H. and J. A. Milbrandt (2015). "Parameterization of Cloud Microphysics Based on the Prediction of Bulk Ice Particle Properties. Part I: Scheme Description and Idealized Tests." In: *Journal of the Atmospheric Sciences* 72 (1), pp. 287–311. DOI: `10.1175/JAS-D-14-0065.1`.

Mossop, S. C. (1976). "Production of secondary ice particles during the growth of graupel by riming." In: *Quarterly Journal of the Royal Meteorological Society* 102 (431), pp. 45–57. DOI: `10.1002/QJ.49710243104`.

Mróz, K., A. Battaglia, S. Kneifel, L. P. D'Adderio, and J. D. Neto (2020). "Triple-Frequency Doppler Retrieval of Characteristic Raindrop Size." In: *Earth and Space Science* 7 (3), e2019EA000789. DOI: `10.1029/2019EA000789`.

Mülmenstädt, J., O. Sourdeval, J. Delanoë, and J. Quaas (2015). "Frequency of occurrence of rain from liquid-, mixed-, and ice-phase clouds derived from A-Train satellite retrievals." In: *Geophysical Research Letters* 42 (15), pp. 6502–6509. DOI: `10.1002/2015GL064604`.

Myagkov, A., P. Seifert, M. Bauer-Pfundstein, and U. Wandinger (2016a). "Cloud radar with hybrid mode towards estimation of shape and orientation of ice crystals." In: *Atmospheric Measurement Techniques* 9 (2), pp. 469–489. DOI: `10.5194/AMT-9-469-2016`.

Myagkov, A., P. Seifert, U. Wandinger, J. Bühl, and R. Engelmann (2016b). "Relationship between temperature and apparent shape of pristine ice crystals derived from polarimetric cloud radar observations during the ACCEPT campaign." In: *Atmospheric Measurement Techniques* 9 (8), pp. 3739–3754. DOI: `10.5194/AMT-9-3739-2016`.

Nakaya, U. (1954). *Snow Crystals, Natural and Artificial*. Harvard University Press, pp. 1–510.

Naumann, A. K. and A. Seifert (2015). "A Lagrangian drop model to study warm rain microphysical processes in shallow cumulus." In: *Journal of Advances in Modeling Earth Systems* 7.3, pp. 1136–1154. DOI: `10.1002/2015MS000456`.

– (2016). "Evolution of the Shape of the Raindrop Size Distribution in Simulated Shallow Cumulus." In: *Journal of the Atmospheric Sciences* 73.6, pp. 2279–2297. DOI: `10.1175/JAS-D-15-0263.1`.

Nelson, J. T. and M. B. Baker (1996). "New theoretical framework for studies of vapor growth and sublimation of small ice crystals in the atmosphere." In: *Journal of Geophysical Research: Atmospheres* 101.D3, pp. 7033–7047. DOI: `10.1029/95JD03162`.

Nelson, J. (1998). "Sublimation of Ice Crystals." In: *Journal of the Atmospheric Sciences* 55.5, pp. 910–919. DOI: `10.1175/1520-0469(1998)055<0910:SOIC>2.0.CO;2`.

Nettesheim, J. J. and P. K. Wang (2018). "A Numerical Study on the Aerodynamics of Freely Falling Planar Ice Crystals." In: *Journal of the Atmospheric Sciences* 75 (9), pp. 2849–2865. DOI: `10.1175/JAS-D-18-0041.1`.

Ori, D., V. Schemann, M. Karrer, J. D. Neto, L. von Terzi, A. Seifert, and S. Kneifel (2020). "Evaluation of ice particle growth in ICON using statistics of multi-frequency Doppler cloud radar observations." In: *Quarterly Journal of the Royal Meteorological Society* 146 (733), pp. 3830–3849. DOI: `10.1002/QJ.3875`.

Oseen, C. W. (1927). *Neuere Methoden und Ergebnisse in der Hydrodynamik*. Akad. Verlagsgesellschaft Leipzig, p. 337.

Oue, M., P. Kollias, A. Ryzhkov, and E. P. Luke (2018). "Toward Exploring the Synergy Between Cloud Radar Polarimetry and Doppler Spectral Analysis in Deep Cold Precipitating Systems in the Arctic." In: *Journal of Geophysical Research: Atmospheres* 123.5, pp. 2797–2815. DOI: `10.1002/2017JD027717`.

Petrovic, J. J. (2003). "Review Mechanical properties of ice and snow." In: *Journal of Materials Science* 38, pp. 1–6. DOI: `10.1023/A:1021134128038`.

Petters, M. D. and T. P. Wright (2015). "Revisiting ice nucleation from precipitation samples." In: *Geophysical Research Letters* 42 (20), pp. 8758–8766. DOI: `10.1002/2015GL065733`.

Pfitzenmaier, L. and U. Löhnert (2023). *"Disdrometer data from Jülich on 31 January 2022", ACTRIS Cloud remote sensing data centre unit (CLU)*. `https://cloudnet.fmi.fi/file/b00ce7b1-483e-4da0-b143-06433ca33ba0`.

Pfitzenmaier, L., C. M. Unal, Y. Dufournet, and H. W. Russchenberg (2018). "Observing ice particle growth along fall streaks in mixed-phase clouds using spectral polarimetric radar data." In: *Atmospheric Chemistry and Physics* 18 (11), pp. 7843–7862. DOI: `10.5194/acp-18-7843-2018`.

Phillips, V. T. J., S. Patade, J. Gutierrez, and A. Bansemer (2018). "Secondary Ice Production by Fragmentation of Freezing Drops: Formulation and Theory." In: *Journal of the Atmospheric Sciences* 75.9, pp. 3031–3070. DOI: `10.1175/JAS-D-17-0190.1`.

Phillips, V. T. J., J.-I. Yano, A. Deshmukh, and D. Waman (2021). "Comment on "Review of experimental studies of secondary ice production" by Korolev and Leisner (2020)." In: *Atmospheric Chemistry and Physics* 21.15, pp. 11941–11953. DOI: `10.5194/acp-21-11941-2021`.

Phillips, V. T., M. Formenton, A. Bansemer, I. Kudzotsa, and B. Lienert (2015). "A parameterization of sticking efficiency for collisions of snow and graupel with ice crystals: Theory and comparison with observations." In: *Journal of the Atmospheric Sciences* 72 (12), pp. 4885–4902. DOI: `10.1175/JAS-D-14-0096.1`.

Phillips, V. T. J., J.-I. Yano, and A. Khain (2017a). "Ice Multiplication by Breakup in Ice–Ice Collisions. Part I: Theoretical Formulation." In: *Journal of the Atmospheric Sciences* 74.6, pp. 1705–1719. DOI: `10.1175/JAS-D-16-0224.1`.

Phillips, V. T. J., J.-I. Yano, M. Formenton, E. Ilotoviz, V. Kanawade, I. Kudzotsa, J. Sun, A. Bansemer, A. G. Detwiler, A. Khain, and S. A. Tessendorf (2017b). "Ice Multiplication by Breakup in Ice–Ice Collisions. Part II: Numerical Simulations." In: *Journal of the Atmospheric Sciences* 74.9, pp. 2789–2811. DOI: `10.1175/JAS-D-16-0223.1`.

Pinsky, M., A. Khain, and M. Shapiro (2001). "Collision Efficiency of Drops in a Wide Range of Reynolds Numbers: Effects of Pressure on Spectrum Evolution." In: *Journal of the Atmospheric Sciences* 58.7, pp. 742–764. DOI: `10.1175/1520-0469(2001)058<0742:CEODIA>2.0.CO;2`.

Pitter, R. L., H. R. Pruppacher, and A. E. Hamielec (1974). "A Numerical Study of the Effect of Forced Convection on Mass Transport from a Thin Oblate Spheroid of Ice in Air." In: *Journal of the Atmospheric Sciences* 31 (4), pp. 1058–1066. DOI: 10.1175/1520-0469(1974)031<1058:ANSOTE>2.0.CO;2.

Podzimek, J. (1966). "Experimental determination of the "capacity" of ice crystals." In: *Stud Geophys Geod* 10, pp. 235–238. DOI: 10.1007/BF02585763.

Polycarpou, A. A. and I. Etsion (1999). "Analytical Approximations in Modeling Contacting Rough Surfaces." In: *Journal of Tribology* 121.2, pp. 234–239. DOI: 10.1115/1.2833926.

Posselt, R., M. Simmel, and S. Wurzler (2004). "Comment on Revision and clarification of "A general hydrodynamic theory for mixed-phase microphysics" [Böhm, J.P., 1999, Atmos. Res. 52, 167–176]." In: *Atmospheric Research* 69.3, pp. 281–287. DOI: 10.1016/j.atmosres.2003.03.001.

Proske, U., V. Bessenbacher, Z. Dedekind, U. Lohmann, and D. Neubauer (2021). "How frequent is natural cloud seeding from ice cloud layers ($< -35\,^{\circ}\mathrm{C}$) over Switzerland?" In: *Atmospheric Chemistry and Physics* 21.6, pp. 5195–5216. DOI: 10.5194/acp-21-5195-2021.

Pruppacher, H. and J. Klett (1997). *Microphysics of Clouds and Precipitation*. Springer Netherlands, p. 954. DOI: 10.1007/978-0-306-48100-0.

Purcell, E. M. and C. R. Pennypacker (1973). "Scattering and Absorption of Light by Nonspherical Dielectric Grains." In: *Atrophysical Journal* 186, pp. 705–714. DOI: 10.1086/152538.

Raghavan, S. (2003). *Radar Meteorology*. Springer Dordrecht, p. 549. DOI: 10.1007/978-94-017-0201-0.

Rasmussen, R. M. and A. J. Heymsfield (1985). "A Generalized Form for Impact Velocities Used to Determine Graupel Accretional Densities." In: *Journal of the Atmospheric Sciences* 42.21, pp. 2275–2279. DOI: 10.1175/1520-0469(1985)042<2275:AGFFIV>2.0.CO;2.

Rasmussen, R. M. and A. J. Heymsfield (1987). "Melting and Shedding of Graupel and Hail. Part I: Model Physics." In: *Journal of Atmospheric Sciences* 44.19, pp. 2754–2763. DOI: 10.1175/1520-0469(1987)044<2754:MASOGA>2.0.CO;2.

Reinking, R. F. (1979). "The Onset and Early Growth of Snow Crystals by Accretion of Droplets." In: *Journal of Atmospheric Sciences* 36 (5), pp. 870–881. DOI: 10.1175/1520-0469(1979)036<0870:TOAEGO>2.0.CO;2.

Riechelmann, T., Y. Noh, and S. Raasch (2012). "A new method for large-eddy simulations of clouds with Lagrangian droplets including the effects of turbulent collision." In: *New Journal of Physics* 14 (6), p. 065008. DOI: 10.1088/1367-2630/14/6/065008.

Ryzhkov, A., P. Zhang, H. Reeves, M. Kumjian, T. Tschallener, S. Trömel, and C. Simmer (2016). "Quasi-Vertical Profiles—A New Way to Look at Polarimetric Radar Data." In: *Journal of Atmospheric and Oceanic Technology* 33.3, pp. 551–562. DOI: 10.1175/JTECH-D-15-0020.1.

Sanjeevi, S. K., J. F. Dietiker, and J. T. Padding (2022). "Accurate hydrodynamic force and torque correlations for prolate spheroids from Stokes regime to high Reynolds numbers." In: *Chemical Engineering Journal* 444, p. 136325. DOI: 10.1016/J.CEJ.2022.136325.

Schlamp, R., H. Pruppacher, and A. Hamielec (1975). "A Numerical Investigation of the Efficiency with which Simple Columnar Ice Crystals Collide with Supercooled Water Drops." In: *Journal of the Atmospheric Sciences* 32.12, pp. 2330–2337. DOI: 10.1175/1520-0469(1975)032<2330:ANIOTE>2.0.CO;2.

Schrom, R. S. and M. R. Kumjian (2016). "Connecting Microphysical Processes in Colorado Winter Storms with Vertical Profiles of Radar Observations." In: *Journal of Applied Meteorology and Climatology* 55.8, pp. 1771–1787. DOI: `10.1175/JAMC-D-15-0338.1`.

Schrom, R. S., M. R. Kumjian, and Y. Lu (2015). "Polarimetric Radar Signatures of Dendritic Growth Zones within Colorado Winter Storms." In: *Journal of Applied Meteorology and Climatology* 54.12, pp. 2365–2388. DOI: `10.1175/JAMC-D-15-0004.1`.

Schwarzenboeck, A., V. Shcherbakov, R. Lefevre, J. F. Gayet, Y. Pointin, and C. Duroure (2009). "Indications for stellar-crystal fragmentation in Arctic clouds." In: *Atmospheric Research* 92 (2), pp. 220–228. DOI: `10.1016/J.ATMOSRES.2008.10.002`.

Sei, T. and T. Gonda (1989). "The growth mechanism and the habit change of ice crystals growing from the vapor phase." In: *Journal of Crystal Growth* 94.3, pp. 697–707. DOI: `10.1016/0022-0248(89)90094-8`.

Seifert, A., C. Köhler, and K. D. Beheng (2012). "Aerosol-cloud-precipitation effects over Germany as simulated by a convective-scale numerical weather prediction model." In: *Atmospheric Chemistry and Physics* 12.2, pp. 709–725. DOI: `10.5194/acp-12-709-2012`.

Seifert, A. and K. D. Beheng (2006). "A two-moment cloud microphysics parameterization for mixed-phase clouds. Part 1: Model description." In: *Meteorology and Atmospheric Physics* 92 (1-2), pp. 45–66. DOI: `10.1007/S00703-005-0112-4/METRICS`.

Seifert, A., J. Leinonen, C. Siewert, and S. Kneifel (2019). "The Geometry of Rimed Aggregate Snowflakes: A Modeling Study." In: *Journal of Advances in Modeling Earth Systems* 11.3, pp. 712–731. DOI: `10.1029/2018MS001519`.

Seifert, A. and S. Rasp (2020). "Potential and Limitations of Machine Learning for Modeling Warm-Rain Cloud Microphysical Processes." In: *Journal of Advances in Modeling Earth Systems* 12 (12), e2020MS002301. DOI: `10.1029/2020MS002301`.

Seifert, A. and C. Siewert (2024). "An ML-Based P3-Like Multimodal Two-Moment Ice Microphysics in the ICON Model." In: *Journal of Advances in Modeling Earth Systems* 16.8, e2023MS004206. DOI: `https://doi.org/10.1029/2023MS004206`.

Seliga, T. A. and V. N. Bringi (1976). "Potential Use of Radar Differential Reflectivity Measurements at Orthogonal Polarizations for Measuring Precipitation." In: *Journal of Applied Meteorology and Climatology* 15 (1), pp. 69–76. DOI: `10.1175/1520-0450(1976)015<0069:PUORDR>2.0.CO;2`.

Sheridan, L. M., J. Y. Harrington, D. Lamb, and K. Sulia (2009). "Influence of Ice Crystal Aspect Ratio on the Evolution of Ice Size Spectra during Vapor Depositional Growth." In: *Journal of the Atmospheric Sciences* 66.12, pp. 3732–3743. DOI: `10.1175/2009JAS3113.1`.

Sheridan, L. M. (2008). "Deposition Coefficient, Habit, and Ventilation Influences on Cirriform Cloud Properties." MA thesis. Dept.of Meteorology, The Pennsylvanian State University, p. 92.

Shima, S., K. Kusano, A. Kawano, T. Sugiyama, and S. Kawahara (2009). "The super-droplet method for the numerical simulation of clouds and precipitation: a particle-based and probabilistic microphysics model coupled with a non-hydrostatic model." In: *Quarterly Journal of the Royal Meteorological Society* 135 (642), pp. 1307–1320. DOI: `10.1002/qj.441`.

Shima, S., Y. Sato, A. Hashimoto, and R. Misumi (2020). "Predicting the morphology of ice particles in deep convection using the super-droplet method: development and evaluation of SCALE-SDM 0.2.5-2.2.0, -2.2.1, and -2.2.2." In: *Geoscientific Model Development* 13.9, pp. 4107–4157. DOI: `10.5194/gmd-13-4107-2020`.

Shupe, M. D., P. Kollias, S. Y. Matrosov, and T. L. Schneider (2004). "Deriving Mixed-Phase Cloud Properties from Doppler Radar Spectra." In: *Journal of Atmospheric and Oceanic Technology* 21.4, pp. 660–670. DOI: `10.1175/1520-0426(2004)021<0660:DMCPFD>2.0.CO;2`.

Slater, B. and A. Michaelides (2019). "Surface premelting of water ice." In: *Nature Reviews Chemistry 2019* 3 (3), pp. 172–188. DOI: `10.1038/s41570-019-0080-8`.

Sölch, I. and B. Kärcher (2010). "A large-eddy model for cirrus clouds with explicit aerosol and ice microphysics and Lagrangian ice particle tracking." In: *Quarterly Journal of the Royal Meteorological Society* 136 (653), pp. 2074–2093. DOI: `10.1002/qj.689`.

Sotiropoulou, G., A. Lewinschal, P. Georgakaki, V. Phillips, S. Patade, A. M. L. Ekman, and A. Nenes (2024). "Sensitivity of Arctic clouds to ice microphysical processes in the NorESM2 climate model." In: *Journal of Climate*. DOI: `10.1175/JCLI-D-22-0458.1`.

Sotiropoulou, G., S. Sullivan, J. Savre, G. Lloyd, T. Lachlan-Cope, A. M. Ekman, and A. Nenes (2020). "The impact of secondary ice production on Arctic stratocumulus." In: *Atmospheric Chemistry and Physics* 20 (3), pp. 1301–1316. DOI: `10.5194/ACP-20-1301-2020`.

Sotiropoulou, G., E. Vignon, G. Young, H. Morrison, S. J. O'Shea, T. Lachlan-Cope, A. Berne, and A. Nenes (2021). "Secondary ice production in summer clouds over the Antarctic coast: An underappreciated process in atmospheric models." In: *Atmospheric Chemistry and Physics* 21 (2), pp. 755–771. DOI: `10.5194/ACP-21-755-2021`.

Sulia, K. J. and J. Y. Harrington (2011). "Ice aspect ratio influences on mixed-phase clouds: Impacts on phase partitioning in parcel models." In: *Journal of Geophysical Research: Atmospheres* 116 (D21), p. 21309. DOI: `10.1029/2011JD016298`.

Sullivan, S. C., C. Barthlott, J. Crosier, I. Zhukov, A. Nenes, and C. Hoose (2018). "The effect of secondary ice production parameterization on the simulation of a cold frontal rainband." In: *Atmospheric Chemistry and Physics* 18 (22), pp. 16461–16480. DOI: `10.5194/ACP-18-16461-2018`.

Sun, Z. and K. P. Shine (1994). "Studies of the radiative properties of ice and mixed-phase clouds." In: *Quarterly Journal of the Royal Meteorological Society* 120.515, pp. 111–137. DOI: `10.1002/qj.49712051508`.

Sutherland, W. (1893). "LII. The viscosity of gases and molecular force." In: *The London, Edinburgh, and Dublin Philosophical Magazine and Journal of Science* 36.223, pp. 507–531. DOI: `10.1080/14786449308620508`.

Takahashi, C. and A. Yamashita (1977). "Production of Ice Splinters by the Freezing of Water Drops in Free Fall." In: *Journal of the Meteorological Society of Japan. Ser. II* 55.1, pp. 139–141. DOI: `10.2151/jmsj1965.55.1_139`.

Takahashi, T. (2014). "Influence of Liquid Water Content and Temperature on the Form and Growth of Branched Planar Snow Crystals in a Cloud." In: *Journal of the Atmospheric Sciences* 71 (11), pp. 4127–4142. DOI: `10.1175/JAS-D-14-0043.1`.

Takahashi, T., T. Endoh, G. Wakahama, and N. Fukuta (1991). "Vapor Diffusional Growth of Free-Falling Snow Crystals between -3 and −23°C." In: *Journal of the Meteorological Society of Japan. Ser. II* 69.1, pp. 15–30. DOI: `10.2151/jmsj1965.69.1_15`.

Takahashi, T. and N. Fukuta (1988). “Supercooled Cloud Tunnel Studies on the Growth of Snow Crystals between-4 and-20°C.” In: *Journal of the Meteorological Society of Japan. Ser. II* 66 (6), pp. 841–855. DOI: `10.2151/jmsj1965.66.6_841`.

Takahashi, T. (1993). “High Ice Crystal Production in Winter Cumuli over the Japan Sea.” In: *Geophysical Research Letters* 20 (6), pp. 451–454.

Takahashi, T., Y. Nagao, and Y. Kushiyama (1995). “Possible High Ice Particle Production during Graupel–Graupel Collisions.” In: *Journal of the Atmospheric Sciences* 52.24, pp. 4523–4527. DOI: `10.1175/1520-0469(1995)052<4523:PHIPPD>2.0.CO;2`.

The 10th International Cloud Modeling Workshop (2024). (Visited on 07/08/2024).

Tippmann, J. D., H. Kim, and J. D. Rhymer (2013). “Experimentally validated strain rate dependent material model for spherical ice impact simulation.” In: *International Journal of Impact Engineering* 57, pp. 43–54. DOI: `10.1016/j.ijimpeng.2013.01.013`.

Tridon, F., A. Battaglia, R. J. Chase, F. J. Turk, J. Leinonen, S. Kneifel, K. Mroz, J. Finlon, A. Bansemer, S. Tanelli, A. J. Heymsfield, and S. W. Nesbitt (2019). “The Microphysics of Stratiform Precipitation During OLYMPEX: Compatibility Between Triple-Frequency Radar and Airborne In Situ Observations.” In: *Journal of Geophysical Research: Atmospheres* 124.15, pp. 8764–8792. DOI: `10.1029/2018JD029858`.

Trömel, S., C. Simmer, U. Blahak, A. Blanke, S. Doktorowski, F. Ewald, M. Frech, M. Gergely, M. Hagen, T. Janjic, H. Kalesse-Los, S. Kneifel, C. Knote, J. Mendrok, M. Moser, G. Köcher, K. Mühlbauer, A. Myagkov, V. Pejcic, P. Seifert, P. Shrestha, A. Teisseire, L. von Terzi, E. Tetoni, T. Vogl, C. Voigt, Y. Zeng, T. Zinner, and J. Quaas (2021). “Overview: Fusion of radar polarimetry and numerical atmospheric modelling towards an improved understanding of cloud and precipitation processes.” In: *Atmospheric Chemistry and Physics* 21.23, pp. 17291–17314. DOI: `10.5194/acp-21-17291-2021`.

Ukkonen, P. (2022). “Exploring Pathways to More Accurate Machine Learning Emulation of Atmospheric Radiative Transfer.” In: *Journal of Advances in Modeling Earth Systems* 14.4, e2021MS002875. DOI: `https://doi.org/10.1029/2021MS002875`.

Um, J., G. M. McFarquhar, Y. P. Hong, S.-S. Lee, C. H. Jung, R. P. Lawson, and Q. Mo (2015). “Dimensions and aspect ratios of natural ice crystals.” In: *Atmospheric Chemistry and Physics* 15.7, pp. 3933–3956. DOI: `10.5194/acp-15-3933-2015`.

Unterstrasser, S., F. Hoffmann, and M. Lerch (2017). “Collection/aggregation algorithms in Lagrangian cloud microphysical models: Rigorous evaluation in box model simulations.” In: *Geoscientific Model Development* 10 (4), pp. 1521–1548. DOI: `10.5194/gmd-10-1521-2017`.

vanZanten, M. C., B. Stevens, L. Nuijens, A. P. Siebesma, A. S. Ackerman, F. Burnet, A. Cheng, F. Couvreux, H. Jiang, M. Khairoutdinov, Y. Kogan, D. C. Lewellen, D. Mechem, K. Nakamura, A. Noda, B. J. Shipway, J. Slawinska, S. Wang, and A. Wyszogrodzki (2011). “Controls on precipitation and cloudiness in simulations of trade-wind cumulus as observed during RICO.” In: *Journal of Advances in Modeling Earth Systems* 3 (2), n/a–n/a. DOI: `10.1029/2011MS000056`.

Vardiman, L. (1974). “The Generation of Secondary Ice Particles in Clouds by Crystal-Crystal Collision.” PhD thesis. Colorado State University, pp. 1–117.

– (1978). “The Generation of Secondary Ice Particles in Clouds by Crystal–Crystal Collision.” In: *Journal of the Atmospheric Sciences* 35.11, pp. 2168–2180. DOI: `10.1175/1520-0469(1978)035<2168:TGOSIP>2.0.CO;2`.

von Blohn, N., K. Diehl, S. K. Mitra, and S. Borrmann (2009). “Riming of Graupel: Wind Tunnel Investigations of Collection Kernels and Growth Regimes.” In: *Journal of the Atmospheric Sciences* 66 (8), pp. 2359–2366. DOI: `10.1175/2009JAS2969.1`.

von Terzi, L. (2023). “Investigating Ice Microphysical Processes by Combining Multi-frequency and Polarimetric Doppler Radar Observations with Lagrangian Monte-Carlo Particle Modelling.” PhD thesis. Universität zu Köln.

von Terzi, L., J. D. Neto, D. Ori, A. Myagkov, and S. Kneifel (2022). “Ice microphysical processes in the dendritic growth layer: a statistical analysis combining multi-frequency and polarimetric Doppler cloud radar observations.” In: *Atmospheric Chemistry and Physics* 22 (17), pp. 11795–11821. DOI: `10.5194/ACP-22-11795-2022`.

Wall, S., W. John, H.-C. Wang, and S. L. Goren (1990). “Measurements of Kinetic Energy Loss for Particles Impacting Surfaces.” In: *Aerosol Science and Technology* 12.4, pp. 926–946. DOI: `10.1080/02786829008959404`.

Wang, P. K. and H. R. Pruppacher (1977). “Acceleration to Terminal Velocity of Cloud and Raindrops.” In: *Journal of Applied Meteorology and Climatology* 16 (3), pp. 275–280. DOI: `10.1175/1520-0450(1977)016<0275:ATTVOC>2.0.CO;2`.

Wang, P. K. (2013). *Physics and Dynamics of Clouds and Precipitation*. Cambridge University Press, pp. 1–460. DOI: `10.1017/CBO9780511794285`.

– (2021). *Motions of Ice Hydrometeors in the Atmosphere*. Springer Singapore. DOI: `10.1007/978-981-33-4431-0`.

Wang, P. K. and W. Ji (2000). “Collision Efficiencies of Ice Crystals at LowIntermediate Reynolds Numbers Colliding with Supercooled Cloud Droplets: A Numerical Study.” In: *Journal of the Atmospheric Sciences* 57.8, pp. 1001–1009. DOI: `10.1175/1520-0469(2000)057<1001:CEOICA>2.0.CO;2`.

Waterman, P. C. (1965). “Matrix formulation of electromagnetic scattering.” In: *Proceedings of the IEEE* 53.8, pp. 805–812. DOI: `10.1109/PROC.1965.4058`.

Welss, J.-N., C. Siewert, and A. Seifert (2024). “Explicit Habit-Prediction in the Lagrangian Super-Particle Ice Microphysics Model McSnow.” In: *Journal of Advances in Modeling Earth Systems* 16.4, e2023MS003805. DOI: `10.1029/2023MS003805`.

Westbrook, C. D. and E. K. Sephton (2017). “Using 3-D-printed analogues to investigate the fall speeds and orientations of complex ice particles.” In: *Geophysical Research Letters* 44.15, pp. 7994–8001. DOI: `10.1002/2017GL074130`.

Westbrook, C. D., R. J. Hogan, A. J. Illingworth, C. D. Westbrook, R. J. Hogan, and A. J. Illingworth (2008). “The Capacitance of Pristine Ice Crystals and Aggregate Snowflakes.” In: *Journal of the Atmospheric Sciences* 65 (1), pp. 206–219. DOI: `10.1175/2007JAS2315.1`.

Wex, H., L. Huang, W. Zhang, H. Hung, R. Traversi, S. Becagli, R. J. Sheesley, C. E. Moffett, T. E. Barrett, R. Bossi, H. Skov, A. Hünerbein, J. Lubitz, M. Löffler, O. Linke, M. Hartmann, P. Herenz, and F. Stratmann (2019). “Annual variability of ice-nucleating particle concentrations at different Arctic locations.” In: *Atmospheric Chemistry and Physics* 19 (7), pp. 5293–5311. DOI: `10.5194/ACP-19-5293-2019`.

Whitaker, S. (1972). “Forced convection heat transfer correlations for flow in pipes, past flat plates, single cylinders, single spheres, and for flow in packed beds and tube bundles.” In: *AIChE Journal* 18 (2), pp. 361–371. DOI: `10.1002/AIC.690180219`.

Woo, S. E. and A. E. Hamielec (1971). “A Numerical Method of Determining the Rate of Evaporation of Small Water Drops Falling at Terminal Velocity in Air.” In: *Journal of the Atmospheric Sciences* 28 (8), pp. 1448–1454. DOI: `10.1175/1520-0469(1971)028<1448:ANMODT>2.0.CO;2`.

Yano, J. I. and V. T. J. Phillips (2011). "Ice–Ice Collisions: An Ice Multiplication Process in Atmospheric Clouds." In: *Journal of the Atmospheric Sciences* 68 (2), pp. 322–333. DOI: `10.1175/2010JAS3607.1`.

Yano, J. I., V. T. J. Phillips, and V. Kanawade (2016). "Explosive ice multiplication by mechanical break-up in ice–ice collisions: a dynamical system-based study." In: *Quarterly Journal of the Royal Meteorological Society* 142 (695), pp. 867–879. DOI: `10.1002/QJ.2687`.

Yoshida, Y., S. Asano, and K. Iwanami (2006). "Retrieval of microphysical properties of water, ice, and mixed-phase clouds using a triple-wavelength radar and microwave radiometer." In: *Journal of the Meteorological Society of Japan. Ser. II* 84.6, pp. 1005–1031.

Young, G., T. Lachlan-Cope, S. J. O'Shea, C. Dearden, C. Listowski, K. N. Bower, T. W. Choularton, and M. W. Gallagher (2019). "Radiative Effects of Secondary Ice Enhancement in Coastal Antarctic Clouds." In: *Geophysical Research Letters* 46.4, pp. 2312–2321. DOI: `10.1029/2018GL080551`.

Yurkin, M. A. and A. G. Hoekstra (2011). "The discrete-dipole-approximation code ADDA: Capabilities and known limitations." In: *Journal of Quantitative Spectroscopy and Radiative Transfer* 112.13, pp. 2234–2247. DOI: `10.1016/j.jqsrt.2011.01.031`.

Zängl, G., D. Reinert, P. Rípodas, and M. Baldauf (2015). "The ICON (ICOsahedral Non-hydrostatic) modelling framework of DWD and MPI-M: Description of the non-hydrostatic dynamical core." In: *Quarterly Journal of the Royal Meteorological Society*. DOI: `10.1002/qj.2378`.

Zhao, X., X. Liu, S. Burrows, P. J. DeMott, M. Diao, G. M. McFarquhar, S. Patade, V. T. J. Phillips, G. C. Roberts, K. J. Sanchez, Y. Shi, and M. Zhang (2023). "Important Ice Processes Are Missed by the Community Earth System Model in Southern Ocean Mixed-Phase Clouds: Bridging SOCRATES Observations to Model Developments." In: *Journal of Geophysical Research: Atmospheres* 128.4, e2022JD037513. DOI: `10.1029/2022JD037513`.

LIST OF ACRONYMS AND VARIABLES

Acronyms

AR	Aspect Ratio
BLT	Boundary Layer Theory
CKE	Collision Kinetic Energy
DDA	Discrete Dipole Approximation
DGL	Dendritic Growth Layer
OGL	Oblate Growth Layer
DWD	Deutscher Wettedienst
DWR	Dual-Wavelength Ratio
EUMETSAT	European Organisation for the Exploitation of Meteorological Satellites
GPS	Global Positioning System
HP	Habit Prediction
HRV	High Resolution Visible
ICON	Icosahedral Nonhydrostatic
IGF	Inherent Growth Function
IMPRINT	Understanding **I**ce **M**icrophysical **P**rocesses by combining multi-frequency and spectral **R**adar polar**I**metry a**N**d super-par**T**icle modeling
IMP	Ice Microphysical Process
INP	Ice Nucleating Particles
IPNC	Ice Particle Number Concentration
IWC	Ice Water Content
JOYCE-CF	Jülich ObservatorY for Cloud Evolution Core Facility
K_{DP}	Specific Differential Phase
LES	Large Eddy Simulation
LPM	Lagrangian Particle Model
LDR	Linear Depolarisation Ratio
LWC	Liquid Water Content
LWP	Liquid Water Path
LWZ	Liquid Water Zone
MASC	Multi-Angle Snowflake Camera
MDV	Mean Doppler Velocity

ML	Machine Learning
NZ	Nucleation Zone
NWP	Numerical Weather Prediction
PR	Polarizability Ratio
PSD	Particle-Size Distribution
PFS	Phillips Fragmentation Scheme
PROM	**P**olarimetric **R**adar **O**bservations meet Atmospheric **M**odelling
QLL	Quasi-Liquid Layer
SEVIRI	Spinning Enhanced Visible and Infrared Imager
SIP	Secondary Ice Production
STSR	Simultaneous Transmit - Simultaneous Receive
TRAIL	**T**rajectory **R**econstruction **A**lgorithm implemented through Image ana**L**ysis
TRIPEx-pol	**TRI**ple-frequency and **P**olarimetric radar **Ex**periment for improving process observation of winter precipitation
UFS	Updated Fragmentation Scheme

Variables

Roman letters

A_{branch}	Fracture area
A_{n}	Estimated asperity number density
A_{asp}	Lateral area of an asperity
a	Equatorial radius
C_{f}	Asperity-fragility coefficient
A	Projected area
b_2	Fraction of the energy available to break asperities
X	Best number
X'	Turbulence modified Best number
δ	Boundary layer thickness
c	Polar radius
C	Capacitance of the ice particle
$C_{\mathrm{DP,S}}$	Drag coefficient
C_{DI}	Inertial drag coefficient
C^{*}_{DI}	Inertial drag coefficient with respect to r^{*}
C_{DP}	Drag coefficient fitted for prolates
C_{DO}	Oseen drag coefficient
q_{res}	Coefficient of restitution
K_0	Collision kinetic energy
K_{c}	Ice fracture toughness
C_{d}	Drag coefficient
V_{crit}	Critical volume
ΔS	Change in surface adhesion energy
D	Maximum dimension
F_{r}	Degree of riming
$\lvert K_{\lambda}\rvert$	Dielectric properties at wavelength λ
D_{v}	Vapor diffusivity
μ	Dynamic viscosity
E_{c}	Collision efficiency
E	Effective modulus of elasticity
$\mathcal{F}$	Crystal fragility
$\mathcal{G}$	Geometry term
K_{d}	Thermal conductivity of dry air

K_0	Initial collision kinetic energy
$K_{\mathbf{fin}}$	Final collision kinetic energy
K	Collision kernel
k	Viscous shape parameter
L_s	Latent heat of sublimation
d_{foci}	Semi length of foci
m	Mass
N_{LWC}	Number of droplets for a specific LWC
N_{frag}	Number of fragments
N_m	Number of monomers
$N_{contact}$	Number of breakable asperities at the point of contact
$n_{branch}(\mathbf{M})$	Number density of breakable asperities
P_{HM}	Rate of ice crystals produced by rime splintering
$\mathcal{P}$	Particle properties
$\vec{v}$	Positional vector
p_{vap}	Vapor pressure
r_{asp}	Lateral radius of an asperity
r_d	Droplet radius
Re	Reynolds number
RR	Precipitation rate
R_{imp}	Impact parameter
R_v	Gas constant of water vapor
S_i	Sticking efficency of ice
S_y	Dynamic yield strength
S_{mono}	Monomers surface area
S_{agg}	Aggregates surface area
sZ_e	Spectral reflectivity
G_c	Fracture energy
T	Temperature
T_s	Surface temperature of the ice particle
f_v	Ventilation coefficient
V_i	Ice volume
v_{imp}	Impact velocity
V_r	Rime volume
v_t	Terminal fall velocity
v_D	Doppler velocity

y_s	Stop distance of the collected particle
G_{break}	Work needed to break a single asperity
z	Height above ground
Z	Radar reflectivity factor
sZ_{DR}	Spectral differential reflectivity
$sZ_{\mathbf{DR,max}}$	Maximum spectral differential reflectivity
Z_{DR}	Differential reflectivity
Z_e	Equivalent radar reflectivity factor

Greek letters

α_{equiv}	Equivalent spherical area
σ_b	Backscattering cross section
Γ	Inherent Growth Function
Γ_f	Gamma function
Γ_ϕ	Function regarding the aspect ratio
ϕ	Aspect ratio
Φ_{DP}	Differential phase shift
ξ_d	Droplet multiplicity
λ	Radar wavelength
ξ_p	Porosity based on shape
ξ	Multiplicity
σ_{kern}	Artificial turbulence modifier
Ξ	Probability to break an asperity
ρ_a	Air density
$\rho_{\mathrm{depo.}}$	Deposition density
ρ_{app}	Apparent density
ρ_{rime}	Density of newly formed rime
ρ_i	Density of solid ice
ζ	Mass fraction of the more fragile particles

ACKNOWLEDGMENTS

PUBLICATIONS

During my time as PhD student the following paper has been published:

J.-N. Welss et al. (2024). “Explicit Habit-Prediction in the Lagrangian Super-Particle Ice Microphysics Model McSnow.” In: *Journal of Advances in Modeling Earth Systems* 16.4, e2023MS003805. DOI: `10.1029/2023MS003805`
My contribution to this publication was writing the manuscript

COLOPHON

This document was typeset using the typographical look-and-feel `classicthesis` developed by André Miede and Ivo Pletikosić. The style was inspired by Robert Bringhurst's seminal book on typography *"The Elements of Typographic Style"*.